Dissertation

submitted to the

Combined Faculties of the Natural Sciences and Mathematics

of the Ruperto-Carola-University of Heidelberg, Germany

for the degree of

Doctor of Natural Sciences

Put forward by

Dipl.Phys. Jan Pitann

born in Rostock, Germany

Date of oral examination: 17$^{\text{th}}$ of October 2012

INFRARED AND RADIO OBSERVATIONS OF THE EARLIEST STAGES OF MASSIVE STAR FORMATION

by

JAN PITANN

Referees: Prof. Dr. Thomas Henning

Prof. Dr. Reinhard Mundt

Infrared and radio observations of the earliest stages of massive star formation

It is assumed that objects which will eventually evolve into high-mass main sequence stars ($M_{\rm final} > 8\,M_\odot$) can initially appear as low- to intermediate-mass young stellar objects that are still accreting mass. By initiating a SPITZER mid-infrared spectroscopic survey of intermediate mass young stellar objects, selected from massive star-forming clumps and infrared dark clouds (IRDCs), an evolutionary sequence was established. A group of particularly young stellar objects (YSOs) was found showing several ice and silicate absorption features. A second group was identified: these objects represent more evolved YSOs that already emit a significant amount of UV radiation and feature shock-excited gas driven by proto-stellar outflows. Importantly, the observed extended emission of cationic polycyclic aromatic hydrocarbons (PAHs) and the analysis of molecular hydrogen indicates the creation of a very young photon dissociation region while the expected radio emission from the associated H II region is still undetectable.
An automated photometric pipeline was developed to detect cold dense cores and extract their far-infrared fluxes in HERSCHEL bolometer maps while taking into account the complicated background and additional instrumental effects. By studying the fragmentation in the high-mass part of the HERSCHEL EPoS program a typical point source separation of $\sim 0.5\,$pc was found throughout the sample. The detected sources are in an evolutionary stage where they are embedded in the dust clumps associated with the parental cloud. This typical source separation is not retained in later stages, such as in young stellar clusters.
Furthermore, a comprehensive case study is presented in which an isolated IRDC region is used to analyze the conditions of massive star formation in the absence of strong external effects. Two point sources found in this region are candidates for evolving into high-mass main-sequence stars. The filamentary star-forming cloud is in free collapse while the embedded molecular clumps are gravitationally bound. The observed dust temperature structure shows that the dark cloud is not isothermal. The locations of temperature minima are in good spatial agreement with the column density peaks. Together with the structure of molecular clumps identified by radio line observations these results confirm that the dust temperatures are lowest in the densest parts of the dark cloud.

Infrarot- und Radiobeobachtung der Frühphasen massereicher Sternentstehung

Es wird davon ausgegangen, dass auch Quellen, die sich letztendlich zu massereichen Sternen entwickeln, anfänglich als akkretierende, junge, stellar Objekte mit geringer oder mittlerer Masse zu beobachten sind. Eine Reihe von jungen stellaren Objekten im mittleren Massebereich aus ausgewählten massereichen Sternentstehungsgebieten wurden mittels Spektroskopie im mittleren Infrarot mit SPITZER beobachtet. Anhand dieser Beobachtungen lassen sich diese Objekte gemäß ihres Entwicklungsstadiums einordnen. Eine erste Gruppe, bestehend aus besonders jungen stellaren Objekten, wurde dabei identifiziert. Diese zeichnet sich durch mehrere charakteristische Eis- und Silikatbanden in den spektroskopischen Beobachtungen aus. Eine zweite Gruppe repräsentiert weiter entwickelte Objekte, die bereits einen beträchtlichen Strahlungsfluss im Ultravioleten aufweisen sowie Gas in Stoßfronten, angeregt durch protostellare Ausflüsse. Ein noch wichtigeres Merkmal sind die ausgedehnten Emissionen geladener polyzyklischer aromatische Kohlenwasserstoffverbindungen (PAK). Zusammen mit der Analyse des vorhandenen molekularen Wasserstoffs lassen sie auf die Entstehung einer sehr jungen photonendominierten Region (PDR) schließen. Die erwartete PDR-Radioemission ist jedoch noch nicht zu beobachten.
Eine automatisierte photometrische Pipeline wurde entwickelt, um kalte Kerne hoher Dichte zu detektieren und Strahlungsdichten dieser Quellen in HERSCHEL-Ferninfrarot-Karten zu vermessen. Das entwickelte Programm wurde optimiert, um den Einfluß des komplizierten Infrarot-Hintergrundes und weitere instrumentenbedingte Beschränkungen zu minimieren. Durch die Untersuchung der Fragmentierung der massereichen Regionen im HERSCHEL-Beobachtungsprogramm EPoS wurde eine typische räumliche Separation der einzelnen Quellen von etwa 0,5 Parsec gefunden. Diese Separation findet sich jedoch nicht in späteren Evolutionsstadien, beispielsweise in junge Sternhaufen.
Ferner wird eine umfassende Fallstudie vorgelegt, in welcher die physikalische Beschaffenheit einer isolierten Dunkelwolke untersucht wird, welche keinen erkennbaren äußeren Einflüssen unterliegt. Zwei der Punktquellen, die in dieser Region gefunden wurden, sind vielversprechende Kandidaten für künftige massereiche Sterne. Diese Sternentstehungsregion besteht nur aus einem einzigen Filament und wird im freien Kollaps beobachtet. Die molekularen Klumpen in dieser Dunkelwolke scheinen jedoch gravitativ gebunden zu sein. Die gemessene Verteilung der Staubtemperaturen zeigt, dass diese Dunkelwolke nicht isothermisch ist. Die tiefsten Temperaturen stimmen räumlich sehr gut mit den höchsten Säulendichten überein. Diese Messungen zeigen, zusammen mit den molekularen Klumpen, die mittels Radio-Emissionslinien identifiziert wurden, dass die tiefsten Staubtemperaturen in den dichtesten Bereichen dieser Dunkelwolke auftreten.

Contents

1. Introduction

Over their entire life-cycle massive stars have a dramatic effect on their environment. During their formation very young massive stars ionize the surrounding molecular gas with ultraviolet radiation creating H II regions, sweeping away material in the vicinity of the young star. At the end of their lifetime massive stars can eject a large fraction of their hull as stellar winds (Wolf-Rayet-stars). When all nuclear reactions ceases and nothing can prevent catastrophic gravitational collapse, a supernova is triggered, and only a neutron star or a stellar black hole remains. If the parental cloud has not already been disrupted by the stellar winds of the massive star, these supernova events can completely destroy small star-forming clouds (Monaco 2004). High-mass stars have an important impact on the dynamics and evolution of galaxies. Supernovae and massive stellar winds contribute significantly to the recycling of the diffuse molecular gas on galactic scales, as the released momentum is a source for turbulence in the interstellar medium (ISM; e.g., Zinnecker & Yorke 2007). Moreover, H II regions (Elmegreen & Lada 1977) and supernova remnants (de Geus 1992) can trigger new star formation. A large fraction of UV flux in our Galaxy is produced by OB stars (e.g., Binney & Tremaine 2008). Furthermore, supernovae are crucial to the chemical enrichment of the universe since heavy elements are created in the rapid or r-process during nucleosynthesis (Burbidge et al. 1957).

However, high-mass stars ($\geq 8\mathrm{M}_{\odot}$) have a much shorter life span and are much smaller in number compared to their low-mass counter parts. In fact, only a few percent of all stars in the Milky Way are of high-mass. Table 1.1 list the abundance and spectral type for certain mass ranges. O and B stars are typically found either in dense, gravitationally bound OB-clusters or in loose, unbound OB associations. About $10-25\%$ of O and $\sim 2\%$ of B stars appear as field stars, but most of these stars are fast runaway stars ejected from their initial cluster.

The key question about the formation of massive stars is which physical processes determine the final stellar mass. To answer this question one has to understand the initial conditions and early formation processes in massive star-forming regions. High-mass stars form in a dense molecular environment which is required to be cold in order to collapse. This cold material emits the bulk of its energy in the mid to far infrared. The advent of infrared space telescopes during the last two decades has opened up this observational domain in an unprecedented way. Despite this observational leap forward, the direct identification of a massive protostars remains challenging. The recent Herschel

Table 1.1. – Mass ranges of high-mass stars.

Mass range	Designation	Spectral type	Rel. Abundance [a]
$8-16\,\mathrm{M}_{\odot}$	Early B-type stars	B3V to B0V	1.4%
$16-32\,\mathrm{M}_{\odot}$	Late O-type stars	O9V to O6V	0.5%
$32-64\,\mathrm{M}_{\odot}$	Early O-type massive stars	O5V to O2V	0.2%
$64-128\,\mathrm{M}_{\odot}$	O-type, late Wolf-Rayet stars	WNL-H	0.09%

[a] adopted from Zinnecker & Yorke (2007), corresponding to a stellar mass function of $dN/d\log M \sim M^{-1.35}$

space mission provides the wavelength coverage, spatial resolution, sensitivity, and dynamic range necessary to unravel the mystery of massive star formation.

Massive star formation is associated with Giant molecular clouds (GMCs)[1]. These are the largest structures in our galaxies with masses of $10^4 - 10^7\,\mathrm{M}_\odot$ and a size of $50 - 200\,\mathrm{pc}$ (Blitz 1993). In the quiescent parts of GMCs the average temperature is about $10 - 15\,\mathrm{K}$. GMCs are highly hierarchically structured on all spatial scales, breaking down into filamentary structures, clumps and cores on smaller scales. Cold and dense gas can be traced by (sub-)millimeter emission and molecular radio line emission.

The more diffuse and less dense parts of a GMC with low densities and temperatures can be hard to detect given the sensitivity and spatial filtering for (sub-)millimeter surveys (such as BGPS, ATLASGAL, SCUBA-legacy). Therefore IRDCs or massive cores which appear to be in isolation might be embedded in larger-scale, less dense, material. Through the literature the sizes and masses given to clumps and cores vary. In this work the definition from Bergin & Tafalla (2007) is applied: cores range from $0.03 - 0.2\,\mathrm{pc}$ with typical masses of 0.5-5 $M_\odot$, while clumps extend over $0.3 - 3\,\mathrm{pc}$ with typical masses of $50 - 500\,M_\odot$.

The scenario of the formation of solar-like stars has been well established over the last decades. The evolutionary sequence for low-mass stars, supported by many observational studies, is shown in Figure 1.1. The different stages are broadly distinguished by the different spectral energy distributions (SEDs); the evolution of the SED can be quantified in a simple way by the spectral index α between $2.2\,\mu\mathrm{m}$ and $10 - 25\,\mu\mathrm{m}$:

$$\alpha = \frac{d\log(\lambda F_\lambda)}{d\log(\lambda)} \tag{1.1}$$

Class 0: This class extended the original classification by Lada (1987). The SED for class 0 objects peaks in the sub-millimeter regime correspond to blackbody temperatures of $15 - 30\,\mathrm{K}$. The observational properties are defined as follows (André et al. 1993, 2000): indirect evidence for a central YSO (e.g. compact centimetre source, collimated CO outflows, internal heating source); a central peak, extended sub-millimeter emission; the ratio of the luminosity emitted longward of $350\,\mu\mathrm{m}$ to the total bolometric luminosity must be higher than 0.5%. Class 0 objects represent a formed, hydrostatic protostar deeply embedded into the contracting dense molecular core. This is the main accretion phase where the envelope mass is still significantly higher compared to the mass of the protostar. Bi-polar outflows have been observed for class 0 objects, which implies that disk-like structures around the protostar could already be in place and that infall occurs non-spherically (modulated by accretion through the disk). This first stage last for $\sim 10^4$ yr.

Class I: These sources are characterized by a spectral index of $\alpha > 0$. The SED of this class is shifted into the far-infrared regime. These sources represent more evolved protostars. The SED features blackbody radiation between 50–100 K from the accreting envelope and additional components of 200–400 K from the disk. An optically thick disk has formed around the protostar, often observed by a $10\,\mu\mathrm{m}$ absorption feature. Bi-polar outflows and jets transport momentum and

[1] In fact, the possibly of isolated high-mass star formation is still a matter of debate. de Wit et al. (2005) found a number of O-stars not associated to clusters, they concluded that $(4 \pm 2)\%$ of the galactic O-stars are not runaway stars and instead have formed in isolation. Gvaramadze et al. (2012) claimed, based on new observations, that almost all of this O-stars are unrecognized runaway stars. Selier et al. (2011) found the compact H II region N33 in the Small Magellanic Cloud (SMC) to be a good candidate for isolated massive star formation.

energy away from the star. Mass is accumulated onto the star mostly by disk-accretion. This stage lasts for $\sim 10^5$ yr.

Class II: This class usually refers to Classical T-Tauri stars with a spectral index of $-1.5 < \alpha < 0$. Outflows have swept away the natal envelope, so that only the naked proto-planetary disk and the T-Tauri star remains. The SED dominated by the contracting pre-main-sequence star peaks in the near-infrared but the contribution from the warm dust in the disk causes an infrared-excess. The typical time period for this phase is $\sim 10^7$ yr.

Class III: This class of source are visible in the optical and near-infrared, showing a spectral index of $\alpha < -1.5$. The SED barely shows an excess. Most of the material in the disk has been dispersed or aggregated into larger bodies and planetesimals. The star is no longer contracting and the nuclear fusion is setting in.

The exact meaning of the term "protostar" is often not completely clear when used in the literature, therefore I assume the following definition for this work: "[...] we reserve the term protostar or protostellar object for a gaseous object in hydrostatic equilibrium (gas pressure forces balance the gas' self-gravity), which has not yet begun hydrogen burning but which will, given time, burn hydrogen." (Zinnecker & Yorke 2007). However the onset of hydrogen burning is not directly accessible to observations; therefore I refer in the later chapters to the more general term "Young stellar object" (YSO) which includes protostars and pre-main-sequence stars, deliberately making no distinction between phases before and after nuclear processes have started.

While low-mass star formation has a well defined pre-main-sequence phase the situation is more complex and poorly understood for the high mass case. For example, in contrast to low-mass star formation, the Kelvin-Helmholtz time [2] is shorter than the formation time of high-mass stars $t_{KH} < t_{SF}$. As a consequence, a massive star starts the hydrogen fusion process sooner than a low mass star; therefore the massive star still accrete a large amount of mass at much later stages, and as late as while entering the main sequence (Beuther et al. 2007). Mostly, over the last decay several competitive formation scenarios have been discussed:

- To form a massive star a *monolithic collapse of a turbulent core* in pressure equilibrium with the surrounding was proposed by McKee & Tan (2003). The high density in a fragmenting core results in high accretion rates of $\sim 10^{-3}\,\mathrm{M}_\odot/\mathrm{yr}$ (in contrast to $\sim 10^{-6}\,\mathrm{M}_\odot/\mathrm{yr}$ for low-mass stars). The typical formation timescale in this model is about 10^5 yr. Using similar theoretical setup Krumholz & McKee (2008) concluded that column densities of at least $1\,\mathrm{g\,cm^{-2}}$ are required to efficiently suppress fragmentation to form a high mass star.

- In the *coalescence scenario* high-mass stars could form in clusters by collisions and merging of protostars of lower mass (e.g. Bonnell & Bate 2005; Bally & Zinnecker 2005). This scenario requires very high protostellar and stellar densities ($\sim 10^8\,\mathrm{pc^{-3}}$), but the highest observed stellar densities in clusters reach $\sim 10^6\,\mathrm{pc^{-3}}$.

- The concept of *competitive accretion* does not need the build-up of high-mass stars from a single massive core or by stellar merging. In this scenario massive stars form in a clustered environment where the material accreted onto a particular protostars can originate from various

[2] This is a typical timescale during which the stars radiates away a large fraction of the energy produced under its own contraction.

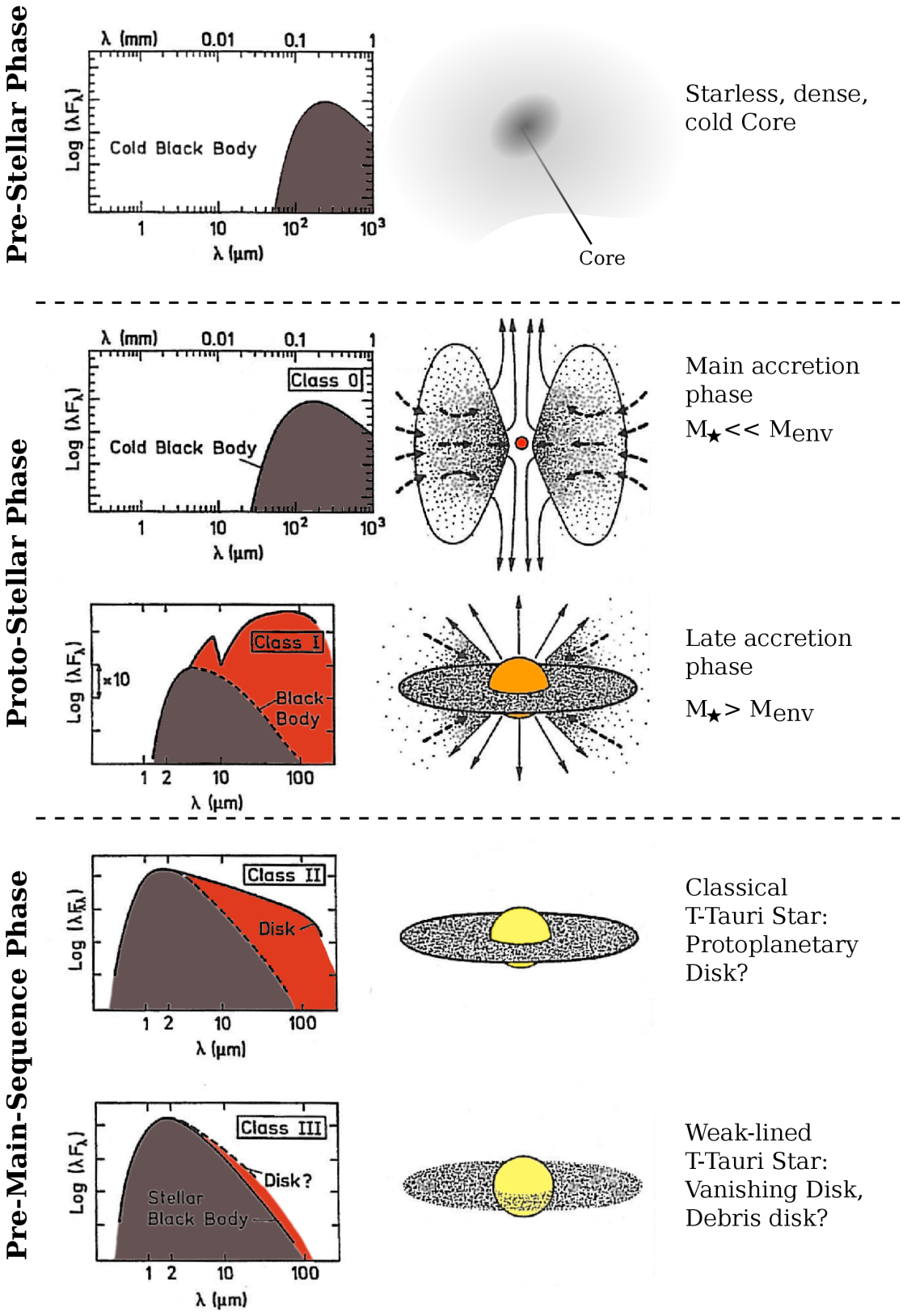

Figure 1.1. – The evolutionary stages of low-mass stars, from a starless/pre-stellar core to the T-Tauri phase, are shown (adopted from André 1994).

parts of the parent cloud (Bonnell et al. 2004). Cluster members compete for the available material. The central objects can accumulate the largest fraction of material and form therefore the most massive stars in the cluster. A major problem of this scenario is that the Bondi accretion (spherically symmetric accretion flow onto an object, Bondi 1952) gets disrupted by radiation pressure as soon as the stellar mass exceeds $\sim 10\,\mathrm{M}_{\odot}$ (Edgar & Clarke 2004). No discontinuity is seen in the IMF at $\sim 10\,\mathrm{M}_{\odot}$ which indicates that competitive accretion is not a significant process at lower masses either (Beuther et al. 2007).

- A more exceptional scenario has been discussed by Elmegreen & Lada (1977) and Deharveng et al. (2010). The H II region formed around a massive YSO can trigger further formation of high-mass stars by gravitationally instabilities in the dense medium at the edge of the ionization and shock front, ionizing radiation acting on a turbulent medium or radiation-driven compression of pre-existing dense clumps.

Regardless of the assumed scenario there is agreement that massive stars form in clusters.

The typical time for the formation of a massive star is $10^5\,\mathrm{yr}$ or less (Osorio et al. 1999). Given this relatively short timescale high-mass stars are still accreting when starting hydrogen fusion. The onset of the hydrogen burning leads to a tremendous increase in luminosity which counters the accretion process. Simulations by Yorke & Sonnhalter (2002) showed that massive stars can in principle be formed via accretion through a disk. In this geometry the radiation can escape perpendicular to the disk, which is often referred to as the "flashlight effect". This calculations can only produce stars up to $43\,\mathrm{M}_{\odot}$. Cavities produced by protostellar outflows can increase the amount of escaping radiation resulting in higher stellar masses (Krumholz et al. 2005a). Even higher stellar masses are possible assuming Rayleigh-Taylor instabilities [3] allow much more material to be accreted (Krumholz et al. 2005b). The formation of a star of more than a hundred solar masses was simulated by Kuiper et al. (2010). They claimed that Rayleigh-Taylor instabilities are not needed to form a massive star. The key to overcome the radiation pressure barrier of $\sim 40\,\mathrm{M}_{\odot}$ was to resolve the dust sublimation front of the disk, and to implement an un-isotorpic IR-shielding in their 2-D calculations to conserve the massive disk.

Based on the observable stages of massive star formation Beuther et al. (2007) purposed an evolutionary sequences for the formation of high-mass stars.

- High-Mass Starless Cores (HMSCs)
- High-Mass Cores harboring accreting low and intermediate-mass protostars which evolve into high-mass stars
- High-Mass Protostellar Objects (HMPOs)
- High-mass stars

Observational results for HMSCs are rare. A number of HMSC candidates were presented by Garay et al. (2004) and Sridharan et al. (2005). Some more unbiased surveys of HMSCs and clouds which are able to form high-mass, based on millimeter observations, were performed by Russeil et al. (2010) and Dunham et al. (2011). The survey by Tackenberg et al. (2012) is based on ATLASGAL $870\,\mu\mathrm{m}$ dust

[3] The Rayleigh-Taylor instability is a hydrodynamic instability occurring at the interface between two fluids of different densities, when the lighter fluids is accelerated into the heaver fluid. In the context of star formation the gas is treated as the heavy fluid accelerated towards the radiation (the light fluid) by the gravitation of the evolving star.

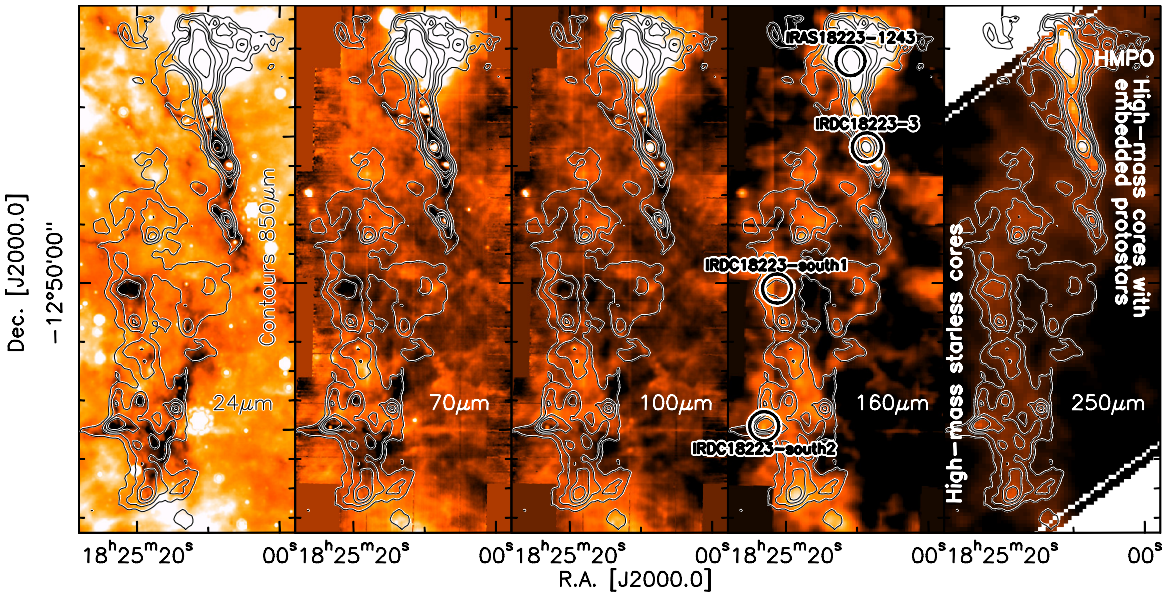

Figure 1.2. – IRDC18223 is a good example for a dark cloud hosting differnt stages of massive star formation. The intensity maps for 24 to 250 μm are shown overplotted with the 850 μm contours (from Beuther et al. 2010).

emission, which provides better spatial resolution and mass sensitivity. In contrast to the previous two surveys the exclusion of mid-infrared point sources is done down to the sensitivity limit of the MIPS 24 μm observations. They observed 20 deg^2 of the sky looking for clumps at distances less than 4 kpc which are able to form stars of more than 20 $M_\odot$. However, the observations indicate, considering a common star formation efficiency and comparing the results with a generic IMF, that $\sim 17\%$ of the identified starless clumps could form a star of $\geq 8\,M_\odot$ (Tackenberg, priv. communication), this result is representative for galactic star-forming regions in a galactocentric distance of $4-8$ kpc. Most of the star-forming gas in our Galaxy is located between these distances (Solomon & Rivolo 1989).

The so-called infrared dark clouds (IRDCs) appear as filamentary opaque structures against the diffuse galactic mid infrared background. As IRDCs are known to be cold ($<$ 20K), dense and reaching high column densities ($\gtrsim 10^{23}$ cm^{-2}), they are suitable environments to form young stellar objects which can evolve into stars of intermediate to high mass (e.g., Carey et al. 2000; Rathborne et al. 2006; Ragan et al. 2006, 2009; Vasyunina et al. 2009). Initially IRDCs were discovered by the Infrared Space Observatory (ISO, Perault et al. 1996) and the Midcourse Space Experiment (MSX, Egan et al. 1998). Cyganowski et al. (2008) and Chambers et al. (2009) identified the so called "green and fuzzies" or "extended green objects" as a star formation tracer mostly occurring in IRDCs; they are caused by rotational lines (S(8)-S(13)) from excited H_2 gas contaminating the green 4.5 μm IRAC band Beuther et al. (2007) argued that Infrared dark clouds (IRDCs) could host HMSCs; in general IRDCs could host several evolutionary stages from HMSCs to HMPOs. Beuther et al. (2010) present a prototypical IRDC which host three different evolutionary stages (see Figure 1.2). In the south a HMSC lacking any point sources emission at 24 μm is found. The middle region contains deeply embedded low to intermediate-mass YSOs that might evolve into high-mass stars. The northern region hosts a bright IRAS-bright HMPO.

In generally, an accreting HMPO has not begun hydrogen fusion yet and is usually accompanied by the formation of a Hot Molecular Core (HMC) and/or Hypercompact H II region (H II , $<$ 0.01 pc).

An Ultracompact H II region (UCH II , $< 0.1\,\mathrm{pc}$) is usually observed in the late HMPO phase by cm-radio free-free emission but can be presented with the final high-mass star for which the accretion has ceased.

If a cloud is only supported by thermal pressure against gravitational collapse, fragmentation on relatively small scales would result. The cloud would become locally unstable if perturbations exceed a certain scale, the so-called *Jeans length*:

$$\begin{aligned} \lambda_J &= \left(\frac{\pi a_T^2}{G\rho_0}\right)^{1/2} \\ &= 0.19\,\mathrm{pc}\,\left(\frac{T}{10\mathrm{K}}\right)^{1/2}\left(\frac{n_{\mathrm{H_2}}}{10^4\,\mathrm{cm}^{-3}}\right)^{-1/2} \end{aligned} \tag{1.2}$$

where $a_t = \omega/k$ is the phase velocity of a sound wave travelling through the isothermal medium and ρ is the isothermal gas density. If thermal pressure is the only effect countering the gravitational collapse, GMCs would convert gas quite fast and efficiently into stars. However, observations do not match this simple scenario in terms of star formation efficiency and formation timescales. Therefore additional forces must be considered to counter the collapse.

One suggested countering force is caused by magnetic fields (Shu et al. 1987), but observational and theoretical studies imply that the effects caused magneto-static fields are too weak to counter the gravitational collapse (Crutcher 1999; Nakano 1998).

Another force against collapse is provided by random non-thermal motions, known as turbulence. Larson (1981) discovered that the velocity dispersion of a cloud down to the core size is related to mass and can be described by a power-law . Cold dense molecular cores or filaments can be produced by gravo-turbulent cloud fragmentation (Mac Low & Klessen 2004); shocks induced by supersonic turbulence can cause local density fluctuations which become unstable, while the cloud remains stable on the global scale supported by turbulence. Simulations by Padoan & Nordlund (2002) show that models with turbulent fragmentation can reproduce the stellar initial mass function (IMF).

However, most of the scenarios and theories cannot be constrained without observations in the infrared regime. This is because in the context of star formation the dust temperatures of interest ranges from 10 (cold pre-stellar cores) to 1000 K (heated dust around evolved protostars), hence the black body radiation emission peaks between 290 and $2.9\,\mu\mathrm{m}$. Beside the thermal continuum emission different absorption and emission bands of scientific interest can be observed in the near, mid, and far-infrared: various silicate species show distinct absorption profiles in the mid-infrared (MIR). Polyclinic aromatic hydrocarbons (PAHs), the most simple organic component of the ISM, have a rich de-excitation spectrum in the MIR. Several atomic transitions are observed from the MIR to FIR, in particular coolants of the ISM as [C II] at $158\,\mu\mathrm{m}$, [O I] at $63\,\mu\mathrm{m}$, [Si II] at $34.8\,\mu\mathrm{m}$, and [Fe II] at $26.0\,\mu\mathrm{m}$. Numerous molecules show rovibrational transition bands in the NIR and MIR. Especially the rotational H2 $\mu\mathrm{m}$ lines from 2 to $28\,\mu\mathrm{m}$ micron are important tracers for excited gas.

The Earths emitted blackbody radiation ($\sim 255\,\mathrm{K}$) gets absorbed by asymmetric molecules, predominately water vapor and CO_2. This makes our atmosphere opaque in the infrared regime. The absorption of incoming light by the Earths atmosphere is shown in Figure 1.3. The FIR is completely blocked, while a few bands become slightly lucent in the sub-millimeter regime with low transmittance at best at high altitudes. In the radio regime (10 mm to 10 m) the atmosphere becomes transparent again, but towards longer wavelengths, electrons in the ionosphere start to shield the incoming electro-magnetic radiation. Therefore, the conventional ground-based observations are limited to the

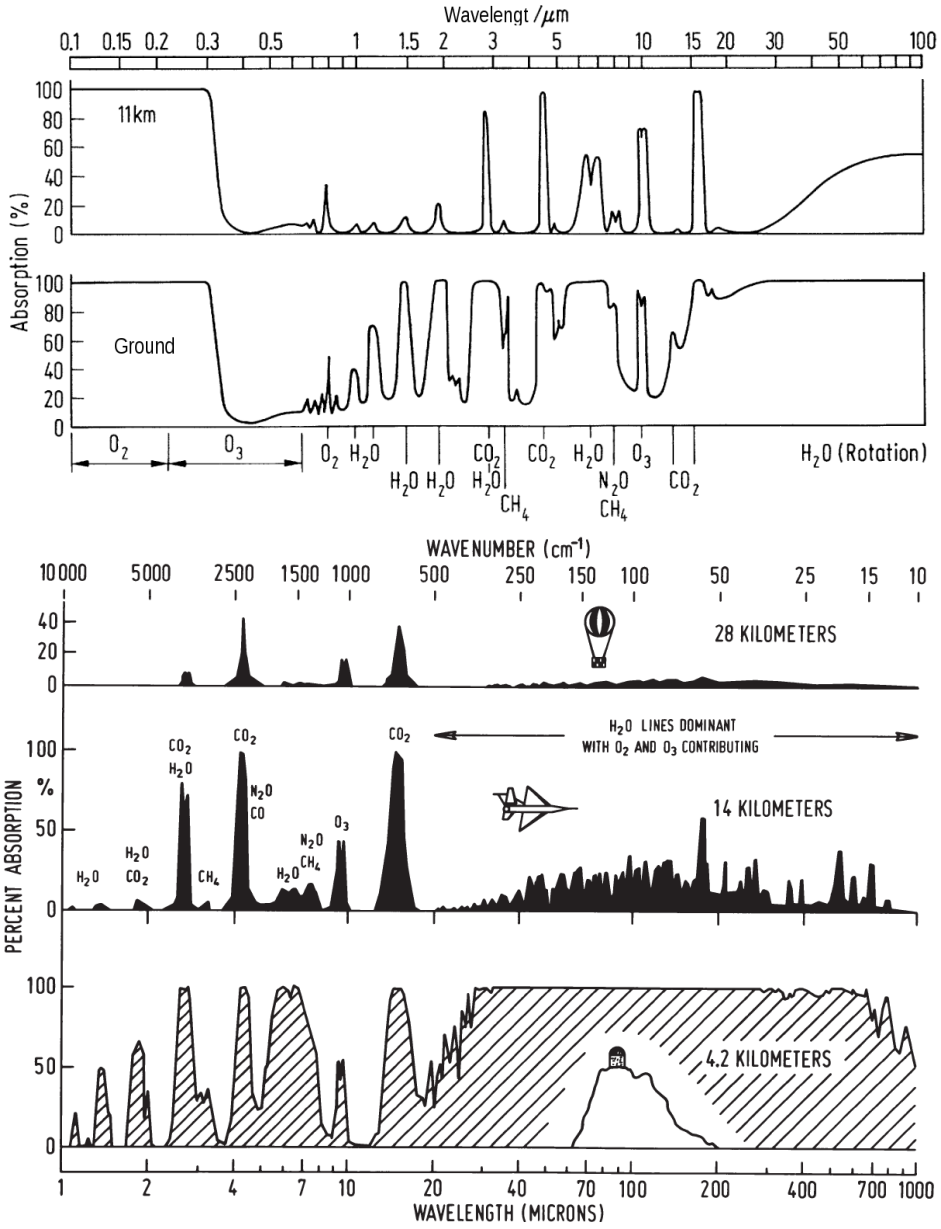

Figure 1.3. – The dependency of the atmospheric absorption profile from wavelength is shown (adopted from Bergmann & Schaefer 2001; Bleeker et al. 2002).

optical, sub-millimeter and radio range. In the radio regime molecular line observations are used as tracers for cold and dense gas.

The inability to perform observations in the mid and far infrared has therefore limited our understanding for the early phase of star formation. One approach to reduce the limitations of ground-based observation is the launch of balloon-borne or airplane-mounted telescopes (see Figure 1.3). Airplanes equipped with telescopes can operate above 99% of the atmospheric water content, but the atmosphere above the aircraft still results in strong background and absorption (Lemke 2009). Moreover, turbulence caused by the telescope hatch and vibrational noise contribute to the observational limitations. After two decades of successful operation, the Kuiper Airborne Observatory (KAO) was decommissioned in 1995. In 2010 the Stratospheric Observatory for Infrared Astronomy (SOFIA) saw first light. Given the low operational and development costs several stratospheric balloon telescopes were launched over the last decades. These can be operated at higher altitudes than airplane mounted telescopes, but suffer from pointing problems.

The full potential of infrared observations was unleashed with the advent of satellite based telescopes which are able to leave the Earths atmosphere. In 1983 the NASA launched the Infrared Astronomical Satellite (IRAS) equipped with a 60 cm cryogenically cooled telescope resulting in a previously unmatched sensitivity. The pioneering 10 month mission of IRAS surveyed about 95% of the sky, cataloging more than $300\,000$ sources at 12, 25, 60, and $100\,\mu\mathrm{m}$ wavelengths.

Given the enormous success of the IRAS mission the ESA announced a European project, the Infrared Space Observatory (ISO), launched in 1995. ISO was equipped with a camera for short infrared wavelengths ISOCAM ($2.5 - 17\,\mu\mathrm{m}$), and the ISOPHOT instrument which consist of an imaging unit at $50 - 240\,\mu\mathrm{m}$ and a spectrograph aover a similar range. The additional two spectrographs for the short ($2 - 45\,\mu\mathrm{m}$, SWS) and long wavelengths ($95 - 197\,\mu\mathrm{m}$, LWS) had relatively high spectral resolution ($R \sim 1\,000 - 25\,000$). The IRAS channel were most sensitive to blackbody peak temperatures between 30 and 300 K; in contrast the peak transmittance of the $170\,\mu\mathrm{m}$ ISOPHOT band corresponds to the peak radiation from 17 K cold dust. Therefore, ISO provided for the first time the opportunity to study the role of cold dust (< 20 K) for the initial conditions of star formation.

Beside these large scale projects, the Midcourse Space Experiment (MSX) should be mentioned. Equipped with a 33 cm mirror this telescope mapped the Milky Way from 4.3 to $21.3\,\mu\mathrm{m}$ between 1996 and 1997. Based on these data Egan et al. (1998) provided one of the first discoveries of IRDCs.

At the time of operation of ISO, NASA already constructed a larger, next generation satellite. The Spitzer space telescope (initially named SIRTF) was launched in 2003 with a 85 cm mirror. Spitzer provided increased sensitivity and resolution compared to ISO. The telescope is equipped with three different instruments. The I, and $8.0\,\mu\mathrm{m}$). The main operation modes of the Multiband Imaging Photometer (MIPS) provided imaging in 24, 70, and $160\,\mu\mathrm{m}$ bands. Spitzer was also equipped with a Infrared Spectrograph (IRS). Although the spectral resolution is significantly lower than for ISO SWS and LWS, IRS provides better spatial resolution and sensitivity by using a long-slit and an echelle spectrograph instead of ISOs chopping technique. The large scale Galactic Legacy Infrared Mid-Plane Survey Extraordinaire (GLIMPSE, Benjamin et al. 2003) was preformed by IRAC and mapped the inner part of the galactic plane ($10° < |l| < 65°$, $|b| < 1°$). A similar survey was done by the MIPS instrument; the MIPS Inner Galactic Plane Survey (MIPSGAL, Carey et al. 2009) provided similar coverage as GLIMPSE ($-62° < l < 63°$, $|b| < 1 - 3°$). Only a fraction of the observations have been evaluated, but the already published studies have contributed significantly to the understanding of star formation.

All these space missions are equipped with primary mirrors smaller than a meter. On the 14^{th} of May 2009 the Herschel Space Observatory was launched by the ESA. Until today it is the space tele-

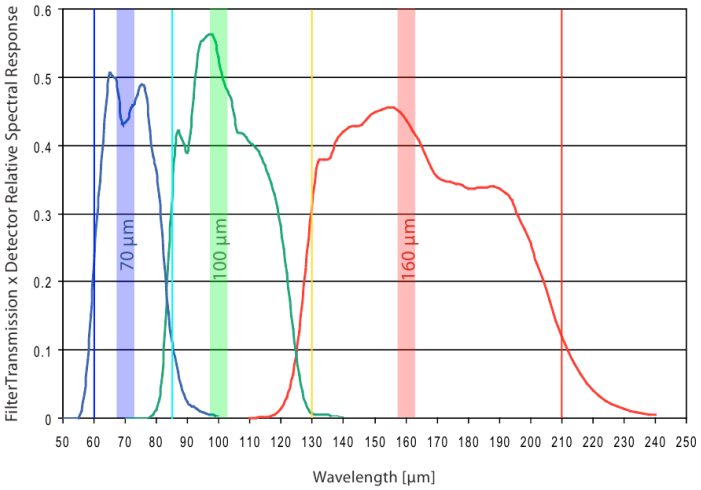

Figure 1.4. – The filter transmission curves for the Herschel/PACS bands are shown (from Poglitsch et al. 2010).

scope with largest primary mirror, measuring 3.5 m, resulting in an unprecedented resolving power in the infrared regime. In contrast to previous infrared space telescopes a mirror of this size cannot be cryogenically cooled. The thermal background signature of the mirror exceeds any astronomical source signal detected by Herschel. For astronomical signal reconstruction, the thermal background is subtracted with spatial chopping techniques. For the first time Herschel covers the complete wavelength range ($70 - 500\,\mu$m) necessary to measure the SED for very cold sources below 20 K. Not only the Wien part of the blackbody radiation is detected, but also the Rayleigh-Jeans tail longwards of $150\,\mu$m is accessible. Herschel carries three different instruments. The Photodetecting Array Camera and Spectrometer (PACS) consist of a dual-band photometer and integral field spectrograph. The Photometer is equipped with three filters 70, 100, and $160\,\mu$m (see Figure 1.4) with a beamsize of $6 - 11''$. The 70 and $100\,\mu$m share the same bolometer array, hence the $160\,\mu$m channel can be operated simultaneously with either the 70 or $100\,\mu$m filter. The PACS spectrograph has a spectral resolution of $1000 - 4000$ for its wavelength range of $55 - 210\,\mu$m. The Spectral and Photometric Imaging Receiver (SPIRE) covers the longer wavelengths (250, 350, and $500\,\mu$m) with a resolution of $18 - 36''$. SPIE and PACS can observe simultaneously in a parallel mode, but with the limitation that either the 70 or the $100\,\mu$m band can be observed. SPIRE is also equipped with a spectrograph for the wavelength range $194 - 671\,\mu$m. Several large programs consist surveys of the galactic plane or galactic star-forming regions. Two surveys are used in this work. The "Earliest Phases of Star formation" program (EPoS) contains a sample of low and high-mass star-forming regions and is described in Chapter 3. The "Herschel infrared Galactic Plane Survey" (Hi-GAL) map the dust in the inner galaxy ($|l| < 60°$, $|b| < 1°$) at 70, 160, 250, 350, and $500\,\mu$m. A comprehensive overview of the first scientific results of Herschel have been published by "Astronomy & Astrophysics" in a special issue in 2010.

1.1. Motivation and Outline

This brief introduction to the theory and observations massive star formation shows how fragmentary our overall picture of the infancy of a high-mass star is. In particular, we know very little about the early conditions of massive star formation, because the lack of observational power in the FIR has, so far, severely limited our understanding. However, the advent of infrared space telescopes already had has a tremendous impact on our understanding of star formation in general. Furthermore, the launch of the Herschel Space Telescope and the Spitzer Space Telescope provide us the opportunity to study the early phases of high-mass star formation in an unprecedented way.

In the context of massive star formation the following questions remain unclear and will be addressed in the observational framework of this thesis:

- Under which conditions does a massive dark cloud collapse?
- How do clouds, which host massive star formation, fragment?
- What is the internal structure of such clouds in terms of density and temperature?
- How do YSOs embedded in these massive star-forming regions evolve before the HMPO phase?

The observational studies I present in this work are predominantly conducted by the space observatories Spitzer and Herschel. The scientific analysis is augmented by sub-millimeter continuum and radio-line data.

The Chapter 2 is based on the Spitzer campaign "IRS spectroscopy of extremely young massive proto-stars" and additional Spitzer archive data. It presents a small spectroscopic survey of 14 sources in 10 different regions. The results are used to characterize the YSOs embedded in cold, massive clumps found in the ISOSS survey. Because they are exposed to similar physical conditions several sources detected in IRDCs are included in the sample. Chapter 3 and 4 are contributions to scientific evaluation of the Herschel GTO project "Early Phases of Star Formation" (EPoS) currently conducted at the Max-Plank-Institute für Astronomie. Chapter 3 details the development of a photometric pipeline for the high-mass part for the EPoS Herschel GTO project. The produced point source catalogs are used to study the fragmentation in the different regions of the EPoS-sample, in particular the average point source separation is discussed. In Chapter 4 a comprehensive case study on the isolated massive star-forming region G048.66–0.66 is presented. Chapter 5 gives the conclusions drawn from this thesis. In Chapter 6 a brief outline on the chemical modeling of IRDCs is presented.

2. Characterizing YSOs in massive cores: A spectroscopic survey in the infrared

In this chapter I present a spectroscopic study of sample of of YSOs, which were detected as point sources at $24\,\mu\mathrm{m}$ with Spitzer/MIPS in cold massive core candidates and IRDCs. I use mid-infrared spectroscopic observation with Spitzer IRS in addition to imaging observations with Spitzer MIPS and sub-millimeter continuum data obtained with SCUBA to characterize our YSO sample. Our sample of YSOs consist of intermediate-mass YSO as show in Table 2.1. Howerever as Beuther et al. (2007) pointed out, accreting protostars embedded into a massive core, which might evolve into a high-mass main-sequence star later on, are usually only of low to intermediate mass ($< 8\mathrm{M}_{\odot}$). It is, therefore, very likely that this sample contains progenitors of high-mass stars. The environment of these YSOs is complex. Given distance to our targets and angular resolution of the used instruments our observations will contain both contributions from the YSOs and the close environment. The results presented in this chapter are interpreted in the context of (previous) multi-wavelength studies to determine the origin of the observed absorption and emission features, disentangling the different components determining the physical conditions for these YSOs. Finally we will discuss our results in terms of evolutionary stages.

2.1. Introduction, Outline

Cloud cores which can form intermediate mass stars have masses of $\sim 10^2 - 10^3 M_{\odot}$, temperatures of $10 - 20$K and appear in most cases as radio-quiet (Arvidsson et al. 2010). In this Chapter a number of star forming regions is studied, which are in an early evolutionary stage, matching these requirements, based on a large-scale unbiased sample of cold cloud cores or infrared dark clouds. Within these regions embedded mid-infrared point sources have been identified. All of these sources except for one are good candidates for intermediate-mass YSOs.

The Orion cloud is one of the nearest and best studied regions for high-mass star formation. Several spectroscopic observation of Orion were performed by the Infrared Space Observatory (ISO). The high-mass YSO IRc2 in Orion was studied by van Dishoeck et al. (1998, see also Figure 2.1) and Wright et al. (2000). Due to the large aperture of ISO's Short Wavelength Spectrograph (SWS), the measured IRc2 spectrum is a superposition of multiple physical components. The extensive number of different spectral features make IRc2 a showcase for spectroscopy of YSOs in the context of massive star formation. The spectrum contains hydrogen recombination lines, ionic fine structure lines and broad UV-pumped PAH emission bands originating from a photon dissociation region (PDR). Thermally excited, rotational and rovibrational lines of H_2 are also observed and can be used to infer the coupling between the molecular gas and dust grains. The PAHs and the smallest dust grains in this region are photoelectrically heated by a central hot object. These observations show solid state absorption features, such as silicates, water, methane and CO_2 ice, originating from a quiescent extended ridge. In addition, shock excited molecular hydrogen was observed for the Orion peaks I and II (Rosenthal et al. 2000, see Figure 2.2) adjacent to IRc2. A detailed study of the molecular gas-phase

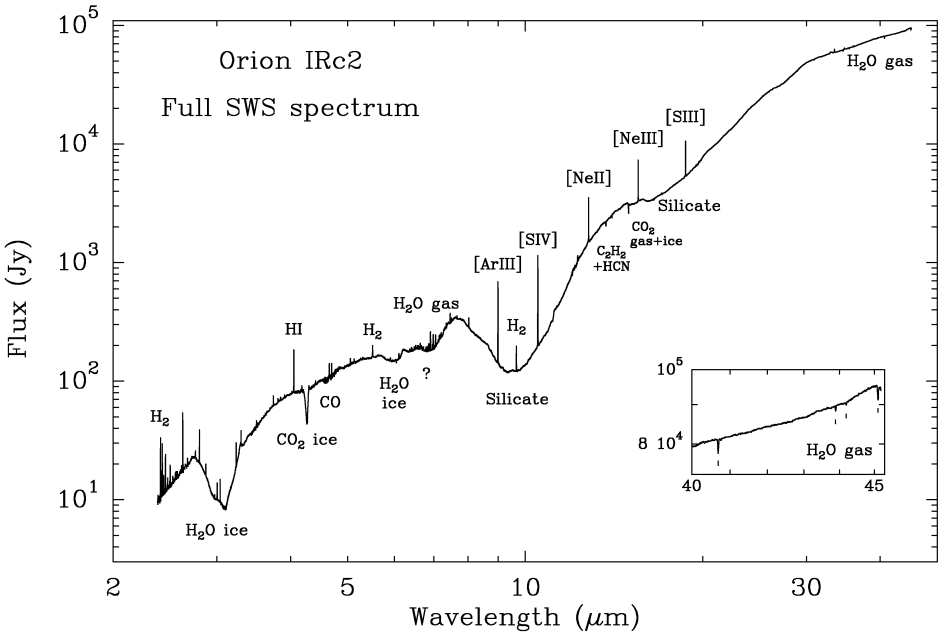

Figure 2.1. – The ISO SWS observation of Orion/IRc2 is a showcase for infrared spectroscopy (van Dishoeck et al. 1998). Multiple physical components of YSO and the close vicinity is covered by the SWS beam, resulting in a combined spectrum showing ice and silicate absorption, gas emission, PAH bands and forbidden atomic lines.

features of CO_2, C_2H_2 and HCN appearing in absorption for IRc2 and to some extend in emission for the Orion peaks can be found in Boonman et al. (2003).

In this Chapter I used data obtained by the Infrared Spectrograph (IRS) (Houck et al. 2004) onboard the Spitzer Space Telescope (Werner et al. 2004). The better spatial resolution and increased sensitivity of Spitzer compared to ISO allows to study a more distant sample of YSOs ($5-10\times$ more distant than Orion), which will be introduced in the next Section. I find similar spectral features as for the Orion IRc2 . They are used to estimate the physical properties of the young stellar objects in the observed star-forming regions. From the $9.7\,\mu\mathrm{m}$ silicate features the optical extinction can be calculated and used for later SED fitting, (see Henning (2010) for a general review on silicates). By classifying PAH bands below $9\,\mu\mathrm{m}$ it is also possible to constrain some properties of the irradiating FUV field (Peeters et al. 2002; Tielens 2008). Class $\mathcal{A}$ PAH spectra are typical for H II and compact H II regions, reflection nebula and YSOs exposed to a similar UV radiation field strength. The typical UV flux intensities are $10^3 - 10^6\ G_0$. The reference spectra for the different PAH classes from Peeters et al. (2002) are given in Figure 2.3. Referring to Tielens (2008), class $\mathcal{A}$ spectra are excited by sources with $T_{eff} > 10000$ K. This class of PAH spectra have a asymmetric feature at $6.2\,\mu\mathrm{m}$, an emission complex peaking at $7.6\,\mu\mathrm{m}$ and a third PAH band at $8.6\,\mu\mathrm{m}$. These PAH features arise mostly from the C−C mode. Strong UV radiation fields and gas densities of $n \sim 10^3 - 10^5$ cm^{-3} are needed to form photon dissociated regions (PDR) associated to molecular gas (Hollenbach & Tielens 1997). The gas densities and the strength of the UV radiation field can be estimated from the ratios of certain forbidden atomic lines (e.g. [Fe II] , [Si II]) and the excited H_2 lines which were created in the deeper layers of the illuminated PDR (Kaufman et al. 2006). Not only in PDRs emission lines of ionized atoms can be observed. J-shocks interacting with the envelope of young protostars leave hot dense gas heated up to 10^5 K. In the region behind the shock front the molecules are dissociated

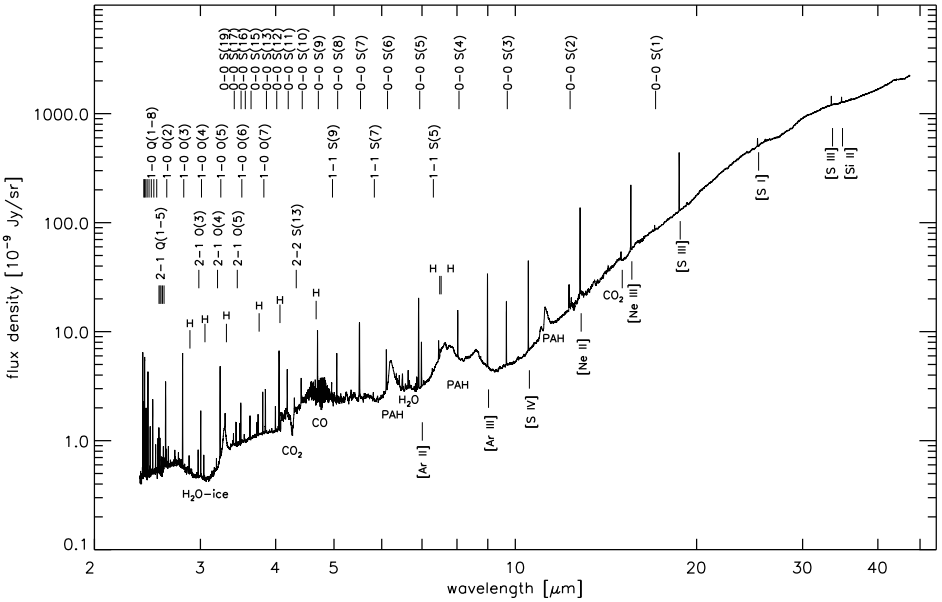

Figure 2.2. – ISO SWS spectrum of Orion Peak 1 shows a rich spectrum of H_2 rotational lines, which are both thermally and shock excited (Rosenthal et al. 2000). Unfortunately most of the energetic lines H_2 line, below $5\,\mu\mathrm{m}$, are not accessible by SPitzer.

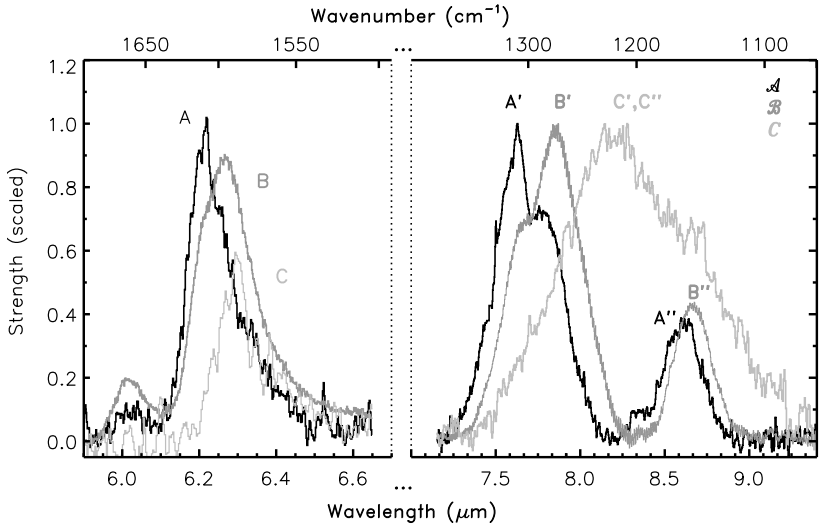

Figure 2.3. – The reference spectra for the different PAH-classes from Peeters et al. (2002): "Shown is (i) the CHII region IRAS 23133 illustrative of class $\mathcal{A}$ (i.e. A, A$'$ and A$''$) with a dominant 7.6 peak (black line), (ii) the Post-AGB star HD 44179 illustrative of class $\mathcal{B}$ (i.e. B, B$'$ and B$''$), peaking at $\sim 7.9\,\mu\mathrm{m}$ (dark grey line) and (iii) the Post-AGB star IRAS 13416 representing class $\mathcal{C}$ (i.e. C, C$'$ and C$''$), with a broad emission feature at $8.22\,\mu\mathrm{m}$ (light grey line). A clear shift in the $7.7\,\mu\mathrm{m}$ complex is present between IRAS 23133 and HD 44179."

and the ionized atoms can be observed by strong infrared emission lines (e.g. [Ne II] $12.8\,\mu\mathrm{m}$, [Fe II] $26\,\mu\mathrm{m}$, [Si II] $34.8\,\mu\mathrm{m}$, [S I] $25\,\mu\mathrm{m}$) (Hollenbach & McKee 1989). The [Ne II] atomic fine structure line intensity depends on the shock velocity. Therefore strong [Ne II] lines can be only observed in high velocity J-shocks ($v_s > 60 - 80\,\mathrm{km\,s^{-1}}$). When the gas is cooling in the relaxation region further downstream from the shock front, H is formed and can be observed as pure rotational lines. In the non-dissociated C-shocks the temperatures never become high enough to dissociate molecular material. Spectral indications for C-shocks are strong molecular lines of H_2, CO, H_2O and OH (Kaufman & Neufeld 1996). Most spectroscopic studies of massive star-forming regions have used data from ISO's Short Wavelength Spectrograph (SWS) and Long Wavelength Spectrograph (LWS). The Infrared Spectrograph (IRS) on-board the Spitzer Space Telescope presents a different instrumental approach. It has a lower spectral resolution, but provides a better spatial resolution and an improved sensitivity compared to ISO. The long slit spectroscopy in the low resolution mode allows spatially resolved observations of selected lines down to a resolution of $1.8''$. Nevertheless multiple emission or absorption features from different spatial positions are still covered by the IRS beam. Therefore an interpretation of the spectroscopic results can be given only when supplemented with multi-wavelength imaging observations. In general, these observations have a better spatial resolution than IRS in the same wavelength order and can therefore be used to trace certain spectral features. For example, the bands from the Spitzers Infrared Array Camera (IRAC, Fazio et al. 2004) and the Multiband Imaging Photometer (MIPS, Rieke et al. 2004) can be used to determine the spatial distribution of excited hydrogen, PAHs and warm dust. In particular the $4.5\,\mu\mathrm{m}$ band is utilized to identify so-called "green and fuzzy" features (Chambers et al. 2009). These features predominantly originate from the (0-0) S(9) H_2 band, mostly attributed to shock excitation (e.g. De Buizer & Vacca 2010). Another excitation mechanism for the S(9) line can be fluorescence, depending on physical parameters (e.g. temperature, H_2 column densities) and dust properties (Black & van Dishoeck 1987).

The next Section 2.2 describes the target selection. In Section 2.3, the observations and the data reduction processes are described. Section 2.4 details the continuum observations and the spectral features. Section 2.5 discusses the different sources and their morphology within the context of previous observations. Section 2.6 will summarize this Chapter.

2.2. Target selection

Krause et al. (2004) detail a number of suitable sources detected with the ISOPHOT $170\,\mu\mathrm{m}$ serendipity survey (ISOSS, Bogun et al. 1996). Due to its high sensitivity, the survey was able to find sources away from the galactic plane. Several regions within this sample were selected based on their distance, luminosity and dust temperature ($12\,\mathrm{K} < T_d \leq 22\,\mathrm{K}$). Later *Spitzer* imaging observations identified point sources within some of these regions (Birkmann et al. 2006, 2007; Hennemann et al. 2008, 2009). A spectroscopic follow up was conducted on these objects. All targets are resolved as bright point sources at MIPS $24\,\mu\mathrm{m}$. Based on their mid-infrared colors, these sources were good candidates for intermediate-mass YSOs. The basic parameters of the selected ISOSS targets are listed in Table 2.1 (top part). In addition to the coordinates and the distances, the stellar mass estimates and the masses of the associated cold cores are given. In the last column the key references for the particular regions are listed. All ISOSS source studied in this Chapter are part of the EPOS sample described in the next Chapter of this work.

The ISOSS regions J18364−0221 East, J20153+3453, J04225+5150, and J23053+5953 have extended PAH emission and warm dust components, which can be identified in the *Spitzer*/IRAC and

Table 2.1. – Sources

Source	RA (J2000)	Dec (J2000)	Distance[a] (kpc)	$M^b_{\rm core}$ ($\rm M_\odot$)	$M^c_{\rm obj}$ ($\rm M_\odot$)	Key Ref.
ISOSS						
J04225+5150 East	$04^{\rm h}22^{\rm m}32^{\rm s}.3$	$+51°50'30''$	5.5	-	5.4-9.0	(BPhD)
J18364−0221 East	$18^{\rm h}36^{\rm m}36^{\rm s}.0$	$-02°21'59''$	2.2	75	-	(B06), (H09)
J18364−0221 West	$18^{\rm h}36^{\rm m}29^{\rm s}.6$	$-02°21'59''$	2.2	280	0.6-2.0	(B06)
J20153+3453 East	$20^{\rm h}15^{\rm m}21^{\rm s}.2$	$+34°53'46''$	2.0	$87-149$	-	(H08)
J20153+3453 West	$20^{\rm h}15^{\rm m}20^{\rm s}.6$	$+34°53'53''$	2.0	$87-149$	4.0-8.5	(H08)
J23053+5953 East	$23^{\rm h}05^{\rm m}23^{\rm s}.6$	$+59°53'56''$	3.5	200	4.1-6.6	(B07)
G010.70-0.13 I	$18^{\rm h}09^{\rm m}57^{\rm s}.8$	$-19°48'17''.6$	3.7	-	5.3-12.0	(P09)
G010.70-0.13 II	$18^{\rm h}09^{\rm m}55^{\rm s}.9$	$-19°48'17''.6$	3.7	-	5.6-6.1	(P09)
G019.27+0.07	$18^{\rm h}25^{\rm m}58^{\rm s}.6$	$-12°03'58''.0$	2.4	113	2.1-4.9	(R06), (C09)
G025.04-0.20	$18^{\rm h}38^{\rm m}09^{\rm s}.6$	$-07°02'30''.0$	3.4	276	5.4-9.6	(R06), (C09)
G028.04-0.46	$18^{\rm h}44^{\rm m}08^{\rm s}.2$	$-04°33'17''.5$	3.2	80	1.3-7.6	(R06), (C09)
G034.43+0.24	$18^{\rm h}53^{\rm m}20^{\rm s}.6$	$+01°28'24''.5$	3.7	301	3.6-6.4	(R05), (R06), (C09)
G053.25+0.04 I	$19^{\rm h}29^{\rm m}31^{\rm s}.9$	$+18°00'40''.0$	1.9	-	3.6-6.4	(R06), (C09)
G053.25+0.04 II	$19^{\rm h}29^{\rm m}31^{\rm s}.7$	$+18°00'33''.2$	1.9	-	2.3-6.1	(R06), (C09)

[a] The distances are obtained from the references in the last column. The kinematic distance for G010.70-0.13 is based on CO data from Dame et al. (2001).

[b] The submillimeter core mass given in the key references for this object, if available. The targets in ISOSSJ20153+3453 are separated by just $10''$, and the submillimeter peak is centered on the western source.

[c] The masses of the point sources were estimated by the SED fitting tool of Robitaille et al. (2007) based on the mid-infrared luminosities and the optical extinctions derived from the silicate bands if present. Because of the missing IRAC counterparts, no mass for the central source was modeled for ISOSS J18364−0221 East and ISOSS J20153+3453 East.

Key References: (BPhD) Birkmann (2007); (B06) Birkmann et al. (2006); (B07) Birkmann et al. (2007); (C09) Chambers et al. (2009); (H08) Hennemann et al. (2008); (H09) Hennemann et al. (2009); (P09) Peretto & Fuller (2009); (R05) Rathborne et al. (2005); (R06) Rathborne et al. (2006)

MIPS 24 μm images, respectively. In the MIPS 24 μm band ISOSS J18364−0221 West appears as an isolated infrared source with weak dust components.

To investigate additional targets similar to those chosen from the ISOSS sample, I selected 24 μm sources associated with cold cloud core candidates from Chambers et al. (2009) that have IRS spectra available in the Spitzer-SSC archive. They are associated with IRDCs located in the galactic plane (called "IRDC sources" hereafter). They are clearly resolved point sources in the MIPS 24 μm and 70 μm bands (Table 2.1, bottom part). Except for G10.70–0.13, 1.2 mm observations show compact cores with masses ranging from 74 to 301 $M_\odot$ (Rathborne et al. 2006). For some of these sources H_2O maser emission was observed indicating ongoing star formation processes (Chambers et al. 2009). Where available, the SCUBA legacy data (Di Francesco et al. 2008) for these regions reveal submillimeter clumps. In contrast to the other IRDC sources the G10.70-0.13 sources are not located within the dark filament of the IRDC but show extended PAH emission such as, for example, the ISOSS J20153+3453 and ISOSS J04225+5150 region.

2.3. Observations and data reduction

2.3.1. Photometry

Table 2.2. – Photometry Apertures

Source	IRAC		MIPS	
	$R_{\rm Ap}$	$R_{\rm Sky}$	$R_{\rm Ap}$	$R_{\rm Sky}$
ISOSS				
J04225+5150 East	2″	6″	5″	13″
J18365−022 East	-	-	6″	13″
J18365−022 West	3.″2	5.″2	13.″2	30″
J20153+3435 [a]	2″	6″	6″	13″
J23053+5953	2″	6″	6″	13″
G10.7−0.13 I	4.″8	10.″8	10.″4	31.″2
G10.7−0.13 II	4.″8	10.″8	10.″4	31.″2
G19.27+0.07	4.″8	12.″0	10.″4	31.″2
G25.04−0.20	7.″2	14.″4	10.″4	31.″2
G28.04−0.46	7.″2	14.″4	10.″4	31.″2
G34.43+0.24	7.″2	14.″4	10.″4	31.″2
G53.25+0.04 I	3.″6	19.″6	10.″4	31.″2
G53.25+0.04 II	3.″6	19.″6	10.″4	31.″2

[a] Only the western source is detected within the IRAC bands. For MIPS at 24 μm the same aperture size was used for the eastern and western sources.

The IRAC and MIPS observations were used described in Birkmann et al. (2006, 2007) and Hennemann et al. (2009, 2008) to measure the integrated fluxes of the ISOSS sources. For the IRDC sources I used data from the Galactic Legacy Infrared Mid-Plane Survey Extraordinaire (GLIMPSE; Benjamin et al. 2003) and the MIPS Inner Galactic Plane Survey (MIPSGAL; Carey et al. 2005).

The `daophot` package in `IRAF` was used to perform this aperture photometry. The resulting SEDs are shown in Figure 2.11 and 2.12. The apertures and annuli used for the sky background estimations for the *Spitzer* photometry are given in Table 2.3.1. Aperture corrections were not applied to the IRAC fluxes due to the inhomogeneous and asymmetric-extended background emission. The initial calibration of the IRAC and MIPS BCD data results in uncertainties of 2% for IRAC (Reach 2005), 4% for MIPS 24 μm (Engelbracht et al. 2007) and 10% for MIPS 70 μm (Gordon et al. 2007). Cosmetic corrections and astrometric enhancements were performed using the MOPEX software package (Makovoz & Marleau 2005). The final images were combined using the IRAF framework. The resulting accuracy for the aperture photometry is estimated to be 7% for the IRAC and 10% for the MIPS 24 μm. For the MIPS 70 μm band, I used PSF photometry to decrease the uncertainties introduced by flux non-linearities (Gordon et al. 2007). The resulting

uncertainty for MIPS $70\,\mu\mathrm{m}$ is estimated to be 20%. For the ISOSS J18364−0221 East region the MIPS $24\,\mu\mathrm{m}$ peak was not detected as a point source in the IRAC image and as such photometry was only performed on the MIPS exposures. IRAC sources were not detected at the position of the eastern submillimeter peak in the ISOSS J20153+3453 region. A cluster of IRAC sources were detected at the position of the western $24\,\mu\mathrm{m}$ source. The photometry was performed on the central object of this cluster; this is also the position on which the IRS slit was centered. The eastern and western targets were resolved at $24\,\mu\mathrm{m}$, but could not be detected separately in the MIPS $70\,\mu\mathrm{m}$ band due to the large beam size. All data points from the eastern and western sources are shown in the same plot (Figure 2.11), and the data points longward of $70\,\mu\mathrm{m}$ are treated as belonging to both sources. $450\,\mu\mathrm{m}$ and $850\,\mu\mathrm{m}$ observations were obtained with SCUBA (Holland et al. 1999) at the James Clerk Maxwell telescope (JCMT) for most of the targets by Birkmann et al. (2006, 2007) and Hennemann et al. (2008, 2009). ISOSS J04225+5150 East was not included in these publications, but existing data from 2001 were reduced for the $450\,\mu\mathrm{m}$ and $850\,\mu\mathrm{m}$ bands. For ISOSS J04225+5150 submillimeter fluxes of $F_{450} = (9.2 \pm 2.8)$ Jy and $F_{850} = (1.5 \pm 0.3)$ Jy were derived from the SCUBA bands. A detailed description of the reduction and analysis process can be found in Hennemann et al. (2008). The absolute photometric accuracy is estimated to be 30% at $450\,\mu\mathrm{m}$ and 20% at $850\,\mu\mathrm{m}$.

The low resolution spectra are plotted into the SEDs in Figures 2.11 and 2.12. The differences between spectra and the IRAC/MIPS photometry can be explained as follows: The observed sources are compacted but extended. The available relative spectral response function is only calibrated for point sources (see next the section). The spectroscopic observations were conducted with a different aperture compared to the IRAC and MIPS photometry. This results in a significant flux difference.

I used the IRAC and MIPS fluxes and the silicate extinction (Table 2.6) with the SED fitting tool from Robitaille et al. (2007) to get an estimate for the source parameters. The resulting source masses M_{obj} are listed in Table 2.1.

2.3.2. Infrared spectroscopy

The spectroscopy was performed with the Infrared Spectrograph (IRS) on-board the *Spitzer Space Telescope*. The observations of the targets selected from the ISOSS sample were performed during the campaign "IRS spectroscopy of extremely young massive proto-stars" (ID: 30919 + 40569). The observation dates, the program ID, the number of observational cycles and the integration times can be found in Table 2.3. To cover the maximum possible wavelength interval ($5.2 - 38.0\,\mu\mathrm{m}$) all four available low resolution channels (SL2, $5.2 - 7.7\,\mu\mathrm{m}$; SL1, $7.4 - 14.5\,\mu\mathrm{m}$; LL2, $14.0 - 21.3\,\mu\mathrm{m}$ and LL1, $19.5 - 38.0\,\mu\mathrm{m}$) and both high resolution channels (SH, $9.9 - 19.6\,\mu\mathrm{m}$; LH, $18.7 - 37.2\,\mu\mathrm{m}$) were used. The spectroscopic slit setup for Spitzer is shown in Figure 2.4. ISOSS J18364–0221 East was the only exception; here the SL2 channel was skipped due to the non-detection of a point source in the IRAC bands. The integration times for the low resolution modes were chosen to achieve a signal-to-noise ratio (S/N) of 100, sufficient to detect faint absorption features. In order to detect faint lines above the relatively bright mid-infrared continuum, a signal to noise ratio of at least 100 was required in the LH module at $24\,\mu\mathrm{m}$. The integration times for the SH module were optimized in order to reach a spectral line sensitivity for H_2 $S(1)$ at $\lambda = 17.03\,\mu\mathrm{m}$, which is two times better than that of the $S(0)$ line. Overall the observations aimed for a line sensitivity better than $3 \cdot 10^{-18}$ W m^{-2} and 5×10^{-18} W m^{-2} for the short and long wavelength orders of the high resolution spectra. All Astronomical Observation Templates (AOTs) were performed in the standard staring mode. The science targets were placed at 1/3 and 2/3 of the slit length to obtain spectra at two nodded positions. The slit overlays are shown for one nod position in Figures 2.22, 2.25, 2.28, 2.30, 2.31, 2.33, and

Table 2.3. – Observation Log

Source	AOR-ID	Obs. Date	t_{ramp} (s), (cycles)				Comments on
		(yy-mm-dd)	SL	LL	SH	LH	Data Quality
ISOSS							
J04225+5150 East	19235328	07-03-15	6,(2)	6,(2)	30,(2)	14,(2)	
J18364−0221 East	23071744	08-04-26	60,(3)	30,(2)	120,(6)	60,(8)	SL2 not observed, bright background emission, SL orders not extracted
J18364−0221 West	23072000	08-04-26	6,(2)	6,(2)	120,(2)	60,(2)	
J20153+3453 East	19236864	06-07-04	14,(4)	14,(2)	120,(3)	60,(4)	The western source dominates SL orders
J20153+3453 West	19237376	06-07-4	6,(2)	6,(2)	30,(5)	14,(5)	
J23053+5953 East	19237888	06-07-31	60,(3)	6,(2)	120,(2)	60,(2)	Flux leakage in SL orders Extended PAH band[a]
G010.70-0.13 I	16943872	06-05-01	6,(1)	6,(1)	6,(1)	14,(1)	
G010.70-0.13 II	16943872	06-05-01	6,(1)	6,(1)	6,(1)	14,(1)	
G019.27+0.07	12091648	05-04-18	60,(2)	14,(2)	-	-	very non-uniform background[b]
G025.04-0.20	17823744	07-05-08	60,(10)	-	-	-	
G028.04-0.46	17823488	07-05-02	60,(10)	-	-	-	extended PAH bands[c]
G034.43+0.24	17824512	07-05-02	14,(34)	-	-	-	extended PAH band[a]
G053.25+0.04 I	17825280	07-06-14	60,(10)	-	-	-	extended PAH band[a]
G053.25+0.04 II	17825536	07-06-14	60,(10)	-	-	-	extended PAH bands[c]

[a] The $11.2\,\mu m$ PAH band is spatially extended over the slit. A polynomial fit is used to estimate the background contribution in this wavelength range.

[b] Because of the very non-uniform background the whole spectrum was extracted with a polynomial background fit.

[c] The $11.2\,\mu m$ and $12.3\,\mu m$ PAH bands are spatially extended over the slit. A polynomial fit is used to estimate the background. A polynomial fit is used to estimate the background contribution in this wavelength range.

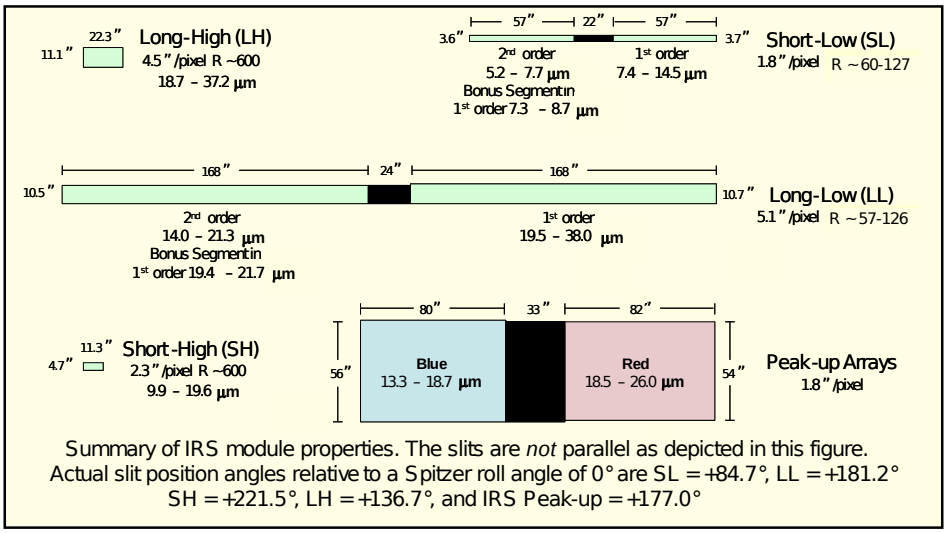

Figure 2.4. – The slit and aperture setup for Spitzer/IRS. (Obtained from the SSC.)

2.35. The slit length covers several ten to hundred thousand AU, as indicated in those plots.

The IRDC sources G025.04-0.20, G028.04-0.46, G034.43+0.24 and G053.25+0.04 I+II were taken in the short wavelength orders only. The observations were carried out with a minimum of 10 cycles. The good sampling results in a high S/N.

Low resolution data extraction

The low resolution data products were obtained in the `droopres` state processed by the *Spitzer* pipeline. For further data reduction a pipeline based partly on the SMART-package together with the spectral extraction tools from the FEPS *Spitzer* science legacy team were used. A detailed description can be found in Bouwman et al. (2006) and Swain et al. (2008). During the reduction process the data products were flatfield and straylight corrected. The correction of rogue and bad pixels was done with a median filter (based on the `irsclean` routine) and visual inspection. The spectral extraction was done with a fixed 6 pixel wide aperture for the short-low (SL) orders and 5 pixel wide aperture for the long-low (LL) orders, referring to spatial widths of $10.8''$ and $25.5''$ in the slit respectively. The local background was subtracted using the two nod positions along the slit from a median combined series of exposures. After the extraction the spectrum was convolved with the relative spectral response function (RSRF). The RSRF for the IRS instrument is only defined for point sources. Due to the compact, but extended nature of the sources a proper absolute flux calibration cannot be achieved for the one-dimensional spectra. Since there is a flux offset between the SL and LL orders and the corresponding slits have different orientations, the one-dimensional spectra are shown in two separate plots in Figure 2.13. Furthermore, the fluxes are given in units of Jy with respect to the used aperture sizes. The Figures 2.5–2.8 show different examples for cross-dispersion profile over wavelength in the SL1 order. In Figure 2.5 the point source cross-dispersion profile clearly exceeds the local background. In contrast, Figure 2.7 is background dominated and no distinct point source profile is detectable. Figure 2.6 reveals a clear point-source profile, but the $11.3\,\mu\mathrm{m}$ PAH line is extended over the whole slit. The source profile in Figure 2.8 appears to be broader and oblate compared to a nominal point source cross-dispersion profile indicating a compact background emission which is barely resolved.

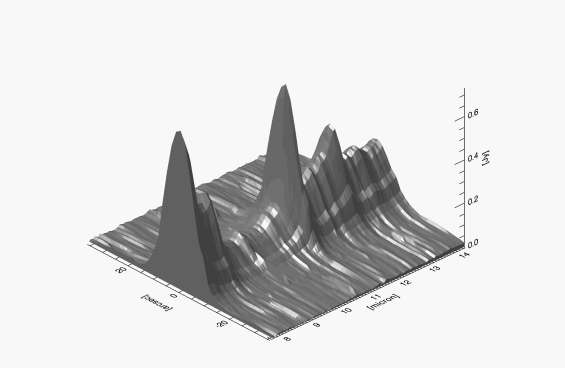

Figure 2.5. – Spectral dispersion map (SL1 order) for ISOSS J04225+5150 East

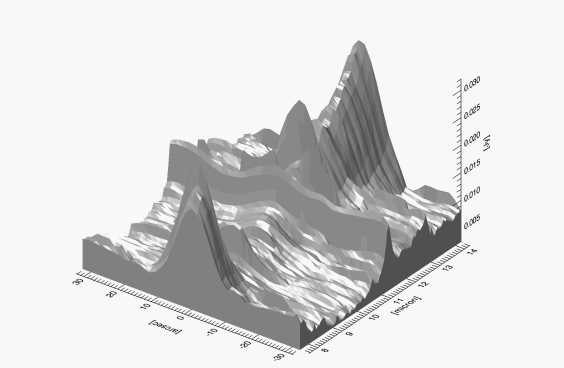

Figure 2.6. – Spectral dispersion map (SL1 order) for ISOSS J23053+5953 East

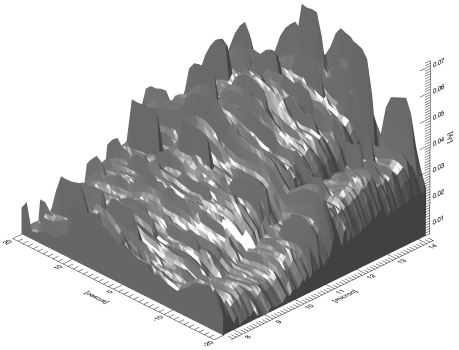

Figure 2.7. – Spectral dispersion map (SL1 order) for ISOSS J18364−0221 East

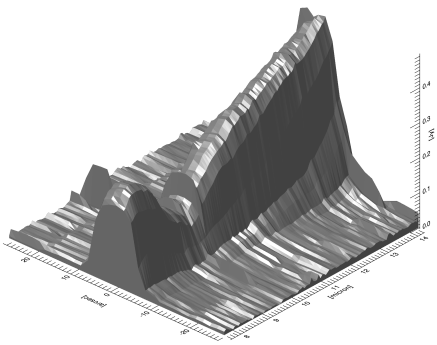

Figure 2.8. – Spectral dispersion map (SL1 order) for ISOSS J18364−0221 West

High resolution data extraction

The high resolution data (SH: short-high orders; LH: long-high orders) were reduced with the c2d pipeline (Lahuis et al. 2006, 2010) starting with the `rsc` data products. Corrections for bad and rogue pixels were performed, as was defringing for all spectral orders. The optimal spectral extractions were obtained using analytically derived cross-dispersion profiles that fit the source profile and extended emission components. The background was determined from additional off-source AOTs for every source. I used the high-resolution data to obtain line fluxes and flux ratios.

Limitations on the extraction process

To analyze the effect of extended emission lines and an inhomogeneous background on the low-resolution spectra, I investigated the dependence of the sources' cross-dispersion profiles as a function of wavelength. Several spectra showed extended spatial profiles, in particular for the $11.3\,\mu\mathrm{m}$ and $12.8\,\mu\mathrm{m}$ PAH bands (e.g Figure 2.6, but with the $11.3\,\mu\mathrm{m}$ feature only). These extended PAH

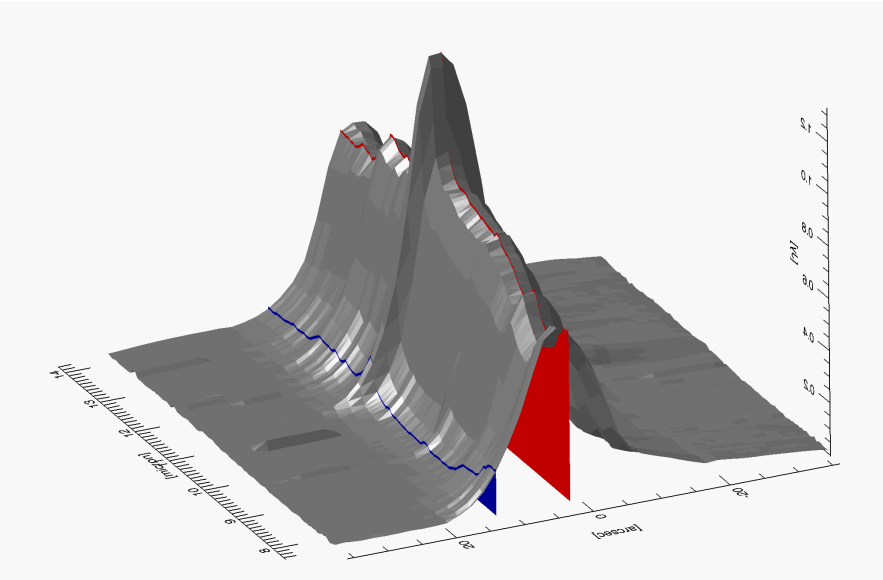

Figure 2.9. – The spectral dispersion maps for ISOSS J20153+3453. The nominal (spatial) positions for the both IRS targets indicated in red for ISOSS J20153+3453 West and blue for ISOSS J20153+3453 East. The wavelength orders SL2 and SL1 are combined in this plot.

background contributions could lead to a background over-subtraction in the resulting low resolution spectra in the nominal FEPS extraction. I compared different extraction methods for the low resolution spectra (Figure 2.10 shows the comparison for two different sources):

- Instead of the median combined background estimate for the FEPS extraction, a 3rd order polynomial was fitted to the local background in each wavelength bin during the FEPS extraction.
- The PSF-extraction from the c2d pipeline was used, which is slightly undersampled for the low resolution case.

Both extraction methods do not significantly differ in the resulting overall continuum, correcting for extended background line emission. For some sources the c2d extraction returns a slightly better S/N for the continuum. In some cases the c2d pipeline did not detect some of the faint H_2 rotational lines. In general the performance of fitting the SL order is better with the FEPS extraction. Based on these facts I chose to process sources which were affected by extended PAH emission with the nominal FEPS extraction and substitute the affected wavelength intervals with the polynomial background fit (see Table 2.3).

ISOSS J18364−0221 East shows bright and non-uniform background emission at short wavelengths ($5.2 - 14.5''$). No source profile could be fit for these wavelength orders and as such no SL spectrum is presented in Figure 2.13. For the ISOSS J20153+3453 region two targets were observed centered on the two MIPS peaks at $24\,\mu\mathrm{m}$. The separation of both MIPS peaks at $24\,\mu\mathrm{m}$ is $10''$. The slit positions of the SL orders overlap for the AOTs taken on both these targets. For the eastern target in this region I did not detect a point source in the IRAC bands, but instead detect a diffuse bulge of emission. The independent source profile could not be obtained for the SL orders of the eastern target since the slit is dominated by the western source, as shown in the spectral dispersion

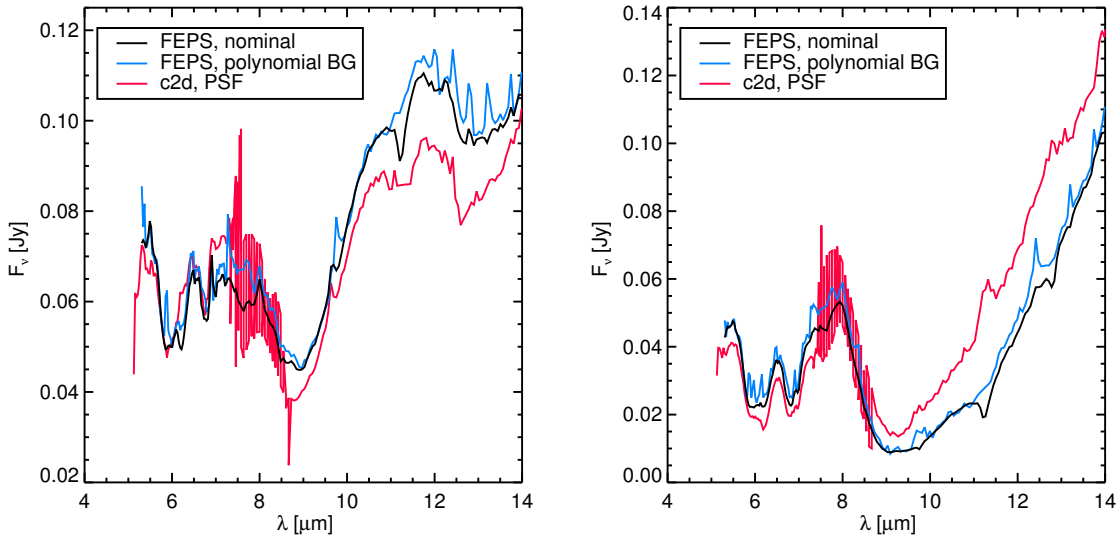

Figure 2.10. – Comparision between the nominal FEPS extraction (black), the FEPS extraction with polynomial background fitting (blue) and the PSF extraction with the c2d pipeline (red). As an example, G053.25+0.04 I and II are plotted in the left and right panel, respectively.

map in Figure 2.9 . The short orders were therefore not extracted for the one-dimensional spectrum. The long wavelength orders (LL) are not affected as these slit positions do not overlap.

The high-resolution spectrum could also not be extracted for this target in the SH orders as the cross dispersion profile could not be fitted with the absence of a point source in SH orders. For ISOSS J23053+5953 East the slit was centered on the peak of the submillimeter clump. The IRAC point source at this position was only partly covered by the slit, which results in a significant flux loss. I can therefore only qualitatively discuss the spectrum below $14.5\,\mu\mathrm{m}$. G019.27+0.07 is affected by a very non-uniform background with bright background emission. The whole spectrum was extracted with third- and fourth-order polynomial background extractions for the SL and LL orders, respectively. It is shown in Figure 2.17 together with the averaged background spectrum at the nominal nod position.

Spatial line analysis

I also investigated the spatial extent of single lines over the low resolution slits (SL,LL). A one-dimensional spectrum was extracted for every spatial pixel position over the slit width. This extraction was performed without a background subtraction. The spectra for the two nod positions were extracted separately and were not median combined. The line flux was calculated from a fitted Gaussian profile after the underlying continuum contribution had been removed using a second-order polynomial. These results are presented in Section 2.4.6.

2.4. Results

2.4.1. Continuum observations and spectral energy distribution

The SEDs were compiled from IRAC, MIPS and SCUBA bands and are presented in Figure 2.11.

Using this data I calculated the bolometric luminosities using:

$$L = 4\pi d^2 \int d\nu F_\nu \tag{2.1}$$

This assumes a spherically symmetric distribution of the luminosity. Of course other non-spherical configurations are possible, for example, the majority of the observed luminosity escapes via outflow cavities. For this reason, the values presented in Table 2.5 are affected by large uncertainties.

The low resolution spectra extracted from the ISOSS sources are presented in Figure 2.13. The spectra from the IRDC sources and the long wavelength orders from ISOSS J23053+5953 East and ISOSS J18364−0221 East are shown in 2.14. Most spectra in the sample are dominated by broad emission bands at shorter wavelengths. Beyond $18\,\mu\mathrm{m}$ the continuum is well defined and shows a steeper slope compared to the shorter wavelengths. For ISOSS J23053+5953 East the IRAC observations reveal a cluster of objects that are not resolved at the longer wavelengths. The contribution from the clustered sources can be seen in the higher fluxes below $9\,\mu\mathrm{m}$. Clustering can also be seen in ISOSS J04225+5150 and ISOSS J20153+3453 West.

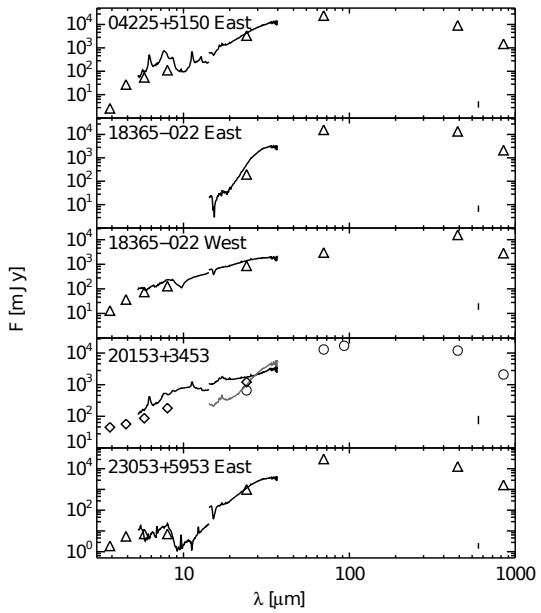

Figure 2.11. – The spectral energy distributions for the ISOSS targets were compiled using IRAC, MIPS and SCUBA data. The used apertures for the Spitzer photometry is stated in Table 2.3.1. The bar in the bottom right of each plot indicates an error of 30% (absolute photometric errors are 7%, 10-20%, 20-30%, for IRAC, MIPS and SCUBA, respectively). The low resolution spectra are overplotted (see also Figure 2.13 and 2.15). The fourth plot shows the results for ISOSS J20153+3453 East and West. Only for the western source IRAC counterparts are detected. The photometric data points (IRAC, MIPS 24 μm) for western source are plotted as diamonds and for the eastern source as circles (MIPS 24 μm only). Longward of 70 μm both sources are not separately resolve. The resulting data points are plotted as circles.

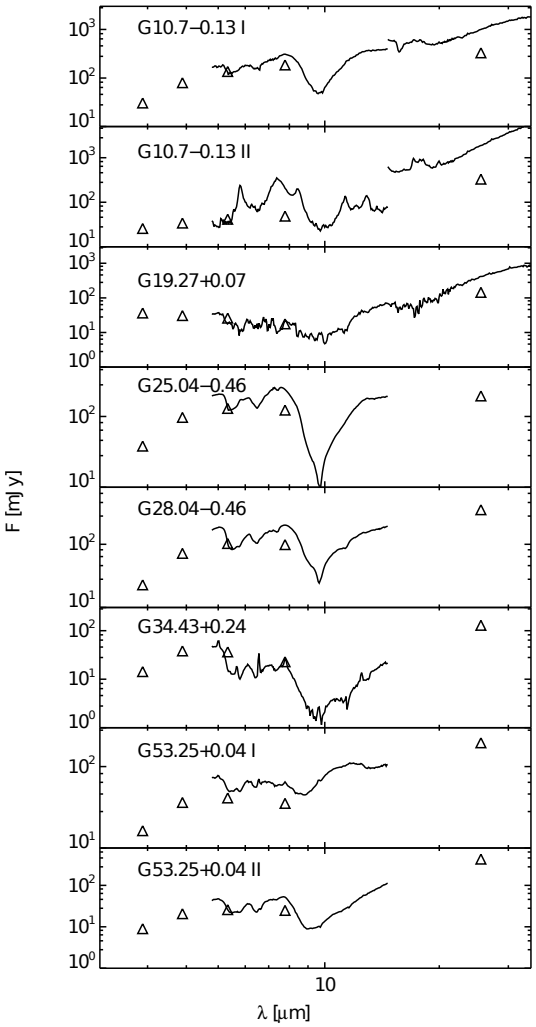

Figure 2.12. – The spectral energy distributions for the IRDC sources were compiled using IRAC and MIPS data. The bar in the bottom left of each plot indicates the absolute photometric error of 10% for the MIPS 24 μm band.

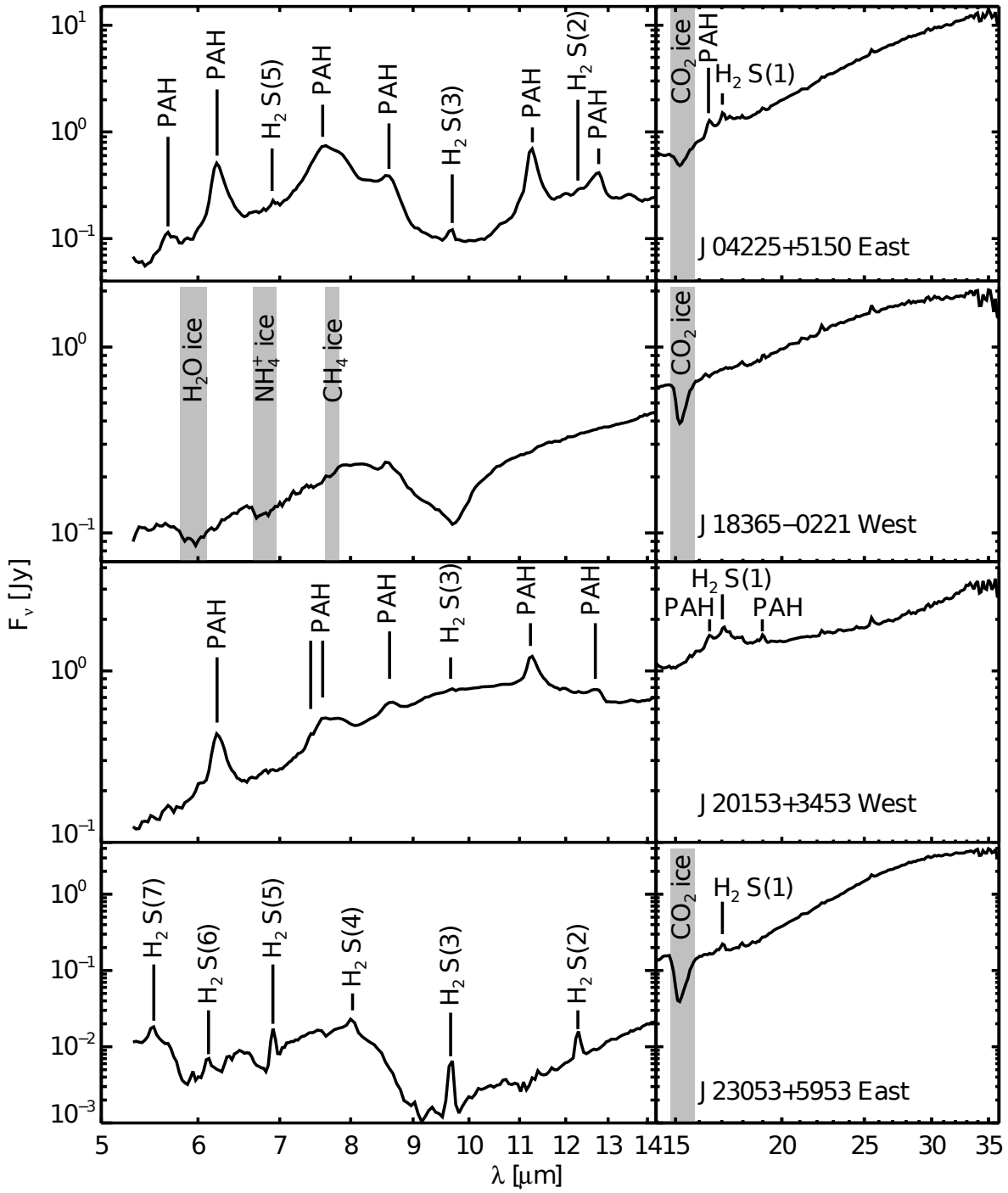

Figure 2.13. – Low resolution spectra for the ISOSS sources. The SL and LL orders are extracted with different apertures size. Therefore the long wavelength orders are more effected by contributions of extended emission and show a clear offset compared to the short wavelengths. The low resolution, long wavelength orders for ISOSS J18365-0221 East and ISOSS J20153+3453 East are show in Figure 2.15. Emission lines are indicated by lines, while absorption bands are underlined in light grey.

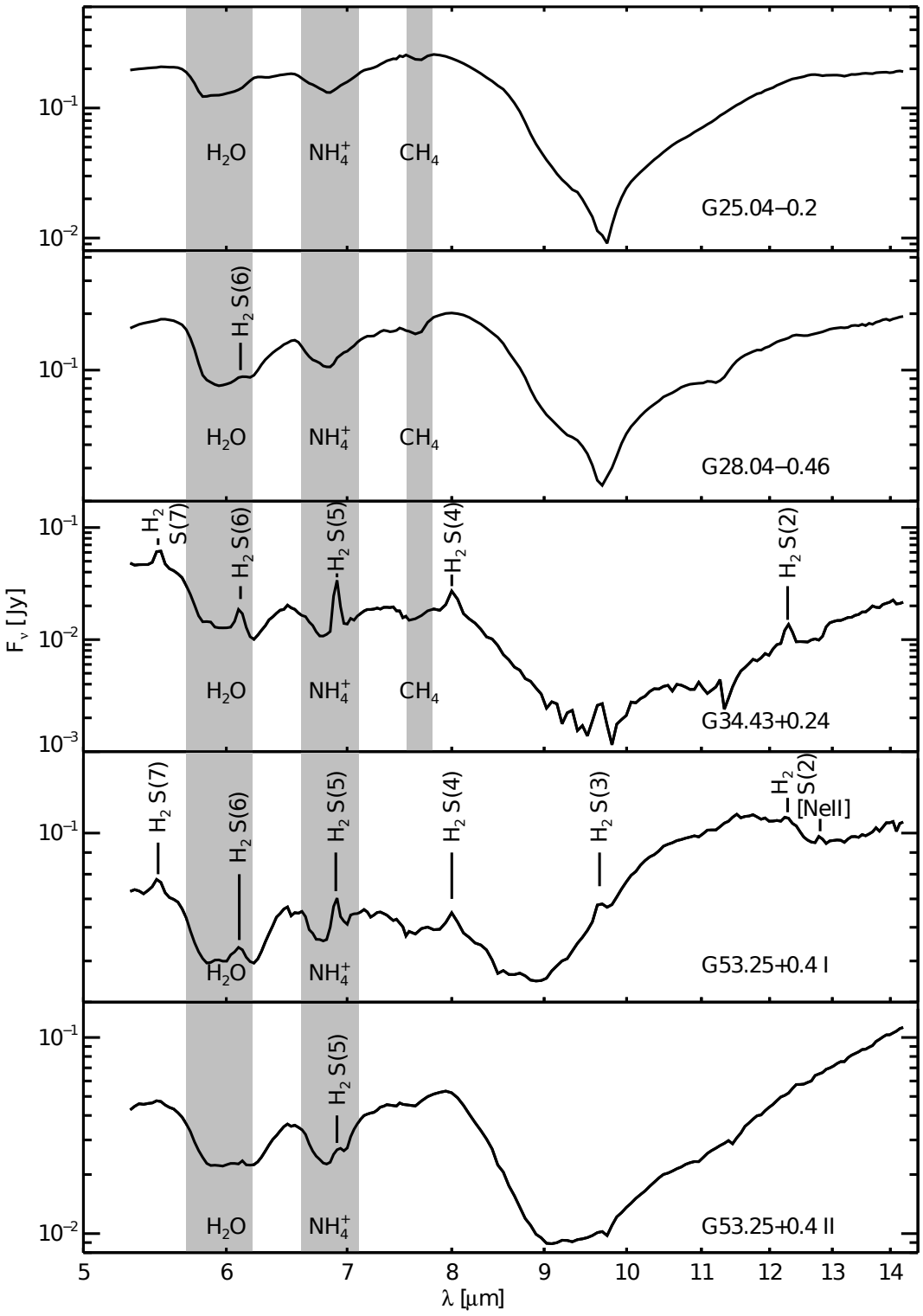

Figure 2.14. – Low resolution spectra for the IRDC sources. The spectra for G10.7−0.13 and G19.27+0.07 are shown in Figure 2.16 and 2.17.

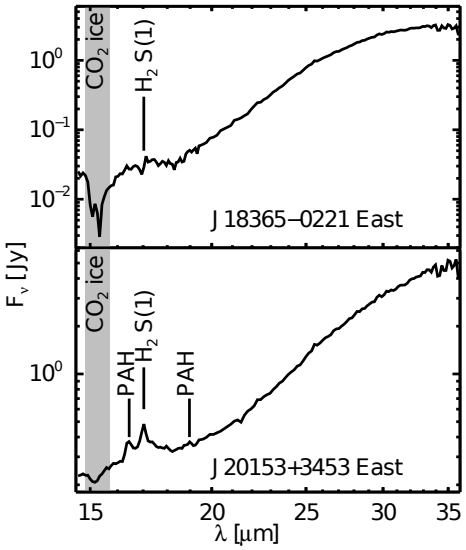

Figure 2.15. – The low resolution spectra for ISOSS J18365 East and J20153+3453 East are shown. Only the long wavelength orders (LL) were extracted for these source and plotted.

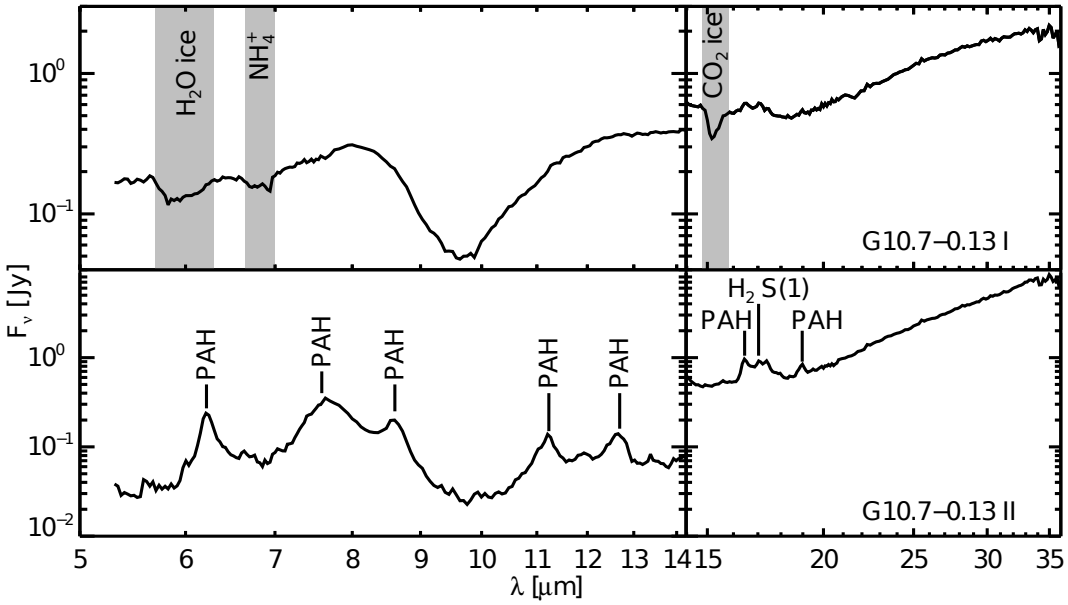

Figure 2.16. – The low resolution spectra for G10.7−0.13 I and II are shown.

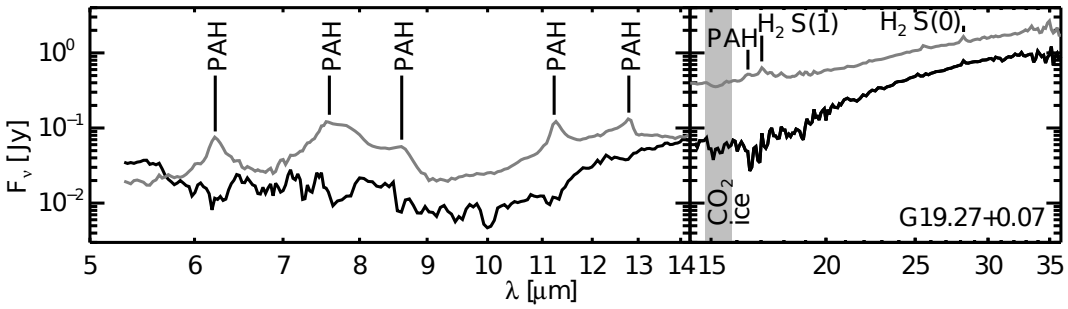

Figure 2.17. – The spectra for G19.27-0.07 are shown. The source spectrum is extracted with a polynomial background fit and is plotted in black. The sources background spectrum is plotted in grey.

2.4.2. Hydrogen emission

Table 2.4. – H_2 (0-0) line parameter

Line	λ [μm]	E_u/k [K]	A_{ul} [s^{-1}]
S(0)	28.2188	509.9	$2.94 \cdot 10^{-11}$
S(1)	17.0346	1015.0	$4.76 \cdot 10^{-10}$
S(2)	12.2785	1682.0	$2.76 \cdot 10^{-9}$
S(3)	9.6649	2503.4	$9.84 \cdot 10^{-9}$
S(4)	8.0258	3474.6	$2.64 \cdot 10^{-8}$
S(5)	6.9091	4586.7	$5.88 \cdot 10^{-8}$
S(6)	6.1089	5829.8	$1.14 \cdot 10^{-7}$
S(7)	5.5115	7196.6	$2.00 \cdot 10^{-7}$

The pure rotational lines $(v' - v'') = (0 - 0)$ detected in the sample range from S(7) to S(0), with corresponding excitation energies of $E_{S_0}/k = 510$ K to $E_{S_7}/k = 7197$ K (e.g. Rosenthal et al. 2000). For 12 out of 14 sources I observed rotational H_2 lines. In general the observed rotational lines originates from either collisional or fluorescence induced excitation. For the collisional induced lines, other mechanisms, besides thermal excitation, such as shock excitation or PDR contributions at the atomic-to-molecular interface must be considered (see Section 2.5). The fluoresces induced transitions are pumped into high ro-vibrational states by a sufficiently high FUV-radiation field (e.g. from PDRs) and decays back to $v' = 0$. In the optical and infrared the exication levels are populated in a characteristic way (e.g. Black & van Dishoeck 1987); fluorescence emission prevails the ro-vibrational and high-rotational levels. In particular the fluorescence exceeds collisional excitation in populating vibrational levels with $v \geq 2$, hence only observed H_2 lines at $\lambda < 2\,\mu$m with transitions $\Delta \geq 2$ are clearly fluorecence dominated. The H_2 transition accessible by IRS are mostly collisional excited. Numerical models for fluorescent (0-0) H(2) transitions indicate that for typical FUV radiation field strengths of $10^2 - 10^3 G_0$ (for PDRs, see Figure 2.27) and sufficiently high gas densities ($n \geq 10^4$ cm^{-3}) the S(3) line should stronger than the S(5) and S(2) line (Black & van Dishoeck 1987). This is not observed for the sources in this sample. IRAC observations of "green and fuzzy " features in regions of massive star-formation by Takami et al. (2012) show that fluorescence emission are only a minor contributor to the rotational lines S(13)-S(3). It is assumed that collisional excitation is the predominant source for the observed rotational H_2 line and fluorescence emission are marginal, but a complete analysis is inaccessible with the lack of H_2 line towards smaller wavelengths as observed by SWS/ISO.

Except for three IRDC sources, the low $J < 2$ lines with low excitation energies ≤ 1015 K were detected which can trace warm gas. Only for one source were all the (0-0) transitions present, from S(0) to S(7). Due to the low signal-to-noise ratio in the low resolution spectra the S(0) line can only be identified in the high resolution spectra. The observed rotational lines are listed in Table 2.5. The high resolution spectra reveal the presence of the S(2) (1-1) (12.93 μm) line for all ISOSS sources apart from the ISOSS J20153+3453 targets. For all targets with detected S(2), S(1) and S(0) lines, the line ratios S(2)/S(1), S(2)/S(0) and S(1)/S(0) are below 1.

2.4.3. PAH features

The PAH bands were identified with the features tabulated in Draine & Li (2007). The 6.2 μm and the 7.7 μm feature originate from pure CC stretching and CH in-plane bending. They, along with the 8.6 μm CH in-plane vibration mode (Tielens 2008), can be clearly detected in ISOSS J04225+5150, ISOSS J20153+3453 West and G010.70-0.13 II (see Figure 2.32). These bands are also observed in the background spectrum of G019.27+0.07, but not in the source spectrum. For these targets the first feature is centered at $6.21 - 6.22\,\mu$m and the PAH emission complex around 7.7 μm is asymmetrical with a peak between 7.57 and 7.64 μm. In each case, a secondary, weaker component is embedded in the red flank of this profile. Based on the profile shape and peak position I conclude that Class

$\mathcal{A}$ PAHs are dominant in these region (Peeters et al. 2002). The $11.2\,\mu\mathrm{m}$ and $12.8\,\mu\mathrm{m}$ features can also be clearly identified in the spectra from these sources. These bands originate from CH out-of-plane bending modes (Tielens 2008). In addition, several PAH bands between 16.2 and $18.2\,\mu\mathrm{m}$ are present, although these feature blend into a plateau (see Figure 2.32, right panel). Similar plateaus have been observed with ISO for some YSO and compact H II regions (Van Kerckhoven et al. 2000). Another broad PAH band is clearly observed between $18.9 - 19.0\,\mu\mathrm{m}$ for ISOSS J04225+5150 East, ISOSS J20153+3453 West and G010.70-0.13 II. Tielens (2008) argued that this feature could arise from highly ionized PAHs.

The $11.2\,\mu\mathrm{m}$ band can appear as a extended bright background emission which is not associated with the source itself. This is the case for ISOSS J18364–0221, ISOSS J23053+5953, G028.04–0.46, G034.43+0.24, G053.25+0.04 I+II. The same effect is also present for the $12.8\,\mu\mathrm{m}$ PAH band for G028.04–0.46 and G053.25+0.04 I. No PAH bands were detected in the background subtracted spectrum from G010.70–0.13 I, although the $6.2\,\mu\mathrm{m}$ feature was observed as an extended background emission. No PAH features were found in the spectrum from ISOSS J18364–0221 West.

Table 2.5. – Physical parameters and Spectral features

Source	Distance [kpc]	L_{bol} [a] [$L_\odot$]	PAH	Ices & Molecular absorptions	Silicate	H_2 [b]	Atomic lines [c]
IRc2[(A)]	0.45		✓	H_2O, CO_2, C_2H_2	✓	✓	[Ne II] , [Ne III] , [P III] , [Fe II] , [S I] , [S III] , [Si II]
ISOSS							
J04225+5150 East	5.5[(B)]	5000	✓	CO_2	✓	S(0)-S(4), S(5)	[Ne II] , [Fe II] , [Si II]
J18364−0221 East	2.2	70[d]	✓	-	-	S(0)	[S I] , [Si II] , [Fe II]
J18364−0221 West	2.2	550	-	CO_2, H_2O, CH_4	✓	-	-
J20153+3453 East	2.0	920	✓	CO_2	✓	S(1)	[Fe II] , [Si II]
J20153+3453 West	2.0	920	✓	-	emiss.	S(1), S(2)	[Fe II] , [Si II]
J23053+5953 East	3.5	2300	✓	CO_2	✓	S(0)-S(7)	[Fe II] , [Si II] , [S I]
G010.70-0.13 I	3.7	39[e]	✓	H_2O, CO_2	✓	S(1)	[Ne II] , [Si II]
G010.70-0.13 II	3.7	18[e]	✓	-	✓	S(1)	[Ne II] , [Si II]
G019.27+0.07	2.4[(C)]	9[e]	✓[f]	CO_2[f]	✓[f]	S(0)[f], S(1)[f]	no hi-res
G025.04-0.20	3.4[(C)]	41[e]	-	H_2O, NH_4^+, CH_4	✓	-	no hi-res
G028.04-0.46	3.2[(C)]	39[e]	✓	H_2O, NH_4^+, CH_4	✓	S(1)	no hi-res
G034.43+0.24	3.7[(D)]	25[e]	✓	H_2O, NH_4^+	✓	S(2), S(4)-S(7)	no hi-res
G053.25+0.04 I	1.9[(C)]	5[e]	✓	H_2O, NH_4^+	✓	S(2)-S(7)	no hi-res
G053.25+0.04 II	1.9[(C)]	4[e]	✓	H_2O, NH_4^+	✓	S(4), S(5)	no hi-res

[a] The bolometric luminosities were estimated using the SEDs shown in Figure 2.11.

[b] The presence of pure rotational lines in the high or low resolution spectra are listed in this column.

[c] Atomic lines which could not be observed due to missing high resolution spectra, were labeled as not available (no hi-res).

[d] Due to the missing IRAC counterparts the calculated luminosity for ISOSS J18364−0221 East represents just an lower limit.

[e] The luminosities for the IRDC sources are calculated with the IRAC and MIPS bands only. [f] Only observed in the background spectrum.

Table References: (A) van Dishoeck et al. (1998); (B) Birkmann (2007); (C) Rathborne et al. (2006)

2.4.4. Silicates and molecular absorptions

I was able to identify several absorption bands in my sample. The $9.7\,\mu\mathrm{m}$ silicate absorption feature was found in most sources of the sample. For ISOSS J20153+3453 West a broad emission component appears between 8 and $13\,\mu\mathrm{m}$ instead of the silicate absorption. I identified absorption bands by water ice ($6.0\,\mu\mathrm{m}$), NH_4^+ ($6.85\,\mu\mathrm{m}$), methane ice ($7.67\,\mu\mathrm{m}$) and carbon dioxide ice ($15.2\,\mu\mathrm{m}$). The presence of those absorption bands and their optical depths are listed in Table 2.6. The IRDC sources, only taken in the short wavelength orders, are not accessible for CO_2 ice detections. To calculate these optical depths, I fitted the spectral continuum using multiple blackbody components and removing possible PAH contamination. This was accomplished with the `PAHFIT` routine described in Smith et al. (2007). I calculated the optical depth τ for the ice features as in Quanz et al. (2007) using

$$\tau = -\ln\left(\frac{F_{obs}}{F_{min}}\right) \tag{2.2}$$

Here, $F_{min}(\lambda)$ is the observed flux of the absorption feature and $F_{cont}(\lambda)$ the fitted continuum flux. In addition to the removal of PAH contributions I utilized the `PAHFIT` routine to calculate $\tau_{9.7}$ for the silicate absorption. The routine is fitting the underlying continuum via multiple blackbody fits and using the silicate profile from Kemper et al. (2004). (For detailed description see Smith et al. (2007).) The optical extinction A_v calculated from $\tau_{9.7}$ is tabulated in Table 2.6.

Table 2.6. – Optical depths.

Source	τ_{H_2O}	$\tau_{NH_4^+}$	τ_{CH_4}	τ_{CO_2}	$\tau_{Silicate}$ [a]	A_v [b]
J04225+5150 East				0.342 ± 0.012	0.57 ± 0.03	7.9
J18364−0221 West	0.256 ± 0.017	0.153 ± 0.010	0.055 ± 0.009	0.51 ± 0.04	1.38 ± 0.07	19.2
J23053+5953 East				0.34 ± 0.11	4.8 ± 0.3	67
G10.70−0.13 I	0.34 ± 0.05	0.24 ± 0.04		0.51 ± 0.06	1.60 ± 0.08	22
G10.70−0.13 II					1.63 ± 0.09	23
G025.04−0.02	0.49 ± 0.05	0.399 ± 0.017	0.118 ± 0.013		2.5 ± 0.2	35
G28.04−0.46	0.84 ± 0.08	0.33 ± 0.04			1.01 ± 0.06	14.1
G34.43+0.24	1.14 ± 0.14	0.44 ± 0.04	0.28 ± 0.05		1.7 ± 0.09	24
G053.25+0.04 I	0.348 ± 0.027	0.174 ± 0.012	0.081 ± 0.010		0.267 ± 0.013	3.7
G053.25+0.04 II	0.43 ± 0.08	0.80 ± 0.08	0.18 ± 0.04		0.47 ± 0.03	6.6

[a] To calculate the silicate optical depth $\tau_{9.7}$ after the correction for possible PAH contamination I used the `PAHFIT` routine (Smith et al. 2007).

[b] The optical extinction A_v was calculated from the silicate bands using the extinction model from Robitaille et al. (2007).

2.4.5. Ionic fine structure lines

Several fine structure lines were detected in the high resolution spectra. The identified lines are listed in Table 2.5 and plotted in Figure 2.18 after a second order baseline fit was applied. The iron line [Fe II] can be detected at $25.99\,\mu\mathrm{m}$ or $35.35\,\mu\mathrm{m}$. The [Si II] appears at $34.82\,\mu\mathrm{m}$. The sulfur line [S I] ($25.25\,\mu\mathrm{m}$) is only detected for two sources in the sample. The neon emission [Ne II] ($12.81\,\mu\mathrm{m}$) always appears on top of a broad PAH feature.

Table 2.7. – Line flux ratios for [Ne II]

	ISOSS J04225+5150	G010.70-0.13 I	G010.70-0.13 II
$\frac{F_{[\mathrm{Ne\ II}]}}{F_{\mathrm{S(2)}}}$	1.04	2.8	2.3
$\frac{F_{[\mathrm{Ne\ II}]}}{F_{\mathrm{S(1)}}}$	0.63	0.36	0.85
$\frac{F_{[\mathrm{Ne\ II}]}}{F_{\mathrm{S(0)}}}$	0.64	0.04	0.44
$\frac{F_{[\mathrm{Ne\ II}]}}{F_{[\mathrm{Fe\ II}]}}$	0.22	-	0.25
$\frac{F_{[\mathrm{Ne\ II}]}}{F_{[\mathrm{Si\ II}]}}$	0.04	0.10	0.5

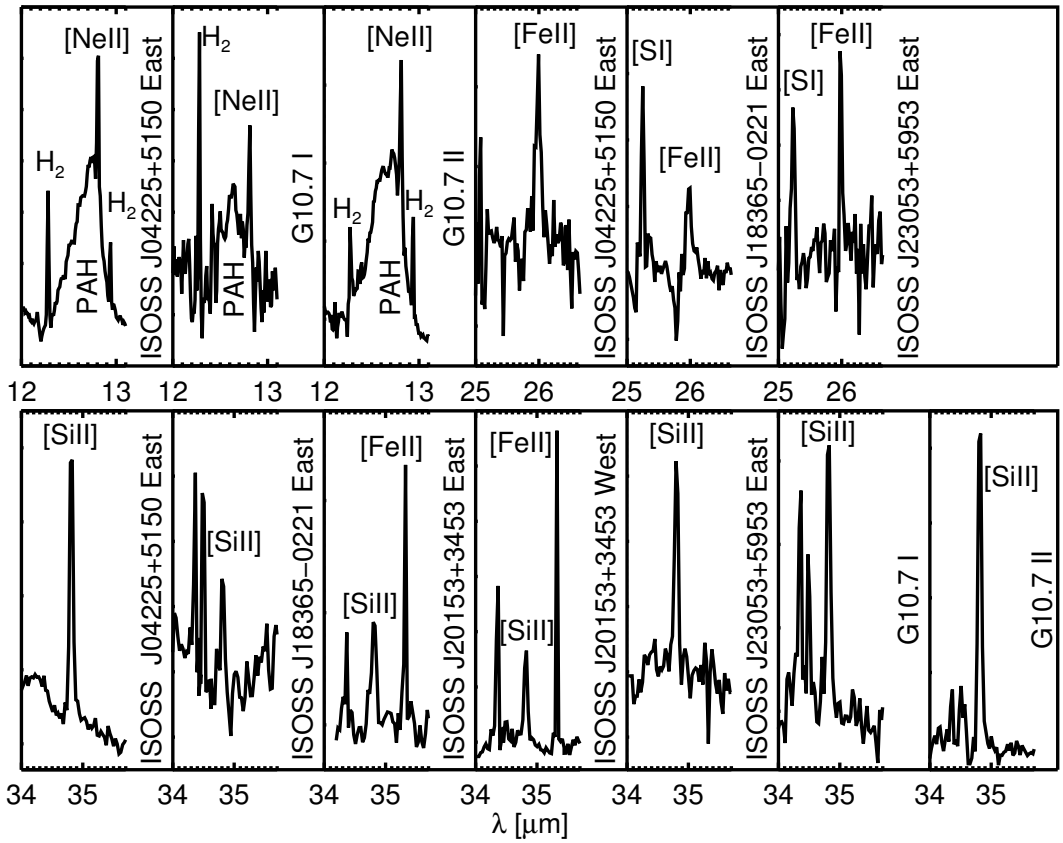

Figure 2.18. – Fine structure lines as observed in the high-resolution spectra.

2.4.6. Spatial extent of lines

The spatial line fits for the ISOSS J20153+3453, ISOSS J04225+5150 and the ISOSS J23053+5953 regions are shown in Figure 2.19, 2.20 and 2.21 respectively. In these figures the relative line fluxes are shown as a function of their spatial distributions. The positions for the line extraction are overlayed for the short (SL) and long (LL) wave length orders and the two different nod observations (in red and blue). For the LL slit positions I only indicate the overlap of the two nodded observations on the IRAC map and not the whole slit length. On top I present the spatial line fits for the long wavelength orders ($14 - 37\,\mu\mathrm{m}$) for the S(1) 0-0 H_2 line and the $16.45\,\mu\mathrm{m}$ PAH feature. The lines where fitted with a 2nd order polynomial for local background estimation and a Gaussian for the line fit. The bottom plots present the line fits for short wavelength orders ($5.5 - 14.5\,\mu\mathrm{m}$) for PAHs and molecular hydrogen lines S(5) and S(3).

For the ISOSS J20153+3453 region I find similar spatial profiles of the 6.2 and $11.2\,\mu\mathrm{m}$ PAH features, which both peak slightly eastwards ($\sim 4-5''$) of the western MIPS maximum at $24\,\mu\mathrm{m}$. The line fluxes from both these PAH features decrease faster towards the east than towards the west. The relative line flux distribution of these features is similar towards the western end of the slit, but, unlike the $11.2\,\mu\mathrm{m}$ feature, the $6.2\,\mu\mathrm{m}$ PAH band cannot be detected eastwards of the eastern MIPS source at $24\,\mu\mathrm{m}$. The two molecular hydrogen lines S(3) and S(5) are not detectable at the western $24\,\mu\mathrm{m}$

MIPS peak location, but instead from two extended features to the east and west of this position.

For ISOSS J23053+5953 East I detect an extended PAH feature at $11.2\,\mu\mathrm{m}$ with almost constant line flux over the entire slit. Although the $6.2\,\mu\mathrm{m}$ PAH feature is not detected in the whole slit, it does have a similar line fluxes distribution to the $11.2\,\mu\mathrm{m}$ feature in the western end. The S(5) H_2 feature is detected to both the east and west of the MIPS peak at $24\,\mu\mathrm{m}$. The S(3) H_2 line is also detected at the MIPS peak position. The $16.45\,\mu\mathrm{m}$ PAH feature is only detected in the vicinity of the MIPS $24\,\mu\mathrm{m}$ source , whereas the S(1) hydrogen line is extended over more than $180''$ in this region.

The spatial line fits for the ISOSS J04225+5150 region are shown in Figure 2.20. The line fluxes for the PAH features at $6.2\,\mu\mathrm{m}$ and $11.2\,\mu\mathrm{m}$ and the S(3) H_2 line peak at the position of the brightest source observed in the IRAC and MIPS bands. The decrease of the line fluxes matches the morphology observed in the IRAC data. The slit for the LL observations partially covered the elongated submillimeter structure observed by SCUBA. While the $16.45\,\mu\mathrm{m}$ PAH and the H_2 S(1) line fluxes decreases in the near vicinity of the central source, the H_2 line appears to be almost constant through the western submillimeter peak.

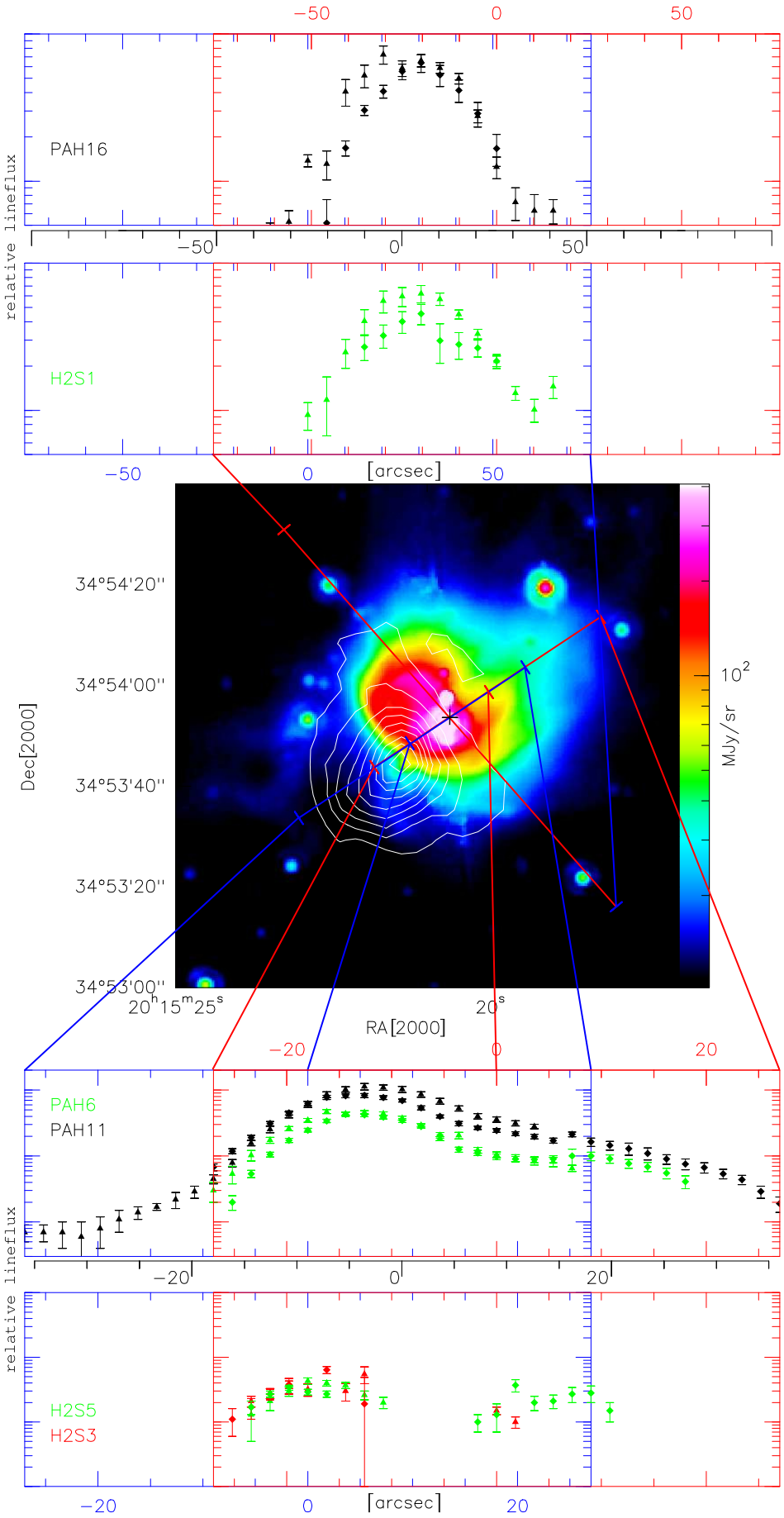

Figure 2.19. – For the low resolution spectra the spatial evolution of several PAH and H_2 lines over the whole slit for the ISOSS J20153+3453 region is presented. The IRAC 8 μm maps is shown and the 450 μm SCUBA contours are overplotted. The slit overlay is explained in Section 2.4.6.

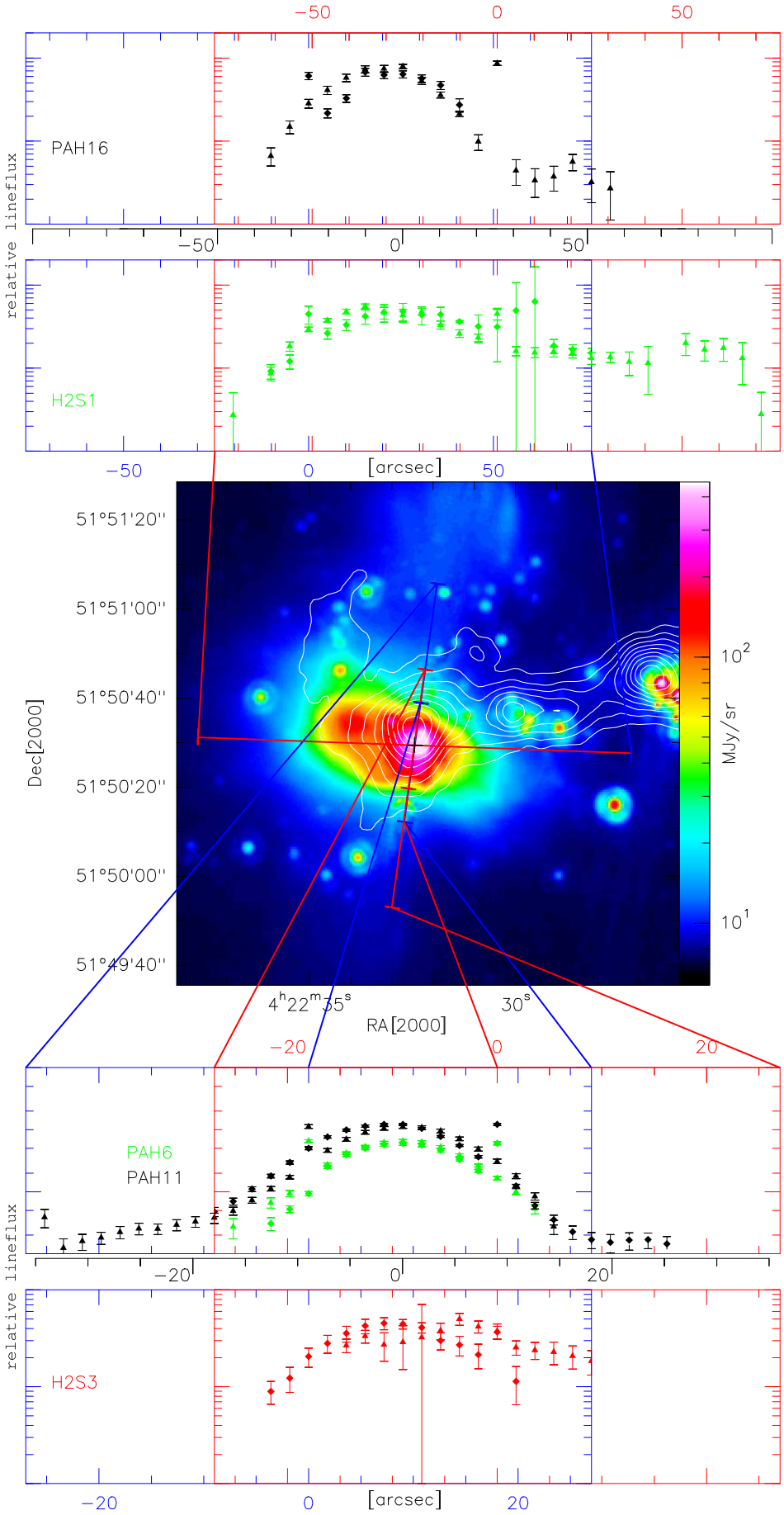

Figure 2.20. – The spatial line fits as in Figure 2.19 for the ISOSS J04225+5150 East region. The IRAC image at 8 µm and the SCUBA contours at 450 µm are used.

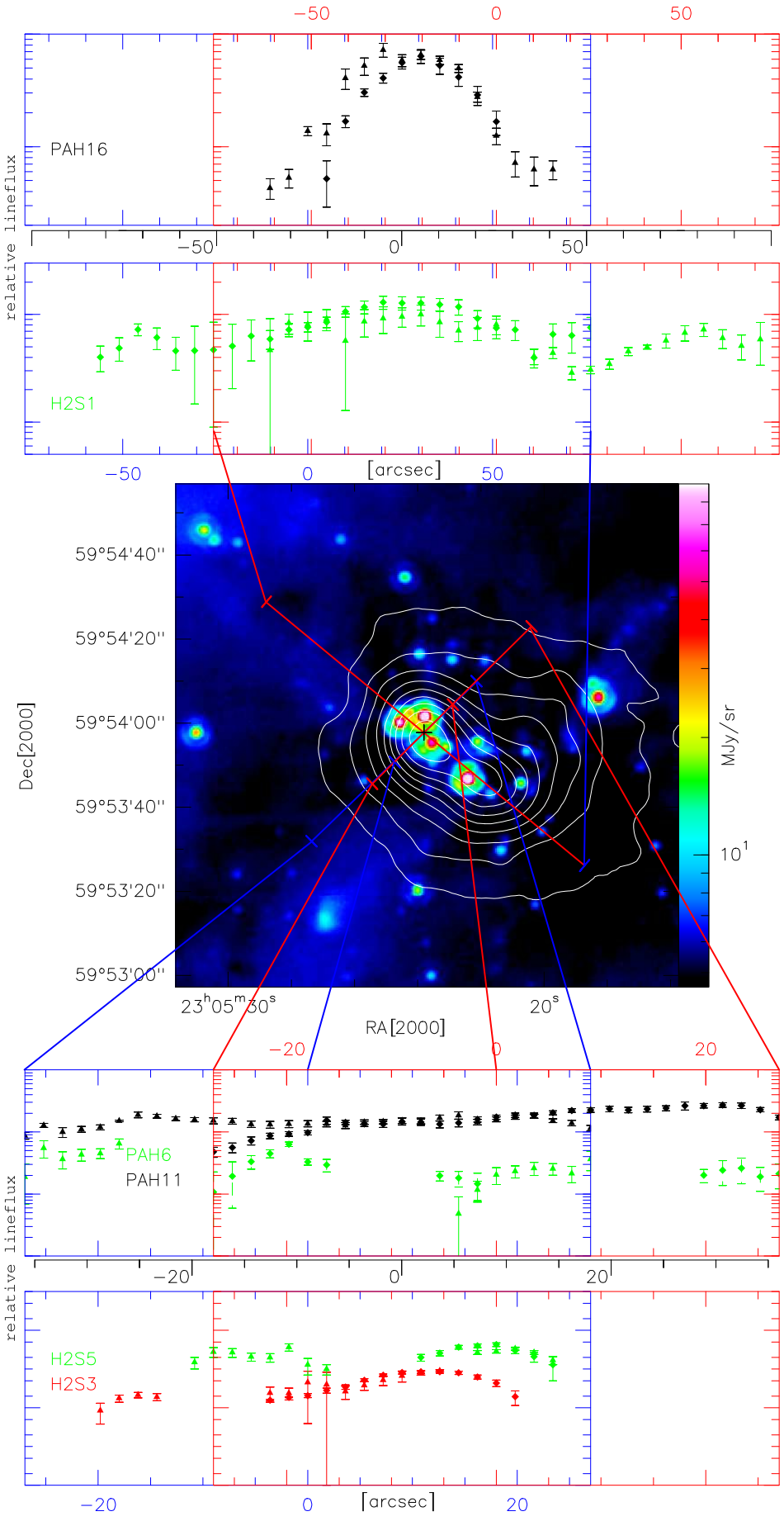

Figure 2.21. – The spatial line fits are shown as in Figure 2.19 for the ISOSS J23053+5953 region. The IRAC image at 8 μm and the SCUBA contours at 450 μm are used.

2.5. Discussion of individual sources

All the sources exhibit a complex morphology in the infrared. Therefore their spectra have to be reviewed in the context of previous observations. The different sources will be discussed individually, sorted by their evolutionary stage. The first sources are the most evolved ones, with indications for PDRs, followed by young, deeply embedded sources with several absorption features.

2.5.1. The ISOSS J20153+3453 region

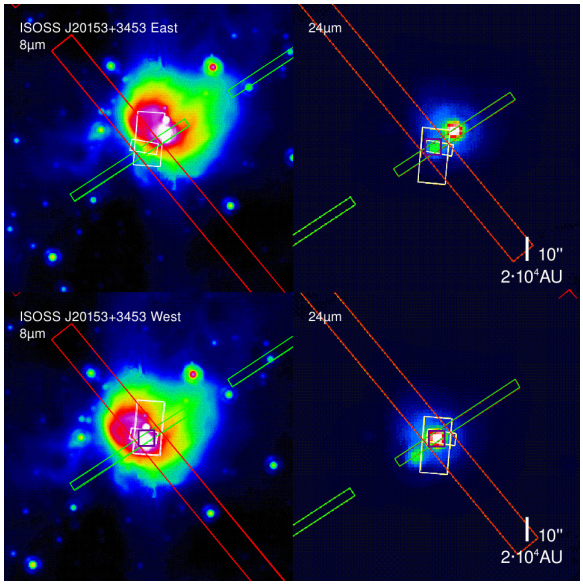

Figure 2.22. – Overlay of the IRS slits for the ISOSS J20153+3453 region. The IRAC 8 μm (left) and MIPS 24 μm (right) images are shown in false colors. North is up, and east is left. The slit positions for the IRS spectroscopy are overplotted for the low-resolution spectra in green (short wavelengths, SL) and red (long wavelengths, LL). The white overplots represent the high-resolution AOTs. The first nod position is indicated in the left and the second in the right panel. The source is indicated by the dark magenta box.

The ISOSS J20153+3453 region, located 2.0 kpc away, was studied by Hennemann et al. (2008). In the MIPS observations at 24 μm, the clump is resolved into an eastern and western component with a separation of 10". A single submillimeter clump was detected close to the eastern source by SCUBA. A dust temperature of $T_d = 15.3 - 17.0$ K and a gas mass of $M = 87{-}149\ M_\odot$ was calculated for the clump. Based on the IRAC colors, the MIPS source at 24 μm associated with the submillimeter peak was assumed to be a class 0/I object. The mass reservoir in this region contains enough gas to form a massive star, but due to the multiplicity of NIR and IRAC sources the interpretation of the further evolution in this region is not straightforward. Another MIPS 24 μm source, surrounded by extended emission, is located on the northwestern limb of the submillimeter clump.

The IRS spectrum of the western MIPS 24 μm source is dominated by several PAH bands. The broad emission feature between $8 - 13$ μm is typical for small, transiently heated dust grains distributed over a wide spatial range around the central sources. Photoelectric heating of the small dust and PAH grains accounts for thermal coupling of the grains to the gas, hence a certain amount of the observed molecular hydrogen must be thermally excited. The smooth spatial distribution of the S(1) H_2 line represents such thermally excited gas (Figure 2.19).

As for the ISOSS J23053+5953 region, the detected [Si II] and [Fe II] lines and the spatial distribution of the S(5) and S(3) H_2 emission can be attributed to J-shock excitation. The elongated "green and fuzzy" structures on the IRAC composite images fits this picture, as well (see Figure 2.24). In contrast to ISOSS J23053+5953 the PAH features in the spectrum of ISOSS J20153+3453 West are identified as class $\mathcal{A}$ according to Peeters et al. (2002) (see section 2.1). Therefore UV field strengths are sufficient to form a PDR. The 18.9 μm feature could represent highly-ionized cationic PAHs (Tielens 2008) and give further evidence for a strong UV radiation. The detected

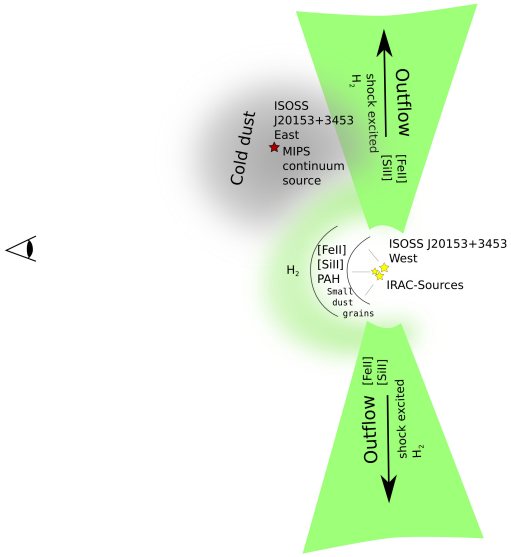

Figure 2.23. – Schematic representation of the ISOSS J20153+3453 region.

[Si II] and [Fe II] lines are not only found for J-shocks, they are know as minor coolants in PDRs (Abel et al. 2005; Hollenbach & Tielens 1997; Kaufman et al. 2006). I tried to fit the observed H_2 line ratios to the PDR models by Kaufman et al. (2006) (see Figure 2.27). The contribution by shock excited H_2 emission might impair the results. Nevertheless, the models show a trend towards higher gas densities in the outer layers of PDR ($n_H > 10^5$ cm^{-3}) and UV radiation fluxes between $10^2 - 10^3$ G_0. Similar results are found for ISOSS J04225+5150 East and G010.70–0.13 (Sec. 2.5.2 and 2.5.3). Although these observations can be interpreted as the result of a PDR, no indication of an associated H II-region can be found in the 20 cm NVSS data. Unfortunately, there are no 6 cm survey products available which are sensitive enough for the detection of an H II region.

One possible interpretation of the morphology of the this region is shown in Figure 2.23. The cationic PAHs and small grains photoelectrically heated by the IRAC sources are seen at the western position. H_2 emission and atomic fine structure lines originating from the warm layers of a PDR, but have been also formed via shocks. A clump of cold dust is located eastwards in the foreground, observed in the submillimeter regime (Figure 2.24). The LL spectrum extracted at the eastern position is centered on the eastern MIPS 24 µm peak. Here a young, deeply embedded continuum source is driving the heating of the submillimeter clump.

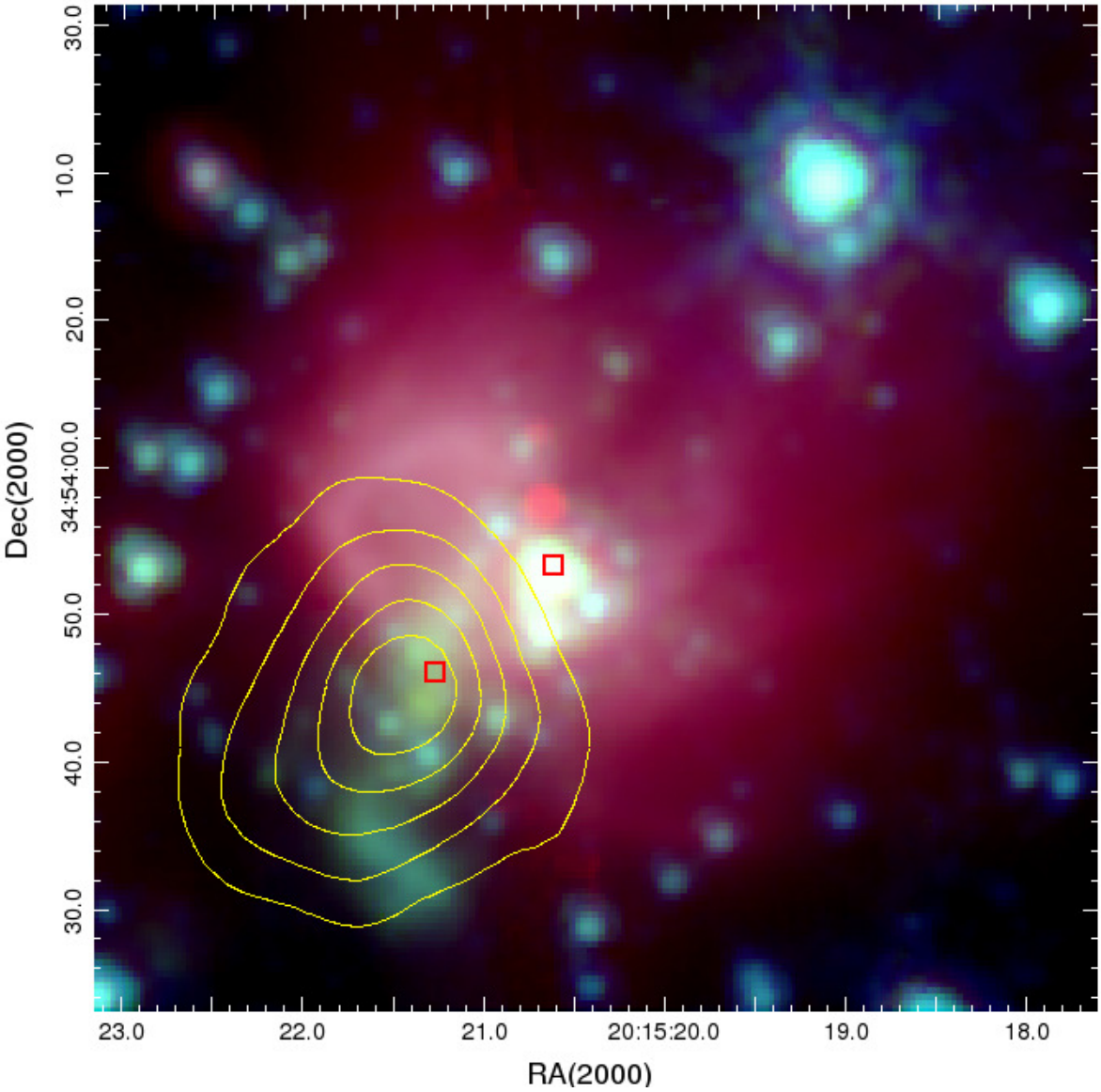

Figure 2.24. – IRAC composite image of the ISOSS J20153+3453 region: The 3.6 μm channel is colorized in blue, 4.5 μm in green and 8.0 μm in red. The contours of the SCUBA observations at 450 μm are shown in yellow. The two MIPS point sources at 24 μm are indicated by the red box points. They are used for the IRS pointing. At position of the eastern MIPS sources and the SCUBA source an elongated "green and fuzzy" feature can be seen.

2.5.2. ISOSS J04225+5150 East

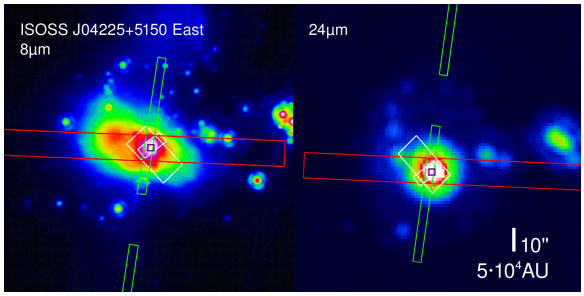

Figure 2.25. – Overlay of the IRS slits for ISOSS J04225+5150 East. Notations are the same as for Figure 2.22.

ISOSS J04225+5150 East shows three compact sources in the mid-infrared and submillimeter regime. The eastern clump has a mass of $M = 510\ M_{\odot}$ and a temperature of $T_d = 17$ K (Birkmann 2007).

The IRAC images show a bright point source with extended PAH emission in the $8\,\mu$m channel, and diffuse H_2 emission at $4.5\,\mu$m. At $24\,\mu$m, the source is surrounded by warm dust. Slightly shifted northwards from the MIPS $24\,\mu$m peak position the center of a submillimeter dust clump is detected by SCUBA (Figure 2.26). ISOSS J04225+5150 East shares several other features with the ISOSS J20153+3453 region: a class $\mathcal{A}$ PAH spectrum, [Si II] and [Fe II] lines. Hence, J-shocks and a PDR have be considered as the origin of these features as for ISOSS J20153+3453 West. However, in contrast to ISOSS J20153+3453, I detected the presence of the [Ne II] line. [Ne II] typically appears towards H II regions (Abel et al. 2005). The presence of the [Ne II] line can also be explained by shock excitation. Hollenbach & McKee (1989) predicted the presence of a strong [Ne II] line only for J-shocks with high shock velocities. The [Ne II] line ratios in Table 2.7 agree with the predictions from Hollenbach & McKee (1989). The H_2 line ratios are similar to ISOSS J20153+3453 West, therefore the results are similar for the PDR modeling (Figure 2.27). The line ratio fitting favor models with higher gas density ($n_H > 10^5 \mathrm{cm}^{-3}$) and UV radiation fluxes between $10^2 - 10^3$ G_0. For ISOSS J04225+5150, both PAH and H_2 are present, with almost constant line strengths in the western direction. The source is associated with an elongated structure of higher dust density observed with SCUBA at $450\,\mu$m. The absorption feature at $10\,\mu$m originates from an outer ridge of dust.

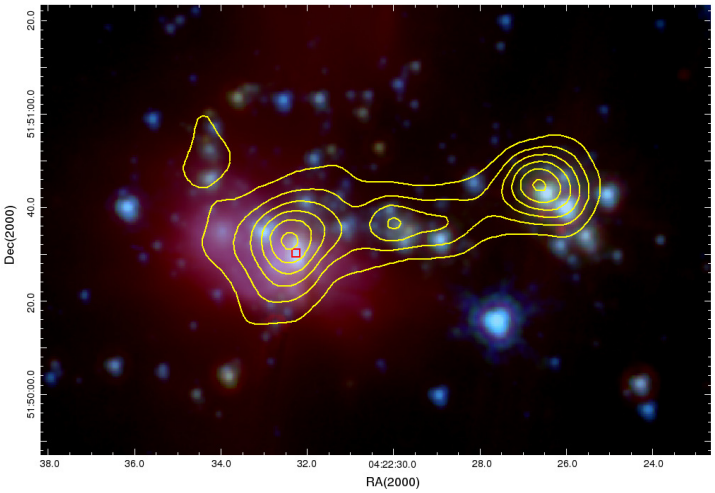

Figure 2.26. – IRAC composite image of the ISOSS J04225+5150 region: The 3.6 µm channel is colorized in blue, 4.5 µm in green and 8.0 µm in red. The contours of the SCUBA observations at 450 µm are overplotted in yellow. The peak position of the MIPS source at 24 µm, which is used for the IRS pointing, is indicated by the red box point.

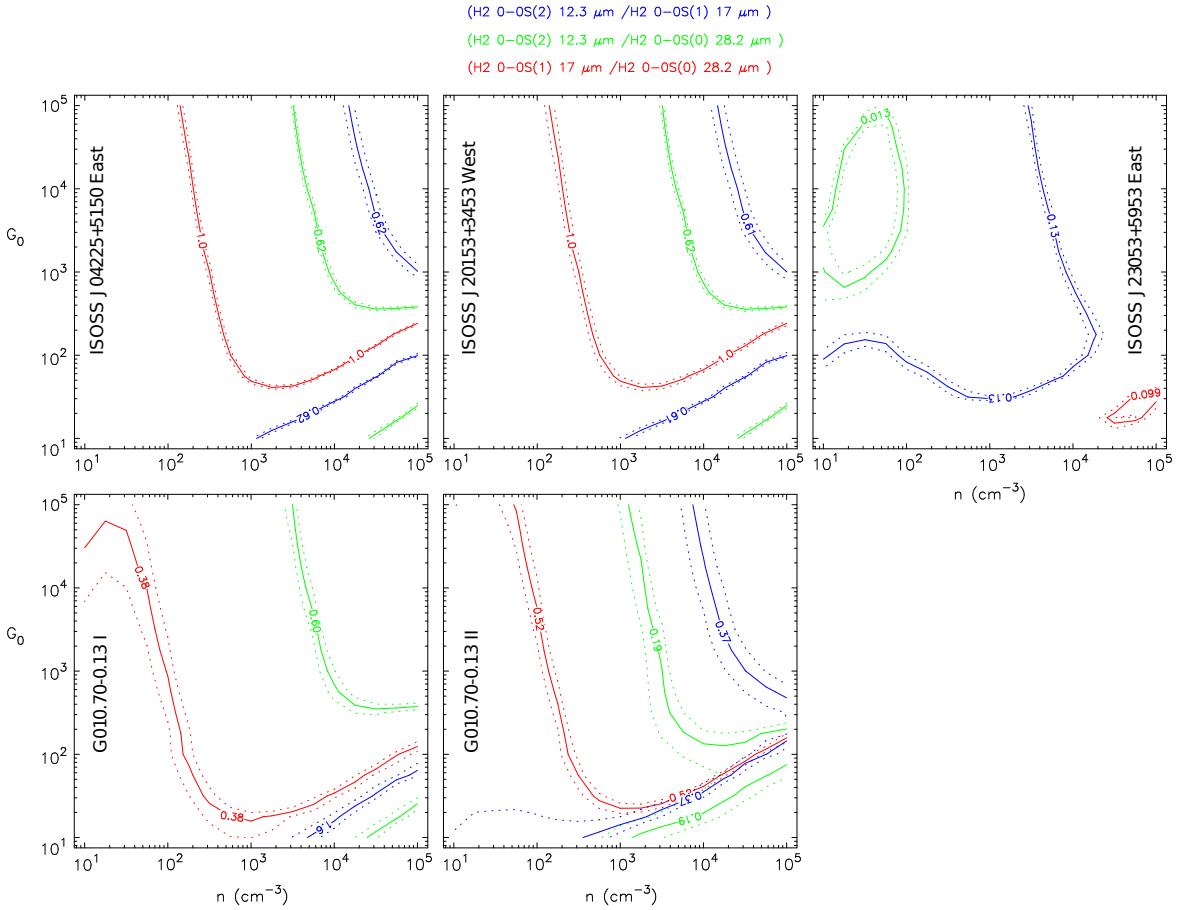

Figure 2.27. – The best fitting PDR models for certain H_2 line ratios from Kaufman et al. (2006) are shown. The line fluxes are obtained from the high resolution orders. For the visualization I used the PDR toolbox (`http://dustem.astro.umd.edu/pdrt/`). To show the contrast, ISOSS J23063+5963 is plotted as a region which do not host a PDR.

2.5.3. G010.70-0.13

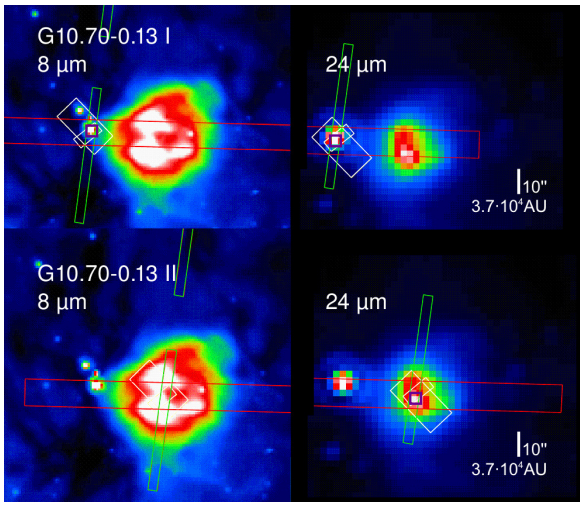

Figure 2.28. – Overlay of the IRS slits for the G010.70–0.13 region. Notations are the same as for Figure 2.22.

The G010.70-0.13 region can be found in the Spitzer dark cloud catalog (Peretto & Fuller 2009).

Two spectra were obtained for this region. The IRAC composite image shows dark filamentary structures against the bright PAH background. Around the eastern MIPS 24 µm peak position *(G010.70-0.13 II)*, extended PAH emission are present in the 8 µm band, as well as warm dust emission in the MIPS maps at 24 µm. A second western MIPS 24 µm source is centered on a strong IRAC point source (G010.70–0.13 I). It is located in the tail of an extended submillimeter clump obtained from the SCUBA legacy program (see Figure 2.29). For G010.70–0.13 I, I identified several absorption features, as NH_4^+, water ice, CO_2 ice, typical for deeply-embedded sources, which are also observed for ISOSS J18364–0221 West as well as the sources in the sample associated with young, embedded sources (discussed in section 2.5.7). Even though no extended H_2 emission was found, the flux ratios for [Ne II] , [Si II] and [Fe II] (Table 2.7) for G010.70–0.13 I+II agree with ratios for J-shocks (Lahuis et al. 2010). The spectrum of G010.70–0.13 II, located to the west, is dominated by PAH bands. Bright UV radiation entails a class $\mathcal{A}$ PAH spectrum. Similar to ISOSS J04225+5150 East and ISOSS 20153+3453 this region shows indications for J-shocks and a PDR, as well. The comparison of the H_2 line ratios with the PDR in Figure 2.27 show a correlation for a gas density of $n \geq 10^5$ cm^{-3} and and a UV flux of $1 - 2 \cdot 10^2$ G_0 for G010.7–0.13 II. The line ratio fit for G010.7–0.13 I did not converge as for the prior spectrum; probably the eastern spectrum is just tracing the outer parts of the PDR and the contribution of shocks to the H_2 lines is stronger in this spectrum. I obtained the 6 cm and 20 cm survey products for this region from the Multi-Array Galactic Plane Imaging Survey (Helfand et al. 2006; White et al. 2005). No indications for an associated H II region were found. My hypothesis is that G010.70-0.13 contains a PDR connected to a very young H II region, which is still optically thick at 6 cm and 20 cm. In such a case, the H II region would not be detected given the sensitivity of these radio observations.

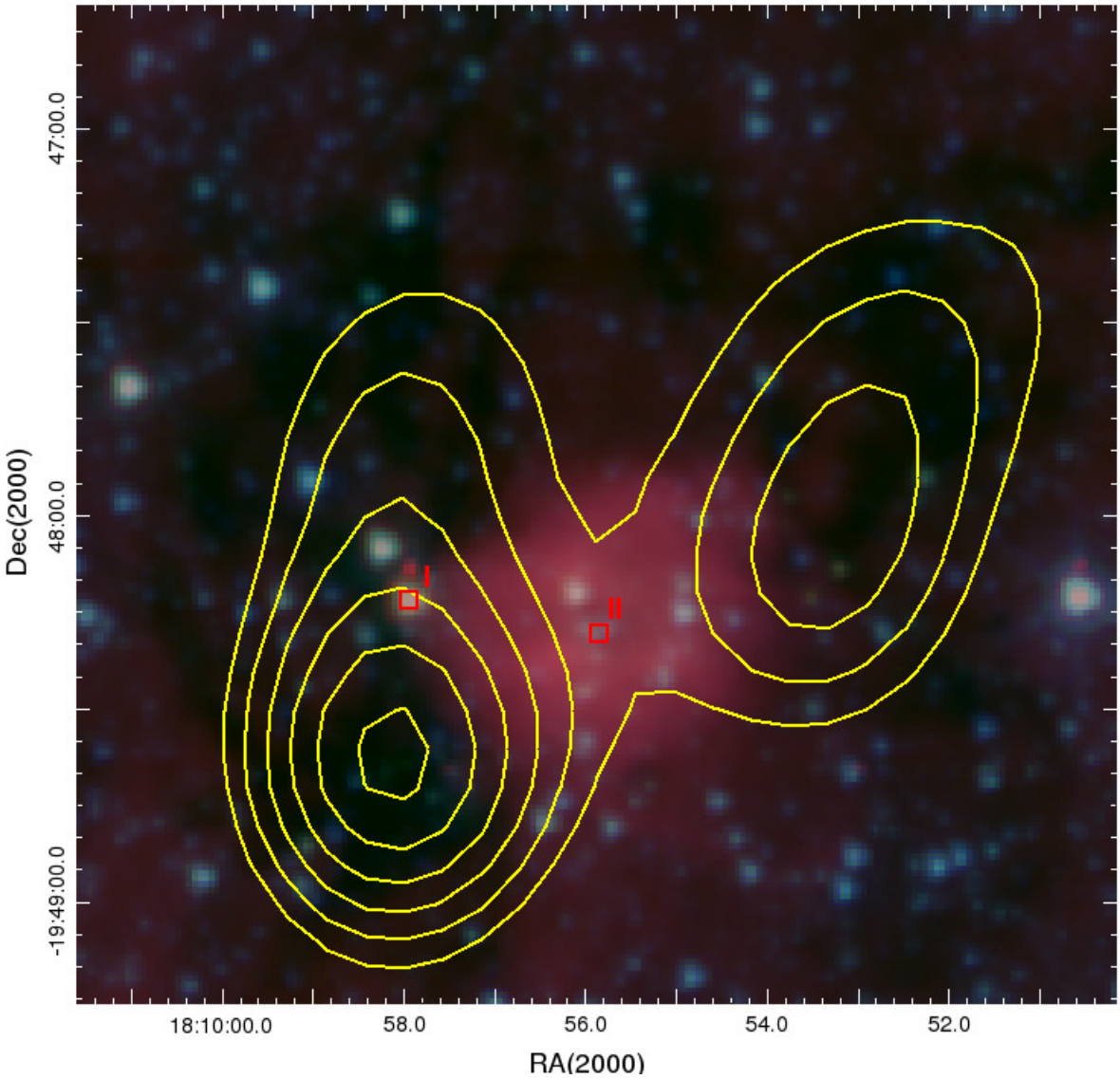

Figure 2.29. – IRAC composite image of the G010.70-0.13 region. The $3.6\,\mu m$ channel is colorized in blue, $4.5\,\mu m$ in green and $8.0\,\mu m$ in red. The peak positions of the MIPS points sources at $24\,\mu m$ are indicated by the red box points. The IRS slits were centered on the position.

2.5.4. ISOSS J18364–0221 East

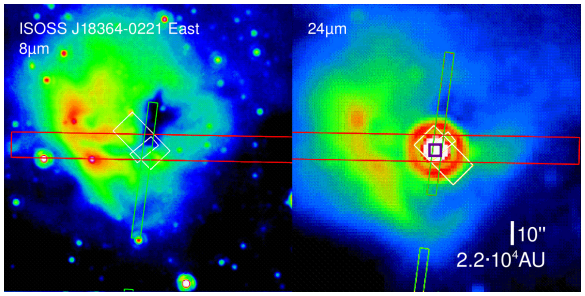

Figure 2.30. – Overlay of the IRS slits for ISOSS J18364–0221 East. Notations are the same as for Figure 2.22.

Interferometric maps of 1.3 and 3.4 mm continuum emission show two cores. One core appears as a point source on the MIPS maps, surrounded by warm dust emission at $24\,\mu\mathrm{m}$. The IRAC observations do not show any point source at this position. The dust mass of both cores was estimated with $12\,\mathrm{M}_\odot$ and $18\,\mathrm{M}_\odot$, with a dust temperature of 22 K and 15 K. Narrow-band NIR observations at $2.122\,\mu\mathrm{m}$ (H_2 S(1) 1-0) are related to outflow lobes, traced by CO(2-1) emission around the MIPS source (Hennemann et al. 2009).

The IRAC bands for $4.5\,\mu\mathrm{m}$ and $5.8\,\mu\mathrm{m}$ show some filaments, tracing H_2 stemming from the outflow. The MIPS $24\,\mu\mathrm{m}$ source is surrounded by extended emission in the $8\,\mu\mathrm{m}$ IRAC band. This band reveals a brighter ridge eastwards.

Although the SL orders only show a non-uniform extended background spectrum, a strong PAH band appears over the whole slit at $11.2\,\mu\mathrm{m}$. The only detected lines are S(1) H_2, [S I] , [Fe II] and [Si II] , which may be shock related. The [S I] emission is not strong in PDRs (Kaufman et al. 2006), but can be found, velocity independent, in J-shocks (Hollenbach & McKee 1989).

Due to the lack of the SL order spectra, no further conclusions can be drawn.

2.5.5. ISOSS J23053+5953 East

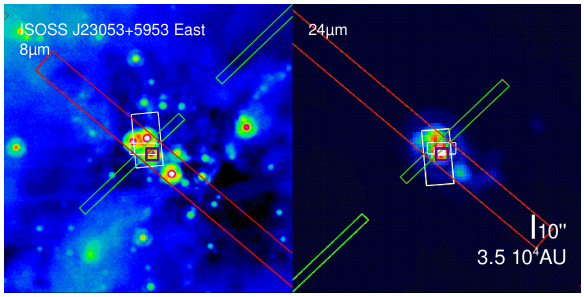

Figure 2.31. – Overlay of the IRS slits for ISOSS J23053+5953 East. Notations are the same as for Figure 2.22.

The ISOSS J23053+5953 region has been studied by Birkmann et al. (2007). It is located at a distance of 3.5kpc. In this region, two submillimeter cores with $T_d = 19.5\,\mathrm{K}\,/\,17.3\,\mathrm{K}$ and a mass of $\approx 200\,\mathrm{M}_\odot$ each were observed. Both cores show signs of infall, as indicated by interferometric HCO^+ measurements. IRAC and NIR imaging show several embedded point sources, surrounded by diffuse PAH emission in the IRAC $4.5\,\mu\mathrm{m}$ images. Narrowband observations ($\lambda = 2.122\,\mu\mathrm{m}$) taken by the Omega 2000 prime focus camera at the Calar Alto 3.5 m telescope show elongated H_2 S(1) 1-0 shock excitation.

The $24\,\mu\mathrm{m}$ MIPS observations show a bright source centered on the eastern submillimeter core, surrounded by extended warm dust emission and two fainter sources. Another faint source appears eastwards close to the peak position of the western submillimeter core.

ISOSS J23053+5953 appears as a deeply embedded source. The extinction, calculated from the $9.7\,\mu\mathrm{m}$ silicate feature, is the highest in the given sample (see Table 2.6). The bright $11.2\,\mu\mathrm{m}$ PAH feature is spatially extended over more than 1' with almost constant line strength, as shown in the spatial line fits (Figure 2.21). The spectrum of ISOSS J23053+5953 East is dominated by neutral PAHs. No spectral indications for a PDR such as e.g. strong cationic PAH bands were found in this region. Furthermore, by fitting the H_2 line ratios to the PDR models by Kaufman et al. (2006) no correlation between density n and FUV intensity G_0 modeled for different line ratios were found (see Figure 2.27).

Therefore the observed forbidden lines of [Fe II] , [Si II] and [S I] do not originate from the hot layers of a PDR. These lines can be formed in the dense hot post-shocked gas of J-shocks (Hollenbach & McKee 1989). Furthermore, the observed [S I] line is never strong in PDRs (Kaufman et al. 2006), but can be observed as a velocity independent emission line in J-shocks (Hollenbach & McKee 1989). The presence of higher H_2 rotation lines are typical for the post-shock gas phase (Lahuis et al. 2006). Therefore, a possible interpretation of the spatial distribution of the S(5) H_2 line is that it represents the distribution of the cooling shocked gas, (the S(5) line was only detected sidewards of the MIPS $24\,\mu\mathrm{m}$ peak position). However, fluorescence pumping can not be completely ruled out as an excitation mechanism. It is expected that fluorescence is only a minor contributor to the S(5) line, but the shock induced decomposition of dust grains and PAHs might lower the FUV-opacity in the post-shocked gas leading to fluorescence emission in the post-shocked gas itself (Takami et al. 2012; Smith et al. 2006). The observed "green and fuzzy" features in the IRAC bands and narrow band imaging ($\lambda = 2.122\,\mu\mathrm{m}$, H_2, S(1), 1-0) reveal the presence of excited H_2. This supports the hypothesis of molecular hydrogen emission from a post-shock relaxation region. The $6.22\,\mu\mathrm{m}$ PAH band is detected towards most of the positions where the S(5) H_2 line was observed. Therefore, the excitation mechanism could be the same for this particular PAH as for the S(5) H_2 lines. No molecular emission from CO, H_2O or OH, indicators for C-shocks, were found. Also the line H_2 ratios disagree with the results of Kaufman & Neufeld (1996).

The symmetric decrease of the S(3) line fluxes around the source position indicates that a predom-

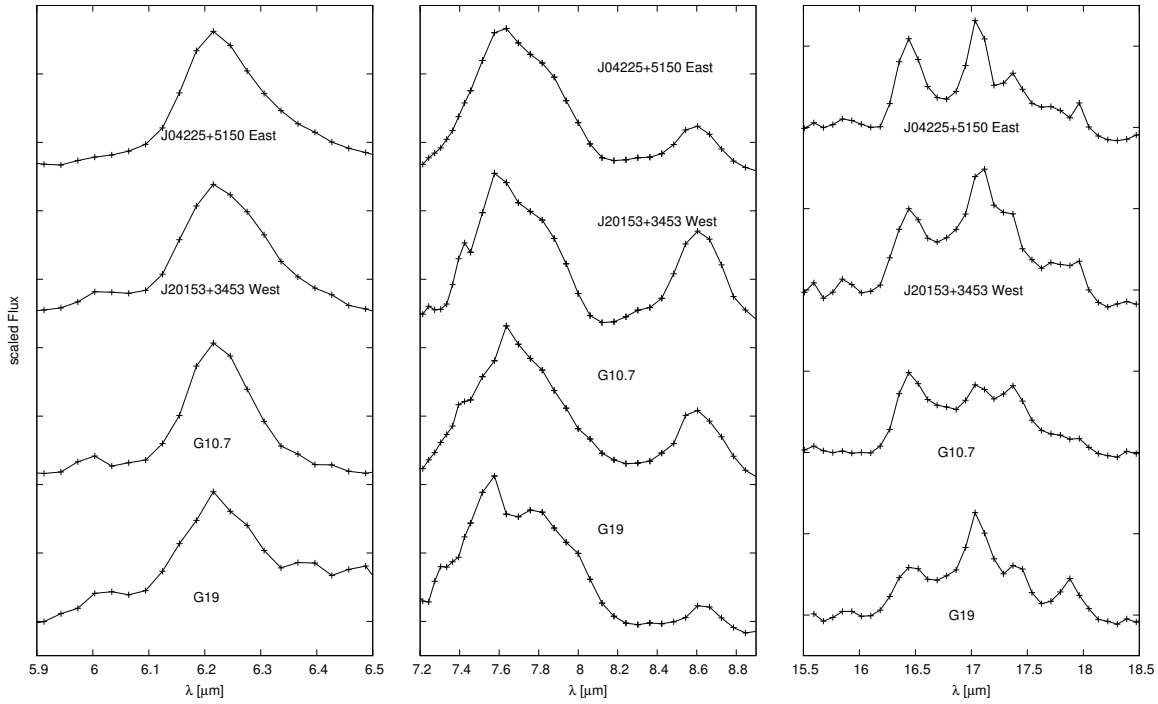

Figure 2.32. – The $6.2\,\mu\mathrm{m}$ (*left*), $7.7/8.6\,\mu\mathrm{m}$ (*center*), and $16/18\,\mu\mathrm{m}$ (*right*) PAH bands. The global and local continuum has been removed, as proposed by Peeters et al. (2002). The $17.03\,\mu\mathrm{m}$ feature is attributed to the H_2 S(1) line. The PAH features for G19.27+0.07 were obtained from the background spectrum.

inant fraction of the gas is thermally excited by the central source. The cooler gas traced by the S(1) line is extended over more than $2\farcs5$. Absorption bands of CO_2 ice and amorphous silicates indicate the presence of an outer ridge of cold material facing the observer.

2.5.6. ISOSS J18364−0221 West - An isolated, icy source

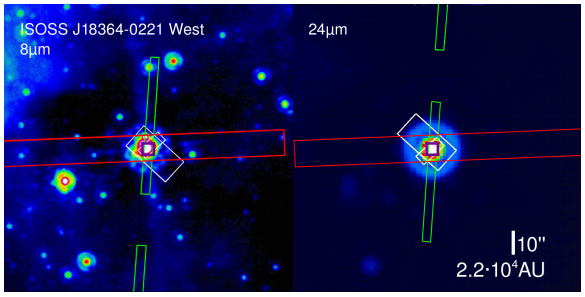

Figure 2.33. – Overlay of the IRS slits for ISOSS J18364−0221 West. Notations are the same as for Figure 2.22.

The ISOSS J18364−0221 region 2.2 kpc away has been studied by Birkmann et al. (2006). These observations show a large scale submillimeter clump with two separate cores in the SCUBA bands. For the western component a mass of $M = 280^{+75}_{-60}\,\mathrm{M}_\odot$ and a temperature $T_d = 12.8\,\mathrm{K}$ was estimated.

The IRAC observations show a bright compact object, some weak extended emission features and a faint point source eastwards on the first airy ring. The bright point source on the northern edge of the airy ring of the central source must be treated as an artifact since it does not show the characteristic IRAC PSF. In the MIPS bands a single point source appears centered on the central bright IRAC source. The cross dispersion profile appears to be oblate and broadened, hence the target is consistent with the IRAC observations of a compact, but extended, source. The spectroscopy shows several ice absorption features and a broad silicate absorption at $9.7\,\mu\mathrm{m}$.

For ISOSS J18364−0221 West, the SED-fitter from Robitaille et al. (2007) favors masses below $2\,\mathrm{M}_\odot$ and accretion rates between $10^{-5} - 3\cdot10^{-4}\,\mathrm{M}_\odot\mathrm{yr}^{-1}$. The modelled envelope and ambient masses are proportional to the accretion rates and range from $0.1 - 10\,\mathrm{M}_\odot$. This is consistent with the scenario of a deeply embedded young low mass proto-star which could presumably evolve into an low to intermediate mass star. Birkmann et al. (2006) already classified this object as a low mass Class I object based on the NIR colors.

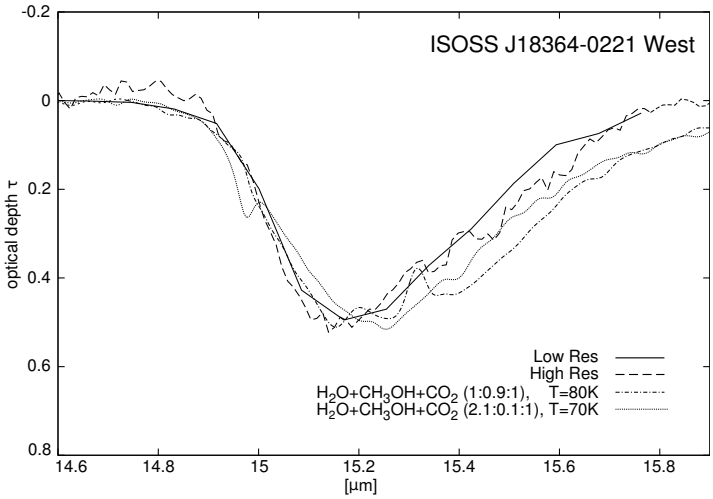

Figure 2.34. – Optical depths of the $15.2\,\mu\mathrm{m}$ ice feature for ISOSS J18364–0221 West. The solid line represents the low-resolution spectrum. The long dashed line represents the high-resolution spectrum. The two other lines represent laboratory absorbance data for an ice mixture of methanol, water and carbon-dioxide for temperatures of 70 and 80 K (White et al. 2009).

The absorption profile for the $15.2\,\mu\mathrm{m}$ ice feature cannot be explained by pure CO_2. I compared the profile of ISOSS J18364−0221 West with different absorption profiles for $H_2O + CH_3OH + CO_2$ mixtures from White et al. (2009). The best fit was found for ice mixtures heated to $70 - 80\,\mathrm{K}$ (Figure 2.34). Therefore the protostar is in fact the heating source of the ice, and not a background object.

2.5.7. Young embedded IRDC sources

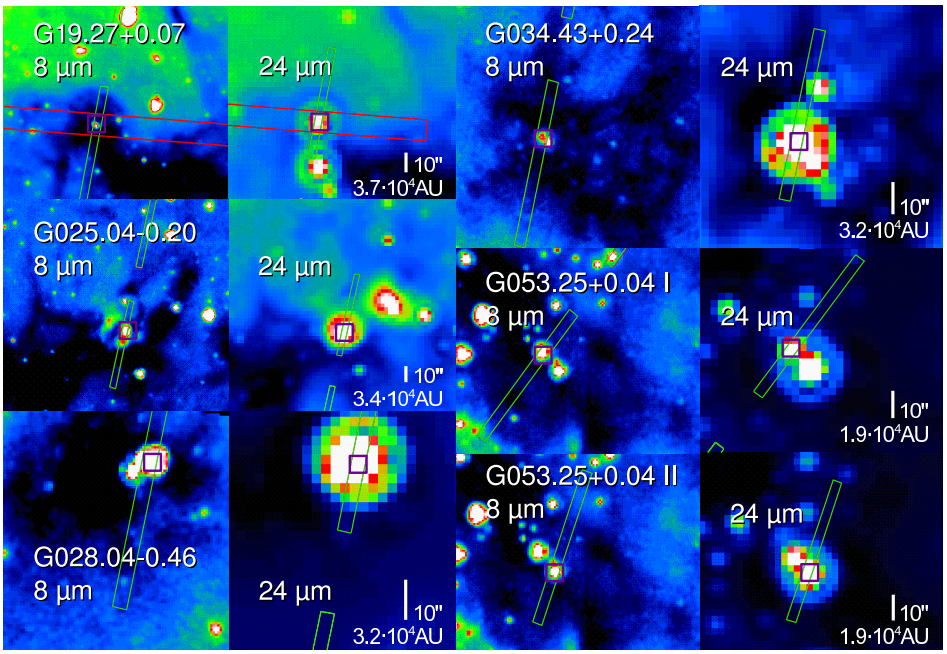

Figure 2.35. – Overlay of the IRS slits for the IRDC sources. Notations are the same as for Figure 2.22.

G019.27+0.07 appears in the IRAC bands as an isolated point source at the north-east extension of an infrared dark cloud filament. The background outside the filament and the shape of the filament is changing depending on the wavelength. This makes the spectral extraction for this source quite difficult. Therefore the source spectrum with a polynomial background fit and the nodded background spectrum is show in Figure 2.17. The $5.8\,\mu\mathrm{m}$ and $8\,\mu\mathrm{m}$ bands show the extinction of the IRDC against the galactic PAH background. The IRAC source is also detected as a point source in MIPS24/70. An extended submillimeter clump is observed at the position of the IRAC/MIPS source as denoted by the contours in Fig 2.36. The clump can also be seen at 1.2 mm, and the core mass was calculated as $113\,\mathrm{M}_\odot$ (Rathborne et al. 2006). H_2O and thermal CH_3OH maser emission was observed with the Green-Bank-Telescope by Chambers et al. (2009). The later maser emission gives an indication to a more evolved evolutionary stage. In the background spectrum of G019.27+0.07 reveals a $\mathcal{A}$ spectrum. This PAH features are not detected towards the source spectrum, hence the UV excitation source can be external. Molecular hydrogen emission is found in the source and background spectra. This is consistent with a slightly extended blob of H_2 observed in the IRAC band at $4.5\,\mu\mathrm{m}$.

G034.43+0.24 is an isolated source found in MIPS and IRAC images. The peak of the submillimeter clump at $850\,\mu\mathrm{m}$ is centered on the $24\,\mu\mathrm{m}$ source position. The extended lobe in the $3.6\,\mu\mathrm{m}$ map of molecular hydrogen lines could be excited by an outflow. The same absorption feature as in ISOSS J18364–0221 West is observed. This supports the hypothesis of a young, deeply-embedded object with outflows. For the remaining targets embedded in infrared dark clouds, no extended hydrogen features were resolved IRAC maps. However, molecular hydrogen emission was detected in G028.04–0.46 and G053.25+0.04 I+II.

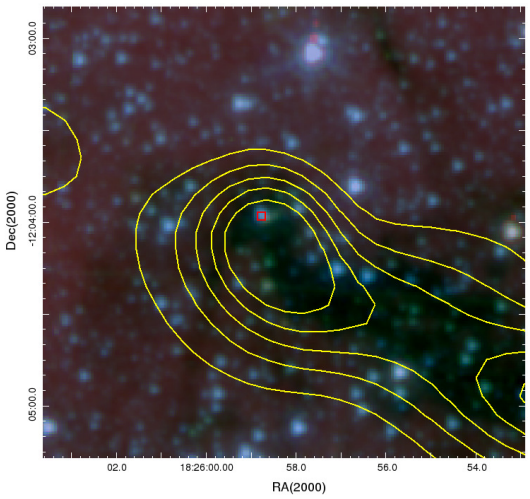

Figure 2.36. – IRAC composite image for G019.27+0.07. The $3.6\,\mu m$ channel is colorized in blue, $4.5\,\mu m$ in green and $8.0\,\mu m$ in red. The peak position of the MIPS points source at $24\,\mu m$ is indicated by the red box points. The IRS slit is centered on the position. The SCUBA observation at $850\,\mu m$ are shown as yellow contours.

2.5.8. Comparison with Orion IRc2

Many of the general features observed in the IRS spectra of my sample are also observed in the spectrum of Orion IRc2 (see Table 2.5). The $9.7\,\mu m$ silicate absorption feature can be found in almost every source. As in IRc2, I find ice features of water, methane and CO_2. NH_4^+ in gas-phase appears in absorption. Several molecular features from IRc2, e.g. SO_2, C_2H_2 and CH_4 (in gas phase), are not present in my sample at the IRS resolution and sensitivity. Most sources show a wide variety of PAH bands. Since the times of the ISO observations of IRc2, there has been remarkable progress in the understanding of PAH composition (Tielens 2008). I constrained the physical properties of the far-UV for several sources from the PAH bands at 6.8, 7.7 and $8.6\,\mu m$. Due to the lower spectral resolution of Spitzer IRS compared to ISO/SWS, features like H_2O in gas phase can not be observed in my sample. Since the spectra of IRS are taken longward of $5.5\,\mu m$ only the 0-0 S(0)-S(7) lines can be observed. The Q and O modes and the higher orders for S remain inaccessible. It is difficult to distinguish between the different excitation mechanisms for molecular hydrogen, as was done for the Orion peaks (Rosenthal et al. 2000), because I am missing these orders at shorter wavelengths. However, the spatial distributions of the S(5) and S(3) lines enable us to discriminate between thermal excitation and shock excitation. For some of the sources in our sample the [Ne II] line is observed in our sample as well, and can be correlated to a PDR or/and J-shock excitation. In contrast to the Orion starforming region I did not find any indications for C-shocks. All spectra in the sample show only a fraction of Orions IRc2 characteristics. Either they show deeply embedded young sources with strong silicate and ice absorption bands, or more evolved sources with indications of PDRs and strong PAH bands below $9\,\mu m$.

2.6. Summary

The Infrared Spectrograph on-board of the Spitzer Space Telescope was used towards a sample of 14 intermediate mass YSO in different evolutionary stages. I present low and high resolution mid-infrared spectra of these sources. The IRS spectra demonstrated how difficult it is to disentangle the complexity of such star-forming regions, because the IRS beam covers multiple physical components. But with the help of previous multi-wavelength studies one can shed light on several physical components and properties. In contrast to previous spectroscopic ISO observations I derived information about the spatial extent of lines using the IRS slit spectroscopy. The spatial distribution of selected PAH and H_2 lines in comparison with previous imaging observation can shed light not only on the YSO but also on their vicinity. The infrared spectroscopy shows two different kinds of sources:

- Young isolated sources, which are still embedded in an envelope of cold dust and ice. These sources tend to still have low to intermediate masses with high accretion rates. Only neutral background PAHs are found for these sources. Several different absorption features as NH_4^+ ($6.75\,\mu\mathrm{m}$), water, methane and CO_2 ice can be found for these sources. Though CO_2 ice can be found for the more evolved sources too. For ISOSS J23053+5953 East the same indications for J-shocks are found as for the more evolve source ISOSS J20153+3453 West (see below).

- The second group of sources is more evolved. I found H_2 pure rotational lines, atomic fine structure lines as [Fe II] , [Si II] and several PAH bands. The presence of [Si II] , [Fe II] and H_2 lines can be explained by J-shocks. For some sources [Ne II] indicates high velocity shocks. The line ratios for [Ne II] and H_2, [Si II] , [Fe II] agree with the predictions for J-shocks. Shock excitation might also explain the spatial distribution of certain H_2 lines for ISOSS J20153+3453 West. There are no indications for C-shocks in our sample. For some sources a class $\mathcal{A}$ PAH spectrum was detected with strong PAH bands below $9\,\mu\mathrm{m}$. All these sources have indications for a PDR. Although the contribution of shock excitations to the H_2 line emission is not known, PDR models (Kaufman et al. 2006) favor higher gas densities ($\geq 10^5\,\mathrm{cm}^{-3}$) and UV field strengths between $10^2 - 10^4\,\mathrm{G}_0$.

3. Photometric extraction on the Herschel High-mass EPoS sample

"... and now for something completely different..."

(John Cleese)

In this chapter the development of a pipeline for the photometric point source extraction for the high-mass part of the Herschel GTO project "**E**arliest **P**hases **o**f **S**tar formation" (EPoS) is described. The derived point source catalogs are used for the EPoS overview paper by Ragan et al. (2012). The extraction technique was also used for the Herschel data in Chapter 4. Moreover, based on the compiled EPoS catalogs I studied the cloud fragmentation of the observed regions and found a typical point source for all regions.

In Section 3.1 an introductions to the sample of massive star-forming regions in the EPoS program is given. In the Section 3.2 I discuss the general limitations set by the obtained data and list the basic consideration for the design of the extraction procedure. In Section 3.3 the extraction process is detailed, including the noise determination, the source masking, background filtering, the photometric procedure itself and the source matching resulting in the final catalogs. The optimal extraction parameters and the overall performance of the pipeline is discussed in Section 3.4.2. In Section 3.5.3 I report the discovery of a common point source separation of $\sim 0.5\,\mathrm{pc}$ for massive star-forming regions in the EPoS sample.

3.1. The EPoS-sample

3.1.1. Scientific goals

For the first time Herschel provides the potential to directly observe the wavelength ($70 - 500\,\mu\mathrm{m}$) range were the cold dust emission from cold ($\sim 10 - 20\,\mathrm{K}$) dust in young star forming regions peaks. The sample of high-mass star-forming regions observed by Herschel is described in the next Section. Herschel can enhance our understanding of the initial condition under which the stars form in this regions. Herschel can shed light on the collapse and fragmentation process in this clouds. In particular with PACS and SPIRE we are able to analyze the temperature and surface density structures in these clouds. Moreover, with the point source catalogs derived in this Chapter we can characterize the dense cores (size $\sim 0.15\,\mathrm{pc}$) where young stellar objects (YSOs) are already present. To assess the cores' physical conditions, we analyze the spectral energy distributions (SEDs) of the cores so that we can study the distributions of luminosities, dust temperatures, and masses.

3.1.2. Target Selection

"**E**arliest **P**hases **o**f **S**tar formation" (EPoS) is a Herschel Guaranteed Time Key Program ($\sim 85\,\mathrm{h}$) consisting of 14 low-mass molecular cloud cores and 45 massive star-forming regions. The high-

mass portion of this program has been compiled from several surveys.

The first part are the "classical" IRDCs, which have been discovered by ISOCAM (Perault et al. 1996), and MSX (Egan et al. 1998) as isolated regions with dark filaments against the bright galactic mid-infrared background. Fifteen nearby IRDCs (< 5 kpc) have been selected from several follow-up surveys (e.g. Carey et al. 1998, 2000; Teyssier et al. 2002; Pillai et al. 2006; Rathborne et al. 2006; Ragan et al. 2006; Vasyunina et al. 2009).

It has been observed that the formation of HMPOs and H II regions can trigger further star formation activity (Deharveng et al. 2010). Therefore, a second class of IRDCs, located in the near vicinity of HMPOs, had been selected. A sample of IRDCs close to HMPOs was compiled from Beuther et al. (2002a,b,c,d) and Sridharan et al. (2002). The cross-correlation of MSX $8.3\,\mu\mathrm{m}$ data with 1.2 mm bolometer observation reveals that for most of these regions gas clumps of more then $100\,\mathrm{M}_{\odot}$ associated to IRDCs (Sridharan et al. 2005). From these IRDCs 14 regions were selected for the EPoS program.

A sample of massive pre-stellar core candidates were identified in the $170\,\mu\mathrm{m}$ ISOPHOT Serendipity Survey (ISOSS). Follow-up observations confirm the cold and dense gas. For the EPoS-program 15 massive ($M > 100\,\mathrm{M}_{\odot}$), compact (elongation $< 3'$), and cold ($T_{\mathrm{dust}} < 18\,\mathrm{K}$) targets where selected. The ISOSS sources are located further outside of the galactic plane therefore the background emission is lower compared to the IRDC regions. Some of the ISOSS regions and their embedded YSOs have already been discussed in Chapter 2. Table 3.1 lists the Herschel observations for each region.

Table 3.1. – EPoS - Observational Log

Source	OD	Obs.ID	Mask	$t_{\rm os}$ [s]	scan leg length [']	PSF rot. [°]
HMSC07029	148	1342185543-46[a]	no mask	315/189	7	95.84
IRDC004.36	324	1342193518-21	ATLAS	378/189	7	90.88
IRDC009.86	484	1342204296-99	ATLAS	378/189	7	264.18
IRDC010.70	299	1342191801-04	ATLAS	990/495	11	89.81
IRDC011.11	148	1342185555-58[a]	ATLAS	840,1440/840,1440[b]	10,20[b]	267.96
IRDC013.90	299	1342191805-08	ATLAS	990/495	11	89.88
IRDC015.05	529	1342207057-60	ATLAS	378/189	7	264.18
IRDC019.30	686	1342217767-70	ATLAS	378/189	7	86.57
IRDC028.34	677	1342216603-06	ATLAS	576/288	8	88.67
IRDC048.66	324	1342193492-95	ATLAS	378/189	7	86.79
IRDC079.31	207	1342187795-98	SCUBA	576/288	8	229.57
IRDC310.39	233	1342188857-60	ATLAS	378/189	7	87.08
IRDC316.72	464	1342203273-76	ATLAS	576/288	8	292.19
IRDC320.27	247	1342189390-93	ATLAS	378/189	7	85.72
IRDC321.73	252	1342189588-91	no mask	576/288	8	87.62
IRDC18102	685	1342217534-37	ATLAS	378/189	7	88.02
IRDC18151	299	1342191813-16	no mask	378/189	7	91.24
IRDC18182	299	1342191809-12	ATLAS	576/288	8	90.37
IRDC18223	148	1342185559-62[a]	ATLAS	432,810/288,486[b]	6,18[b]	265.568
IRDC18306	705	1342219056-59	ATLAS	378/189	7	81.16
IRDC18308	705	1342219052-55	ATLAS	378/189	7	81.20
IRDC18310	705	1342219060-63	ATLAS	378/189	7	81.08
IRDC18337	705	1342219064-67	ATLAS	378/189	7	80.78
IRDC18385	705	1342219070-73	ATLAS	378/189	7	79.86
IRDC18437	540	1342209033-36	ATLAS	378/189	7	253.38
IRDC18454	299	1342191819-22	ATLAS	648/324	9	93.96
IRDC18530	540	1342209029-32	ATLAS	378/189	7	251.62
IRDC19175	325	1342193546-49	ATLAS	378/189	7	85.67
IRDC20081	205	1342187767-70	SCUBA	378/189	7	229.77
ISOSSJ04225	285	1342191010-13	SCUBA	378/189	7	263.44
ISOSSJ06114	484	1342204232-35	SCUBA	378/189	7	89.34
ISOSSJ06527	485	1342204309-12	no mask	378/189	7	85.41
ISOSSJ18364	148	1342185563-66[a]	SCUBA	315/189	7	263.68
ISOSSJ19357	324	1342193496-99	SCUBA	378/189	7	88.93
ISOSSJ19486	205	1342187759-62	SCUBA	378/189	7	226.57
ISOSSJ19557	205	1342187755-58	SCUBA	378/189	7	227.12
ISOSSJ20093	205	1342187763-66	SCUBA	378/189	7	229.65
ISOSSJ20153	205	1342187751-54	SCUBA	378/189	7	229.08
ISOSSJ20298	205	1342187747-50	SCUBA	378/189	7	231.45
ISOSSJ21311	205	1342187771-74	SCUBA	378/189	7	241.71
ISOSSJ22164	184	1342187003-06[a]	SCUBA	990/495	11	272.49
ISOSSJ22478	207	1342187809-12	SCUBA	378/189	7	257.48
ISOSSJ23053	207	1342187813-16	SCUBA	378/189	7	259.70
ISOSSJ23129	212	1342188063-66	SCUBA	378/189	7	256.58
ISOSSJ23287	215	1342188102-05	SCUBA	378/189	7	257.29

The first column list the observed regions. The upper part of the table represents the "classical" IRDCs, the middle part consists of IRDCs in the near vicinity of HMPOs, and the bottom part is compiled from the ISOSS survey (see text). The second column list the Operational Day (OD) of Herschel when the observation was performed. In the third column the ID tag for each observation is given. The fourth column indicates which sub-millimeter instrument was used to create the source masks. The on-source time is listed in the fifth column. The last column presents the angle by which the nominal Vesta psf needs to be rotated to match the scan direction of the science frame before used in the PSF photometry.

[a] observed as part of the Science Demonstration phase (SDP)

[b] for these observations the scan leg lengths were different for the two scan directions. The first two scan times are given for the blue/green scan mode and the two different scan directions, the last two scan times correspond to the green/red scan mode. The scan leg setup was done manually without optimization for homogeneous coverage.

3.2. Demands and Limitations on the photometric extraction

For the observed star-forming regions and in particular for the IRDCs one faces very heterogeneous background emission over a wide spatial scale, since the PACS wavelengths (70, 100, and $160\,\mu\mathrm{m}$) cover the transition between absorption and emission of cold ($\sim 10 - 20\,\mathrm{K}$) dust. Furthermore, point source are difficult to disentangle from compact features in the filamentary structures in these star-forming regions. The proper identification of the point sources is the core issue in characterizing them. The most powerful pattern recognition tool is doubtlessly the human eye. Unfortunately, the source detection based on visual inspections is strongly biased towards every individual. And to survey carefully 135 exposures is barley a feasible task. Therefore, and to provide robust statistics which can be reproduced for the whole EPoS-sample, an automated routine for the source detection and flux extraction is needed. In the search for an suitable flux extraction algorithm one has to either chose aperture photometry or PSF photometry. We select a PSF-photometry based approach because it handles the non-uniform background better than an aperture-based method. We only use PACS wavelengths because at 6-11$''$ resolution, we resolve "core" scales at typical IRDC distances, whereas SPIRE probes larger scales at wavelengths where the colder filament overwhelms emission profile of the IRDC. We therefore base our identification and flux extraction on the `starfinder` algorithm with several customizations that will be described in the following sections.

3.3. The photometric extraction

3.3.1. The ingredients

All PACS data were observed with a medium scan speed of $20''/\mathrm{s}$. The observational ID and the operational day, as well as the scan leg length and the on-source scan times are listed in Table 3.1. All observations were taken with two orthogonal scan directions. If not mentioned differently in Table 3.1, the number scan legs and their separations were optimized for homogeneous coverage.

The reduction of the Herschel data products are divided into several levels. The level-0 data products contain only the raw telemetry as measured by the telescope. In the level-1 reduction process basic calibrations are performed and technical units are converted into physical units. The available first level PACS data products from the local EPoS-data-pool were reduced with the HIPE-pipeline version 6.0. The second level data products were processed using the SCANAMORPHOS package (Roussel 2012). In doing so the detector timelines are matched with the orientation of the telescope on the sky and two dimensional maps are created. The high-frequency noise is computed, linear baselines are subtracted to remove potential brightness drifts and brightness discontinuities are masked. Even though the native bolometer pixel size is $3\farcs2$ for the $70\,\mu\mathrm{m}$ and $100\,\mu\mathrm{m}$ band, the pixel scale in the final data products were refined to a smaller pixel scale. By defining a narrow scan leg separation the overlap of the single scans allows us to use a finer pixel grid to detect faint point sources, which can not be detected on a $3\farcs2$/pixel grid. The data set was reduced with a pixel-size of $1''$ for each PACS band. The native bolometer pixel size for the $160\,\mu\mathrm{m}$ band is $6\farcs4$, but the $1''$ per pixel resolution was also chosen here to keep the resulting maps consistent with the other bands.

For the photometric extraction an empirical PSF of the Vesta asteroid[1] is used. It was provided by the PACS instrumentation team. To insure the best possible photometric results the second level reduction for the Vesta-PSF images is also done by SCANAMORPHOS. Because the science frame

[1] It was observed as part of the calibration measurements at operational day 160.

and PSF frame have different orientations of the detector with respect to the scan direction of the telescope, the PSF was rotate for each region (see Table 3.1).

Parts of the `StarFinder`[2] package (Diolaiti et al. 2000) were used to create a automatic pipeline scripts for the PACS PSF extraction. `StarFinder` is a GUI-based algorithm written in the `IDL` script language. Minor changes were applied to the `StarFinder` code itself (e.g., data type conversation etc.) to insure the compatibility with the PACS data products. `StarFinder` was initially designed to perform PSF photometry on Adaptive Optics images of crowed stellar fields. It can either construct an empirical PSF from the given exposure or use every provided empirical PSF. `StarFinder` extracts flux and position of the sources in an image by partitioning the whole exposure into sub-images on a regular grid and fitting the data to the model below

$$h(x,y) = s_0(x,y) + \sum_{n=1}^{N_s} f_n p(x - x_n, y - y_n) + b(x,y) \tag{3.1}$$

where $s_0(x,y)$ is the contribution of sources outside the sub-image, N_s is the number of stars, f_n is the flux and x_n, y_n the position of the fitted fluxes of the n-th source, $p(x,y)$ is the PSF, and b(x,y) the background contribution. The fitting is done with a least square error minimization. The estimated noise (see Section 3.3.2) is used to weight the data in the parameter optimization process. `StarFinder` utilize a Newton-Gauss algorithm. The principle algorithm of `StarFinder` can fail to detect fainter companions with a separation of less then 2 FWHM of the primary source. In multiple iterations `StarFinder` can try to fit additional source to the residuals. This procedure, called de-blending, can separate faint companions down to 0.5 FWHM. An important parameter is the spatial concurrence of the detected source with the PSF. A method to measure it, originating from pattern recognition, is correlation coefficient (Gonzalez & Woods 1992):

$$c(a,b) = \frac{\sum_{x,y} \left[i\left(x,y\right) - \bar{i} \right] \left[p\left(x-a, y-b\right) - \bar{p} \right]}{\sqrt{\sum_{x,y} \left[i\left(x,y\right) - \bar{i} \right]^2} \sqrt{\sum_{x,y} \left[p\left(x-a, y-b\right) - \bar{p} \right]^2}} \tag{3.2}$$

where i is the flux array of the detected source and p the flux array containing PSF profile, while $\bar{i}$ and $\bar{p}$ are the corresponding mean values of the profiles. The correlation coefficient is depending on the offsets a and b. By maximizing the correlation coefficient a measure of similarity between the detected source and the PSF is derived. For an axially symmetrical shaped source the resulting offsets for the maximal correlation coefficient would be the centroid position of the source. Hereafter, the term "correlation coefficient" is used for the maximum of the correlation coefficient for a source. For the source fitting and the de-blending `StarFinder` requires a lower limit on this correlation coefficient, called "correlation threshold" hereafter. The selection of this threshold is crucial for the number of detected sources. In general, a lower threshold results in more false detections, while a high threshold might miss faint sources or sources with a complicated local background.

For the background estimation each sub-image is interpolated using the `sky/mmm` routine from the `daophot` package. The resulting background estimate is fitted to the initial image with a slanted plane to remove gradients.

The developed photometric extraction involves several steps. The principle mode of operation is illustrated in Figure 3.1. The extraction finally performed on the sample is highlighted by the

[2] The version 1.6 was used. The IDL source code can be downloaded from `http://www.bo.astro.it/StarFinder/`.

green connectors in the flowchart. This final extraction is called “nominal extraction” hereafter. The extraction process breaks down in: the noise determination (Section 3.3.2); masking out parts not belonging to the star-forming region, filtering and determining point source positions (Section 3.3.3), performing the final PSF-photometry and matching sources in the three bands (Section 3.3.4).

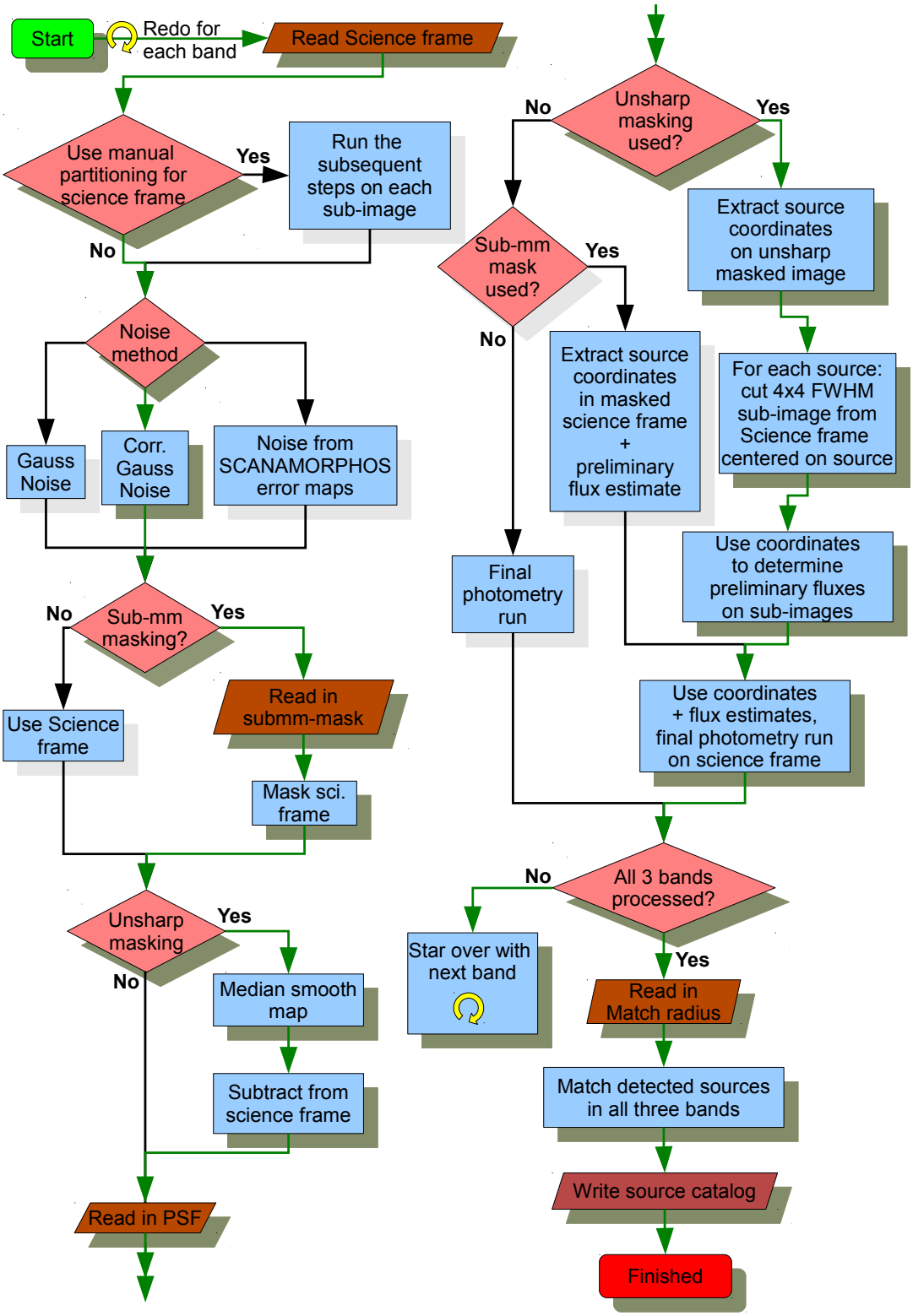

Figure 3.1. – The flowchart for the photometric extraction. The green connectors represent the nominal extraction chosen for the EPoS-sample.

3.3.2. Noise determination

The determined noise level is predominately used to set the threshold for the source detection. Alleged source are considered as detection, if the measured fluxes are above $5\,\sigma$ and show spatial concurrence in all three PACS-bands (see Section 3.3.4).
To estimate noise levels in the maps three different approaches were tested:

- First pure a Gaussian distributed noise was estimated. `StarFinder` histogram fitting algorithm was used to estimate the mean background noise.

- The computed Gaussian distributed noise is underestimating the real noise level since the PACS detector suffers from a non-negligible pixel-to-pixel correlation. Furthermore artifacts and lower coverage increase the noise towards the edges of the PACS maps. To account just for the noise in the inner parts of the image map the median smoothed weight-maps from the SCANAMOPRHOS baseline subtraction procedure were used to create exposure masks. Only within these masks the noise was estimated with a cutoff value of 50% of the weight maximum. Based on calibration observations of α-Ceti the correlated noise level depending on the pixel size can be calculated, using (Hendrik Linz 2012, private communication):

$$\text{ratio} = \begin{cases} c_1(sz_{px}/3.2'')^{c_2}, & \text{for PACS 70 and } 100\,\mu\text{m} \\ c_1(sz_{px}/6.4'')^{c_2}, & \text{for PACS } 160\,\mu\text{m} \end{cases} \tag{3.3}$$

  where sz_{px} is the pixel scale chosen for the maps, divided by the native pixel size one the detector. The coefficients c_1 and c_2 are given in Figure 3.2. To correct for the pixel-to-pixel correlated noise the Gaussian distributed noise estimate has to be divided by $ratio$.

- In a third approach the SCANAMOPRHOS errors maps were used as a noise estimator. The error map computed by Scanamorphos contains the statistical estimate of the error on the mean in each pixel, taking into account the weighting of the data by $1/\sigma^2$ (Helene Roussel 2011, private communication).

The two later methods were tested for several regions with different extraction parameters (e.g. correlation thresholds, different background sizes, different median filters, etc.). The third method suppresses artificial detections more efficiently, but reduces the number of true detections in comparison to a Gaussian noise approach, especially when using the unsharp masking. The Gaussian distributed noise estimate with pixel-to-pixel correction was chosen for the nominal extraction, because it results in the best detection performance when used with unsharp masking.

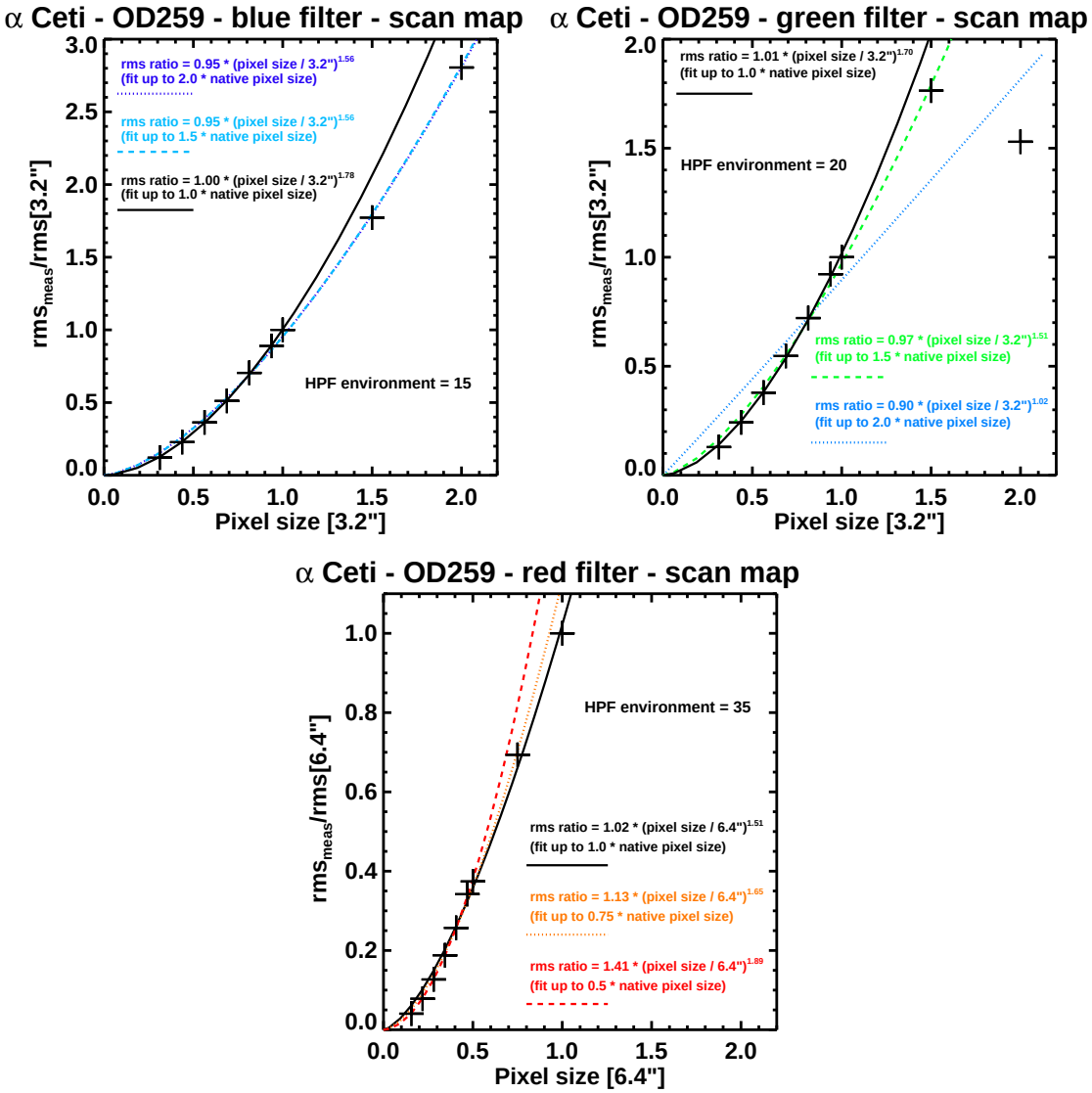

Figure 3.2. – The correlated noise ratios calibrated for all PACS bands by observations of the red giant α Ceti (by courtesy of Hendrik Linz).

3.3.3. Masking, filtering, and source coordinate determination

The number of artifacts can be drastically increased in map by diffuse heterogeneous structures as entailed by, e.g., nearby giant molecular clouds (GMCs), supernova remnants etc. To reduce the number of false detections a further step is introduced, a masking with sub-millimeter maps. For most of the regions in the EPoS-sample either ATLASGal (Schuller et al. 2009) or SCUBA legacy (Di Francesco et al. 2008) data are available (see Table 3.1).

A technique to create these sub-millimeter masks was developed by Jochen Tackenberg for ATLASGal maps. But it can also be applied to SCUBA observations. Due to the limited sensitivity of the APEX observations a certain fraction of cloud dust is not detected. To account for missed emission the sub-millimeter masks are "blured" by several smoothing steps. The whole procedure is described below.

1. As a first step the SPIRE map at $500\,\mu\mathrm{m}$ for the region was utilized. From the SPIRE weight map only pixel with a value higher then $25\,\sigma$ were selected, all other pixels were masked as zero. The resulting maps are smoothed using a smoothing radius which prevents holes in the resulting exposure-maps.

2. The corresponding sub-millimeter map was projected on the WCS from the SPIRE exposure map and interpolated on the SPIRE $500\,\mu\mathrm{m}$ pixel scale. All pixels in the sub-millimeter maps outside the SPIRE exposure mask are removed.

3. The smoothing of sub-millimeter map is done by convolving it with a Gaussian kernel with a $189\farcs6$ FWHM.

4. The smoothed and masked sub-millimeter map is passed to the `clumpfind` algorithm. A lower threshold of $0.8 \cdot 10^{20}\,\mathrm{cm}^{-2}$ (derived from flux 3 times the RMS noise) was used. Pixels outside the areas detected by `clumpfind` were excluded. The resulting map is used as the final sub-millimeter map.

5. Finally the sub-millimeter map is interpolated on the PACS pixel scale.

`StarFinder` with the background estimator based on `mmm/daophot` has proven ineffective to distinguish between faint sources, compact background emission and failed to detect sources in narrow filaments. To improve the source detection and determination source coordinates, my own filtering was applied. An unsharp masking filter is used, i.e. a median smoothed map is subtracted from the original science image. This results in the suppression of the large scale background contribution and a contrast enhancement for small scale features. The unsharp masking dose not significantly alter the PSF of the point sources and so emphasize point sources, see Figure 3.3 and 3.4, bottom panels. A smoothing radius of $9''$ was used for the blue and green band. As a side-effect of the $1''$ pixel size in the red maps the weight map imprints are emphasized, appearing as a orthogonal grid of stripes in the exposures (see the last panel in Figure 3.3 and 3.4). By testing different smoothing radii, a value of $20''$ was found as good compromise to reduce this stripping without overshooting the smoothing and degenerating the point source PSFs. A first PSF-photometry run is used to determine the source position. These coordinates are passed to the `StarFinder/fitstars` to determine preliminary fluxes, to be used in the final photometry run. If unsharp masking was used, sub-frames of 4×4 FWHM size were created from the science frames centered on the detected source to produce these flux estimates. For all photometric runs (positioning, flux estimate and final run) a $5\,\sigma$-clipping was applied.

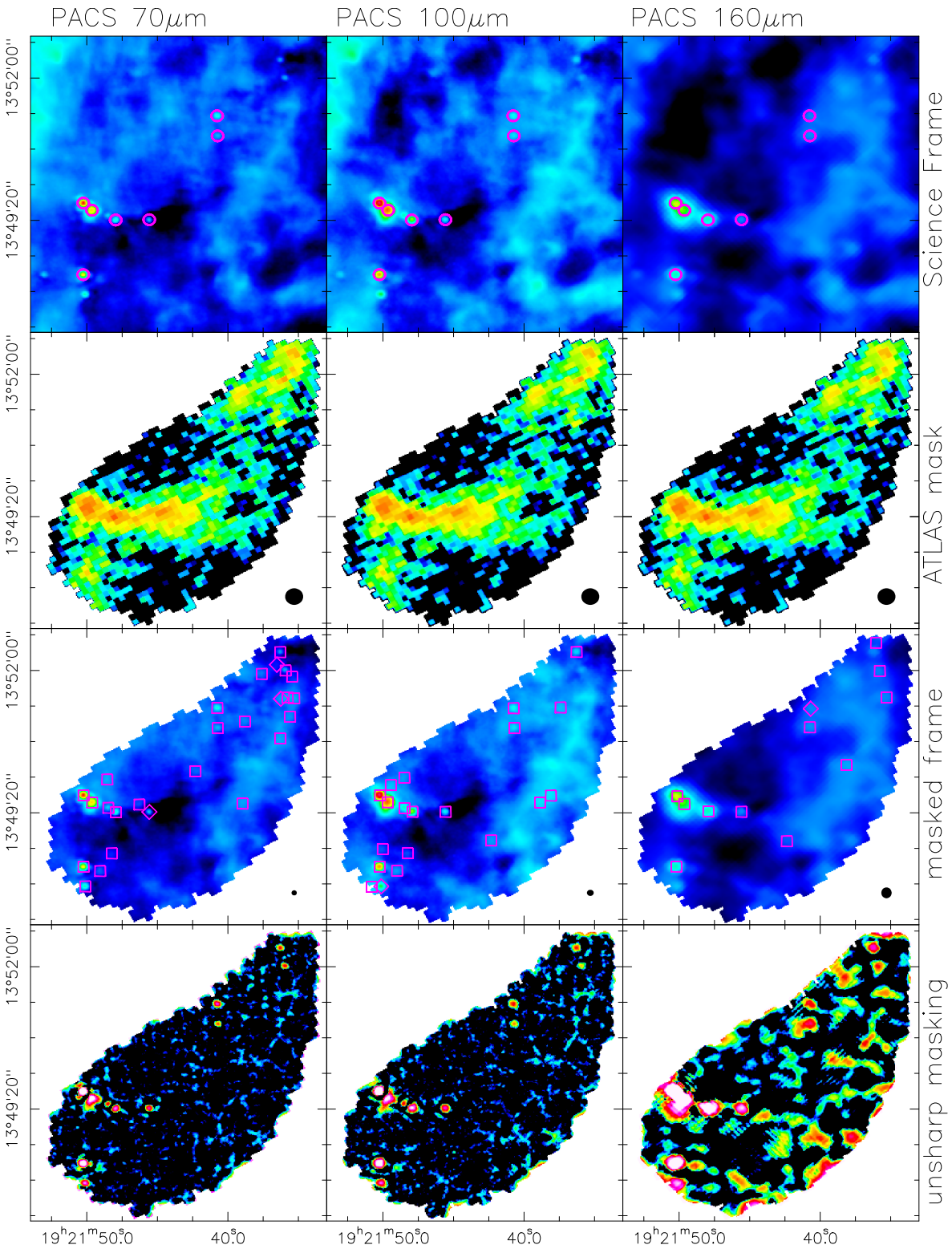

Figure 3.3. – The different extraction steps are shown for G48. The panels from the left to the right represents the blue (70 μm), green (100 μm), and red (160 μm) PACS channel. In top panels the original SCANMORPHOS images are shown. The sub-millimeter mask are plotted in the panels in the second row. The mask is produced from ATLASGAL observations.

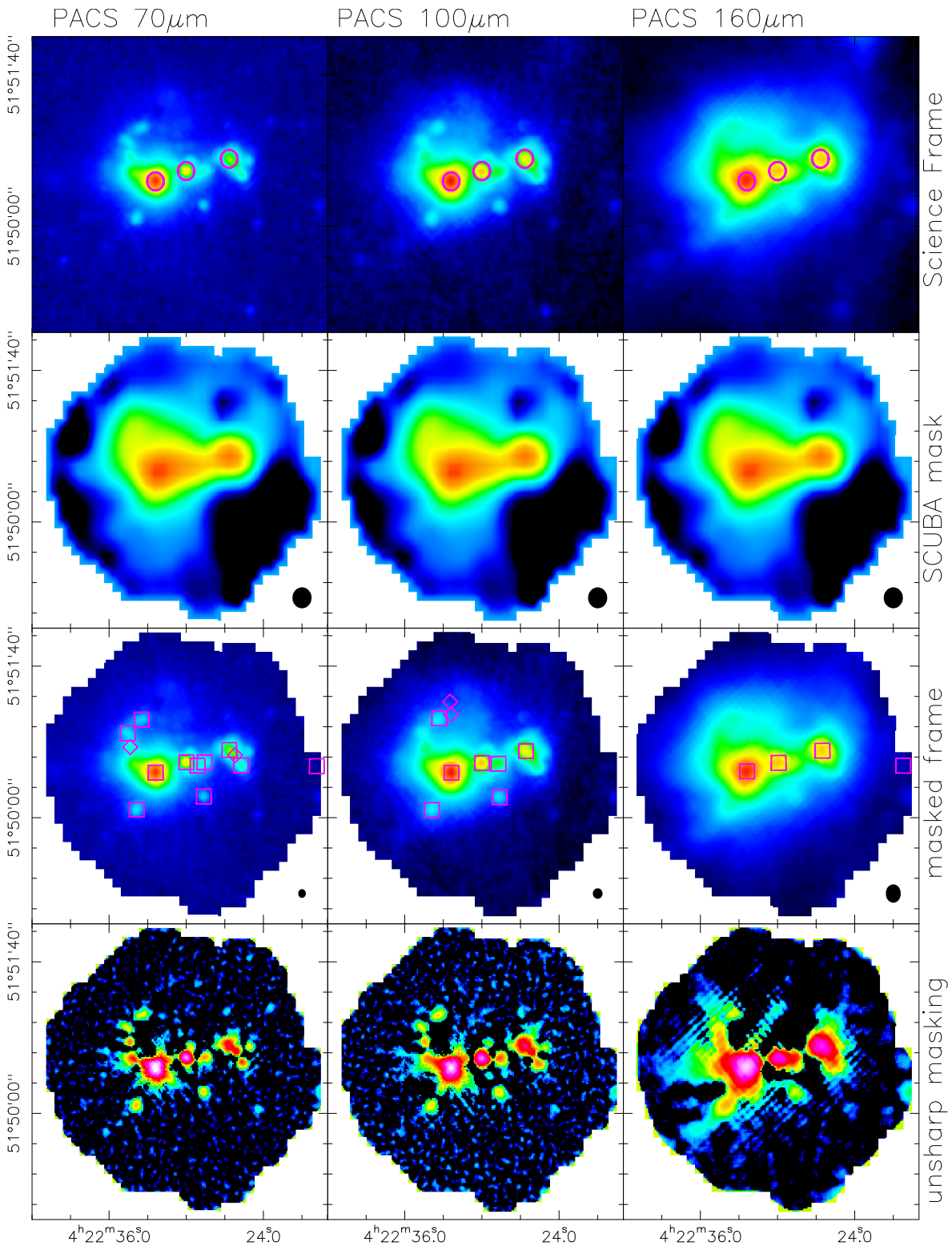

Figure 3.4. – The different extraction steps are shown for ISOSS J04225+5150 East, as in Figure 3.3. The mask is produced from SCUBA observations.

3.3.4. Photometry and source matching

In the final photometric run the pre-determined star-positions and flux estimates are passed to the `StarFinder` routine. The detection of further sources is suppressed in this final run, only subpixel-shifts on the provided source are performed. With the given flux estimates the psf-fitting (see Equation 3.1) is repeated to optimize the resulting fluxes. At least 10 iterations are enforced. A second exit condition is a photometric convergence of about 0.1% between two iterations. After the photometry is finished in every band the resulting sources are matched to create a finale source catalog. To be finally treated as a detection, a source has to be detected at, at least, 5σ in each band and it is required to be spatial concurrent within $6''$. A 6 pixel radius was chosen to be consistent with the $11\farcs2$ FWHM of the $170\,\mu\mathrm{m}$ band. The final catalogs contain the matched sources, but also each detection in every single band.

3.4. Benchmarking

3.4.1. Determine the optimal extraction parameters

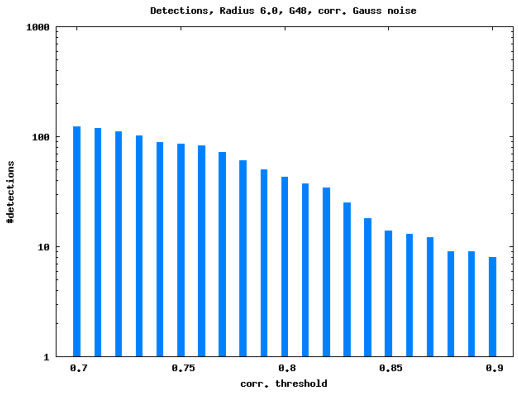

Figure 3.5. – Number of detected sources matched in all three bands are given, depending on the lower threshold for the correlation coefficient. The photometric extraction was done with Gaussian distributed noise corrected for pixel-to-pixel correlation (see Section 3.3.2 page 59).

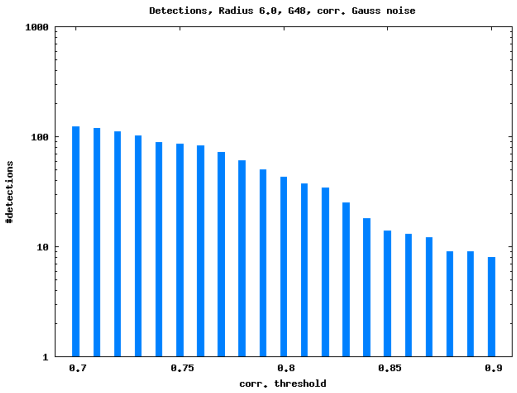

Figure 3.6. – The same plot as in Figure 3.5 utilizing the nominal extraction with unsharp masking and corrected noise estimates.

For an optimal source detection one has to determine the best values for certain (technical) parameters. The first parameter is the size of the background aperture. If the source detection is done on the science frame only, without any masking, the number of detected source and the number of artifacts is strongly depending on background area. The source detection done on the unsharp masked images is much more robust against changes of the background size. Too large values result in mingling the local background with nearby sources. The optimal background size for the source detection (in the unsharp mask frame) on the EPoS sample is estimated with $5\times$ the PSF-FWHM in the corresponding band. For the final photometry run on the science frame a background size of just $2\times$ the PSF-FWHM is used, since the local background is computed only in the absorption filaments for embedded sources.

The second and most delicate parameter is the correlation threshold, the lower limit on spatial concurrence of the source PSF with model PSF (see Equation 3.2 and the following explanation on page 56). This represents the general trend in the sample: without the unsharp masking the artifacts got suppressed with higher correlation thresholds, while sources on compact emission features got suppressed at a similar rate, resulting in a smooth distribution in the histogram. By the unsharp masking the most of the compact emission features got removed, hence the number of detections decreases drastically. While the artifacts are normal smoothly distributed in the threshold histogram without the unsharp masking, the “real” point-sources group for certain coefficients. Finally 0.79 is chosen for the correlation threshold because numerous regions in the sample share steps or plateaus in the threshold histogram for this value. This value represents also an optimal compromise between the number of real detections, extraction artifacts and missed sources.

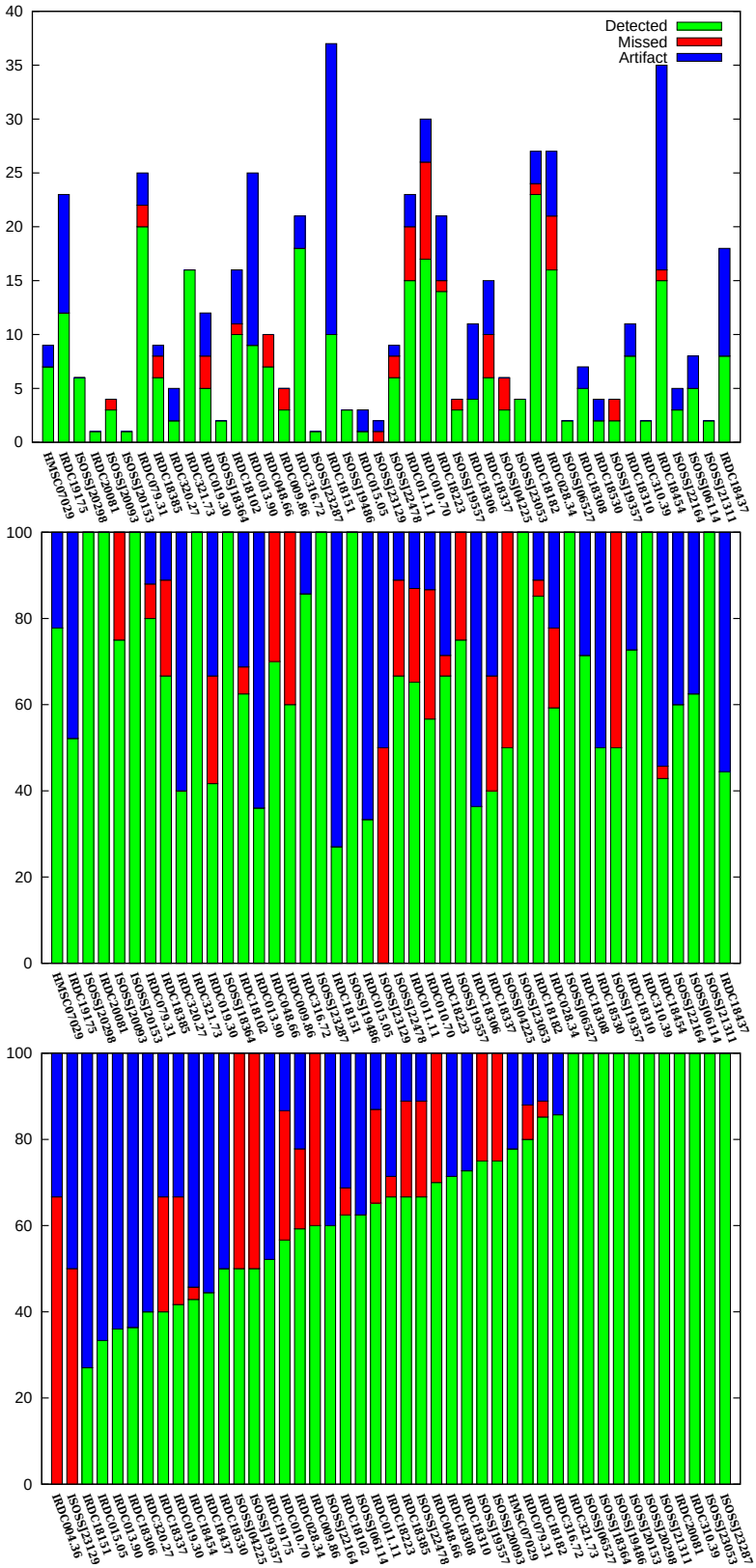

Figure 3.7. – The detection performance of the nominal extraction is shown. The *top panel* shows total numbers, the regions are sorted by kinematic distance. The *middle panel* presents the same results but in relative numbers (%). The *bottom panel* is sorted by completeness, also in relative numbers (%). In the last row of Table A.1 the results of the nominal point source extraction with a correlation threshold of 0.79 are classified. Detections, which are positively identified as real point source, are plotted in green, artifacts in blue and missed sources in red.

3.4.2. Detection Performance

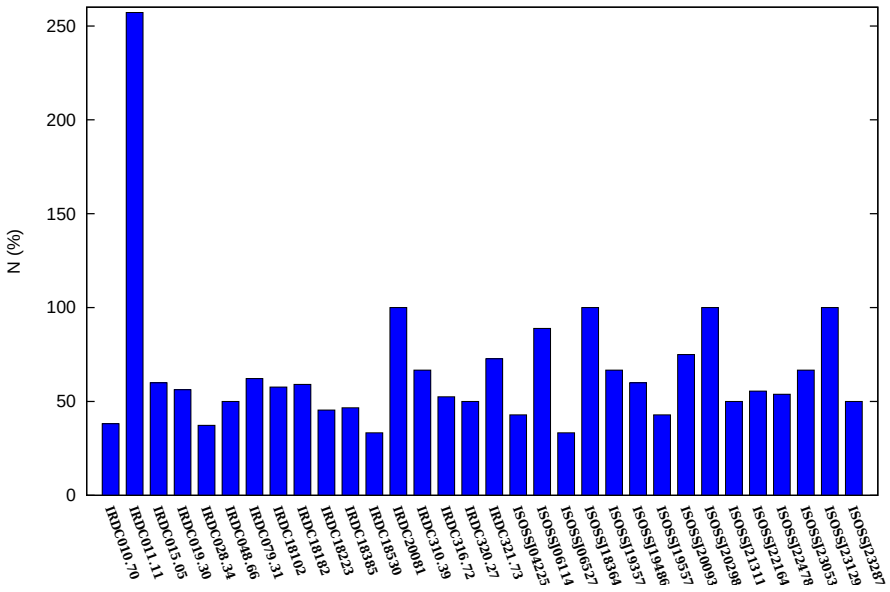

Figure 3.8. – The amount of additional source detected by only utilizing the $70\,\mu\mathrm{m}$ and $160\,\mu\mathrm{m}$ PACS bands. Regions where the majority of the additionally detected source are obvious artifacts are omitted.

To evaluate the detection performance of the nominal extraction the results are subjected to a visual inspection. The detected sources in a region are classified as either real point-sources or artifacts; furthermore the number of missed point-sources is counted. As mentioned early this classification by the human eye is undergoing a significant personal bias, but it is so far the best way for a qualitative assessment of the pipeline. The results are tabulated in the last row of Table A.1 and visualized in Figure 3.7. For the whole high-mass EPoS sample the nominal extraction returns 455 detections, 303 are identified as real point sources but 152 detections must be classified as artifacts. The visual inspection show 51 sources missed in the nominal extraction. The detection performance for the nominal extraction in the high-mass EPoS-sample, i.e., the ratio of detected real point sources to all detections and the missed sources, is $(66 \pm 5)\%$. In 24.4% of the regions all point sources are positively identified without extraction artifacts or missing point sources. For two regions (4.4% of the sample) the nominal extraction was not able to identify any real point source. Figure 3.7 (middle panel) shows the relative detection performance sorted by the distance of each region in ascending order. It appears that the detection performance is not correlated to the distance of a region, hence the algorithm performance does not worsen with distance.

By limiting the sample to detections in all PACS band only, numerous sources only present in two bands are missed. The lower native resolution of the red PACS detector can suppress the detection of faint point sources with compact background emission features at $160\,\mu\mathrm{m}$. Moreover, the line contamination can hamper the point source detection, in particular compact background emission of the strong ISM coolants [O III] at $88\,\mu\mathrm{m}$ and [C II] at $158\,\mu\mathrm{m}$ might blur the source PSF. Figure 3.8 presents the amount of additional source if only the source detection in the blue and green band is required. For several regions the number of artifacts increase drastically, these regions are omitted in Figure 3.8. Especially the IRDCs with neighboring HMPOs show high very non-uniform background variations and high brightness levels.

3.5. Fragmentation in the EPoS sample: Point source separations

Apart from the classical spherical collapse several other scenarios have been discussed. Because of the filamentary structure found in star-forming regions the idea of a isothermal cylindrical collapse (Chandrasekhar & Fermi 1953) was revived. The theory predicts a typical scale of the spatial separation of cores within a star-forming region. Recent studies of IRDCs (e.g., Jackson et al. 2010; Beuther et al. 2011; Miettinen 2012) compared observational results to this predictions and found typical separations between $0.75 - 0.9$ pc, while the separation for G48.66–0.22 is significantly smaller (see to Section 4.4). The point-source detections presented in this Chapter provide a sample large enough perform a statistical analysis of the point-source separations.

To shed light on the nature and origin of the point-source separations, I will discuss the following questions in this Section:
What is the typical point-source separation in the different regions in the EPoS sample? Is the separation connected to the total mass-reservoir? If such correlations exist are they only valid for cylindric/filamentary configurations or more general?

3.5.1. Minimal Spanning Trees

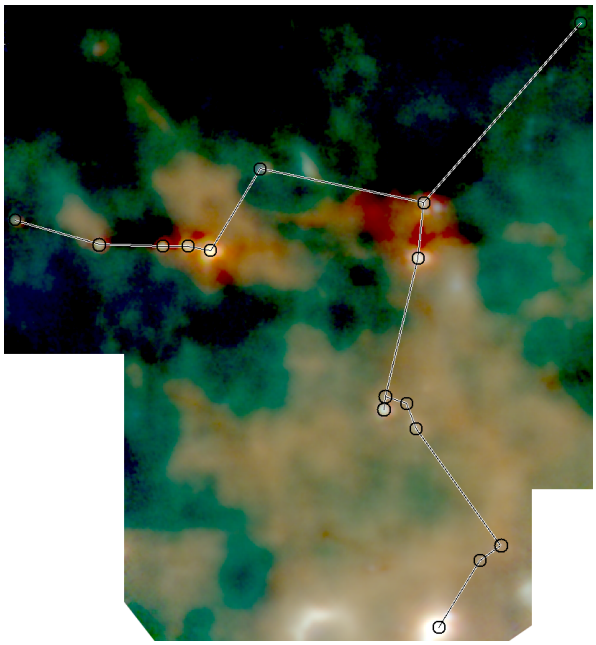

Figure 3.9. – A minimum spanning tree connecting the detected point sources in IRDC321.73.

For a set of N points the number of possible connection is $N(N-1)/2$. To address this problem let us treat the set of point source positions as a weighted undirected graph. Each point source represents a vertex and each connection between them an edge. The weights of the edges are given by the distances between the point sources. To assess the separation of the point sources only the distances to the nearby neighbors are of relevance. Therefore a set of edges with minimum distances has to be found. Allowing cycles in this set would give a higher weight to point sources which are part of the cycle, hence only $(N-1)$ edges and no cycles are allowed (a tree). Finally, one need to find a set of

edges, where the sum of all weights (distances) become minimal. This can be done by selecting the edges with a minimum spanning tree algorithm (MST[3]). To implement the MST the Prim algorithm was utilized (Prim 1957). It is growing the MST from a single vertex, choosing minimal weighted edges and avoiding cycles until all vertexes are connected. From the point source positions in the catalogs (derived in Section 3.3) the angular separation between each source in a calculated. From this values the adjacency matrix as the input to the MST algorithm was compiled.

MST were already successfully utilized to investigate the large scale clustering properties of YSO in certain Herschel/HiGAL fields (Billot et al. 2011). Figure 3.9 shows the MST connecting the detected point sources in IRDC321.73. Table 3.2 presents the average and median MST edge length in the samples. Thereafter I refer to the average edge length $\overline{m}$ as the point source separation.

3.5.2. Observational biases

In Figure 3.12 the total cloud mass for each region, derived from submillimeter maps, is plotted against the point source separation. The plot reveals a trend of larger separations towards higher cloud masses for the IRDCs. Ragan et al. (2012) showed that the IRDC cloud masses increase with distance. Therefore it is not surprising to find a higher point source separation for more distant IRDCs in Figure 3.14. This plot shows that most point source separations are several times higher than the limit set by resolution, in other words resolution does not bias the sample. However the kinematic distances of IRDCs in the EPoS sample are linked to the galactocentric distances (see Figure 3.13). Therefore it is not clear from the outset, that the mass-separation dependency is only a selection effect by kinetic distance, since for example the ISRF could have a influence on the fragmentation. However, separation and distance seem not to be correlated for IRDCs between $1.9 - 4.0$ kpc (indicated by the dotted lines in Figure 3.14). Just plotting the IRDCs in this limited range of distances results in a separation-mass scatter plot as in Figure 3.15. No correlation between the separation and the IRDC masses are found, hence the trend seen in Figure 3.12 is presumably just a selection effect induced by the trend of higher masses for more distant IRDCs and not physical effect based on the galactocentric distance. The distribution of separation through the sample is independent from distance (see next section and Figure 3.11).

Another bias is that one must assume the projected separations are the real separation. We have no line of sight information to correct for the orientation of each region.

3.5.3. Typical separations

In the histogram in Figure 3.10 the distribution of separations peaks at ~ 0.5 pc and 45% of the regions exhibit an average point-source separation between $0.2 - 0.8$ pc. Performing a visible inspection on the sample I divided the EPoS sample into two categories: filamentary and non-filamentous. Both histograms Figure 3.10b and 3.10c show a similar peak and distribution for the point source separation. The same is true for the distance independent histograms: Figure 3.11 show the histograms normalized by the distance. Therefore it can be concluded that the point source separation is independent of mass, morphology and distance.

I compared the typical separations to the average of the thermal Jeans lengths, which can be written as:

$$\lambda_J = \frac{c_s}{G\Sigma} \tag{3.4}$$

[3]When the weights in the MST represent spatial distances the algorithm is sometimes refereed to as an "Euclidean minimum spanning tree" (EMST).

and where c_s is the thermal sound speed[4], and Σ the surface densities derived from the ATLASGAL line-of-sight column densities towards the point sources. The computed thermal Jeans lengths are lower by an order of magnitude compared to the thermal Jeans length, therefore thermal Jeans instability is not the dominant fragmentation mode. Turbulent motions broaden the emission of the affected gas compared to the thermal linewidths. For a subsample of EPoS regions radio line surveys are available. Line widths of NH_3 observations for the several IRDCs near to HMPOs are obtained from (Sridharan et al. 2005). Additionally I choose HCO^+, because of its high critical density[5] and good signal-to-noise ratio in the subsequent studies. The linewidths for HCO^+ are obtained from Vasyunina et al. (2011) and Chapter 4. In Figure 3.16 linewidth is plotted against separation. No correlation is found, hence there are no indications for a connection between the internal turbulence state of the cores to the point source separation in the cloud.

My approach to explain the typical value found for the core separations is a physical selection effect. All observed regions have roughly the same evolutionary stage. They all passed the starless stage and show embedded heating sources in MIPS $24\,\mu\mathrm{m}$, cold dust is still present for all clouds revealed by sub-millimeter emission. In the subsample with regions near to a HMPO the point source are barely detected near the HMPO, due to the high confusion level in the background emission, so most of the sources are detected in the IRDCs.

Arzoumanian et al. (2011) and Peretto et al. (2012) found a typical filament width of ~ 0.1 pc, which introduces another typical spatial scale. Given the distance for the majority of the regions in the EPoS sample the observations lack the spatial resolution to review filament widths on a 0.1 pc scale. However, with the filament width and the average point source separation, two independent measures for a spatial scale independent of mass and distance are found in IRDCs. By measuring filament widths one is utilizing a morphological feature itself, in contrast using minimum spanning trees to evaluate the point source separation provides a method giving the same results independent of the observed morphology. Billot et al. (2011) used a unbiased point source catalog derived from PACS and SPIRE (extraction technique described in Molinari et al. 2011) to access clustering properties in two Hi-GAL fields with the help of MST. The distribution of point source separations and source densities found in this survey does not show a similar distribution with a single peak, as in this work. This supports the hypothesis that the typical point source separation found in the EPoS sample is indeed due to limitation of the sample to an early evolutionary stage.

Near infrared studies for young stellar clusters found no distinct surface densities of stars for young stellar clusters, instead a smooth distribution has been reported by Bressert et al. (2010, and references within), which indicates a wide range of average star separations for different clusters. Therefore distinct spatial scales might be only present in the early environments with cold and dense gas as in IRDCs and the ISOSS-sources and be washed out during the evolution towards stellar clusters.

[4]The typical thermal sound speeds vary from $0.17 - 0.24\,\mathrm{km/s}$ for typical temperatures of $10 - 20\,\mathrm{K}$, derived from $c_s = 0.3\sqrt{T/30\mathrm{K}}\ \mathrm{km\,s^{-1}}$ (McKee & Tan 2002).

[5]The critical density n_{crit} denotes the minimum densities at which collisions depopulate the upper state and decay through radiation.

Table 3.2. – Point source separation

Source	Distance [a] [kpc]	$M_{\rm IRDC}$ [b] [$M_\odot$]	N [c]	$\overline{m}$ [d] [pc]	median(m) [e] [pc]	R_{submm}^{eff} [f] [pc]	Q [g]	Type [h]
IRDC310.39	5.02	1398	2	0.47	0.47	1.17	0.47	f
IRDC316.72	2.76	3165	23	0.70	0.67	1.64	1.47	f
IRDC320.27	2.25	156	7	0.70	0.86	0.52	1.25	f
IRDC321.73	2.32	564	15	0.88	0.70	-	-	f
IRDC009.86	2.66	143	3	0.57	0.83	0.52	0.81	nf
IRDC010.70	3.46	4413	21	1.71	1.61	2.53	4.18	nf
IRDC011.11	3.41	5045	21	1.38	1.30	2.32	3.58	f
IRDC013.90	2.59	1747	29	0.57	0.54	1.58	1.42	nf
IRDC015.05	2.95	160	3	0.57	0.99	0.52	0.82	nf
IRDC019.30	2.36	624	8	1.13	1.16	0.91	2.62	f
IRDC028.34	4.52	15011	24	1.41	1.46	3.11	3.15	f
IRDC048.66	2.63	217	7	0.61	0.44	0.63	1.30	f
IRDC079.31	1.56	803	25	0.52	0.50	-	-	f
IRDC18102	2.60	1464	16	0.71	0.90	0.69	1.55	nf
IRDC18151	2.65	872	44	0.81	0.76	-	-	nf
IRDC18182	3.44	2760	26	1.13	1.03	1.86	2.72	f
IRDC18223	3.50	3501	21	1.20	0.90	2.15	2.82	f
IRDC18306	3.64	1603	11	1.68	1.66	1.45	3.29	f
IRDC18308	4.43	3148	6	1.93	1.37	1.81	4.42	f
IRDC18310	4.91	4098	11	1.61	1.34	2.02	3.66	nf
IRDC18337	3.66	4152	17	1.30	1.58	2.14	3.03	nf
IRDC18385	3.13	987	7	1.20	1.30	1.12	2.12	nf
IRDC18437	5.40	9035	20	1.63	1.54	3.57	4.20	f
IRDC18454	5.35	47521	39	1.89	1.88	5.47	4.65	nf
IRDC18530	4.60	4205	5	2.52	3.44	1.99	4.36	nf
IRDC19175	0.78	71	23	0.16	0.15	0.33	0.37	f
HMSC07029	0.63	40	10	0.25	0.18	-	-	nf
ISOSSJ04225	4.24	404	3	0.58	0.68	-	-	f
ISOSSJ06114	5.91	-	7	3.06	2.23	-	-	nf
ISOSSJ06527	4.80	437	2	0.32	0.32	-	-	nf
ISOSSJ18364	2.35	99	2	1.11	1.11	-	-	nf
ISOSSJ19357	4.75	134	2	0.27	0.27	-	-	f
ISOSSJ19486	2.75	71	3	0.40	0.57	-	-	f
ISOSSJ19557	3.52	110	3	0.85	1.11	-	-	f
ISOSSJ20093	1.15	2	3	0.29	0.32	-	-	f
ISOSSJ20298	0.95	13	6	0.19	0.16	-	-	f
ISOSSJ21311	5.85	482	3	0.30	0.40	-	-	nf
ISOSSJ22164	5.29	448	5	1.19	1.52	-	-	nf
ISOSSJ22478	3.23	104	7	0.43	0.24	-	-	nf
ISOSSJ23053	4.31	488	3	0.78	1.17	-	-	nf

(a) The kinematic distance

(b) The total mass of the each region was calculated from the sub-millimeter emission (obtained from Ragan et al. 2012)

(c) The number of detected point sources

(d) The average point source separation (the mean MST edge length) for each region

(e) The median MST edge length for each region

(f) The effective radius $R_{eff} = \sqrt{A/\pi}$ of each region from the clumpfinder run on the ATLASGAL data (870 μm) during the mask creation process in Section 3.3.3

(g) This structural parameter is given by $Q = \overline{m}/\overline{s}$, where $\overline{m}$ is the mean MST edge length and $\overline{s}$ the average correlation length of the sources in a region (see text).

(h) f – filamentary regions, nf – non-filamentary regions

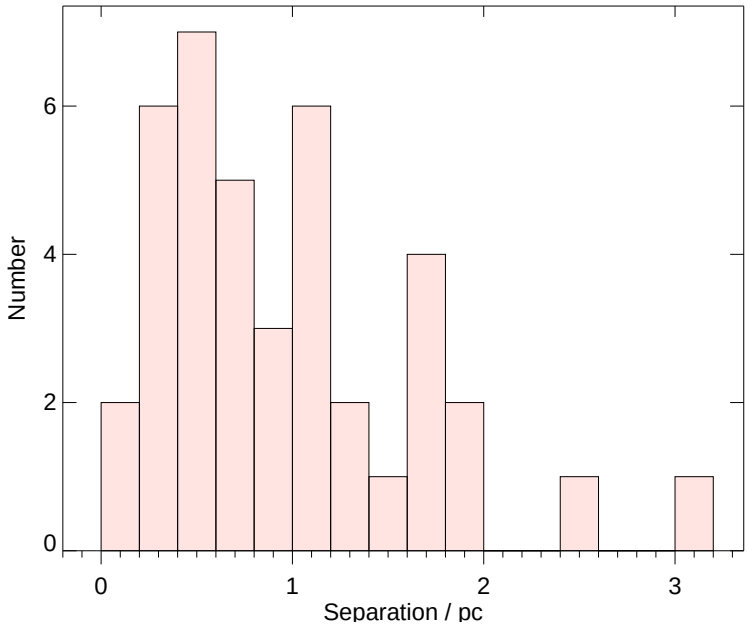

(a) All regions

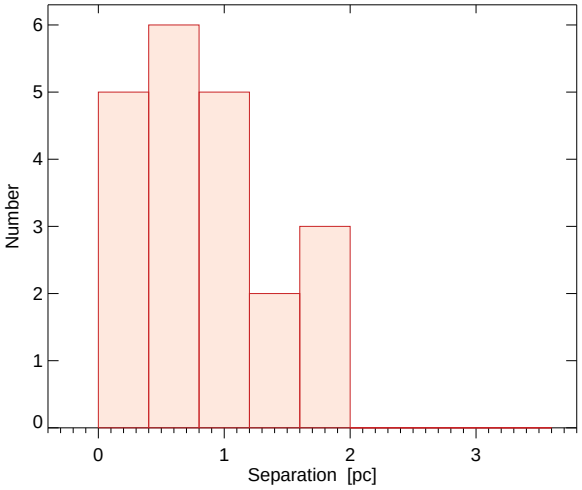

(b) Only filamentous regions

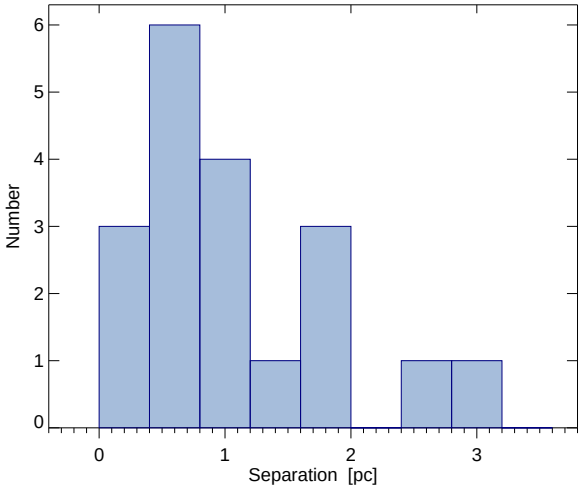

(c) Only non-filamentous regions

Figure 3.10. – The distribution of average point-source separations for the regions in the sample is shown in these histograms.

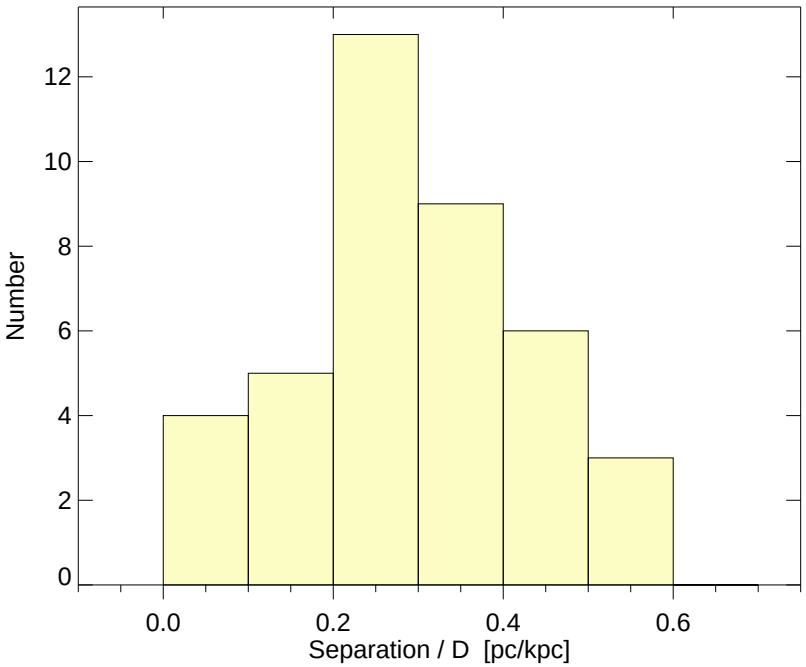

(a) All regions

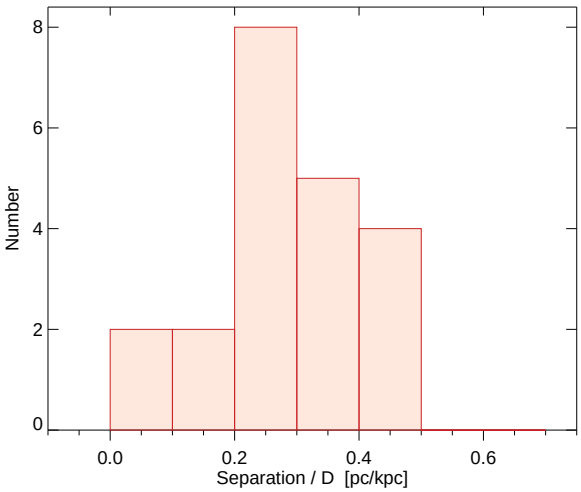

(b) Only filamentous regions

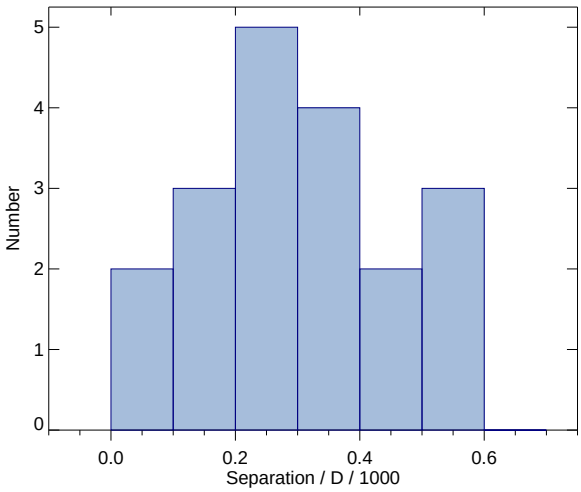

(c) Only non-filamentous regions

Figure 3.11. – The distribution of average point-source separations normalized by their kinematic distance is shown in these histograms.

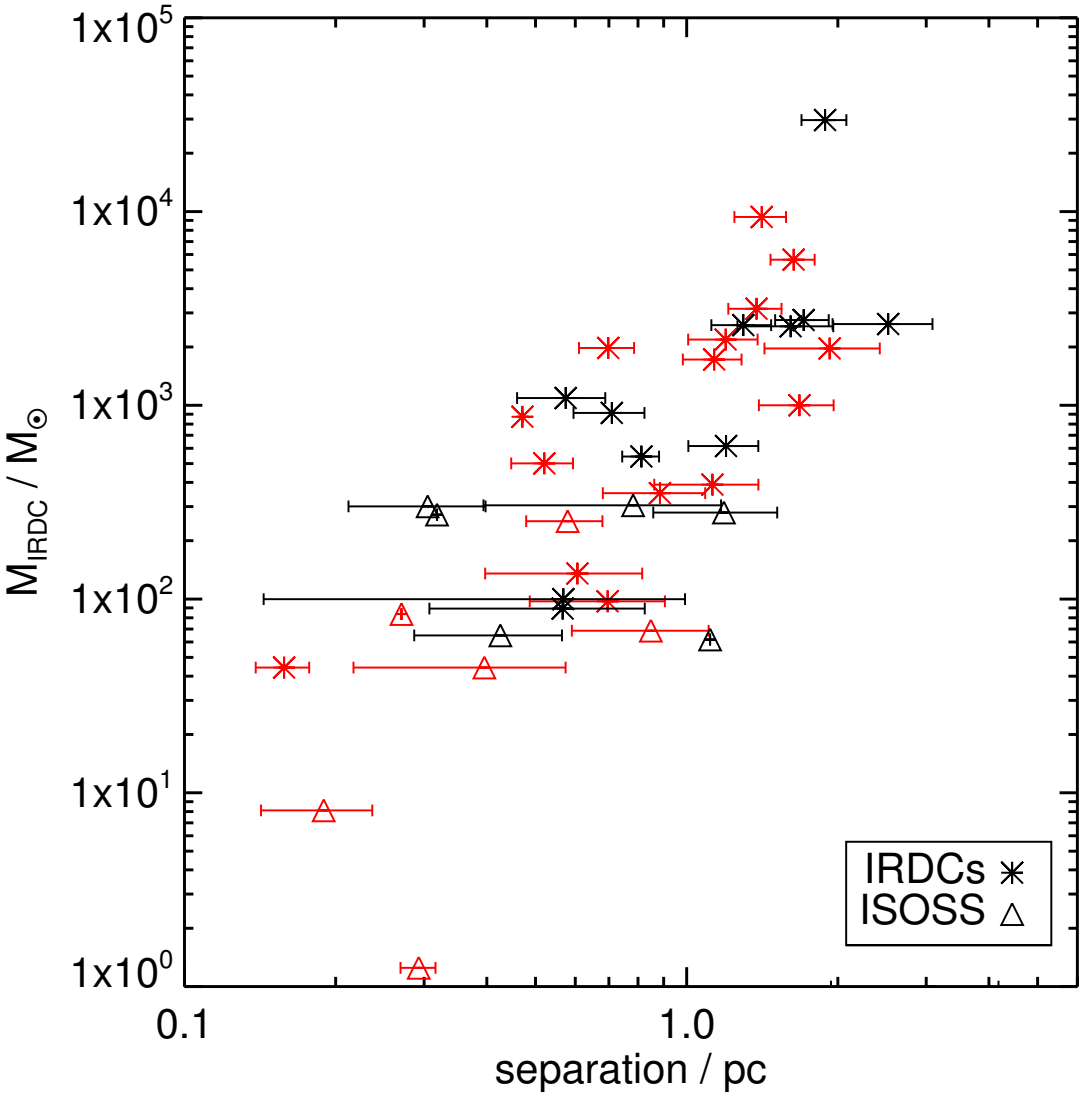

Figure 3.12. – The correlation between the average point source separation and the total mass of a region is shown. Regions with a filamentous structure are plotted in red. IRDCs marked by a *, while a Δ represents regions from the ISOSS survey.

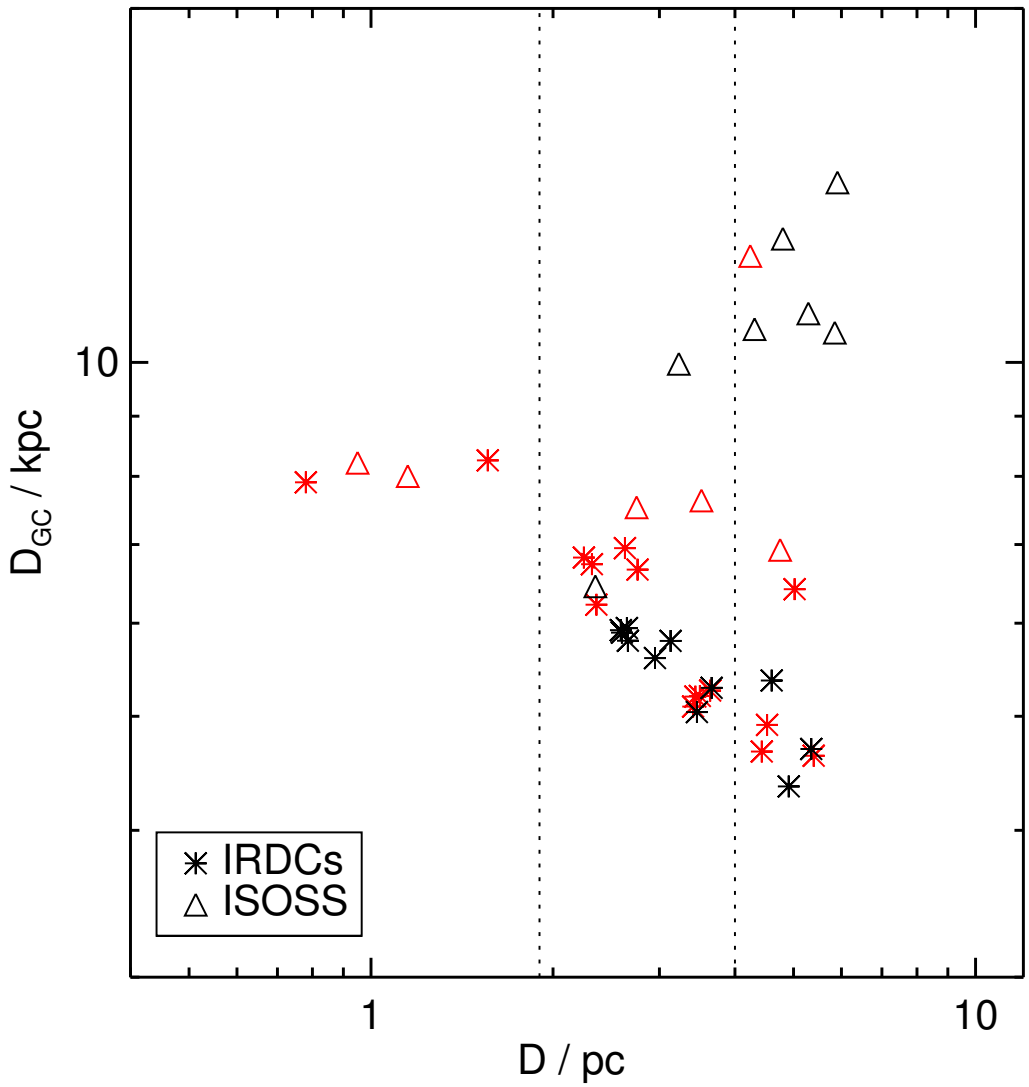

Figure 3.13. – The kinematic distance is plotted against the galactocentric distance for each region, using the same conventions as in Figure 3.12.

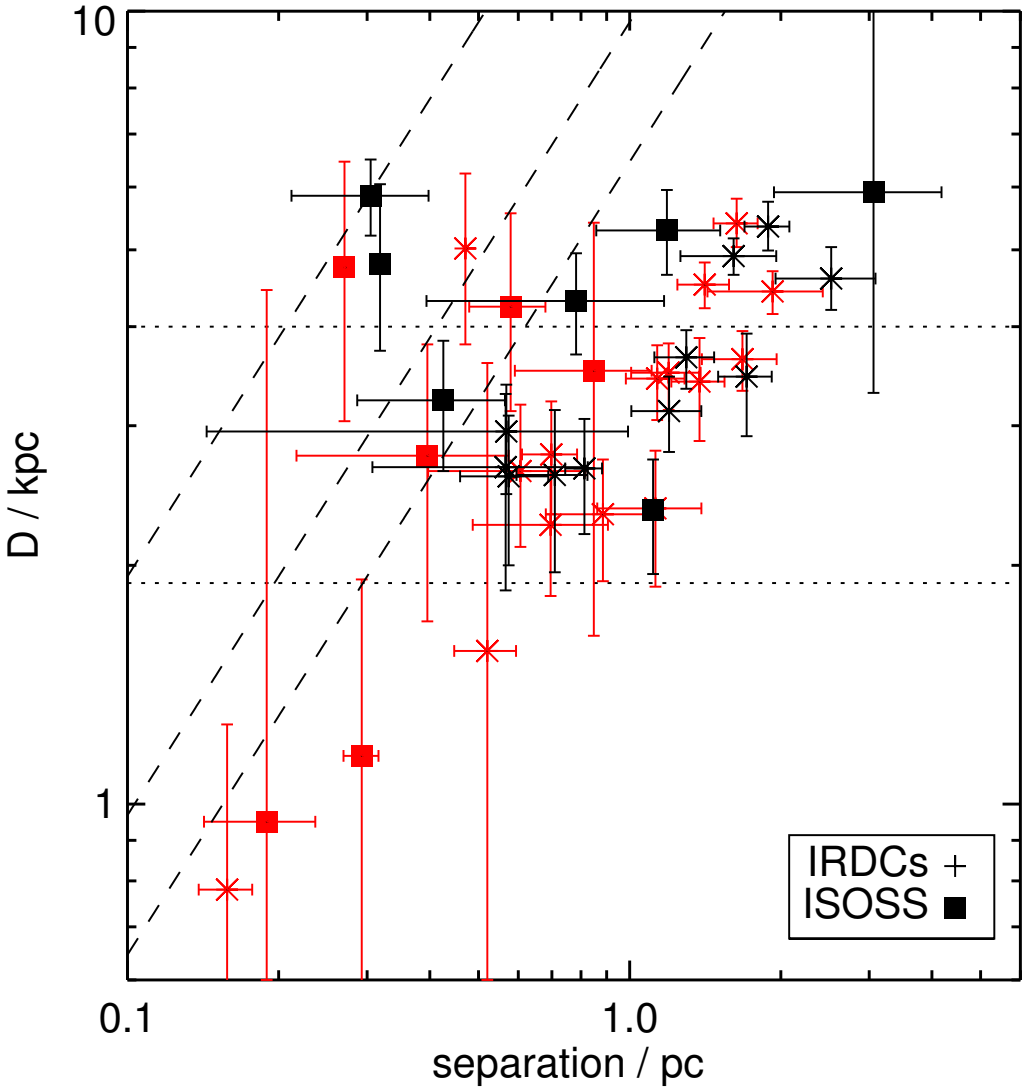

Figure 3.14. – The correlation between the average point source separation and the kinematic distance of the region is shown, using the same conventions as in Figure 3.12. The dotted lines indicate the range of the sample plotted in Figure 3.15. The dashed lines denote one, two and three times the resolution limit at a given distance (from left to right respectively).

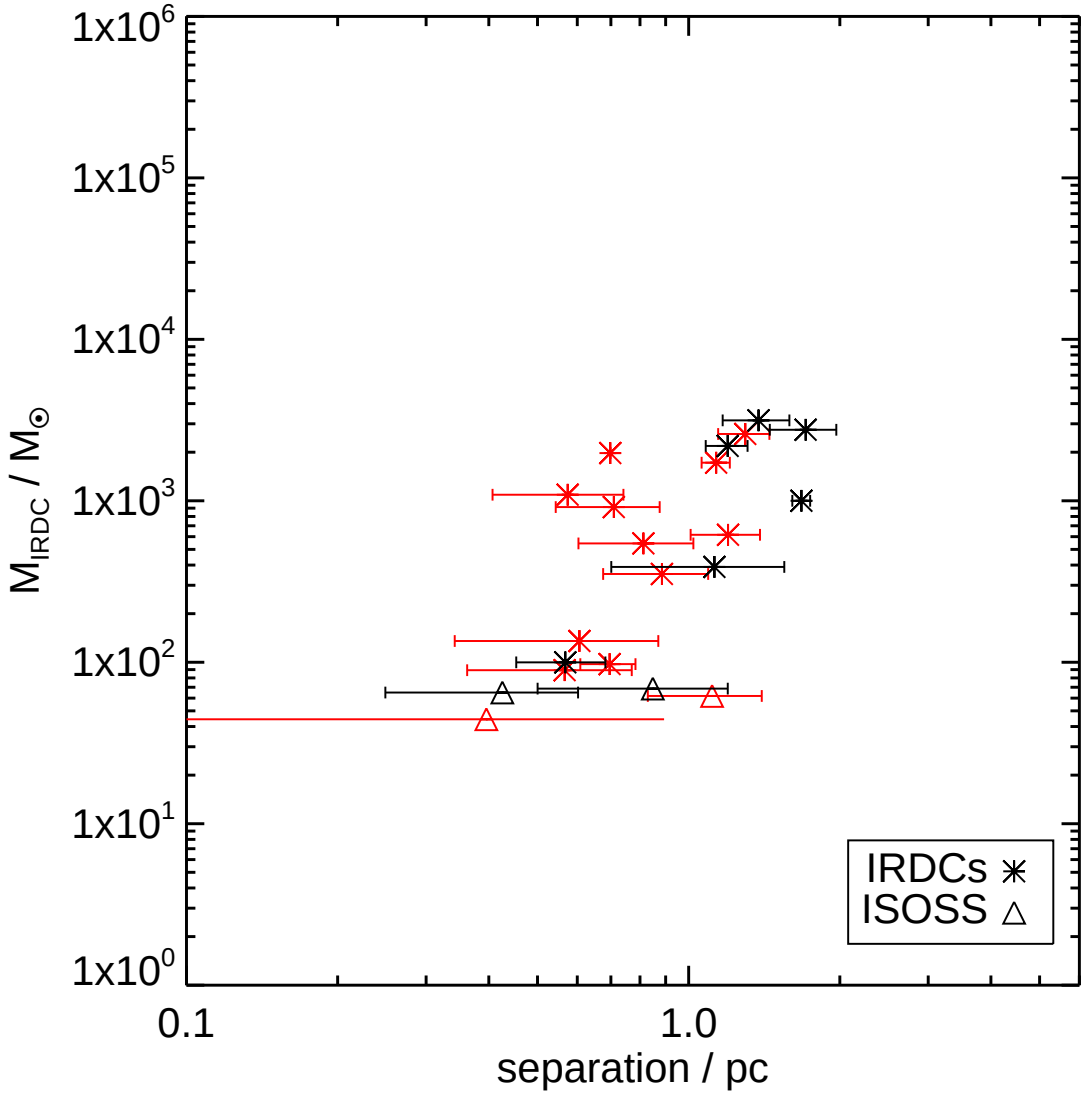

Figure 3.15. – Point source separation against cloud mass is shown as in Figure 3.12, but only regions with kinimatic distances of 1.9 to 4.0 kpc are plotted.

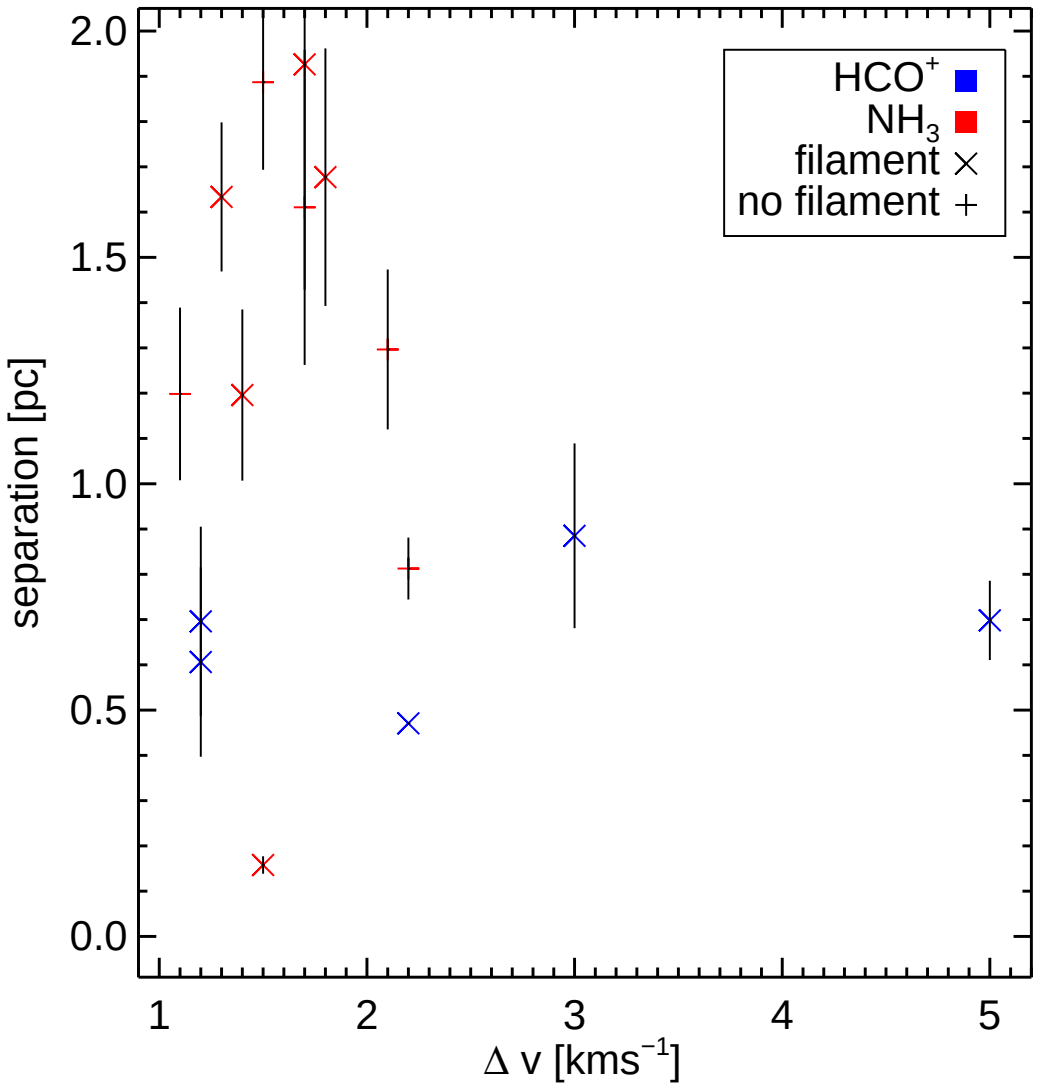

Figure 3.16. – The scatter-plot for the molecular linewidths against point source separation is shown. The NH_3 are obtained from Sridharan et al. (2005). The HCO^+ data were compiled from Vasyunina et al. (2011) and Chapter 4.

3.5.4. Outlook: Structural behavior and the clustering properties of IRDCs

The distribution of the normalized separations $\overline{m}/D_{kin}$ appear to be asymmetric around the peak value (Figure 3.11), although this is presumable a truncation at shorter separation due to limiting resolution, a more physical explanation should not be excluded a priori. It could be possible that hierarchical mechanisms as sub-clustering of sources in IRDCs could introduce such asymmetry. For example let us consider two different IRDCs: in the first one shows a smooth distribution of point sources, while in the second cloud the point sources form multiple clusters associated to, e.g., sub-millimeter peaks. Assuming that the typical point source separation of 0.5 pc is caused by the local fragmentation in the natal clump, this would imply that the point source separation in the first IRDC is similar to the local separations in the each cluster in the second IRDC. Presumably the cluster separation would be significantly higher than the local point source separation. However the inter-cluster connections are also represented by edges in the spanning tree. Depending on the number clusters and separation lengths of the clusters the average MST edge length could significantly increase in a clustered IRDCs, which would explain the asymmetric distribution with the 'tail' towards longer separations in the Figure 3.10 and 3.11. Although these considerations are highly speculative, it shows that further studies are needed to study the structural properties of IRDCs.

To classify the structure of stellar clusters Cartwright & Whitworth (2004) introduced $\mathcal{Q}$

$$\mathcal{Q} = \frac{\overline{m}}{\overline{s}} \tag{3.5}$$

the ratio between the medium MST edge length and the correlation length $\overline{s} = \langle s \rangle / R_{\rm eff}$, where $\langle s \rangle$ is the average pair separation[6] and $R_{\rm eff} = \sqrt{A/\pi}$ is the effective radius of the $870\,\mu{\rm m}$ ATLASGAL emission computed by clumpfinder. A value of $0.45 \leq \mathcal{Q} \leq 0.8$ represents fractal sub-clustering, while $0.8 \leq \mathcal{Q} \leq 1.5$ is more representative for a smooth density gradient. In Table 3.2 $\mathcal{Q}$ is listed for sources with ATLASGAL masks. For most regions in the given sample one is limited by low number statistics. The sources with the highest number of detected sources should be most suitable but most of them show unphysically high values of $\mathcal{Q}$. It appears that the $\mathcal{Q}$-ratio is not the appropriate method to analyze the structural behavior of non-spherical configurations. Cartwright& Whitworth (2008) suggested an alternative method the so-called "Fry-plot". This technique can quantity and visualize any directional bias in the probability density function of point sources in a clustered environment. Future studies of the EPoS sample could utilize this technique. However, a way to enhance the validity of any statistical analysis of the EPoS sample is to increase the number of point sources. As shown in Section 3.4.2 by omitting the $160\,\mu{\rm m}$ PACS band with the coarser resolution in the photometric extraction can lead to a significant increase of point sources. To optimize the detection performance a new set of parameters (background aperture, correlation threshold) needs to be determined and a more aggressive filter settings are required for the unsharp masking to reduce the level of background confusion.

Recently Tackenberg et al. (2012, submitted to A&A) discovered a large scale, physical connected filamentary structure including multiple IRDCs. This filament provides a promising target to study further the clustering behavior of very young YSOs. Inside the filament a large number of infrared sources can be found. To find small and large scale clustering one could create a MST for the whole 55 pc filament. The single clusters and sub-clusters could be detected by defining certain cutoffs for the spanning tree edges as in Billot et al. (2011). Moreover, the correlation function of the point

[6]The average pair separation is the mean distance of all possible connections.

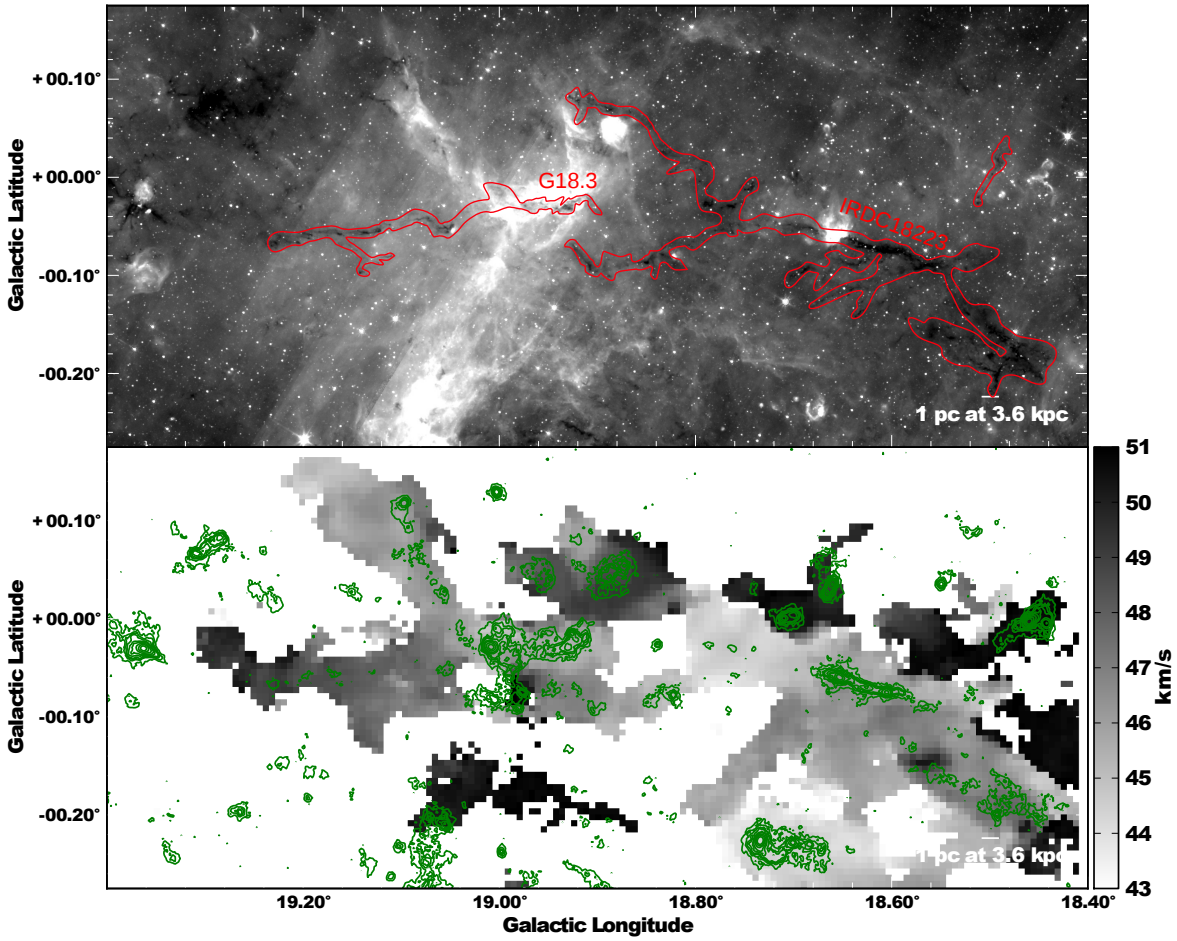

Figure 3.17. – A system of multiple IRDCs is seen in the IRAC 8 μm channel as a large scale dark filament, spanning more than 55 pc (top panel, both panels are taken from Tackenberg et al., 2012 subm. to A&A). The smooth transitions between the different velocity components in the GRS-^{13}CO map (bottom panel, overplotted with the ATLAS-GAL 870 μm emission) show indeed that the large-scale filament is physically connected.

sources with the peaks in the ATLAS-GAL maps or the NICER extinction maps from Kainulainen et al. (2011) should be studied to trace down the physical conditions under which clustering might occur. Over all further studies, as suggested, could shed light on the question if collapse and fragmentation occurs hierarchically over a wide range of spatial scales, from GMC, over dark cloud and clump size down to the typical scale of cores, or if there is an upper cut off for spatial scales in the formation process.

4. G48.66–0.22: A case study of an isolated, simply structured site of massive star-formation

In this Chapter a case study of massive star-forming is presented. The IRDC G48.66–0.22 provides an excellent target to study the collapse and fragmentation in a filamentary environment, because of its isolate nature and simple structure. Through the characterization of the resulting point sources an evolutionary stage can be assessed and a mass prediction for the final star or cluster can be made. Molecular line observations give further information about the morphology and clues to the pressure support in the source. The freeze-out in G48 will be excessed by studying CO depletion in the central part of the IRDC. Most importantly, the Herschel maps are utilized to study the temperature and column density structure of G48.

4.1. Introduction

Most of the current theories about the formation of IRDCs treat the collapsing gaseous medium as isothermal. With the Herschel observatory, we have the spatial resolving power, sensitivity and dynamic range to study the temperature and column density structure of IRDCs in more detail. First results from Herschel indicate a non-isothermal temperature structure of IRDCs (Peretto et al. 2010) from SED fitting with minimum temperatures down to 10 K. Wilcock et al. (2012) compared Herschel observations with radiative transfer models. Tracing deeper into the core than SED fitting the resulting temperature profiles go down to 11.5 K (sample average). Further studies analyzed the temperature structure in IRDCs with temperatures higher by more than 5 K. Battersby et al. (2011) present large scale temperature maps of IRDCs. Beuther et al. (2011) studied the IRDC18454 near the W43 mini-starburst and present dust temperature maps. Further investigations have to clarify if the majority of IRDCs show similar minimum temperatures or if clumps with warm central temperatures exist. This classification is essential for the understanding of the formation process. The comparison between dust and gas temperatures can shed light on the efficiency of the gas-dust coupling at densities typical for IRDCs. Furthermore, a well constrained dust temperature structure can provide critical input for chemical models of IRDCs, in particular the dust grain surface reactions.

In this Chapter I present results from the Herschel GTO key program - “Early Phases of Star Formation” (EPoS). The high-mass portion of this program is compiled from different surveys. The sample includes a sub-sample of “classical” IRDCs, a selection of IRDCs in the near vicinity of high-mass proto-stellar objects (HMPOs) and cold, massive, compact sources detected by the ISO Serendipity Survey (ISOSS). In Section 3.1 of the previous Chapter a more comprehensive introduction to the EPoS sample is given.

This Chapter presents a case study of one “classical” IRDC, G048.66−0.29 (henceforth called “G48”). In addition to the Herschel PACS and SPIRE data I provide mid infrared, sub-millimeter continuum data and mid-infrared, millimeter line data. The kinematic distance to G48 was determined

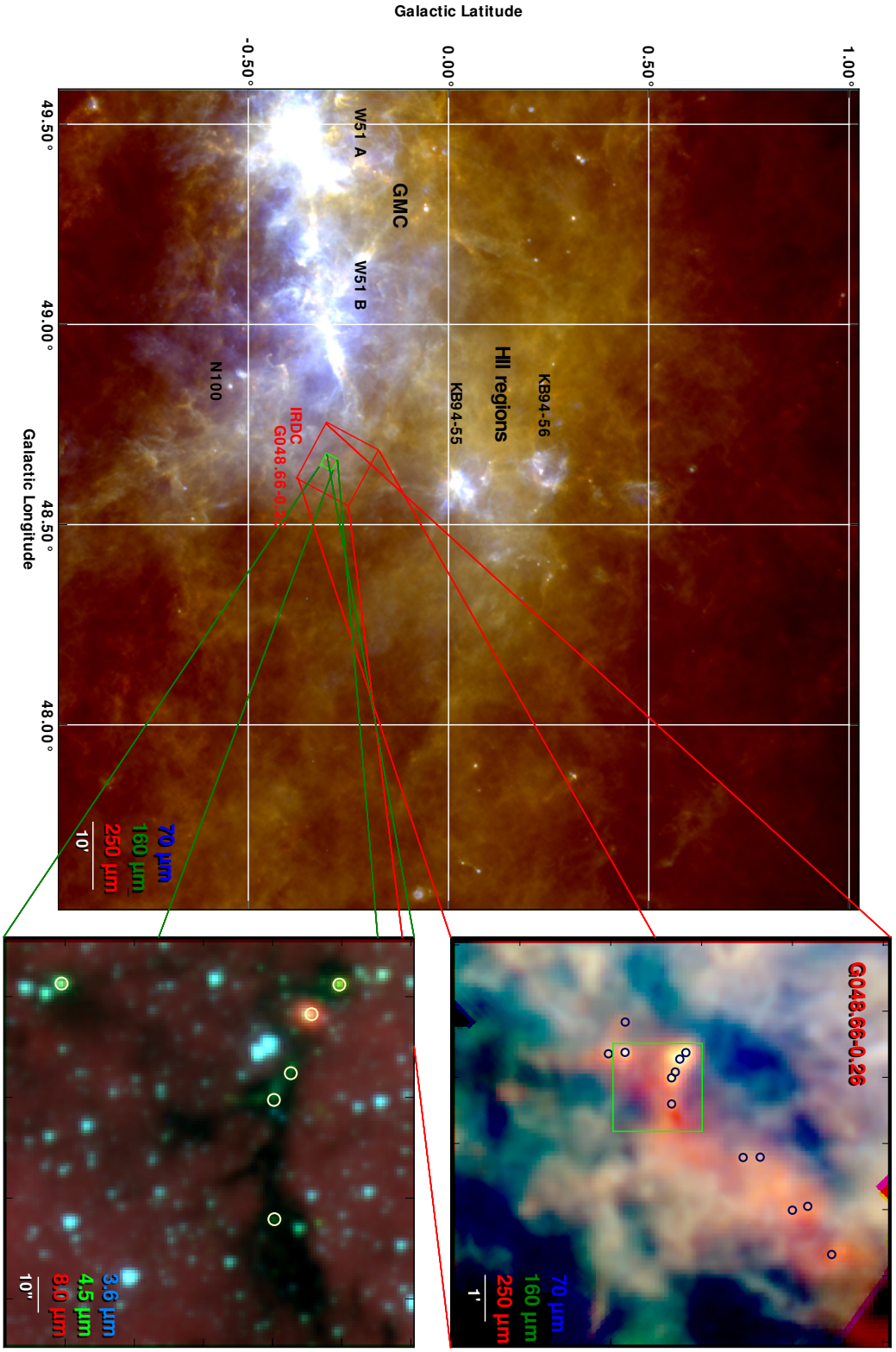

Figure 4.1. – The *top panel* presents a Herschel map of the galactic neighbourhood of G48. The dominant feature to the left of G48 is the Giant Molecular Cloud complex of W51. Two HII regions described by Kuchar & Bania (1994) are located above G48. Below G48 the infrared bubble N100 appears. The map is composed of the PACS band at 70 µm (blue), 160 µm (green) and SPIRE at 250 µm (red) from the Hi-GAL field 48_0. The *bottom right panel* is a zoom into the whole IRDC. It uses the same Herschel bands, utilizing the EPoS observations. The *bottom left panel* shows the central part of G48 as an IRAC 3-color image (3.5, 4.8, 8.0 µm). The green band shows elongated lobes attributed to shock-excited H_2, sometimes refereed to as "green and fuzzy" features "or extended green objects" (EGOs). The detected Herschel point-sources from Section 4.3.4 are indicated by circles in the right panels. All intensities are plotted with logarithmic scaling in all maps.

to be ~ 2.5 kpc (Ormel et al. 2005; Simon et al. 2006) or 2.6 kpc (this work).

G48 appears to be projected near the GMC W51, which is in fact twice as distant as the IRDC. G48 appears isolated and, therefore, one can assume it is not strongly influenced by local heating sources. Furthermore G48 has a quite simple monofilamentary structure. By comparing the observational results from this isolated IRDC to more complex IRDCs, one can constrain the dominant effects at work for star formation in IRDCs.

Simon et al. (2006) estimated from ^{13}CO observations an average density for H_2 associated with G48 of $\sim 3 \cdot 10^3\,\mathrm{cm}^{-3}$, a peak column density of $8.8 \cdot 10^{21}\,\mathrm{cm}^{-2}$ and a LTE mass of $\sim 580\,\mathrm{M}_\odot$ for the cloud. Ormel et al. (2005) identified three different clumps with masses from 91 to 130 $\mathrm{M}_\odot$ using SCUBA and MSX observations. By modeling the internal velocity structure of these clumps using HCO^+ $(3-2)$ and $(4-3)$ they found that the line-widths decrease outside the cloud, indicating a decrease in turbulent motions outwards of the clumps. This suggests that the star formation activity inside these clumps down to the core scale is driven by turbulence. van der Wiel & Shipman (2008) identified 13 YSOs in the vicinity of G48. The majority of these objects belong to "Stage I" referring to the classification scheme of Robitaille et al. (2006) and have low to intermediate masses. From a comparison of [CI] and ^{13}CO data Ossenkopf et al. (2011) inferred the presence of a young photodissociation region (PDR) ionized by the YSOs inside of G48.

The next section describes the observations, the data reduction and some basic data processing steps for Herschel, Spitzer, sub-millimeter continuum and molecular line observations. Section 4.3 details the scientific analysis and the direct results. In Section 4.3.1 the structure and vicinity of G48 is described. The temperature mapping, utilizing Herschel, SCUBA and ATLASGAL data, is delineated in Section 4.3.2. The subsequent Section 4.3.3 compares the column densities with other observations and estimates mass for the whole IRDC. Section 4.3.4 addresses the fitting and classification of point sources from the MIPS $24\,\mu\mathrm{m}$ and PACS bands. Section 4.3.5 contains the analysis of the molecular line data. The concluding Section 4.4 discusses the results in respect to previous studies of IRDC and theoretical considerations. The last Section 4.5 summarizes the main results.

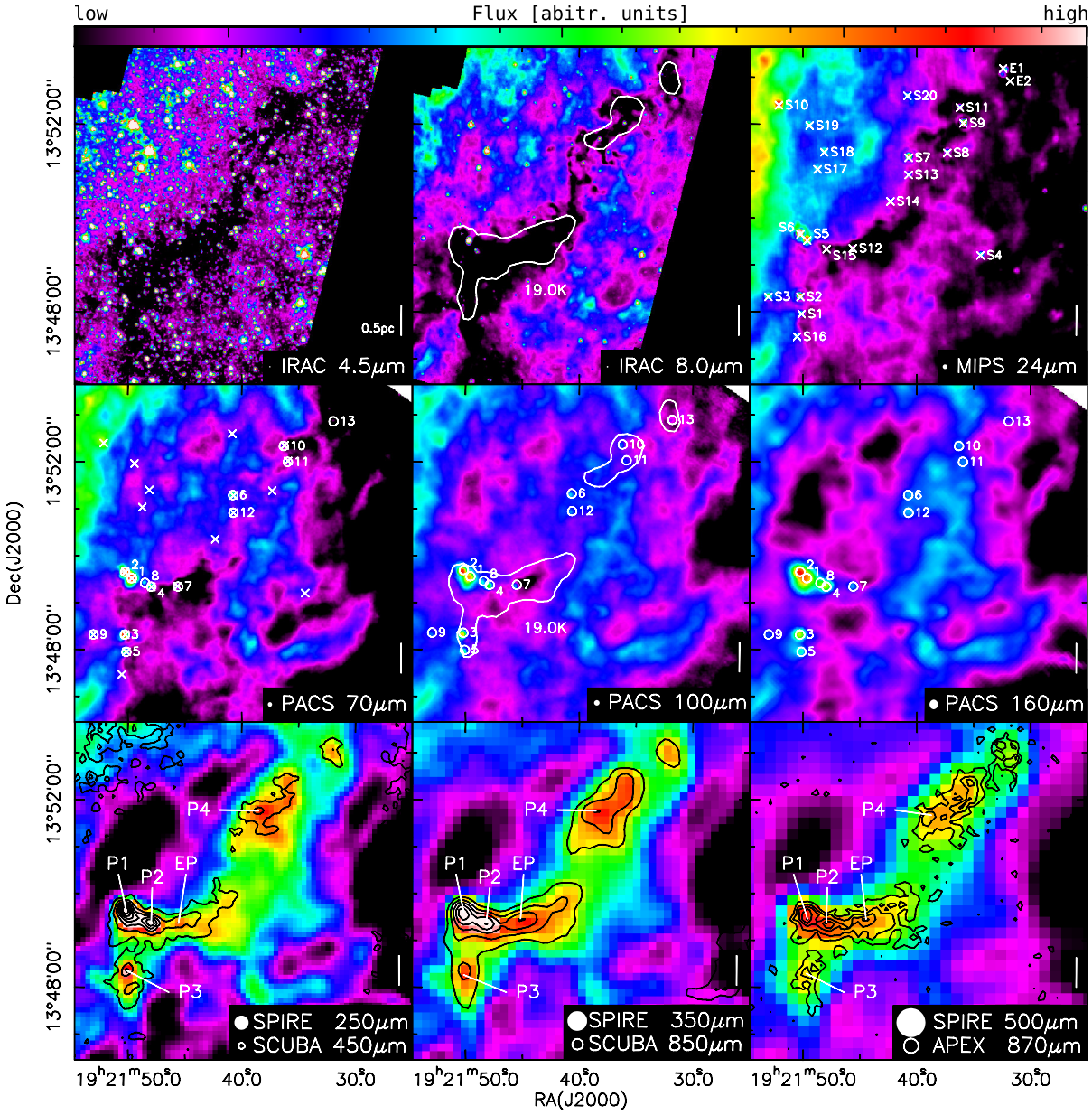

Figure 4.2. – The intensity plots for G48 are shown in the different Spitzer, PACS and SPIRE channels. Each plot is shown on a linear scale to highlight absorption or emission at each wavelength band; the top color bar indicates the relative flux scale. The positions of the 24 μm point sources as characterized by van der Wiel & Shipman (2008) are indicated by red crosses in the MIPS 24 μm and PACS 70 μm maps. The MIPS 24 μm sources from van der Wiel & Shipman (2008) are labeled "Sx" while two additional 24 μm sources associated to G48 are labeled "E1" and "E2". The detected sources in the PACS bands are marked by the green circles. The radius of the circles imply the fitting radius between the different bands. The SPIRE maps are overlayed by SCUBA 450 μm, 850 μm and ATLASGAL 870 μm contours, respectively. The corresponding beam sizes for Spitzer, PACS and SPIRE are indicated with circles in each panel. An isothermal contour of 19 K from the temperature fitting (Section 4.3.2) is overplotted for IRAC 8 μm and PACS 100 μm. The beam size of the observations plotted in contours are plotted as open ellipses. The white bar (right side) gives a projected distance of 0.5 pc on the map.

4.2. Observations, Data reduction and processing

4.2.1. Herschel

G48 was observed by EPoS and the "Herschel infrared Galactic Plane Survey" (Hi-GAL) project with the Photometer Array Camera and Spectrometer (PACS, Poglitsch et al. 2010) and the Spectral and Photometric Imaging Receiver (SPIRE, Griffin et al. 2010) on board of the Herschel Space Observatory (Pilbratt et al. 2010). The EPoS PACS scan maps at $70\,\mu\mathrm{m}$, $100\,\mu\mathrm{m}$ and $160\,\mu\mathrm{m}$ were obtained with the medium scan speed of $20''$/s and the nominal scan leg length of $7'$. The data were processed to Level-1 using HIPE. A second level deglitching was applied to flag bad data values by σ-clipping flux values mapped on to each pixel. The 'time ordered' option was used, and a $25\,\sigma$-threshold was applied. The level-2 reduction was conducted with the SCANAMORPHOS (Roussel 2012) version 5.0. The maps in each band were reduced with a pixel-size of $1\farcs0$/px.

The EPoS SPIRE scan maps at 250, 350, and $500\,\mu\mathrm{m}$ were obtained with a scan speed of 30"/s. They were reduced up to level-1 using HIPE version 5.0with the calibration pool 5.1. The final level-2 reduction was done with SCANAMORPHOS version 9.0 using the 'galactic' option. The pixel sizes are $6.0''$/px at $250\,\mu\mathrm{m}$, $10.0''$/px at $350\,\mu\mathrm{m}$ and $14.0''$/px at $500\,\mu\mathrm{m}$.

To include a larger coverage the raw data products from the Hi-GAL Open Time Key Project were obtained. These observations were carried out in the PACS/SPIRE parallel mode with a scan speed of $60''$/s, resulting in large scale maps. The 70 and $160\,\mu\mathrm{m}$ PACS maps have been reduced using HIPE 8.0, applying the same options as for the EPoS PACS data. Level-2 processing has been performed with SCANAMORPHOS version 15. The pixel size is $3\farcs2$/px for both maps. The 250, 350 and $500\,\mu\mathrm{m}$ SPIRE maps were reduced up to level-1 using HIPE version 8.0 with the calibration tree 8.1. SCANAMORPHOS version 15 was used to produce the level-2 maps. The pixel size is the same as for the EPoS SPIRE maps. The final maps are presented in the left panel of Figure 4.1. The Hi-GAL maps are used for the temperature mapping in Section 4.3.2.

Due to the diffuse and heterogeneous background emission varying on a wide range of spatial scales, it is more robust to perform PSF photometry than aperture photometry. Therefore, the PSF photometry software `starfinder` (Diolaiti et al. 2000) was used for the point source detection and flux extraction for the PACS bands. The latest empirical PSF of the Vesta asteroid was used (OD 160), obtained from the Herschel Science Archive (HSA), since an empirical PSF derived from sources in G48 is noise dominated and therefore less acceptable. For consistency the PSF maps were reprocessed with SCANMORPHOS and rotated to the orientation of the maps. The noise in the PACS maps is not white noise, since it suffers from pixel-to-pixel correlations induced, e.g., by non-thermal low-frequency noise. To calculate the average noise in the map a Gaussian distributed noise was assumed, but corrected by a factor for the pixel-to-pixel correlation.

The major source of confusion in the source detection is the complicated background. In particular the bright background towards the GMC returns numerous false detections. Therefore, only the parts of the PACS maps were included that correspond to regions in the ATLASGAL map (see Section 4.2.3) with fluxes above a $3\,\sigma$-level. To further improve the detection efficiency an unsharp-mask-filter was applied in each PACS-band by subtracting a median smoothed map from the respective science-frame. With this procedure I avoid false detections, and miss three obvious sources for the automated detection run. These sources were then included in the catalog identified by eye as clear detections. With the compiled fixed source positions the final photometry was performed on the non-filtered science frames. To be considered a detection a source must meet the following conditions: it must have a source flux above the $5\,\sigma$ noise level and be detected in all PACS bands within the FWHM

of the $160\,\mu\mathrm{m}$ PACS PSF ($\sim 11\farcs2$). The results of the point source extraction are reported in Section 4.3.4. The given fluxes are already color-corrected for the source temperatures[1]. Further details of the source extraction are given in the EPoS high-mass overview paper (Ragan et al. 2012).

4.2.2. Spitzer

I obtained the Spitzer IRAC and MIPS maps from the Galactic Legacy Infrared Mid-Plane Survey Extraordinaire (GLIMPSE, Benjamin et al. 2003) and the MIPS Inner Galactic Plane Survey (MIPSGAL, Carey et al. 2009). The $24\,\mu\mathrm{m}$ MIPSGAL maps were processed with the MIPS Data Analysis Tool (DAT v3.10; Gordon et al. 2005) starting from the `raw` data products.

I used the $8\,\mu\mathrm{m}$ IRAC map to create an extinction map. PSF photometry was performed on this map, using the `starfinder` package. An averaged, empirical PSF was used to remove all the point sources in this field. The residual map was used to calculate the optical depths, as described by Vasyunina et al. (2009), using:

$$\tau = \ln\left(\frac{I_{\mathrm{BG}} - I_{\mathrm{fore}}}{I_{\mathrm{IRDC}} - I_{\mathrm{fore}}}\right) \tag{4.1}$$

where I_{IRDC} is the flux derived from the IRDC directly, I_{BG} is the contribution by background material directly behind the IRDC and I_{fore} characterizes the foreground emission.
Point-source fluxes from MIPS $24\,\mu\mathrm{m}$ used in Section 4.3.4 were also obtained with `starfinder`. For MIPS PSF photometry I utilized a model PSF computed by the `STINYTIM`[2] program, based on `TINYTIM` for the HST (Krist 2002).

The spectrum, shown in Figure 4.3, was obtained from the Infrared Spectrograph (IRS) on-board the Spitzer Space Telescope. The observation (AOT: 12093696) was taken from the Spitzer Heritage Archive (SHA) as part of the "Infrared Dark Clouds in the Inner Galaxy" program. I used a pipeline partly based on the SMART-package and the FEPS spectral extraction tools (Bouwman et al. 2006; Swain et al. 2008, see also Section 2.3.2 in Chapter 2). The background subtracted on-source spectrum and the background spectra from the off-source nod-positions is shown in Figure 4.3. Only the long wavelength-order (LL) is reduced, since the slit for the short wavelength did not cover any point source in the IRDC. The LL slit did only cover about 60% of the SMART-source PSF, which leads to a flux leakage in the continuum flux. But line shapes and line fluxes should be unchanged for the source spectrum, except for a lower S/N-ratio. A strong [SIII] emission appears over the whole IRS-slit, leading to an artifact in the source spectrum due to an over-subtraction of the background. The source spectrum was corrected for this artifact using a polynomial background fit (described in Section 2.3.2 on page 21) to24).

[1] `http://herschel.esac.esa.int/twiki/pub/Public/PacsCalibrationWeb/cc_report_v1.pdf`

[2] `http://irsa.ipac.caltech.edu/data/SPITZER/docs/dataanalysistools/tools/contributed/general/stinytim/`

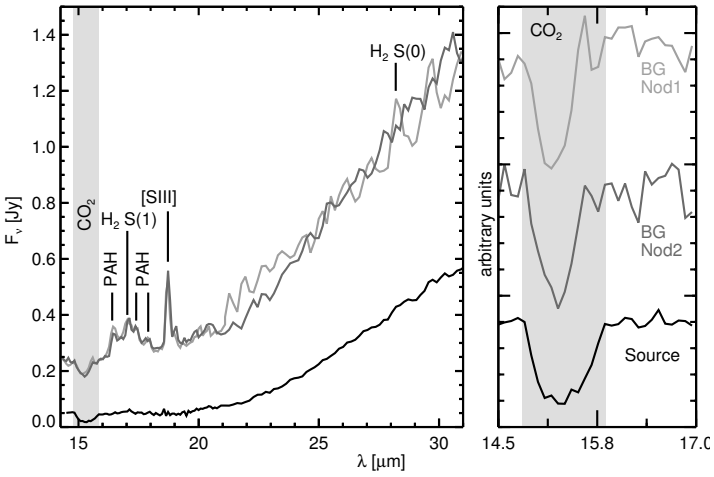

Figure 4.3. – The LL-spectrum from Source 2 from IRS/Spitzer is shown. In the left panel the source spectrum is plotted in black and the extracted background spectra are shown in grey. The background spectrum extracted in the first nod position (BG Nod 1) pointed towards the GMC, while the second background spectrum is taken at the western edge of the IRDC (BG Nod 1). The atomic [S III] line is present as a bright extended emission over the whole slit. The CO_2 ice absorption band is underlined in light grey. The right plot shows the baseline subtracted CO_2 profiles. The on-sources profile is significantly broader and different in shape compared to the nodded background profiles. This implies different ice temperatures and mixing ratios (with e.g., H_2O and CH_3OH, see White et al. 2009).

4.2.3. Sub-Millimeter imaging

I utilized sub-millimeter data from the SCUBA Legacy Catalogue (Di Francesco et al. 2008). The 450 and $850\,\mu\mathrm{m}$ were part of the fundamental catalog. Given the better sensitivity of the survey, the $870\,\mu\mathrm{m}$ observations from the "APEX Telescope Large Area Survey of the Galaxy" (ATLASGAL, Schuller et al. 2009) were used in the temperature fitting (Section 4.3.2) and to determine column densities (Section 4.3.3). The corresponding beam size for the ATLASGAL data is around $19\farcs2$.

4.2.4. Millimeter line observations

Molecular line data were obtained using the 22 meter MOPRA radio telescope and the MOPRA spectrometer (MOPS), operated by the Australian National Facility (ATNF). The observations were performed with the 3 mm band receiver (90 GHz) in the "On-the-fly Mapping" mode (OTF) with a beam size of $36''$ at 86 GHz and $33''$ at 115 GHz. Using MOPS in the "Zoom" setup allows to observe 13 lines simultaneously (^{13}CS, C_2H, CH_3CCH, CH_3CN, $H^{13}CN$, HCO^+, $H^{13}CO^+$, HCCCN, HCN, HNC, HNCO, N_2H^+, SiO). Most of these lines are good tracers for dense gas (see Vasyunina et al. 2009, for a detailed description of each molecular species). Only in the HCN, HNC, HCO^+ and N_2H^+ maps line emission are detected above $3\,\sigma$. The spectrometer configuration results in a velocity resolution of $\sim 0.11\,\mathrm{kms}^{-1}$. The main beam efficiency varies between 49% at 86 GHz and 44% at 100 GHz (Ladd et al. 2005). The typical system temperatures were between 210 and 290 K and the average rms noise level was $\sim$ Jy/beam. The ^{13}CO (1-0) data products were obtained from the Galactic Ring Survey (GRS, Jackson et al. 2006) performed by the Five College Radio Astronomy Observatory (FCRAO). With a angular resolution of $46''$ the beam of FCRAO is somewhat larger than that of MOPRA.

The ^{13}CO (2-1) and $C^{18}O$ (2-1) maps were obtained using the 230 GHz heterodyne receiver array (HERA, Schuster et al. 2004) at the IRAM 30 m telescope. The average FWHM of the HERA beam is $11\farcs3$, which is much better compared to MOPRA or FCRAO.

Table 4.1. – Molecular lines

Molecule	Trans.	ν_r GHz	ΔV_{therm} kms^{-1}	A_{ul} 10^{-5}s^{-1}	E_u K	n_{crit} cm^3	beamsize arcsec	Instrument	Obs. Date
HCO^+	$1-0$	89.188523	0.166	3.0	4.28	$2.1\cdot10^5$	$38''$	MOPRA	2010 Jul 7-9
HCN	$1-0$	88.631602	0.172	2.4	4.25	$1.5\cdot10^6$	$38''$	MOPRA	2010 Jul 7-9
HNC	$1-0$	90.663568	0.172	2.690	4.35	$3.2\cdot10^5$	$38''$	MOPRA	2010 Jul 7-9
N_2H^+	$1-0$	93.173700	0.166	3.6	4.47	$1.8\cdot10^5$	$38''$	MOPRA	2010 Jul 7-9
^{13}CO	$1-0$	110.201354	0.166	0.0063	5.29	$1.9\cdot10^3$	$44''$	FCRAO	Archive data
^{13}CO	$2-1$	220.398684	0.166	0.0604	15.87	$2.0\cdot10^4$	$11\farcs25$	IRAM/HERA	2012 Jan 23
$C^{18}O$	$2-1$	219.560319	0.163	0.0601	15.81	$1.9\cdot10^4$	$11\farcs25$	IRAM/HERA	2012 Jan 23
CH_3C_2H	9_0-8_0	153.8172	0.142	8.75			$16''$	IRAM/EMIR-FTS	2011 Jun 10/12
CH_3C_2H	9_1-8_1	153.8142	0.142	8.44			$16''$	IRAM/EMIR-FTS	2011 Jun 10/12
CH_3C_2H	9_2-8_2	153.8054	0.142	7.55			$16''$	IRAM/EMIR-FTS	2011 Jun 10/12
CH_3C_2H	9_3-8_3	153.7907	0.142	12.52			$16''$	IRAM/EMIR-FTS	2011 Jun 10/12
CH_3C_2H	5_1-4_1	85.455665	0.142	0.1948	19.53		$38''$	MOPRA	2010 Jul 7-9
$H^{13}CN$	$1-0$	86.339860	0.169	2.2256	4.14	$2.6\cdot10^6$	$38''$	MOPRA	2010 Jul 7-9
$H^{13}CO^+$	$1-0$	86.754288	0.164	3.8534	4.16	$1.9\cdot10^5$	$38''$	MOPRA	2010 Jul 7-9
SiO	$2-1$	86.846960	0.135	2.927	6.25	$1.9\cdot10^6$	$38''$	MOPRA	2010 Jul 7-9
C_2H	$2-1$	87.316925	0.179	0.1528	4.19		$38''$	MOPRA	2010 Jul 7-9
HNCO	$4_{0,4}-3_{0,3}$	87.925238	0.137	0.9024	10.55	$4.5\cdot10^6$	$38''$	MOPRA	2010 Jul 7-9
HC_3N	$10-9$	90.978865	0.125	5.812	24.01	$7.5\cdot10^4$	$38''$	MOPRA	2010 Jul 7-9
CH_3CN	5_1-4_1	91.985316	0.140	6.0800	20.39		$38''$	MOPRA	2010 Jul 7-9
^{13}CS	$2-1$	92.494308	0.134	1.4124	6.66	$5.0\cdot10^5$	$38''$	MOPRA	2010 Jul 7-9

The columns list, the molecular species, the transition, the rest frame frequency, the thermal line width at 17.3K, the Einstein coefficient, the upperstate energy, the critical densities and the angular resolution for the observations, the used instrument, from left to right, respectively. The upper part of the table presents the detected molecular lines, while the bottom part lists the MOPRA lines lacking a $3\,\sigma$-detection.

To acquire methylacetylene ($CH_3C{\equiv}CH$) data observations were performed with the IRAM 30 m telescope in position switching mode. For these observations the EMIR receiver with Fast Fourier Transform Spectrometer (FTS) as a backend was used. Total time On source and Off source was 33 min. The Off source position was chosen $600''$ away from the On source position. The On source position was pointed at $19^{\rm h}21^{\rm m}49^{\rm s}.9$ $+13^\circ49'34\farcs7$ (FK5, J2000). The pointing was check every hour, giving a pointing accuracy better than $3''$. The typical system temperature during observations was about 200 K. At 153 GHz the telescope beam size is $16''$ and the beam efficiency is 0.73. The data were analyzed using GILDAS/CLASS software.

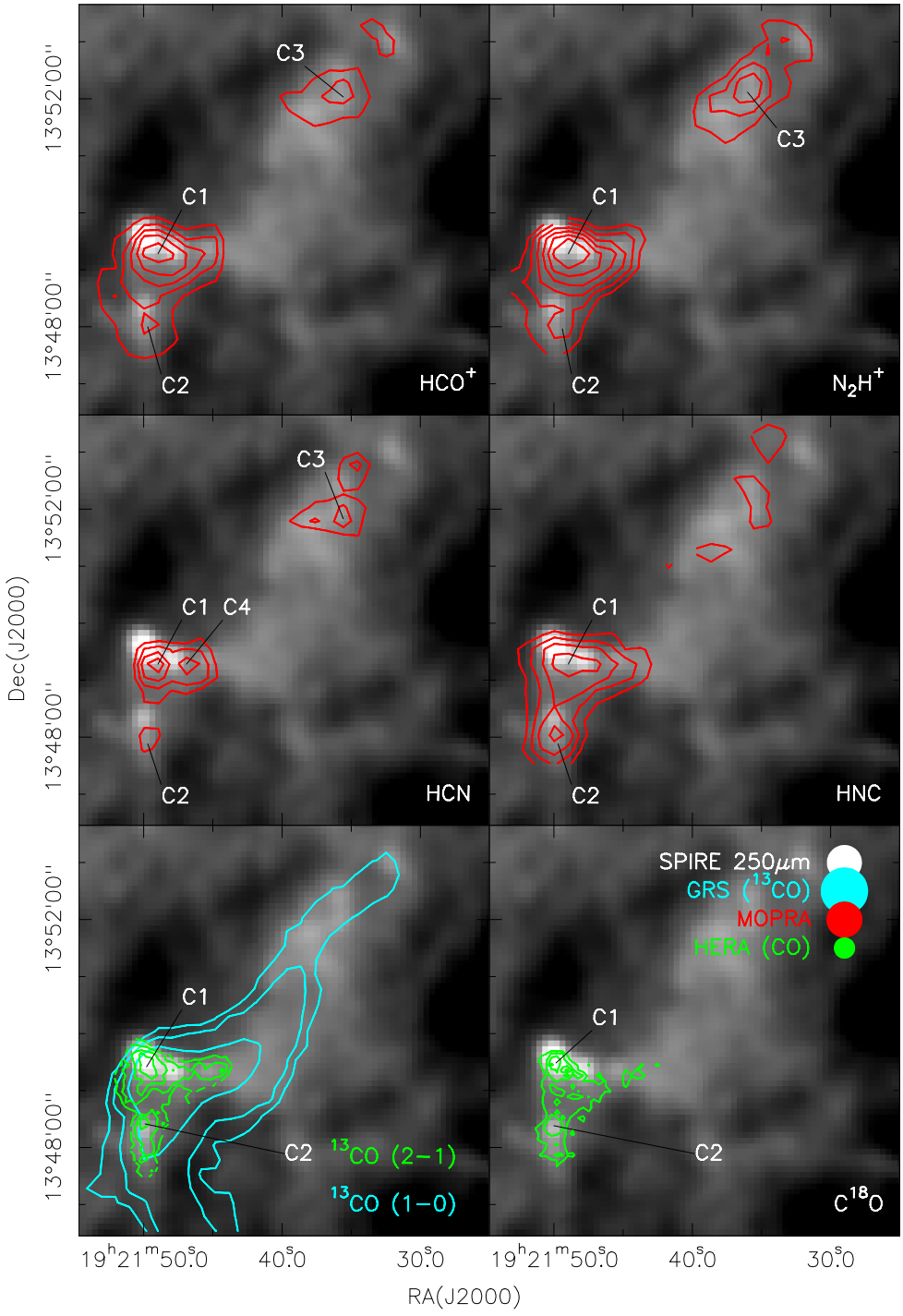

Figure 4.4. – The integrated line intensities of the indicated species are shown as contours overlaying the 250 μm SPIRE map. The contours in the top and middle panels refer to the MOPRA observations, while the bottom panels present the CO data. The beam sizes are indicated in the last panel. The contours for the different line transitions are: HCO^+: from 0.3 to 1.5 K km s^{-1} in steps of 0.3 K km s^{-1}; HCN: from 0.2 to 0.8 K km s^{-1} in steps of 0.1 K km s^{-1}; HNC: from 0.2 to 0.8 K km s^{-1} in steps of 0.1 K km s^{-1}; N_2H^+: from 0.5 to 2.0 K km s^{-1} in steps of 0.25 K km s^{-1}; ^{13}CO (1-0): from 0.8 to 2.9 K km s^{-1} in steps of 0.7 K km s^{-1}; ^{13}CO (2-1): from 2.0 to 9.5 K km s^{-1} in steps of 1.5 K km s^{-1}; $C^{18}O$ (2-1): from 0.7 to 2.7 K km s^{-1} in steps of 0.5 K km s^{-1}

4.3. Results

4.3.1. Morphology - From large to small scales

The left panel of Figure 4.1 shows the galactic neighborhood of G48. The image is composed of the 70, 160 and 250 μm Hi-GAL maps in blue, green and red, respectively. A global brightness gradient towards the outer parts of the galactic plane is present over the whole image. In the vicinity of G48 the GMC W51 is observed. The cloud complex W51A and W51B have an angular distance of $\sim 15'$ and $\sim 50'$ to G48, respectively. The EPoS maps (Figure 4.1, top right panel), in particular the PACS observations, show a brightness gradient towards W51 and the infrared bubble N100 (Churchwell et al. 2006). W51 and G48 are not physically connected since recent observations place W51 twice as far away ($\sim$5.4 kpc Sato et al. 2010) as G48.

In the Spitzer IRAC 8 μm and the MIPS 24 μm channel the IRDC appears as the typical dark filamentary absorption feature against the diffuse galactic emission background (see Figure 4.2). G48 is extended over $\sim 7\farcm5$ in the north-south direction. The dark cloud can be roughly divided into three parts. The central region of the IRDC appears as a elongated structure of $\sim 2\farcm3$ in east-western orientation. This region has the brightest sub-millimeter emission. The western part of the central region shows the highest extinction in the Spitzer maps. Only this part of the IRDC appears in clear absorption in all three PACS channels. Furthermore this part is clearly associated with the most massive sub-millimeter clump, called "extinction peak" (EP, with a mass of $\sim 130\,M_\odot$ from SCUBA observation) in Ormel et al. (2005). The eastern part of the central IRDC only shows clear extinction in the Spitzer bands. In the Herschel PACS maps this region is dominated by compact background emission from embedded point sources, in particular Source 1 (see Section 4.3.4). The central region, as the rest of G48 appears as a diffuse emission structure in the SPIRE maps, but two compact sources can be identified in the eastern central part. The peak positions of these emission features detected at 250 μm and 350 μm are in good agreement with the peak positions of two sub-millimeter clumps (P1 with 91 $M_\odot$ and P2 with 100 $M_\odot$) identified by Ormel et al. (2005). Due to the lower resolution of the 500 μm SPIRE channel the two positions are not resolved.

The structures found south- and northwards of the central part of the IRDC appear more diffuse in the Spitzer bands and are barley recognizable in the PACS channels. In contrast, in the SPIRE bands this diffuse absorption features appear as an elongated emission structure. While this emission is diffuse in the northern part, compact emission is detected in good agreement with the SCUBA and ATLASGAL data in the southern part of the IRDC. The associated sub-millimeter peak was called "P3" in van der Wiel & Shipman (2008) (see Figure 4.2).

4.3.2. Herschel temperature map

To create temperature and column density maps of G48 I used Herschel maps and ground based sub-millimeter data. In brief, the basic steps I have taken to fit the temperature and column density maps are as follows:

1. The global background flux offsets are estimated from the large scale Hi-GAL maps and subtracted from the maps.

2. All data (PACS at 160 μm, SPIRE at 250 and 350 μm, SCUBA at 450 μm, and ATLASGAL 870 μm) were convolved to a common limiting beam size (SPIRE 350 μm) and converted to uniform units (Jy/arcsec^2).

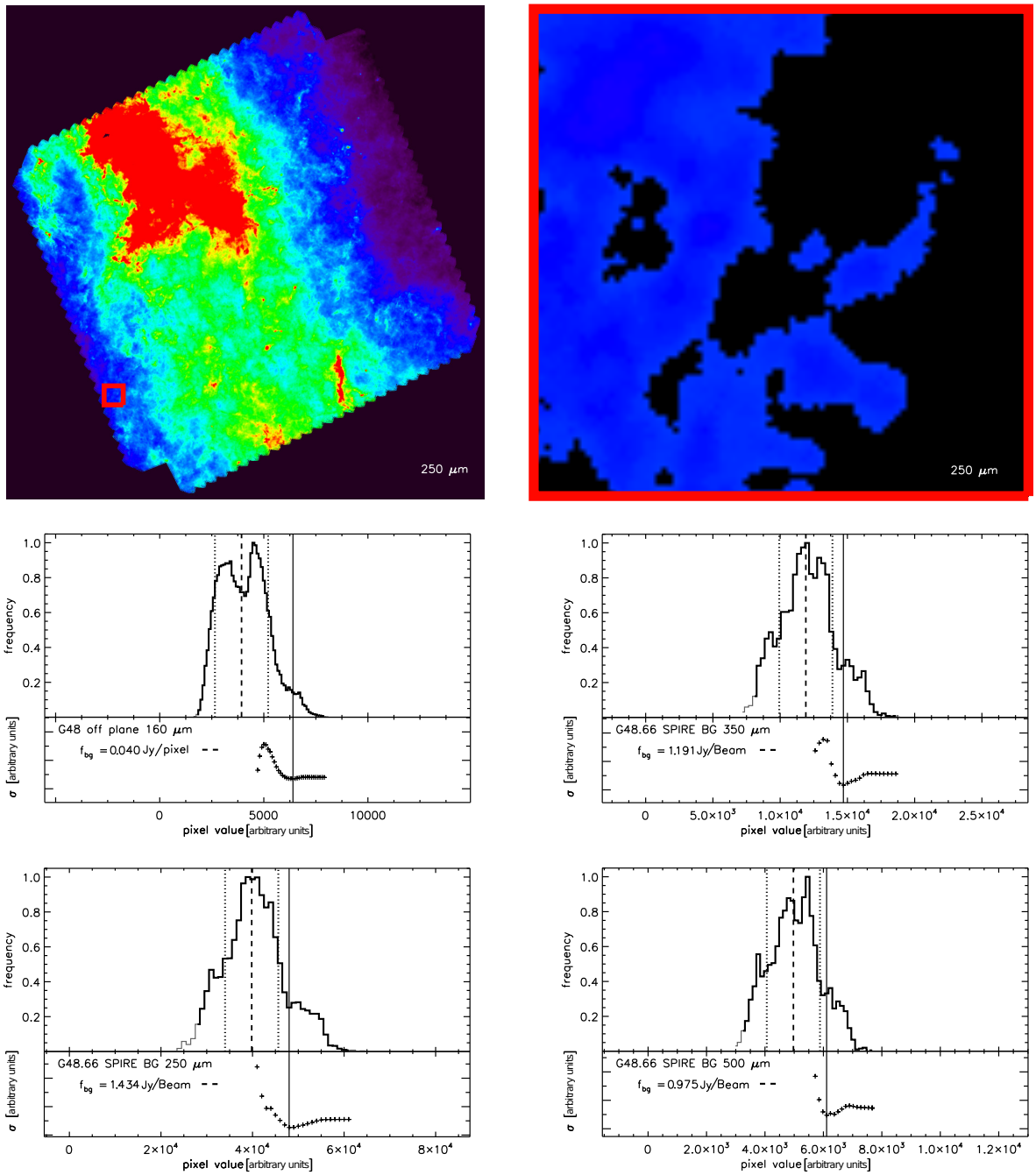

Figure 4.5. – The upper left panel shows the imprint of the Galactic plane in the SPIRE 250 μm band. The red box encircles the region for the background estimate (coordinates given in the text). The upper right panel shows this background region after removing the non-Gaussian contributions from the 250 μm map. The middle and bottom plots present the results of the background fitting for the different Hi-GAL bands. In the histograms the best-fit mean pixel flux is indicated by th dashed line, while the dotted line indicates the bist-fit σ. The flux bin with the minimum σ value is flagged by the solid line; all bins with higher fluxes contain significant non-Gaussian contributions. The numbers in the plots indicate the computed background and σ values. Even tough, the SPIRE 500 μm map is not used in the convolution and SED-fitting the result from the background-fitting is given anyway.

3. In the final fitting process an SED was fitted to each pixel using a modified black body function, requiring at minimum three data points for the SED.

For the final pixel-to-pixel SED fitting a careful preparation of the initial data is needed. A complete description of the data treatment and fitting process is given in Launhardt et al. (in prep.). The observed globules in Launhardt et al. (in prep.) are more isolated and suitable background flux offsets can be calculated within the EPoS maps. Unfortunately, the larger extent of the IRDC, the imprint of the adjacent GMC and infra-red bubble (see Section 4.3.1), and the limited map sizes prevent a reasonable background determination. To overcome these limitations I utilized Herschel maps from the Hi-GAL program which cover a much larger area. I extracted the background fluxes from a low-emission region off the galactic plane located at $19^{\rm h}23^{\rm m}26^{\rm s}.018$ $+12^\circ37'28''.06$ (J2000) with a box size of $500''$ [3].

The method used to extract the background fluxes on this field with adopted from Stutz et al. (2009). I apply an iterative Gaussian fitting algorithm to the pixel flux distribution in a selected region of a *Herschel* image. This approach assumes that the pixel values distribution (namely the noise) is approximately Gaussian. However, the high flux tail of the pixel flux histogram, which is dominated by point-sources and extended emission contributions is non–Gaussian and rejected from the analysis. Figure 4.5 presents the histogram of pixel flux values and the fitting results for the different wavelength bands. As an example, the the $250\,\mu{\rm m}$ is also shown in the top two panels.

The fitting procedure, aimed at minimizing the contribution of point sources and extended emission from my zero–flux–level estimate, is carried out as follows.

Starting from the maximum peak in the histogram, a Gaussian function is fitted, and at each one more adjacent higher flux bin is included. For every iteration the standard derivation σ_i from the best fit is stored and shown in the lower panel of Figure 4.5. The solid line indicates the minimum σ; I adopt the mean value of the Gaussian best-fit that corresponds to this minimum value of σ. This mean flux value should represent the ideal compromise between the including the maximum amount information (or bins) in the fit while still rejecting bins affected by sources. The bins containing source flux could potentially severely bias a simple mean flux value over a given region. In this way I attempt to estimate the zero level contribution of the flux to the images. The adopted mean value is overplotted as dashed line in Figure 4.5. This value is used as the global background estimate, purged from contributions of point-sources or compact emission. I note that this analysis is performed at the native resolution of each band in order to maximize the information contained in the flux histogram.

Finally background levels of 0.040 Jy/pixel and 1.434, 1.191 Jy/beam were computed for 160, 250 and $350\,\mu{\rm m}$, respectively.

Battersby et al. (2011) used a large scale Gaussian profile to remove the Galactic background from their observed Hi-GAL maps before the SED-fitting. Herschel temperature maps of a sub-region were created by Beuther et al. (2012) without any global background subtraction. For the lower temperature (< 25 K) both methods just differ by $1-2$ K (Henrik Beuther 2012, private communication). My maps appear to be more sensitive to the background determination (see Footnote 3 on page 92), however changing my estimated background level by $\pm 50\%$ does not have a significant impact on the derived temperatures.

For the SED fitting all Herschel maps (PACS $160\,\mu{\rm m}$, SPIRE 250 and $350\,\mu{\rm m}$) were convolved to the SPIRE $350\,\mu{\rm m}$ beam, using the kernels from Gordon et al. (2008). For the sub-millimeter

[3] I also determined the background offsets from a field with low spatial variations and almost no compact emission inside the galactic plane. But the resulting temperature maps from the SED fitting were suspiciously high (> 20 K inside the IRDC). Therefore, I decided to estimate the background offsets further outside of the galactic plane.

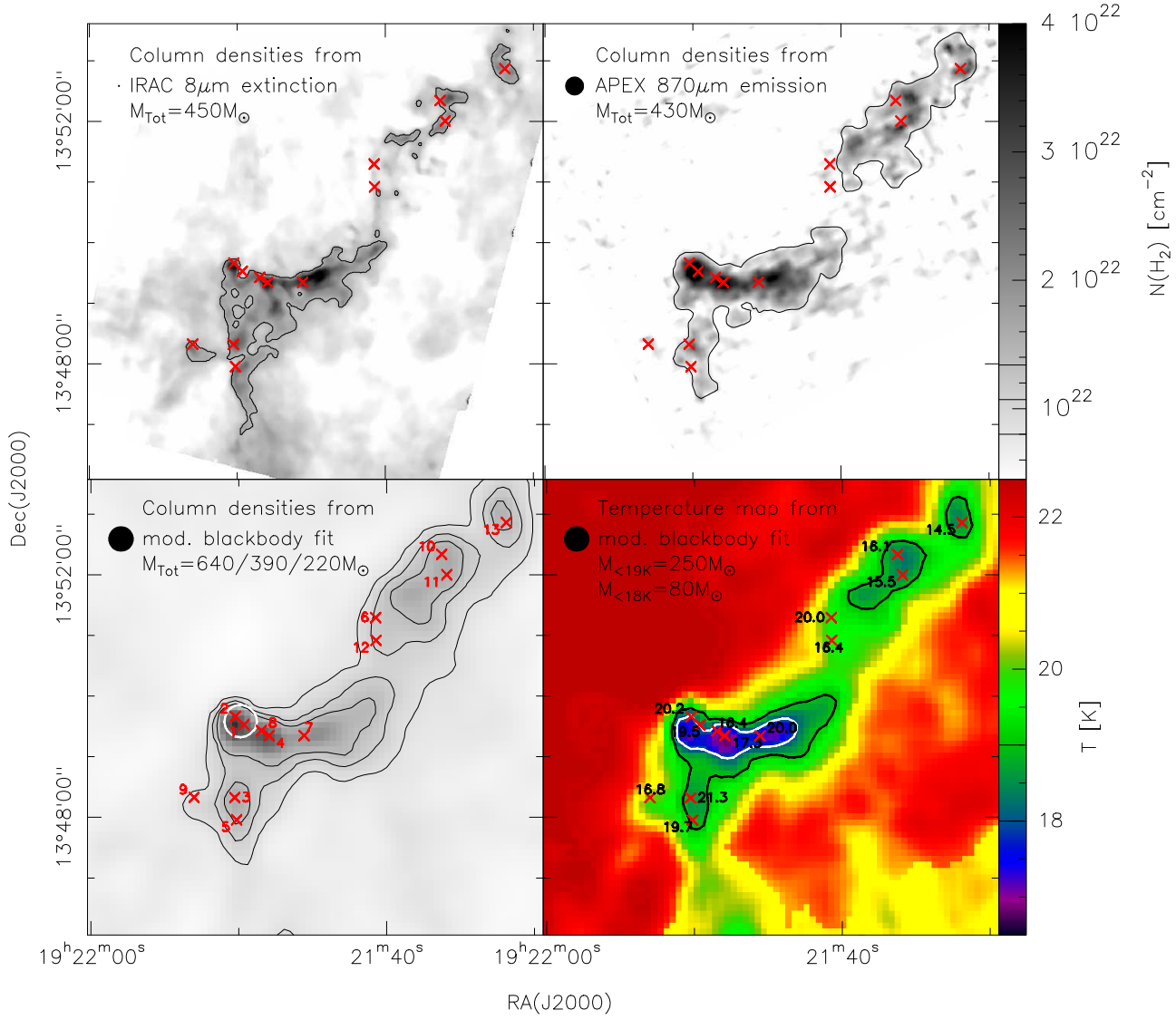

Figure 4.6. – The top two panels show H_2 column density maps obtained from IRAC 8 µm extinction (left) and ATLASGAL 870 µm (right) observations. In these top panels the column density thresholds for the mass determination are shown as contours: within the contour of $1.34 \cdot 10^{22}$ cm^{-2} a mass of 450 $M_\odot$ is enclosed for IRAC 8 µm while the $0.85 \cdot 10^{22}$ cm^{-2} ATLASGAL contours contain 430 $M_\odot$ of material. The bottom two panels show the column density (left) and temperature (right) maps from the modified black fitting (Section 4.3.2 and 4.3.3) of the Herschel, SCUBA and ATLASGal maps. The point sources from Section 4.3.4 are indicated by ×. The contours indicate column densities of $0.85 \cdot 10^{22}$, $1.10 \cdot 10^{22}$, and $1.34 \cdot 10^{22}$ cm^{-2} and encircle 640, 390, and 220 $M_\odot$ respectively. The white circle indicates the pointing and beam size of the CH_3C_2H observations, which indicates a gas temperature of 26 ± 7 K. The temperatures from the point source fitting are indicated in the last plot. This temperature map is overplotted with isothermal contours of 19 K (black) and 18 K (white). These isotherms incorporate 250 $M_\odot$ and 80 $M_\odot$ for 19 K and 18 K, respectively.

maps (SCUBA $450\,\mu\mathrm{m}$ and APEX $870\,\mu\mathrm{m}$) a Gaussian kernel was used. For this step all maps were calibrated in units of Jy/arcsec^2.

In the resulting maps the remaining emission per pixel is assumed to be well represented by modified blackbody emission:

$$S_\nu(\nu) = \Omega\big(1 - e^{-\tau(\nu)}\big) B_\nu(\nu, T_\mathrm{d}) \tag{4.2}$$

with

$$\tau(\nu) = N_\mathrm{H}\, m_\mathrm{H}\, R\, \kappa(\nu) \tag{4.3}$$

where $S_\nu(\nu)$ is the observed flux density for a given frequency ν and solid angle Ω (all fluxes are normalized to 1 Jy/arcsec^2, $\tau(\nu)$ is the optical depth, $B_\nu(\nu, T_\mathrm{d})$ the Planck function, T_d the dust temperature, m_H the proton mass, R the dust-to-gas mass ratio, and $N_H = 2 \cdot N(\mathrm{H_2}) + N(\mathrm{H})$ the total hydrogen column density. For the column density map (Figure 4.6, bottom left) I assume that all hydrogen is present as molecular gas in G48. For the dust opacity κ I adopt the model from Ossenkopf & Henning (1994) for thin ice mantels and a gas density of 10^5 cm^{-3}. For the hydrogen-to-dust mass ratio I adopted a value of $R = 110$ (e.g., Sodroski et al. 1997). To account for helium and heavy elements one would choose the total gas-to-dust mass ratio 1.36 times higher. A modified black body function, as in Equation 4.2 was fitted individually for each pixel using N_H and T_d as free parameters with a χ^2-minimization. The Hi-GAL data includes only the 70 and $160\,\mu\mathrm{m}$ maps for the PACS bands. To avoid contributions from stochastically heated small grains I exclude the $70\,\mu\mathrm{m}$ band (Pavlyuchenkov et al. 2012). Usually the fluxes in the three remaining Herschel bands are well constrained and provide a good fit to the modified black body function. To avoid erroneous SED fitting, only pixels with valid fluxes in at least these 3 Herschel bands were included.

The temperature map (Figure 4.6, bottom right) shows a steep drop at the boundaries of G48 within the resolution limits set by the size of the convolution kernels (a 19 K contour is overplotted on the IRAC map at $8\,\mu\mathrm{m}$ and PACS at $100\,\mu\mathrm{m}$ in Figure 4.2). In the central region of G48, with the strongest sub-millimeter emission, the temperatures drop below 18 K (white contour in Figure 4.6, bottom right). The local minima agree with the position of the sub-millimeter peaks P1 (17.1 K), P2 (16.8 K), and EP (17.1 K). In general the temperatures which are observed here are higher than the ones (10-15 K) found by Ormel et al. (2005) for P1, P2, and EP. The upper limit on the temperature uncertainties is 0.3 K inside the IRDC, where dust emission is detected in the ATLASGAL maps. The uncertainties where derived by altering the subtracted global background level by $\pm 50\%$, forcing the fitter to run with or without local background estimates and using different beam sizes for the convolution. It should be mentioned that the temperatures outside G48 are not very reliable because of the brightness gradient introduced by W51 and N100, as mentioned earlier. In the column density and temperature maps (Figure 4.6) the point source positions and temperatures are indicated.

The temperatures derived at the locations of the point sources in the large–scale temperature map are discrepant from the temperatures derived by fitting the individual SEDs of said point-sources, the later of which were extracted at native resolution. This discrepancy is not surprising as it is caused by beam convolution in the temperature map and the inclusion of longer wavelengths.

4.3.3. Column densities

To estimate the column densities for G48 I utilized three different methods; mid-infrared extinction map from IRAC at $8\,\mu\mathrm{m}$, sub-millimeter dust emission and modified blackbody fitting including Herschel and sub-millimeter data (see Section 4.3.2).

The IRAC $8\,\mu\mathrm{m}$ extinction maps provides an estimate of the optical depth per pixel (see Section

4.2.2). These optical depths were converted into column densities (Figure 4.6, bottom left) using:

$$N_{\mathrm{H_2}} = 1.086\ \tau / C_{ext} \tag{4.4}$$

Where τ is the optical depth per pixel and C_{ext} is the extinction cross-section. The nature of the mid-infrared extinction law below $10\,\mu\mathrm{m}$ in IRDCs and massive star-forming regions is still a matter of debate (e.g., Butler & Tan 2009). In agreement with findings of Indebetouw et al. (2005) I used an extinction factor of $R_V = 5.5$ to parametrize the extinction cross-section C_{ext}. I choose $C_{ext} = 4.62 \cdot 10^{-23}\,\mathrm{cm}^2$ from Weingartner & Draine (2001, (case B)). The derived column densities also depend on the assumed R_V value and, therefore, the used extinction cross-section. The extinction factor $R_V = 3.1$ is more representative of the diffuse ISM and would result in significantly higher column densities. Another effect for the $8\,\mu\mathrm{m}$ extinction is the saturation of the column density for high values, therefore the masses based on IRAC $8\,\mu\mathrm{m}$ discussed further below can only be lower limits (for a detailed discussion, see Vasyunina et al. 2009).

The second method to determine the hydrogen column densities utilizes the dust emission detected in the $870\,\mu\mathrm{m}$ map from ATLASGAL:

$$N_{\mathrm{H_2}} = \frac{R F_\nu}{B_\nu(\nu, T_d) m_{\mathrm{H_2}} \kappa\, \Omega} \tag{4.5}$$

where F_ν is the sub-millimeter flux, $R = 110$ the gas-to-dust ratio, $B_\nu(\nu, T_d)$ the Planck function for a given wavelength ($870\,\mu\mathrm{m}$) and dust temperature ($T_d = 17.3\,\mathrm{K}$ or $19.2\,\mathrm{K}$, see below), $m_{\mathrm{H_2}}$ the mass per hydrogen molecule, and Ω the beam size. I adopt a mass absorption coefficient of $\kappa = 1.47\,\mathrm{cm^2 g^{-1}}$ from Ossenkopf & Henning (1994, thin ice mantel, $10^5\,\mathrm{cm}^{-3}$, as in Section 4.3.2).

I have three independently derived column density maps: IRAC $8\,\mu\mathrm{m}$, ATLASGAL $870\,\mu\mathrm{m}$, and the SED fitted map combining Herschel and ATLASGAL. Each one requires to make different and independent assumptions in order to derive column densities; furthermore, they also vary widely in angular resolution.

For example, the $8\,\mu\mathrm{m}$ extinction map, which has a resolution of $\sim 3''$, requires an assumption of a certain extinction factor for the dust extinction cross-section, optically thin emission and the local background contribution (I_{BG} in Equation 4.1), but is temperature independent. Furthermore for bright IRAC point-sources with compact background emission the residuals of the PSF removal can result in an underestimate of local column density (see e.g., source 1 in Figure 4.6, top left).

For the ATLASGAL $870\,\mu\mathrm{m}$ map, with a resolution of $\sim 19''$, always a fixed temperature is assumed, it requires optically thin emission and a dust opacity at the wavelength of interest.

While the SED-fitted map also requires a dust model assumption, it contains information from multiple wavelengths and simultaneously derives $N_{\mathrm{H_2}}$ and temperature for each pixel, under the assumption that the mass is well-represented by a modified black body and assuming a fixed spectral index β. Therefore the derived column densities can be considered more robust compared to the two previous methods. However, the SED-fitted map also has the lowest resolution of the three methods considered here, with final convolved beam size of $25''$, equivalent to $\sim 0.3\,\mathrm{pc}$ at the distance of G48. Here I discuss the integrated masses for these three independent methods.

The total mass of G48 can be calculated within a contour of interest using the column densities mask (shown in Figure 4.6):

$$M = \sum_i a_{\mathrm{px}}\ m_{\mathrm{H_2}}\ N_i(\mathrm{H_2}) \tag{4.6}$$

where a_{px} is the pixel area, $m_{\rm H_2}$ and $N_i({\rm H_2})$ the column density per pixel.

The masking contours for the IRAC extinction map were chosen by visual inspection. This contour results in a threshold of 32.15 MJy/sr, which correspond to a column density of $1.34 \cdot 10^{22}\,{\rm cm^{-2}}$. A total H_2 mass of $450\,{\rm M_\odot}$ is enclosed in these contours (see Figure 4.6, top left panel).

I assume a temperature of 17.3 K (the median point source temperature, see Section 4.3.4) for the ATLASGAL derived column density map (Figure 4.6; top right panel). The column density threshold is adopted to be at 3×the RMS noise level (~ 50 mJy/beam), corresponding to $N(H_2) = 0.85 \cdot 10^{22}\,{\rm cm^{-2}}$. The resulting total mass inside this column density contour is M($H_2 = 430\,{\rm M_\odot}$. For comparison, the median *Herschel* derived temperature (Figure 4.6;bottom right panel) in this same region is 19.2 K. If I adopt this temperature instead of 17.3 K, as assumed above, the column density threshold becomes $N(H_2) = 0.75 \cdot 10^{22}\,{\rm cm^{-2}}$ and the total enclosed ATLASGAL mass is $M(H_2) = 675\,{\rm M_\odot}$.

For reference, applying a column density threshold of $1.34 \cdot 10^{22}\,{\rm cm^{-2}}$ (derived from the from IRAC 8 μm column density map) is equivalent to applying a 18 K isotherm to the *Herschel* derived column density map, and results in thresholds that encompass approximately the same spatial extent of the three SCUBA peaks from Ormel et al. (2005). The mass enclosed within these thresholds differ by only $20 - 30\%$ compared to the total mass ($320\,{\rm M_\odot}$) of these three peaks.

The total mass for G48 derived from the $8\,\mu{\rm m}$ extinction ($450\,{\rm M_\odot}$) and the $870\,\mu{\rm m}$ ($430\,{\rm M_\odot}$) emission are remarkably similar. Furthermore, the average column density threshold for both maps corresponds to a Herschel derived total mass of $M(H_2)$ =390 ${\rm M_\odot}$), also in excellent agreement with the other estimates. Considering the uncertainties in the various assumptions, such as the dust properties, uncertainties in background flux levels, and variations in beam sizes I find that the mass agreement for G48 is strikingly good across different methods and compared to previous work.

In general the column density for the diffuse emission in G48 is comparable for all three methods. For EP, P1, P2, P3 and P4 the peak column densities agree within 18% for the ATLASGAL and the Herschel maps. However, the peak column densities derived from the $8\,\mu{\rm m}$ extinction are significantly higher then the fitted Herschel maps. The peak columns can be higher up to 75%.

Table 4.2. – Point sources

Source	R.A. (J2000)	Dec (J2000)	$F_{24\mu m}$ [mJy]	$F_{70\mu m}$ [mJy]	$F_{100\mu m}$ [mJy]	$F_{160\mu m}$ [mJy]	T_L K	L_L $L_\odot$	M_L $M_\odot$	L_H $L_\odot$	Comments[a]
1	$19^h21^m49^s.65$	+13°49′31.″26	102.7	1764	4086	6931	18.3	48.2	14.3	36.1	S5, P1
2	$19^h21^m50^s.24$	+13°49′39.″28	241.1	3702	6931	10712	17.9	35.5	11.9	38.0	S6, P1
3	$19^h21^m50^s.26$	+13°48′18.″96	119.5	1730	3659	4745	20.9	17.7	2.4	14.6	S2, P3
4	$19^h21^m47^s.95$	+13°49′20.″37	2.8	460	1807	4717	17.2	15.1	6.3	2.8	S15, P2
5	$19^h21^m50^s.13$	+13°47′57.″00	27.7	474	902	1474	19.8	5.5	1.0	4.5	S1
6	$19^h21^m40^s.76$	+13°51′17.″42	102.7	365	494	693	16.8	2.4	1.2	6.5	
7	$19^h21^m45^s.58$	+13°49′20.″51	8.7	299	842	1370	19.5	4.8	1.0	1.7	S12, EP
8	$19^h21^m48^s.48$	+13°49′25.″26	-	210	865	4668	17.4	13.3	5.3	-	P2
9	$19^h21^m53^s.01$	+13°48′19.″15	34.7	139	174	357	16.5	1.1	0.6	2.8	S3
10	$19^h21^m36^s.30$	+13°52′20.″23	31.8	132	780	2209	16.8	7.9	3.8	1.6	S11
11	$19^h21^m35^s.95$	+13°51′59.″97	115.5	121	177	521	15.6	1.7	1.3	4.4	S9
12	$19^h21^m40^s.73$	+13°50′54.″91	20.2	115	303	894	15.6	3.2	2.4	1.5	S13
13	$19^h21^m31^s.93$	+13°52′51.″82	4.6	61	131	516	14.5	1.7	1.9	1.0	

[a] Sx are the associated MIPS $24\,\mu{\rm m}$ from van der Wiel & Shipman (2008), Px and EP are the associated sub-millimeter peaks.

4.3.4. Point source Classification

In Table 4.2 I present the fluxes of the 13 point sources which were detected in all three PACS bands. Except for source 8, all PACS detections have counterparts in MIPS $24\,\mu\mathrm{m}$. Source 13 was not included in the van der Wiel & Shipman (2008) sample, but is detected as a point source at $24\,\mu\mathrm{m}$ (E2 in Figure 4.2). If one would allow point source detection in only two PACS bands this would add only one more obvious point source. This source is also detected at $24\,\mu\mathrm{m}$ (E1), but at $100\,\mu\mathrm{m}$ the source appears only as a compact and diffuse emission blob. The observational results are to vague to trace down possible sources as, e.g., line contamination, for this bluring. However the distance to Source 13 (E2) is $\sim$ 0.24 pc which is close to the median separation discussed in Section 4.4, and therefore would not change the outcome of this discussion. All detected sources are aligned along the mid-infrared filaments of the IRDC. Even though the emission gradient towards the GMC (on the eastern edge of my maps) is brighter and contains some compact emission features, no PACS point sources are detected outside the IRDC filaments.

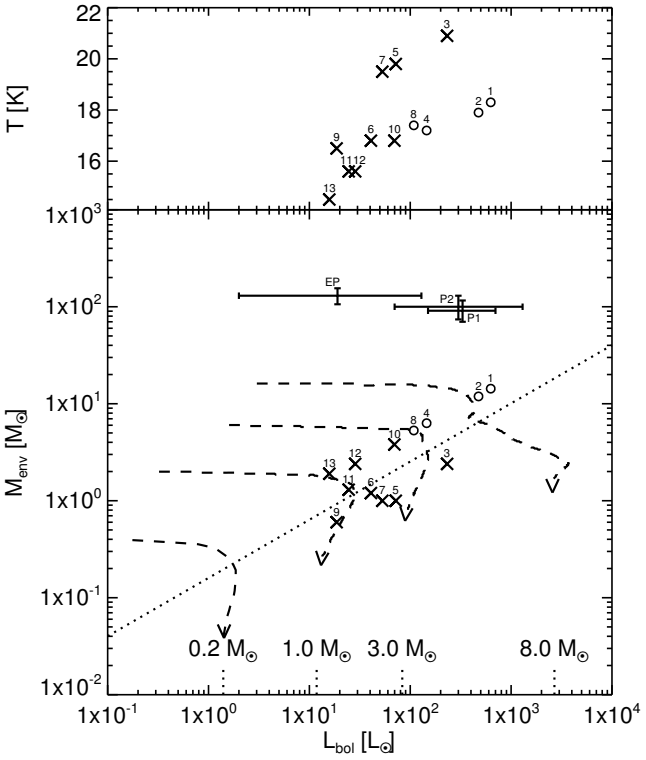

Figure 4.7. – The core temperatures (upper panel) and cold envelope mass (lower panel) are plotted against bolometric luminosities.Bolometric luminosities are derived from IRAC, MIPS and PACS bands. The numbers identify the point sources characterized in Section 4.3.4. The dashed lines represent the evolutionary tracks for YSO from André et al. (2008). The finale stellar masses (ZAMS) of those tracks are given above the lower axis.

As in Section 4.3.2, I used a modified blackbody function to constrain the parameters of these point sources (Figure 4.8), utilizing the dust model by Ossenkopf & Henning (1994, thin ice mantles, $10^5\,\mathrm{cm}^{-3}$). The sources detected at $24\,\mu\mathrm{m}$ cannot be fitted by a single component fit, since the warmer part of the envelope in the direct vicinity of the evolving protostar is contributing significantly to the $24\,\mu\mathrm{m}$ fluxes. Due to the rapidly increasing optical depth towards the innermost regions around the point-sources one only observes surface contributions of surrounding layers of warm dust. The calculations of mass and temperature assume optically thin material.

The $24\,\mu\mathrm{m}$ data are highly sensitive to geometric effects in protostellar cores (see Dunham et al. 2008; Ragan et al. 2012). A proto-star in which outflows have carved a cavity in its natal core will be detectable at $24\,\mu\mathrm{m}$ if the line of sight is aligned with the cavity. In particular the shocked molecular hydrogen, visible as green structures in Figure 4.1 (right, bottom panel), traces high velocity outflows. They originate from the rotational S9-S11 transition of excited H_2 in the IRAC $4.5\,\mu\mathrm{m}$ band. They are generally referred to as either "green and fuzzy features" (Cyganowski et al. 2008) or "extended green objects" (EGOs, Chambers et al. 2009). Because the $24\,\mu\mathrm{m}$ flux arises primarily from the warm material immediately surrounding the proto-star (and not the cold outer region of the core), I do not include the $24\,\mu\mathrm{m}$ flux in my SED fit to the PACS data but instead fit a second modified blackbody

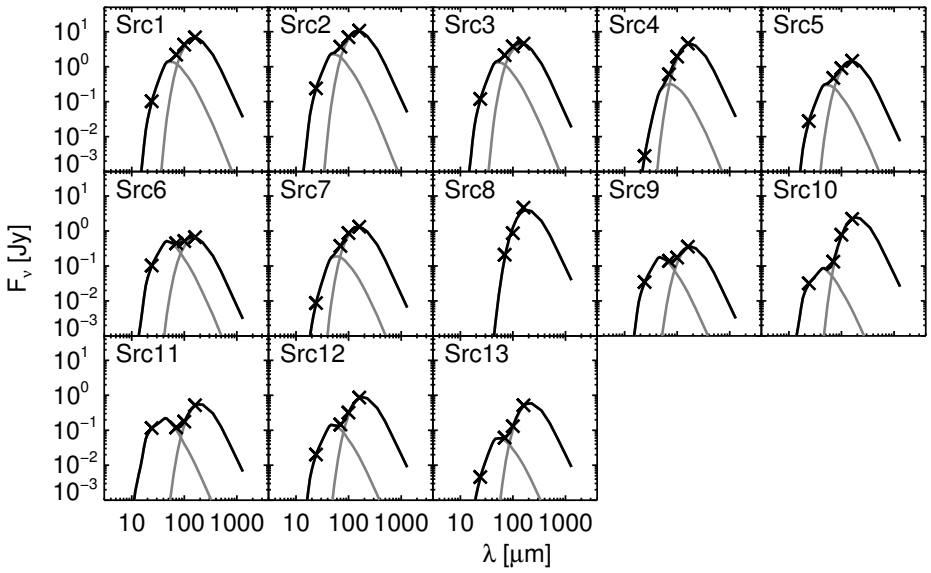

Figure 4.8. – The modified blackbody fits for the detected sources (see Section 4.3.4).

component (see Figure 4.8). The best fit to the SED results from the sum to these two components. For Source 8, I used one modified blackbody function. The fit parameters are presented in Table 4.2.

The four most massive sources in the sample are located in the central part of the IRDC in the direct vicinity of the sub-millimeter peaks P1 and P2. They cover a mass range from 5.4 to 14.3 $\mathrm{M}_{\odot}$. From these sources, Source 8, is the only PACS source without a MIPS $24\,\mu\mathrm{m}$ counterpart. Source 1 and 2 are the brightest and most massive sources in the sample. They are associated with the SCUBA peak P1 and have a close separation of $\sim 12''$. Source 1 appears on top of a compact and diffuse background emission complex. Only a faint source with $0.9\,\mathrm{M}_{\odot}$ is associated with the EP-SCUBA-peak of Ormel et al. (2005). The point sources associated to P3 in the southern part of G48 have only $\sim 1-2\,\mathrm{M}_{\odot}$.

In Figure 4.7 I present the bolometric luminosities (IRAC to PACS) and the envelope masses ($\lesssim 0.15\,\mathrm{pc}$) and the temperatures derived from cold components of the modified blackbody fits. In the luminosity-mass plot the dotted line follows the relation $M_{env} \sim L_{bol}^{0.6}$ and corresponds approximately to threshold, where 50% of the initial core mass being converted into stellar mass ($M_{\star}$). Sources with $M_{env} > M_{\star}$ and a high sub-millimeter to bolometric luminosities ratio $L_{\geq 350\mu m}/L_{bol} > 0.005$ are considered to be Class 0 (André et al. 2000). Source 1 and 2 as well as Source 4 and 8 are detected as single SPIRE sources. But the fitted blackbodies indicate that the sub-millimeter fluxes should be equal for both sources in each case. For each source I calculate the sub-millimeter luminosity $L_{\lambda \geq 350\mu m}$ with 50% of the corresponding SPIRE fluxes. All four sources mentioned before are good Class 0 candidates since $L_{\geq 350\mu m}/L_{bol} > 0.005$ and $M_{env} > M_{\star}$. Source 1 and 2 have the highest envelope masses, and, as indicated by evolutionary tracks (adopted from André et al. 2008), both can evolve into high-mass Zero Age Main Sequence stars (ZAMS) with $M_{ZAMS} \gtrsim 8\,\mathrm{M}_{\odot}$. Assuming these sources are in a very young evolutionary stage, they are completely dominated by the accretion luminosity (Krumholz et al. 2007).

Table 4.3. – Upper limits for non detected line species

Line	Line intensity [a] [kms^{-1}K]	Column density [10^{12} cm^{-1}]
CH_3C_2H	0.50	
$H^{13}CN$	0.53	3.8
$H^{13}CO^+$	0.52	0.7
SiO	0.51	1.2
C_2H	0.52	
HNCO	0.48	6.4
HCCCN	0.48	2.0
CH_3CN	0.50	2.9
^{13}CS	0.53	5.9

[a] Upper limits are the integrated intensity a Gaussian-shaped line with a FWHM of 1 kms^{-1} would have at an peak intensity level of three times the RMS noise.

Table 4.4. – Clumpfinder parameters

Molecule	lower threshold [a] %	step [a] %
N_2H^+	5.0	5.0
HCO^+	5.8	5.8
HCN	8.5	3.4
HNC	18.6	9.3
^{13}CO (1-0)	35.2	2.3
^{13}CO (2-1)	31.4	6.3
$C^{18}O$ (2-1)	8.8	5.5

[a] The minimum detection thresholds and the contrast steps for `clumpfinder` are give in relation to the peak value in the corresponding map.

4.3.5. Molecular Line Emission

To determine the parameters from the mapping line data, I used the GILDAS/CLASS [4] package. As mentioned before there are line detections (CL$> 99.73\%$) associated to the IRDC in the HCO^+, N_2H^+, HCN, HNC, ^{13}CO and C^{18}Omaps . While the line fitting for HCO^+, HNC and CO is done straightforward with a single Gaussian profile, N_2H^+ and HCN have a resolved hyperfine structure with multiple components. For N_2H^+ a model profile containing seven hyperfine-structure components was fitted utilizing the GILDAS/HSF routine. The presented N_2H^+ maps containing the integrated line flux, line width and velocity correspond the line center of the strongest component (93.17378 GHz , $J = 1 \rightarrow 0$, $(F_1F) = 2,3 \rightarrow (1,2)$). The hyperfine-structure of HCN shows a triplet of components, and in contrast to N_2H^+, the relative line strength of each component vary for different IRDCs (Afonso et al. 1998; Vasyunina et al. 2011). Given the noise level of the HCN map one could not retrieve an averaged profile. The fitting of the physical parameters is done on the strongest component.

The derived integrated line fluxes, velocities and line widths are compiled in Table 4.5. This Table gives also the effective radius (see below), the total column density, the abundance and the traced mass. HCO^+ and HCN are good tracers for dense gas because of their high critical densities. N_2H^+ has a lower critical density (see Table 4.1), but is not strongly effected by depletion from freeze-outs on grain surfaces. For CO the critical density is, depending on the transition, one or two orders of magnitudes lower, than for N_2H^+. The total column density for a certain molecular species can be calculated with

$$N_u = \frac{8\pi A_{ul} k \nu^2}{hc^3} \int T_{mb} dv \tag{4.7}$$

$$N_{tot} = \frac{N_u Q_{rot}(T)}{g_u} \exp(-E_u/T) \tag{4.8}$$

where A_{ul} is the Einstein coefficient, ν the rest frequency of the transition, N_u and E_u the upper state column density and energy, Q_{rot} the rotational partition function and g_u the statistical weight of

[4] `http://www.iram.fr/IRAMFR/GILDAS/`

the upper level. The general physical parameters[5] for the observed lines are given in Table 4.1. The abundance for a molecule is given in relation to the H_2 column density derived from the SED-fitted map from Section 4.3.2. To calculate the abundances for the different molecular species I used a median temperature estimate of 17.3 ± 0.6 K. This is the average temperature derived from the cold component for all point sources in G48 (see Section 4.3.4). For the molecular line maps without any 3σ detection the upper limits for line intensity and column density, based on the noise estimates, are given in Table 4.3.

Following Ragan et al. (2006) the mass of each clump observed in the line maps is estimated using an assumed distance of 2.6 kpc, an approximate size based on the extent of molecular emission, the molecular column densities, and approximate abundance calculated at the peak of absorption.

In Figure 4.4 the SPIRE 250 μm images are shown and overplotted by the different line intensity maps. I used the `clumpfind` (Williams et al. 1994) package to identify the different clumps in the molecular tracers. Four different clumps were found by clumpfinder, hereafter named C1-C4. The detection parameters for `clumpfinder` are given in Table 4.4. C1, C2 and C3 are detected in HCO^+, HCN and N_2H^+. An additional clump C4 is detected in HCN. In the ^{13}CO (1-0) GRS map only C1 is detected. While C1 and C2 are detected in the HERA CO (2-1) maps and in HNC. Because `clumpfind` does not make any assumption about the clump morphology an effective circular radius

$$R_{eff} = \sqrt{A/\pi} \tag{4.9}$$

is given in Table 4.5, where A is the area fitted by `clumpfind`. Because the resolution of the HERA observations is three times better than MOPRA, the emission is less diluted and I therefore derive smaller R_{eff}. All line maps show the strongest emission in the central part of the IRDC. The maps HCO^+, N_2H^+, HNC, and ^{13}CO show an elongated structure in east-western orientation. HCN shows two distinct peaks (C1, C4); these peaks are shifted by $\sim 30''$ south-west of the compact SPIRE emission. All other MOPRA molecular tracers peak at C1, and while the maps appear shifted from the compact SPIRE emission, it is within the pointing error of MOPRA. The peak positions for the HERA CO maps are much better aligned with the SPIRE peaks. In contrast to the observed HCO^+ (1-0) emission, the HCO^+ (3-2) observation from Ormel et al. (2005) show multiple emission peaks. Their eastern emission peak is centered on the SCUBA clump, but the western emission is more diffuse. With the given spatial resolution of MOPRA ($38''$) it is likely that one only observes a single integrated emission peak for HCO^+ from these multiple unresolved emitting sources.

About $1\farcm3$ southwards of the central region another fainter emission peak (C2) can be found for HCO^+, HCN, HNC, N_2H^+, ^{13}CO(2-1) and C^{18}O. It is not coincident with the compact SPIRE and sub-millimeter emission in this region. In the integrated line flux map for ^{13}CO(1-0), no compact emission clump was found by `clumpfind`. The emission appears just as a diffuse extended lobe from the central peak. In the north-western part of the IRDC, where only diffuse emission appears in the SPIRE and sub-millimeter regime, the line data are much more noisy. For HCO^+, HCN and N_2H^+ a compact emission peak (C3) can be identified, while ^{13}CO shows a elongated diffuse emission lobe.

The three SCUBA clumps modeled by Ormel et al. (2005) incorporate a mass reservoir of $\sim 320\,M_\odot$. The masses derived for this region from the HCO^+, HCN, HNC, N_2H^+ and ^{13}CO observations differ by up to 20%. Given the uncertainties for the mass estimates, this is a good agreement.

[5] The parameters can be obtained from the Leiden Atomic and Molecular Database (LAMBDA). `http://www.strw.leidenuniv.nl/~moldata/`

CH_3C_2H is a good temperature probe in dense molecular clouds (e.g., Bergin et al. 1994). Four CH_3CCH transitions are detected: $J = (9-8)$, $K = 0, 1, 2, 3$, measured line integral intensities, calculated column densities for every particular transition using formulae 1-2 from Bergin et al. (2004). Finally the excitation diagram was computed and the excitation temperature and column density in the region were estimated. The resulting temperature is 26 ± 7 K and the column density $(3.0 \pm 1.5) \cdot 10^{12}$ cm^{-2}. All necessary values, like E_u - the upper state energy, g_u - degeneracy and others, were taken from the CDMS data base (Müller et al. 2001)

In Figure 4.9 (bottom panel) the position-velocity (p-v) plots are shown for ^{13}CO and C^{18}O (2-1). In the p-v plot for C^{18}O only a single velocity component is present. For ^{13}CO two components are present at a 50″ offset, which refers to the spatial position of the Source 1 in the PACS points-source catalog and the sub-millimeter peak P1. Due to the small spread of just $\sim 1.5\,\mathrm{kms}^{-1}$ it is questionable that this structure originates from an outflow cone. Other possible explanations could be a large rotational envelope or just two core-like dense CO structures along the line-of-sight. With the lack of additional observations with higher sensitivity and spatial resolution, no robust conclusions can be drawn.

With the isotopic abundance ratios of $[^{12}\mathrm{C}]/[^{13}\mathrm{C}] = 60$ and $[^{16}\mathrm{O}]/[^{18}\mathrm{O}] = 500$ the HERA ^{13}CO and C^{18}O abundances correspond to ^{12}C^{16}O abundances of $\sim 1 - 1.5 \cdot 10^{-5}$. The expected CO abundance at a given Galactocentric distance[6] (D_{GC}) can be computed from the following relationship (Fontani et al. 2012, and ref. within):

$$X^{\mathrm{E}}_{\mathrm{C^{16}O}} = 8.5 \cdot 10^{-5} \exp(1.105 - 0.13 D_{\mathrm{GC}}/D_{\mathrm{kpc}}) \tag{4.10}$$

For G48 with $D_{\mathrm{GC}} = 7.1$ kpc this results in an expected CO abundance of $X^{E}_{\mathrm{C^{16}O}} = 1.0 \cdot 10^{-5}$ thus consequently $X^{\mathrm{E}}_{\mathrm{C^{18}O}} = 2.0 \cdot 10^{-7}$ and $X^{\mathrm{E}}_{^{13}\mathrm{CO}} = 1.7 \cdot 10^{-6}$. Comparing this expected values with the observed CO abundances gives the depletion factor:

$$f_D = \frac{X^{\mathrm{E}}_{\mathrm{CO}}}{X^{\mathrm{obs}}_{\mathrm{CO}}} \tag{4.11}$$

Using the preceding isotopic abundance ratios results in average depletion factors of $f_D^{^{13}\mathrm{CO}} = 3.3$ and $f_D^{\mathrm{C^{18}O}} = 3.7$ for G48.

CO_2 ice is detected in the Spitzer spectra. In Figure 4.3 the Spitzer/IRS spectrum for Source 2 is shown. The observed shape of the CO_2 ice absorption feature at $15.2\,\mu\mathrm{m}$ is different for the source spectrum compared to the background spectra, therefore the temperature and the mixing ratio with other species (e.g., H_2O, CH_3OH) should be different (see, e.g., White et al. 2009). The low spectral resolution of the IRS/LL2 spectral order does not allow a proper fitting of temperature and mixing ratio to the laboratory data. Most likely the source CO_2 profile originates from ice coated grains in the dust envelope of the embedded proto-star. The presence of CO_2-ice does not provide direct evidence for CO freeze-out, since the conditions under which the surface conversion $\mathrm{CO + OH} \xrightarrow{\mathrm{surf}} \mathrm{CO_2 + H}$ takes place are still under debate (e.g., Garrod & Pauly 2011). In the gas-phase CO_2 is predominantly

[6] For this calculation the distance of the sun to the galactic center is assumed with 8.4 ± 0.6 kpc (Reid et al. 2009).

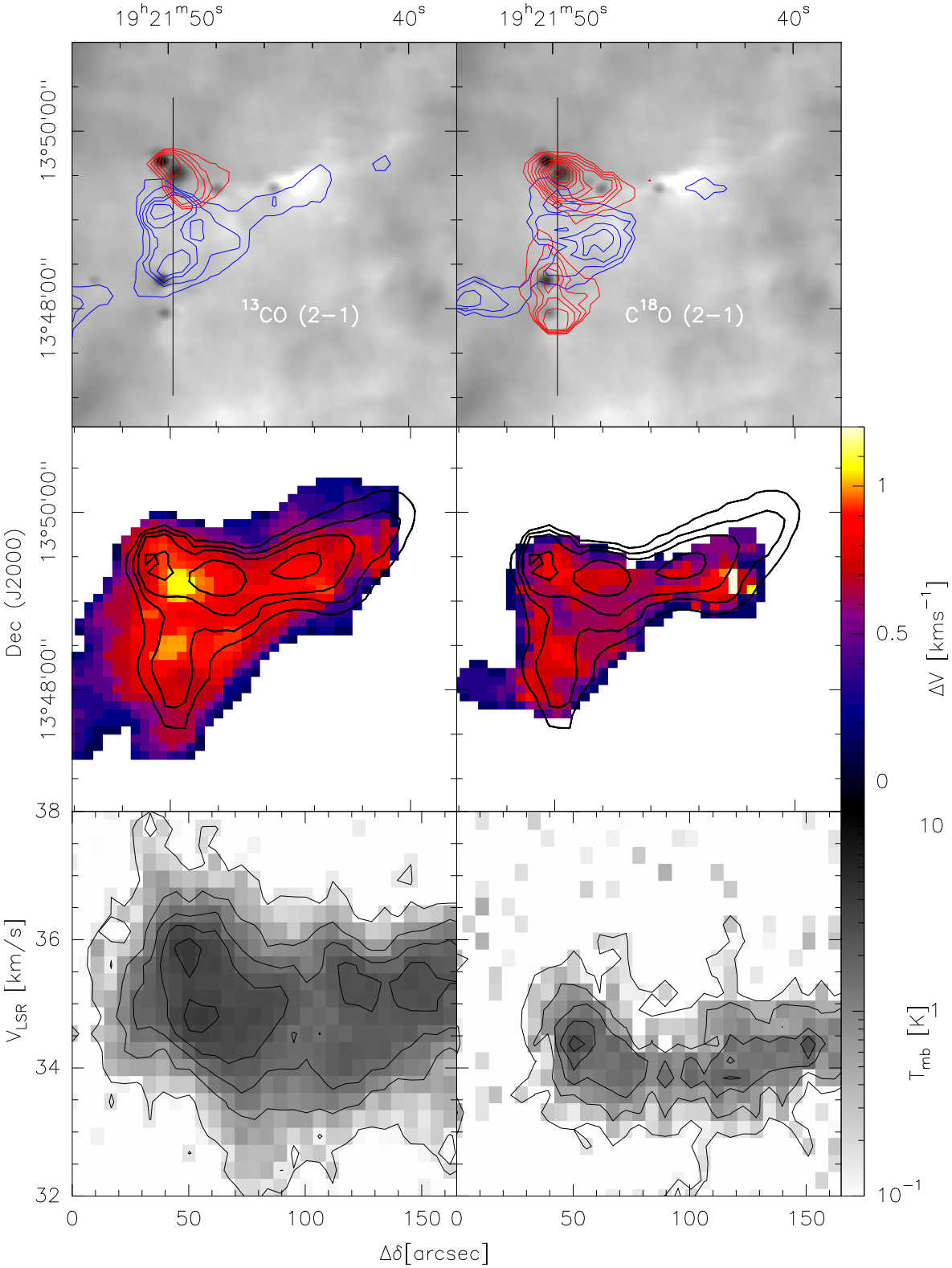

Figure 4.9. – In the top panel the contours of the line intensities for ^{13}CO (left) and C^{18}O (right) is plotted over the inversed PACS 70 µm image. For ^{13}CO (HERA) the blue contour is integrated between $30.0 - 34.0\,\mathrm{kms}^{-1}$ and the red contour between $36.0 - 40.0\,\mathrm{kms}^{-1}$. The integration in the C^{18}O HERA map is done over a more narrow range, due to higher noise level, with $32.0 - 33.5\,\mathrm{kms}^{-1}$ (blue) and $34.5 - 36.0\,\mathrm{kms}^{-1}$ (red).
The middle plot shows the linewidth for the HERA CO data. The overplotted contours are the isotherms of 17.5, 18.5, 19.0, and 19.5 K (see Figure 4.6).
The bottom plot shows the position-velocity diagram for ^{13}CO and C^{18}O. The spatial orientation of the p-v-plot is indicated in the top panels by a black vertical line.

produced by the following reaction

$$\mathrm{HCO} + \mathrm{O} \longrightarrow \mathrm{CO_2} + \mathrm{H}$$
$$\mathrm{CO} + \mathrm{OH} \longrightarrow \mathrm{CO_2} + \mathrm{H}$$
$$\mathrm{CO} + \mathrm{O} \longrightarrow \mathrm{CO_2} + \mathrm{H}$$

To the last two reactions an activation energy barrier of 80 K or higher is assigned (Garrod & Pauly 2011). Therefore, gaseous CO_2 creation becomes effective in cores which already have an internal heating source. The CO_2 ice cannot be easily hydrogenated on dust grain surfaces though, so it will remain a terminal species of the CO evolution in lukewarm regions (Dmitry Semenov 2012, private communication).

4.3.6. Distance

The LSR velocities found for the different clumps and molecular species do not differ by more than $3\,\sigma_V$. This results in a error weighted mean velocity of $\langle V_{LSR} \rangle = 33.91 \pm 0.05\,\mathrm{kms}^{-1}$. With this value I calculated a kinematic distances of 2.6 ± 0.6 kpc for G48 using the recent kinematic model from Reid et al. (2009). This distance is used for all calculations in this Chapter.

The Hi-GAL three color image (Figure 4.1) shows G48 at a close projected distance to the GMC W51 and several objects, as e.g., H II regions, infrared bubble and other bright point-sources. Water maser observation estimates a distance of ∼5.4 kpc for W51 (Sato et al. 2010). Known distances of infrared bubbles (Sarah Kendrew 2012, private communication) and sources from the RMS survey catalog (e.g., massive YSO, H II regions Urquhart et al. 2008) in the vicinity of G48 have a distance of more than 5 kpc. Moreover, no CO is detected in the global GRS maps outside of G48 at its typical LSR velocities.

I therefore conclude that G48 is an isolated region making it an unique IRDC.

4.4. Discussion

G48 is a quite isolated IRDC of a distance of 2.6 kpc. Consequently, G48 provides nonpareil observations of the collapse and fragmentation of a IRDC without the effects of external feedback, except for the diffuse ISRF.

I have derived line of sight averaged Herschel column density and temperature maps for this source, and find minimum temperature of 16.8 K, and outer temperatures of $\sim$ 23 K. The corresponding column densities range from $\sim 3 \cdot 10^{22}\,\mathrm{cm}^{-2}$ at in central part of G48 to $\sim 1 \cdot 10^{22}\,\mathrm{cm}^{-2}$ at the outer edges where the sensitivity drop sharply.

In this section I will discuss these results in combination with a wealth of other observations with the goal placing this unique source in an evolutionary context and determining its physical properties.

The comparison of the line data for G48.66 with other IRDCs show results for N_2H^+ which are similar to other IRDCs, while the HCO^+ results are different. The average line width of HCO^+ is $1.2\,\mathrm{kms}^{-1}$ which is significantly lower compared to other IRDCs. A typical value is $\sim 3.2{-}3.3\,\mathrm{kms}^{-1}$ (Vasyunina et al. 2011; Zhang et al. 2011). For N_2H^+ I observed an average line width of $1.8\,\mathrm{kms}^{-1}$. Similar mean line widths were observed for other IRDCs with $1.8\,\mathrm{kms}^{-1}$ by Vasyunina et al. (2009) and $2.0\,\mathrm{kms}^{-1}$ by Ragan et al. (2006). The mean column density of $2.4 \cdot 10^{12}\,\mathrm{cm}^{-2}$ for N_2H^+ in G48 is similar to the column density found for other IRDCs by Gibson et al. (2009). Comparing the amount of CO freeze out one finds that the depletion factor is strongly dependent on the chemical

age of the IRDC, hence the depletion varies drastically for different IRDCs. Hernandez et al. (2011) reports a depletion factor of 5 for G035.39.-0033 which is a young IRDC of $\gtrsim 7 \cdot 10^4$ yr similar to G48. In contrast Miettinen et al. (2011) found no depletion for their sample, and argued that this it is connected to a more evolved stage of their IRDCs where the increased star formation activity leads to sublimation of CO from the grain surfaces. Fontani et al. (2012) reports higher values of $f_D = 5 - 74$ for several southern IRDCs, the reason for this higher depletion factors is not completely clear, but might be explained by tracing denser regions of the cores by utilizing higher $C^{18}O$ (3-2) transitions, compared to my $C^{18}O$ (2-1) observations. In the gaseous inter clump medium N_2H^+ is destructed in the following reaction: $N_2H^+ + CO \longrightarrow HCO^+ + N_2$ (Bergin & Tafalla 2007). The presence of N_2H^+ is consistent with the low CO abundance induced by the freeze-out on the dust-grain surfaces.

By comparing their HCO^+ observations to clump-models Ormel et al. (2005) found an increase of turbulent motions towards the inner part of the clump. Their observations have higher resolution by a factor of two. Therefore, the observations in this work are not good enough to trace down turbulence in the same way, but the increasing MOPRA linewidths inwards of the clumps are in agreement with the findings of Ormel et al. (2005). The HERA CO data have a higher resolution than their observations, but due to the low critical density of CO one traces a larger column that might be dominated by envelope material also along the line of sight. Therefore, CO does not qualify as a good turbulence tracer.

To assess the dynamical state of the molecular clumps I calculate the virial mass, using the line width Δv:

$$M_{\rm virial} = k_2 R \Delta v^2 \tag{4.12}$$

whereas $k_2 = 126$ for a $n \sim 1/r^2$ profile (MacLaren et al. 1988) and R is the effective radius of the molecular clumps. I also calculated the virial parameter α which is given by the ratio between the kinetically energy $E_{\rm kin}$ and the potential energy $E_{\rm pot}$:

$$\alpha = \frac{2E_{\rm kin}}{E_{\rm pot}} = \frac{M_{\rm vir}}{M} \tag{4.13}$$

A value of $\alpha \lesssim 1$ represents a virial equilibrium, while $1 < \alpha < 2$ is present for pressure confined clumps (Bertoldi & McKee 1992), and $\alpha > 2$ indicates a gravitationally unbound clump. The virial mass and the virial parameter are presented in Table 4.5. Traced by multiple molecular species all clumps appear to be gravitationally bound. The wide spread of the derived virial parameters from the different molecular species make it difficult to distinguish between the different gravitational bound modes. However, the clumps C1 and C2 appear to be in virial equilibrium, with $\alpha_{\rm C1} = 0.4 \pm 0.3$ and $\alpha_{\rm C2} = 0.9 \pm 0.7$, but C3 seems to be off equilibrium just confined by the surface pressure.

In the central part of the IRDC a concentration of point sources is found. The projected median separation of PACS-point-sources is ~ 0.3 pc, which is approximately the average separation in the central part of G48. This separation is about three times smaller than in other IRDCs[7]. The median separation in the R1 fragment of the Coalsack dark cloud is even an order of magnitude higher compared to G48 (Beuther et al. 2011). The key question is how to explain these different values. One could assume that I just suffer from a projection effect in G48. Considering one sees an elongated filament and given the observed morphology it is a feasible assumption that G48 is aligned face-on towards the line-of-sight. Even if one would assume that G48 is aligned off by $\pi/4$ this would just

[7] The separation is about 0.9 pc for the IRDCs G011.11–0.12 (Henning 2010) and G049.40–0.01 (Kang et al. 2011); and 0.75 pc for G304.74–1.32 (Miettinen 2012).

account for a factor of $\sqrt{2}$. In contrast to G48 the mass reservoirs in the other sources is significantly higher and the other dark clouds do not share the isolated nature of G48. Even though the point source separation is not depending on the cloud mass (see Section 3.5.3), however, the external feedback can have a crucial impact on the fragmentation. Recent observation of G28.34+0.06 found a separation of just 0.16 pc (Wang et al. 2011). Interferometric data analyzed in this work found substructures on a ~ 0.01 pc scale inside the cores (~ 0.1 pc).

Given the wide spread of source separation it should be discussed if G48 exhibit the same mode of collapse as the IRDCs with larger separation or if some substantially different physical processes can account for the smaller separation. To address this question I compare the observational results to analytical considerations. A first simple analysis is to compare the source separation to the Jeans length. The separation in G48 is still several times larger than the thermal Jeans length ($\lambda_{\rm J} \approx 0.08\,{\rm pc}$ at $10^5\,{\rm cm}^{-3}$, 19 K). Therefore, a thermal Jeans instability is not the dominant fragmentation mode. Fragmentation below this spatial scale has been observed for several massive cores (e.g., Hennemann et al. 2009; Wang et al. 2011).

A first way to assess the spatial separation scale is to consider the collapse of a cylinder (with a radius R_c) of an incompressible fluid. It is predicted that several cores form, periodically placed at a characteristic length scale $\lambda_{\rm frag} = R_c$ (Chandrasekhar & Fermi 1953). For an infinite cylinder of isothermal self-gravitating gas the characteristic fragmentation scale is $\lambda_{\rm frag} = 22H$, where H is the isothermal scale height $H = c_s/(4\pi/G\rho_c)^{1/2}$ and c_s the thermal sound speed, G the gravitational constant and ρ_c the central density in the cylinder (Nagasawa 1987). When a isothermal cylinder with a given radius is embedded into a uniform medium the separation is $\lambda_{\rm frag} \approx 22H$ for $R \gg H$, but for the opposite case $R \ll H$ the length scale is again $\lambda_{\rm frag} \approx 11H$ (Jackson et al. 2010). Given the measured temperatures the typical thermal sound speed is $c_s = 0.23\,{\rm kms}^{-1}$ in G48. With $0.5 - 0.8$ pc the width of the filament is much larger than the scale height. The calculated length scale $\lambda_{\rm frag} = 22H \approx 0.3$ pc (with $n = 10^5\,{\rm cm}^{-3}$, $c_s = 0.23\,{\rm kms}^{-1}$) is the same as the measured separation in G48. However, $\lambda_{\rm frag}$ is affected by uncertainties, since the real value of the central density is unknown. Moreover, the most regular positioning of sources occur in the central part of the IRDC along a clearly changing temperature profile which is a distinct derivation from the isothermal assumption.

Another crucial parameter is the virial line mass. An isothermal, nonmagnetic, self-gravitating filament in the absence of external pressure is in hydrodynamical equilibrium as long as the mass per unit length does not exceed $m_{\rm vir} = 2\sigma^2/G$, where σ is the velocity dispersion in the gas. If the filament is only thermally supported the velocity dispersion is given by the thermal sound speed c_s (Ostriker 1964), while in the case of additional turbulence support the velocity dispersion is given by $\sigma = \Delta v/\sqrt{8\ln 2}$ (Fiege & Pudritz 2000), where Δv is the velocity dispersion. The critical line mass for a thermally supercritical filament in G48 is $M_{\rm line}^{\rm therm} = 24\,{\rm M}_\odot/{\rm pc}$, whereas the critical line mass calculated by the mean linewidth of G48, to account also for turbulent motions, is $M_{\rm line}^{\rm crit} = 71\,{\rm M}_\odot/{\rm pc}$. I straightened the filament of G48 utilizing a set of non-uniform cubic splines (Kocsis et al. 1991) and calculated the mass in each pixel, binning the pixels results in an average line mass of 174 $\rm M_\odot$/pc (see Figure 4.10). The observed line masses are ~ 2.5 larger than the critical line mass, indicating that the G48 filament does not contain enough internal support to counter the collapse while the contributions from magnetic fields are expected to be negligible (see below). Line masses observed for other IRDC seem to exceed $M_{\rm line}^{\rm therm}$. For strongly fragmented cores with significantly lower mass in Taurus line masses similar to $M_{\rm line}^{\rm therm}$, hence predominately thermal support, were observed (Schmalzl et al. 2010). In contrast to G48 several IRDCs show line masses below or similar to $M_{\rm line}^{\rm crit}$. This cannot be explained by the evolutionary stage of the IRDCs alone. The young and starless

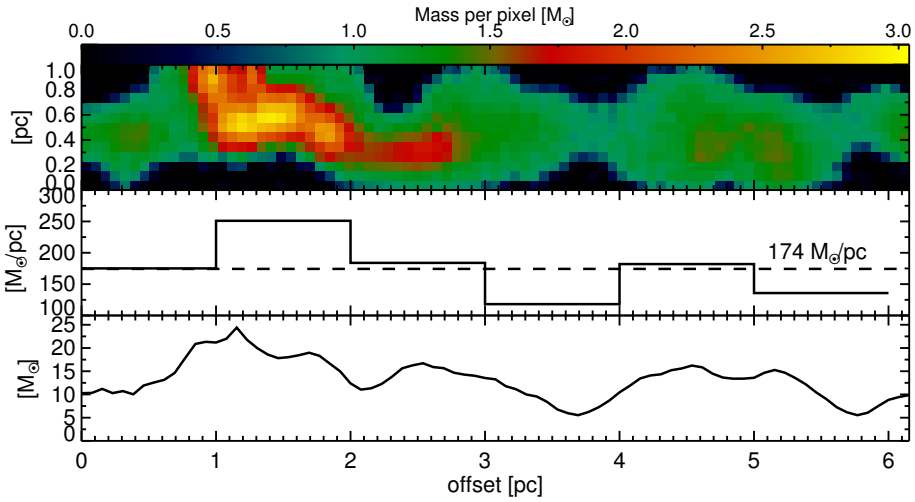

Figure 4.10. – Line masses of the straightened filament of G48 are presented. The upper panel shows the mass per pixel. In the lower plot presents the masses summed over the width of the filament (hence the column of the upper plot). In the middle plot the masses are binned to 1 pc. The average line mass for G48 is given by the dashed line.

Coalsack cloud and the adjacent G304.74+01.32 show line masses of less or equal to $M_{\rm line}^{\rm crit}$ (Beuther et al. 2011; Miettinen 2012, respectively). G48 and the Nessie IRDC are more evolved, showing signs of more active star formation such as "green and fuzzy" features, but the later region still shows line widths a factor 5 below the critical value for turbulence support (Jackson et al. 2010). Furthermore the presence of magnetic fields do not change the critical line mass significantly (Fiege & Pudritz 2000). However the higher line mass of 385 $M_\odot$ for the more evolved Orion A cloud (Jackson et al. 2010) supports the view increasing line masses along the evolutionary sequence.

The typical filament width seen in Figure 4.10 is $0.5 - 0.8$ pc. Peretto et al. (2012) and Arzoumanian et al. (2011) found typical filament widths of $0.08 - 0.1$ pc. This widths are a factor ~ 3 smaller compared to the SPIRE 350 μm. IRAC provides a much better resolution, but using the IRAC column density contours shown in Figure 4.6, results in an estimated filament width of $0.15 - 0.27$ pc. Arzoumanian et al. (2011) calculated the line mass for their filaments. All filaments have line mass below the average line mass for G48 and most of the filaments are in contrast to G48 below the critical thermal line mass. Also most of the filaments in the Pipe Nebula are thermally subcritical (Peretto et al. 2012). These results might indicate a trend of larger filament widths towards supercritcal filaments (with respect to turbulence).

Recent studies have shown that the temperature structure is non-isothermal. Preliminary results were shown by Peretto et al. (2010) for G030.49+0.96 using SED-fitting. The minima in their temperature maps are aligned with the column density peaks as in G48 the subsequent studies. The minimum temperatures for G030.49+0.96 are lower compared to G48 and the two following studies. The work of Battersby et al. (2011) and Beuther et al. (2012) show similar temperature ranges as for G48. While Battersby et al. (2011) provided a large scale temperature and column density map, Beuther et al. (2012) present a more detailed study of IRDC 18454 adjacent to the mini-starburst W43. In contrast to IRDC 18454, G48 provides a temperature map of an externally undisturbed filament with the better resolution of the convolution to the SPIRE 350 μm beam (as for G030.49+0.96, IRDC 18454 data were convolved to the SPIRE 500 μm beam). The low temperature in the central

parts for all of these IRDCs represent the very young age of this sources. Wilcock et al. (2012) used a different approach. They compared radiative transfer models with the observed embedded cores in IRDCs in the Spitzer and Herschel bands. They found core temperature profiles with minimum temperatures of $8 - 11\,\mathrm{K}$ which increase by $\sim 10 - 17\,\mathrm{K}$ towards the edge of the core. While my temperature mapping only observe an average line-of-sight temperature of the optically thin material, the RT model can retrieve temperature profiles along the line of sight. Since these profiles probing also the optically thick regime, the minimal temperatures are obviously lower. On the other hand, the RT models require an assumption about the geometry of the cores and cannot reassemble the diffuse temperature structure of the whole IRDC.

The temperature profile for G48 shows a drop towards the inner part of the detected sub-millimeter peaks. Theoretical considerations show that gas-phase coolants, as C^+ and CO, are efficient for low densities, while the energy transfer between gas and dust is the dominant cooling process for higher densities (Glover & Clark 2012). With the presence of IRAC and MIPS $24\,\mu\mathrm{m}$ point sources one would expect to see the imprint of this embedded heating sources in the temperature maps. The SPIRE $350\,\mu\mathrm{m}$ beam size limits the resolution of my temperature maps to $\sim 0.3\,pc$ so that the embedded heating sources remain unresolved. The dust temperature mapping as presented in this work can provide a versatile tool to test the predicted coupling between gas and dust. IRAM pointed observations of methylacetylene ($CH_3C{\equiv}CH$) of the peak position of the sub-millimeter peak P1 results in a gas temperature of $26 \pm 7\,\mathrm{K}$. Although this gas temperature is 7 K higher than the dust temperature the difference is not significant due to the high uncertainty in the gas temperature estimate. However the trend to higher gas temperatures is a good motivation for further observations for $CH_3C{\equiv}CH$ or NH_3. Especially gas temperature mapping can provide useful information on the gas-dust coupling at higher densities in molecular clumps. Future work should study the relation between dust temperature structures and gas temperature maps as provided by ammonia (as in Pillai et al. 2006; Ragan et al. 2011) or methylacetylene line observations. Such data should provide further observational evidence for the predicted strong thermal coupling between gas and dust at higher densities.

The northern and southern extent of the IRDC (hosting C2 and C3) show a much flatter temperature profile with higher temperatures compared to the central part of the filament. Furthermore the column densities are lower towards C2 and C3. This leads to the conclusion that the gas and dust densities are lower in these parts of the G48. Pure isothermal cylindrical collapse can hardly explain this density gradient. Hartmann & Burkert (2007) showed by modeling the density structures for the Orion A cloud that, even in the isothermal case, a simple initial arrangement of a slightly rotating gas sheet can result in filamentary structures with complex density structures.

As in the studies mentioned above, it is a clear finding of this work that the dust temperatures are non-isothermally distributed in a IRDC. What impact could the modeling of thermal profiles have? Thermal line broadening is significantly smaller compared to the observed linewidths. Therefore, a change of local temperature should not have a notable influence on the turbulence structure inside the core. On the other hand the thermal profile towards the core can play an important role in the support against fragmentation, since the Jeans mass is strongly dependent on temperature as $M_\mathrm{J} \sim T^{3/2}\rho^{-1/2}$. Theoretical studies of clustered star formation utilizing polytropic equations of states $P \sim \rho^\gamma$ and temperature dependent density profiles $T \sim \rho^{\gamma-1}$ indicate that the number of fragments in a cloud is strongly dependent on the polytropic index γ (Li et al. 2003). For the non-isothermal case ($\gamma \neq 1$) the polytropic index reflects the balance between cooling and heating. Deriving dust temperatures maps as in this work is the first step towards a better understanding of spatial distributed cooling and heating inside the core. A more detailed discussion of thermal properties can be found in e.g., Larson (2005) and Commerçon et al. (2011).

4.5. Summary

The following gives a brief summary of the results presented in this Chapter:

- G48 is an isolated mono-filamentary IRDC. The GMC W51, observed in the same field, is twice as distant as G48.
- The dark filament observed by Spitzer is not detected in the PACS bands. Only the region of highest extinction, in the central part, is seen in absorption at 70 to $100\,\mu\mathrm{m}$. The filament is clearly seen in emission in the SPIRE bands beyond $250\,\mu\mathrm{m}$, is in good agreement with the sub-millimeter emission maps from SCUBA and ATLASGAL.
- I present reliable temperature and column density maps based on pixel-to-pixel SED fitting of the Herschel, SCUBA legacy and ATLASGAL maps. Regions of low emission outside of the galactic plane were utilized to estimate the global background level for the Herschel maps. The location of the temperature minima are well aligned with the sub-millimeter and column density peaks. The temperatures drop to 17.5 K in the central part of G48. The heating by embedded MIPS $24\,\mu\mathrm{m}$ point sources is not detected due to beam dilution.
- I derive a total mass of $390\,\mathrm{M}_\odot$ for G48, applying a threshold of $1.1 \cdot 10^{22}\,\mathrm{cm}^{-2}$ to the SED fitted Herschel column density maps.
- "Green and fuzzy" features from IRAC ($3.6 - 8\,\mu\mathrm{m}$) reveal the central parts of the IRDC as the sites of most active ongoing star formation.
- I detect 13 point sources in all three PACS bands. Only one source lacks a MIPS $24\,\mu\mathrm{m}$ counterpart.
- SED fitting to these sources results in core masses of $0.6 - 14.3\,\mathrm{M}_\odot$, while the bolometric luminosity ranges between 15 and $630\,\mathrm{L}_\odot$. The two most massive cores (Source 1 and 2) have masses of 14.3 and $11.9\,\mathrm{M}_\odot$ and a bolometric luminosity of 630 or $475\,\mathrm{L}_\odot$, respectively. Comparing their light-to-mass ratio to evolutionary models, both sources are likely to evolve into high-mass stars with $M \gtrsim 8\,\mathrm{M}_\odot$. When applying the definition from low-mass star formation, four cores are good candidates for class 0 objects.
- The point source separation in G48 is significantly smaller than in other IRDCs, but in best agreement with the predictions by the isothermal cylindrical collapse model.
- It is possible that the lack of external feedback can influence the point source separation.
- The average line mass of the G48 filament is $174\,\mathrm{M}_\odot\,\mathrm{pc}^{-1}$. Compared to theoretical predictions the whole filament is collapsing, even under the assumption of internal turbulent support.
- According to my virial analysis the molecular clumps found in G48 are gravitationally bound.
- The presented radio line observations are consistent with previous observations by Ormel et al. (2005), which deduced increasing turbulent motion towards the inner parts of the cores.
- Several molecular species were detected , such as HCO^+, HCN, HNC, N_2H^+, ^{13}CO, $C^{18}O$ (and CH_3CCH). The mapping observation showed several molecular clumps associated to the sub-millimeter peaks.

- I found CO depletion towards the molecular clumps C1 + C2 with factor of $f_D \approx 3.5$.
- The low abundance of CO towards the sub-millimeter peaks P1 and P2 permit relative high abundances of N_2H^+.

Table 4.5. – Molecular line observations

Src	RA (J2000)	Dec (2000)	$R_{\rm eff}$ [a] arcsec	V_{LSR} [b] km · s^{-1}	Δv [c] km · s^{-1}	$\int T_{mb}dv$ [d] K · km · s^{-1}	$N(X)$ [e] 10^{12}cm^{-2}	Abundace [f] $\frac{N(X)}{N(\rm H_2)} \cdot 10^{-10}$	$M(X)$ [g] [M$_\odot$]	$M_{\rm vir}$ [h] [M$_\odot$]	$\alpha_{\rm vir}$ [i]
HCO^+											
C1	$19^h21^m48^s.958$	$+13°49'17''.04$	60	33.90 (0.16)	1.41 (0.13)	3.84	5.0	2.0	310	193	0.62
C2	$19^h21^m51^s.016$	$+13°47'47''.03$	50	33.92 (0.12)	1.00 (0.21)	1.64	2.3	1.6	100	81	0.81
C3	$19^h21^m35^s.569$	$+13°52'02''.04$	45	34.20 (0.16)	1.3 (0.3)	1.40	1.6	1.2	150	123	0.82
HCN											
C1	$19^h21^m48^s.958$	$+13°49'17''.04$	40	34.0 (0.4)	1.30 (0.23)	1.29	8.9	3.5	230	109	0.47
C2	$19^h21^m51^s.016$	$+13°47'47''.03$	42	33.8 (0.3)	1.1 (0.3)	0.84	6.1	4.3	50	82	1.64
C3	$19^h21^m35^s.569$	$+13°52'02''.04$	40	33.7 (0.4)	1.6 (0.4)	1.04	7.5	4.9	115	165	1.43
C4	$19^h21^m46^s.898$	$+13°49'17''.04$	41	34.4 (0.5)	1.28 (0.16)	1.04	7.2	3.7	165	109	0.66
HNC											
C1	$19^h21^m48^s.958$	$+13°49'17''.04$	63	33.81 (0.11)	0.58 (0.16)	1.27	2.7	1.1	450	34	0.08
C2	$19^h21^m51^s.016$	$+13°47'47''.03$	47	33.77 (0.12)	0.38 (0.11)	2.01	4.5	3.1	95	11	0.12
C3	$19^h21^m35^s.569$	$+13°52'02''.04$	39	33.91 (0.28)	0.63 (0.23)	0.83	1.8	1.2	140	25	0.18
N_2H^+											
C1	$19^h21^m48^s.958$	$+13°49'17''.04$	72	33.60 (0.17)	1.47 (0.25)	4.69	68.7	27.0	370	251	0.68
C2	$19^h21^m51^s.016$	$+13°47'47''.03$	71	33.59 (0.11)	1.10 (0.22)	2.92	45.0	31.5	85	139	1.64
C3	$19^h21^m35^s.569$	$+13°52'02''.04$	50	33.8 (0.5)	2.9 (0.7)	2.06	31.4	20.5	165	679	4.15
^{13}CO (1-0)											
C1	$19^h21^m48^s.449$	$+13°49'17''.90$	76	33.72 (0.11)	0.60 (0.11)	8.53	$2.0 \cdot 10^4$	$7.9 \cdot 10^3$	380	44	0.12
^{13}CO (2-1)											
C1	$19^h21^m48^s.449$	$+13°49'17''.90$	19	35.1 (0.22)	1.2 (0.3)	14.9	$1.6 \cdot 10^4$	$6.3 \cdot 10^3$	60	44	0.73
C2	$19^h21^m51^s.016$	$+13°47'47''.03$	16	34.9 (0.3)	1.1 (0.3)	5.9	$6.4 \cdot 10^3$	$4.5 \cdot 10^3$	40	31	0.78
C^{18}O (2-1)											
C1	$19^h21^m48^s.449$	$+13°49'17''.90$	18	34.2 (0.3)	0.70 (0.25)	2.3	$1.2 \cdot 10^3$	$4.9 \cdot 10^2$	55	14	0.25
C2	$19^h21^m51^s.016$	$+13°47'47''.03$	15	34.02 (0.20)	0.59 (0.21)	1.6	$8.6 \cdot 10^2$	$6.0 \cdot 10^2$	30	8	0.27

[a] Effective radius from clump finder,

[b] rest frame velocities,

[c] line width,

[d] Integrated line intensities,

[e] column density of the observed molecular species,

[f] Abundance of the molecular species with respect to H_2, N_{H_2} is calculated from the 870 µm data (and 8 µm extinctions in brackets),

[g] mass estimates from molecular line maps, see text,

[h] virial mass $M_{\rm vir} = 126 R_{\rm eff} \Delta v^2$, see text,

[i] virial parameter $\alpha = M_{\rm vir}/M$

5. Conclusions

Chapter 2 and 4 already gave a summary of the corresponding results. The first part of Chapter 3 gives an introduction to the developed photometric pipeline and details on the detections in the EPoS sample. In the second part of Chapter 3 the detection of a common point source separation and the implication for future studies are discussed. Therefore I will discuss the results of thesis chapters within the framework of the questions posed in Section 1.1.

In Chapter 2 a spectroscopic survey of YSOs found in massive clumps was performed. In in direct response to question, *"How do YSOs embedded in massive star-forming regions evolve before the HMPO phase?"*, from Section 1.1, the following results were found: All of these sources except for one are good candidates for intermediate-mass YSOs. Given the natal mass reservoir of these sources, some might evolve into high-mass stars. The sample can be divided into two groups of sources representing two different evolutionary stages. The first group consists of particularly young stellar objects that are deeply embedded into the natal dust envelopes. They are characterized by several absorption bands: silicate features, water ice, methane ice, CO_2 ice, and NH_4^+ absorption. The CO_2 ice band can be utilized to distinguish a truly embedded source from a fore- or background star. For example, the CO_2 absorption profile for ISOSS J18364–0221 West was fitted with a high ice temperature ($\sim 70 - 80\,\mathrm{K}$) rather than the typical cloud temperature ($< 20\,\mathrm{K}$), hence the CO_2 ice must have been heated by the YSO. A second group shows more evolved sources. Several indications for J-shocks are observed for these sources. More importantly, these sources show extended PAH emission that have been exposed to a high UV radiation field, creating a PDR. Moreover, the line analysis of molecular gas was used to constrain the physical properties of the PDR. For none of these source radio emission typical for H II regions was observed. However, the current survey data products lack the sensitivity and spatial resolution to draw solid conclusions. Further observations should be performed to clarify if a HCH II region is already associated with these sources, since they might represent the transition from the phase of embedded YSOs in a massive mass reservoir to phase of HMPOs accompanied by HCH II regions.

What did we learn about the collapse and fragmentation of clouds which host massive star formation? It is known that massive star formation occurs hierarchically. The dark cloud G48, studied in detail in Chapter 4, is undisturbed by nearby star formation or other feedback effects. In G48 one can observe this hierarchy of structures, from large to small scales. The dark cloud itself consist of a single filament spanning several parsec. One substantial finding of this Chapter is that the entire filament is collapsing under its own weight. While the thermal pressure in filaments of other star-forming regions is usually not enough to withstand the collapse, it is observed that turbulence provides enough support in several IRDCs. However, this is not the case for G48; moreover, supercritical filaments with respect to turbulence are rarely found (the most notable exception to this being the Orion integral shapped filament). The reason why the virial line masses for G48 are so high, in other words why G48 is collapsing, remains unclear. Compared to the large EPoS sample the G48 cloud mass is average. The isolated and undisturbed nature of G48 might have an influence on the physical conditions found therein. This motivates further detailed studies on the virial state of the EPoS sample to find other regions with a lack of turbulent support. However, stepping further down in the hierarchy to smaller

scales yet, one finds molecular clumps ($0.3 - 0.9$ pc). The virial analysis of the line observations of G48 reveals their structures to be gravitationally bound. On the core scale (0.15 pc) G48 fragments into several point sources, two of which presumably host precursors to high-mass stars. These compact Herschel sources show a regular spacing, particularly in the central and densest region of the IRDC. Motivated by this result I investigated fragmentation on the core scale in the entire high-mass sample of EPoS. Thereby, I found a common separation of ~ 0.5 pc for all regions independent of the cloud mass, distance, and morphology. In contrast, for G48 we find the tentative indication that the point source separation is somewhat smaller, of the order of ~ 0.3 pc. The detected sources are in similar evolutionary stages to the sources discussed in Chapter 2. Overall, across the EPoS sample, this common separation might be a distinct property of objects prior to HMPOs. In G48 it is observed that more point sources are detected in the vicinity of molecular clumps. Therefore, future work should study the clustering properties of IRDCs and other massive star-forming regions to pin down the physical conditions responsible for the point source separation and hence a fixed fragmentation scale.

What is the internal structure of dark clouds in terms of density and temperature? Most theories for massive star formation assume the collapse of an isothermal medium. In contrast, recent Herschel observations show that all dense regions where stars form are non-isothermal, neither on the scale of the whole cloud nor on the core scale. The temperature map presented for G48 in Chapter 4 also shows varying temperatures across the whole filament. Moreover the peaks in the fitted column density maps and the molecular line maps, which are tracers for dense gas, are in good spatial agreement with the Herschel-fitted temperature minima. This confirms that the lowest temperatures in the cloud are related to the region with the highest densities.

As discussed previously, Chapter 4 presents a simply structured, undisturbed region of massive star formation. We know that different evolutionary stages ranging from HMSC to HMPOs can be present in IRDCs. Therefore, it is difficult to characterize IRDCs in terms of their compact source content by age or evolution. However, using the level of external disturbance of the star-forming cloud may provide another classification scheme. One could compare the physical conditions found in relatively isolated IRDCs and ISOSS regions to regions in the vicinity of large H II regions, supernova remnants, or bright HMPOs. Such a comparison may shed light on the influence of external feedback on the processes within the cloud itself. The analysis of G48 in Chapter 4 provides a template to evaluate the physical conditions for other regions in the EPoS sample.

The last chapter gives an outlook for the chemical modeling of IRDCs and briefly preliminary results are shown.

6. Outlook on chemical modelling of IRDCs

6.1. Introduction

Since their discovery, many radio observations of molecular lines have been conducted in IRDCs (e.g. Carey et al. 1998; Ragan et al. 2006; Battersby et al. 2010; Cyganowski et al. 2009; Brogan et al. 2011; Miettinen 2012; Sakai et al. 2012). These studies only focused on a few, mostly simple-structured molecules. Therefore, first approaches to model these lines and parametrize the physical conditions of the IRDCs utilized only simple molecules (e.g. Gibson et al. 2009). Recently, studies have utilized a wider range of molecular species including more complex molecules like acetonitrile (CH_3CN), Cyanoacetylene (HC_3N), Methylacetylene (CH_3C_2H) and Methanol (CH_3OH) (Vasyunina et al. 2011; Foster et al. 2011; Sakai et al. 2008, 2010). One of the most comprehensive line surveys has been carried out by Vasyunina et al. (2011) with MOPRA. The same molecular species were observed towards G48 with a similar MOPRA setup as described in Chapter 4.2.4. Based on their previous MOPRA observations Vasyunina et al. (2012) developed a simple chemical model to reproduce the line observations including physical parameters such as temperature, density and chemical age.

In this Chapter, the first results of fitting the line observations from the previous Chapter to two different chemical models are presented and implications for future studies are outlined.

6.1.1. Chemical models

To model the chemical evolution of G48 two different models are used. A 0-dimensional model was introduced by Vasyunina et al. (2012). The used density and temperature remain constant during modeling of the chemical evolution of the IRDC. Therefore large-scale dynamical processes, such as collapse or heating, are excluded (although the adsorption and evaporation is included). This approach is often referred to as a "pseudo-time-dependent" model.

Another one-dimensional model was developed by Dmitry Semenov, which is also a steady-state model, i.e., physical parameters such as temperature, and density stay constant over time. For the 1-d model an isothermal gas with a $n \sim r^{-3/2}$ density profile is assumed. A physical size of 0.46 pc is used (the physical beam size for G48) for the model, the inner boundary starts at $r = 0.0046$ pc with the inner density n_0.

Both models incorporate three different chemical reaction networks: the first one representing the gas-phase reaction, the second is the accretion/desorption network that includes the interface between gas-phase and grain surface reaction via adsorption and evaporation, while the last network epitomizes the reactions on the grain surface.

The 0-d model uses chemical reaction networks based on the "KInetic Database for Astrochemistry" (KIDA[1] Wakelam et al. 2012). The kinetic data in KIDA consist of several hundred molecular species and a network of several thousand reactions and reaction rates of chemical species found in the ISM. The reaction network includes gas-phase reactions, surface reactions on the dust grain surface

[1] http://kida.obs.u-bordeaux1.fr

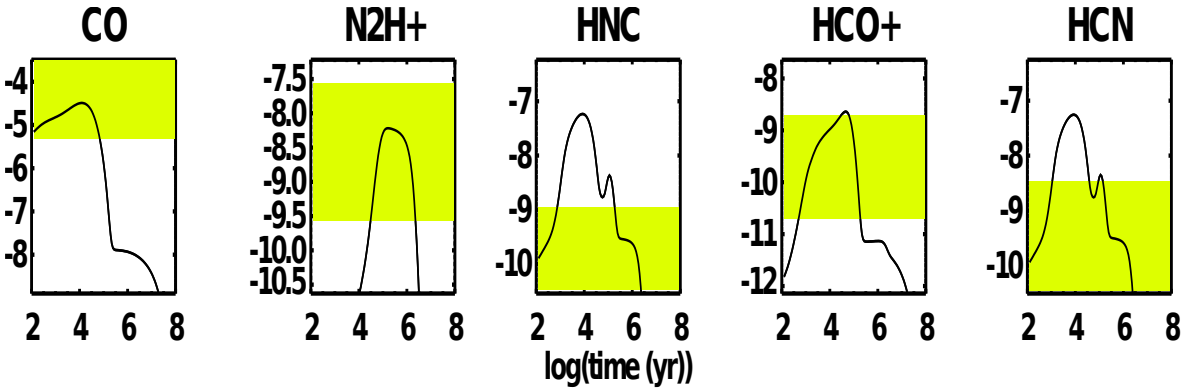

Figure 6.1. – This plot shows the chemical evolutions for the five detected molecules in G48 at 18 K and 10^5 cm^{-3}, indicated by the black line. The observed abundances are overplotted by green boxes, assuming an uncertainty of $\pm$ an order of magnitude.

and the transitions between gas and grain surface via desorption of surface species through thermal evaporation (> 15 K) and cosmic ray desorption and accretion.

The 1-d model works in a similar fashion, and is mostly based on the KIDA precursor, the OSU (Ohio State University) database[2] with all recent updates to the reaction rates from KIDA (as of May 2012), but including additional surface reactions from Garrod & Herbst (2006).

In general both models derive the chemical evolution by solving a set of differential equations (Semenov et al. 2010):

$$\frac{dn_i^g}{dt} = \sum_{l,m} k_{lm}^g n_l^g n_m^g - n_i^g \sum_{i \neq l} k_l^g n_l^g + k_i^{\mathrm{des}} n_i^s - k_i^{\mathrm{acc}} n_i^g \tag{6.1}$$

$$\frac{dn_i^s}{dt} = \sum_{l,m} k_{lm}^s n_l^s n_m^s - n_i^s \sum_{i \neq l} k_l^s n_l^s + k_i^{\mathrm{des}} n_i^s - k_i^{\mathrm{acc}} n_i^g \tag{6.2}$$

where n_i^g and n_i^s are the gas-phase and surface concentrations, k_{lm}^g, k_l^g, k_{lm}^s and k_l^s the reaction rates for the gas-phase and surface, k_i^{des} and k_i^{acc} are the accretion and desorption rates.

6.2. Results

We applied both models to the abundances found in the clump C1 for G48 for the different molecular species (listed in Table 6.1). While only the detected lines can be fitted to the 0-d model, the 1-d model excepts also upper limits for undetected lines.

For the 0-d model a fixed temperature of 18 K is assumed (adopted from the dust-temperature map in Section 4.3.2 and a fixed density of 10^5 cm^{-3}. Figure 6.1 shows the plot of the chemical gas-phase-evolution modeled for a given temperature and density with the observed abundances. Figure 6.2 shows the number of molecular species, $C(t)$, where the modeled abundance agree to within an order of magnitude with the observational value for a given time. The confidence parameter k_i for a

[2] http://www.physics.ohio-state.edu/~eric/research.html

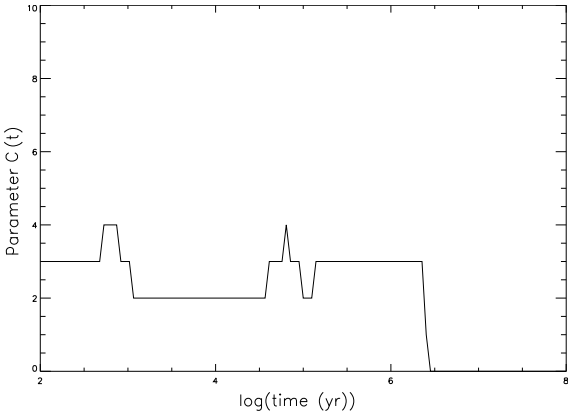

Figure 6.2. – The number of fitted molecules plotted against time for the 0-d model

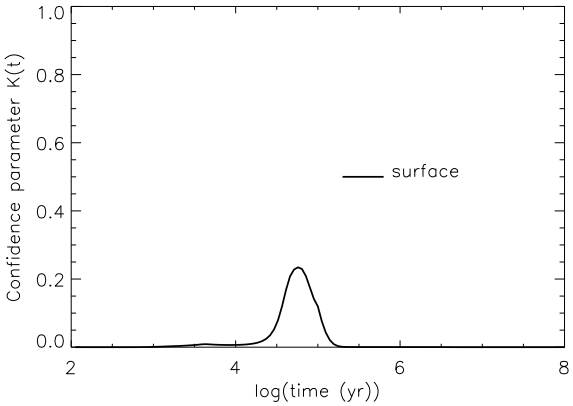

Figure 6.3. – The confidence parameter plotted against time for the 0-d model

single species i is adopted from Garrod et al. (2007):

$$k_i(t) = \mathrm{erfc}\left(\frac{|\log(\chi_{\mathrm{obs}}) - \log(\chi_{\mathrm{mod}})|}{\sqrt{2}\,\sigma}\right) \tag{6.3}$$

where χ_{obs} is the observed abundance, χ_{mod} the abundance predicted by the model and $\sigma = 1$. The confidence parameter shown in Figure 6.3 is from the species with the worse agreement between observational and modeled abundances.

The number of simultaneously fitted species $C(t)$ show two maxima, the first for a very young chemical age of $< 10^3$ yr, which is unlikely, since G48 already host embedded proto-stars and show indications for outflows, hence it must be older. The second, sharp peak occurs at $6.3 \cdot 10^4$ yr, but the second peak just consists of a single data point. The major problem with fitting the different molecular species in context of the modeled predictions is the fitting the low observed abundances for HCN and HNC to the CO abundances for chemical ages older than 1000 yr. Pointed IRAM observations on C1 have detected similar abundances for HCO^+, N_2H^+ and CO, but HCN and HNC seem to be an order of magnitude higher (Thomas Gerner 2012, private communication). The HCN and HNC maps were the most noisy ones. The noise induced prevented robust detection of the wings for a faint line scan and lead, especially with line deviating from a Gaussian profile, to an underestimate of the integrated line flux. Consequently, this leads to an underestimate of the column density for HCN and HNC.

In contrast to the 0-d model the 1-d model also considers the upper limits for the undetected lines. For this model the fitting returns two different solutions: A very unlikely young solution with a chemical age of $100 - 1000$ yr with too high temperatures (~ 37 K) and an modeled overestimate of HCN and HNC by two orders of magnitude. A second model provides more realistic results (Table 6.2), the temperatures in this run is 9 K lower than the observed dust temperatures. The resulting modeled age of G48 is an order of magnitude larger than for the 0-d model.

The main problem for both models is the observational underestimate of HCN and HNC. Such low abundance of both species occurs only at very young and late stages. As mentioned before higher abundances for both molecules are observed for the same region, which could indicate a chemical age of $\sim 10^4$ yr.

Table 6.1. – Input abundances

Species	N $[10^{12}\mathrm{cm}^{-2}]$	Abundance 10^{-10}
HCO^+	5.0	2.0
HCN	8.9	3.5
HNC	2.7	1.1
N_2H^+	68.7	27.0
^{13}CO	$1.6 \cdot 10^4$	$6.3 \cdot 10^3$
$C^{18}O$	$1.2 \cdot 10^3$	$4.9 \cdot 10^2$
$^{12}C^{16}O$		$\sim 1.210^5$
Upper limits:		
H13CN	3.8	
H13CO+	0.73	
SiO	1.2	
HNCO	6.4	
HC3N	2.0	
CS	5.9	
CH3CN	2.9	

Table 6.2. – Results chemical 1-D model

Species	N_{obs} $[\mathrm{cm}^{-2}]$	N_{model} (a) $[\mathrm{cm}^{-2}]$	$\frac{N_{\mathrm{obs}}-N_{\mathrm{model}}}{N_{\mathrm{obs}}+N_{\mathrm{model}}}$
H2	$2.54 \cdot 10^{22}$	$7.17 \cdot 10^{21}$	0.56
CO	$3.05 \cdot 10^{17}$	$3.04 \cdot 10^{17}$	0.00115
HCO+	$5.00 \cdot 10^{12}$	$4.43 \cdot 10^{13}$	0.797
HCN	$8.90 \cdot 10^{12}$	$9.39 \cdot 10^{12}$	0.0269
HNC	$2.70 \cdot 10^{12}$	$1.55 \cdot 10^{13}$	0.704
N2H+	$6.80 \cdot 10^{13}$	$1.61 \cdot 10^{13}$	0.617
SIO	$1.20 \cdot 10^{12}$	$1.63 \cdot 10^{11}$	0.761
HNCO	$6.40 \cdot 10^{12}$	$4.17 \cdot 10^{10}$	0.987
HC3N	$2.00 \cdot 10^{12}$	$1.08 \cdot 10^{10}$	0.989
CS	$5.90 \cdot 10^{12}$	$1.13 \cdot 10^{12}$	0.679
CH3CN	$2.90 \cdot 10^{12}$	$8.97 \cdot 10^{10}$	0.940

6.3. Conclusions

Despite the observational inconsistencies and different results from both models, there are several lessons to be learned.

Due to the underestimate of HCN and HNC both models had problems fitting the observed abundances correctly. This suggest another observational strategy: the mapping observations are important to study the morphology of molecular clumps and can reveal differences in spatial distribution of abundances, for example, the depletion of CO and N_2H^+ (e.g., Ragan et al. 2006). In general the mapping observations are more noisy at a certain position, compared to pointing observations. Mapping observations can be used to establish the positional peak-up for further pointing observations. Subsequently conducted pointing observations can provide more accurate abundance as an input for the chemical models.

Herschel observations enable us to derive direct dust temperatures as input for the modeling. The current Herschel temperature mapping assumes optical thin emission, and except for HCO^+ the observed lines are optical thin, so that the line emission originates from the same range of extinction also traced by the temperature mapping. Using directly observed dust temperatures can improve the modeling of the desorption/accretion network, since the thermal desorption rate directly depends on the dust temperature. The used 1-d model considers an isothermal configuration. Dust temperature profiles could also be used to adjust a non-thermal setup. While SED fitted maps are convolved to the coarse beam at longer wavelengths, the comparison of the observations to radiative transfer models could result in more suitable profiles (as in Wilcock et al. 2012).

Estimating the "age" of a star forming region is an complex endeavor, since the chronological onset of physical processes, such as the start of a cloud collapse or the ignition of the fusion process in YSOs, is barley accessible by observations. The concept of a "chemical age" presents a new approach to address the evolution of a clump. Further progress in the modeling and a larger pool of observations is needed to calibrate the chemical evolution to the established evolutionary sequences for sites of massive star formation.

Bibliography

Abel, N. P., Ferland, G. J., Shaw, G., & van Hoof, P. A. M., The H II Region/PDR Connection: Self-consistent Calculations of Physical Conditions in Star-forming Regions, 2005, ApJS, 161, 65

Afonso, J. M., Yun, J. L., & Clemens, D. P., HCN in BOK Globules: A Good Tracer of Collapsing Cores, 1998, AJ, 115, 1111

Allamandola, L. J., Tielens, A. G. G. M., & Barker, J. R., Interstellar polycyclic aromatic hydrocarbons - The infrared emission bands, the excitation/emission mechanism, and the astrophysical implications, 1989, ApJS, 71, 733

Allen, M., & Robinson, G. W., The molecular composition of dense interstellar clouds, 1977, ApJ, 212, 396

André, P., Ward-Thompson, D., & Barsony, M., Submillimeter continuum observations of Rho Ophiuchi A - The candidate protostar VLA 1623 and prestellar clumps, 1993, ApJ, 406, 122

André, P., Observations of protostars and protostellar stages, 1994, The Cold Universe, 179

André, P., Ward-Thompson, D., & Barsony, M., From Prestellar Cores to Protostars: the Initial Conditions of Star Formation, 2000, Protostars and Planets IV, 59

André, P., Minier, V., Gallais, P., et al., First $450\,\mu\mathrm{m}$ dust continuum mapping of the massive star-forming region NGC 3576 with the P-ArTéMiS bolometer camera, 2008, A&A, 490, L27

Arvidsson, K., Kerton, C. R., Alexander, M. J., Kobulnicky, H. A., & Uzpen, B., A Sample of Intermediate-mass Star-forming Regions: Making Stars at Mass Column Densities $< 1\,\mathrm{g\,cm^{-2}}$, 2010, AJ, 140, 462

Arzoumanian, D., André, P., Didelon, P., et al., Characterizing interstellar filaments with Herschel in IC 5146, 2011, A&A, 529, L6

Bally, J., & Zinnecker, H., The Birth of High-Mass Stars: Accretion and/or Mergers?, 2005, AJ, 129, 2281

Battersby, C., Bally, J., Jackson, J. M., et al., An Infrared Through Radio Study of the Properties and Evolution of IRDC Clumps, 2010, ApJ, 721, 222

Battersby, C., Bally, J., Ginsburg, A., et al., Characterizing precursors to stellar clusters with Herschel, 2011, A&A, 535, A128

Benjamin, R. A., et al., Churchwell, E., Babler, B. L., GLIMPSE. I. An SIRTF Legacy Project to Map the Inner Galaxy, 2003, PASP, 115, 953

Bergin, E. A., Goldsmith, P. F., Snell, R. L., & Ungerechts, H., CH_3C_2H as a temperature probe in dense giant molecular cloud cores, 1994, ApJ, 431, 674

Bergin, E. A., & Tafalla, M., Cold Dark Clouds: The Initial Conditions for Star Formation, 2007, ARAA, 45, 339

Bergmann, L., & Schaefer, C. 2001, Berlin, New York: de Gruyter, "Lehrbuch der Experimentalphysik - Band 7 - Erde und Planeten", 2nd edition

Bertoldi, F., & McKee, C. F., Pressure-confined clumps in magnetized molecular clouds, 1992, ApJ, 395, 140

Beuther, H., Schilke, P., Gueth, F., et al., Multiple outflows at the earliest stages of massive star formation, 2002, A&A, 387, 931

Beuther, H., Schilke, P., Menten, K. M., et al., High-Mass Protostellar Candidates. II. Density Structure from Dust Continuum and CS Emission, 2002, ApJ, 566, 945

Beuther, H., Schilke, P., Sridharan, T. K., et al., Massive molecular outflows, 2002, A&A, 383, 892

Beuther, H., Walsh, A., Schilke, P., et al., CH_3OH and H_2O masers in high-mass star-forming regions, 2002, A&A, 390, 289

Beuther, H., Churchwell, E. B., McKee, C. F., & Tan, J. C., The Formation of Massive Stars, 2007, Protostars and Planets V, 165

Beuther, H., Henning, T., Linz, H., et al., From high-mass starless cores to high-mass protostellar objects, 2010, A&A, 518, L78

Beuther, H., Kainulainen, J., Henning, T., Plume, R., & Heitsch, F., The Coalsack near and far, 2011, A&A, 533, A17

Beuther, H., Tackenberg, J., Linz, H., et al., The onset of high-mass star formation in the direct vicinity of the Galactic mini-starburst W43, 2012, A&A, 538, A11

Billot, N., Schisano, E., Pestalozzi, M., et al., Clustering Properties of Far-infrared Sources in Hi-GAL Science Demonstration Phase Fields, 2011, ApJ, 735, 28

Binney, J., & Tremaine, S. 2008, Galactic Dynamics: Second Edition, by James Binney and Scott Tremaine. ISBN 978-0-691-13026-2 (HB). Published by Princeton University Press, Princeton, NJ USA, 2008.,

Birkmann, S. M., Krause, O., & Lemke, D., Very Cold and Massive Cores near ISOSS J18364-0221: Implications for the Initial Conditions of High-Mass Star Formation, 2006, ApJ, 637, 380

Birkmann, S. M., Krause, O., Hennemann, M., Henning, T., Steinacker, J., & Lemke, D., A massive protostellar core with an infalling envelope 2007, A&A, 474, 883

Birkmann, S. M., The early phases of massive star birth, 2007, PhD Thesis, University of Heidelberg

Black, J. H., & van Dishoeck, E. F., Fluorescent excitation of interstellar H_2, 1987, ApJ, 322, 412

Bleeker, J. A. M., Geiss, J., & Huber, M. C. E. 2002, The Century of Space Science, Volume I, 3

Blitz, L., Giant molecular clouds, 1993, Protostars and Planets III, 125

Bogun, S., Lemke, D., Klaas, U., et al., First data from the ISOPHOT FIR Serendipity survey, 1996, A&A, 315, L71

Bondi, H., On spherically symmetrical accretion, 1952, MNRAS, 112, 195

Bonnell, I. A., Vine, S. G., & Bate, M. R., Massive star formation: nurture, not nature, 2004, MNRAS, 349, 735

Bonnell, I. A., & Bate, M. R., Binary systems and stellar mergers in massive star formation, 2005, MNRAS, 362, 915

Boonman, A. M. S., van Dishoeck, E. F., Lahuis, F., Doty, S. D., Wright, C. M., & Rosenthal, D., Gas-phase CO_2, C_2H_2, and HCN toward Orion-KL, 2003, A&A, 399, 1047

Bouwman, J., Lawson, W. A., Dominik, C., Feigelson, E. D., Henning, T., Tielens, A. G. G. M., & Waters, L. B. F. M., Binarity as a Key Factor in Protoplanetary Disk Evolution: Spitzer Disk Census of the η Chamaeleontis Cluster, 2006, ApJL, 653, L57

Bressert, E., Bastian, N., Gutermuth, R., et al., The spatial distribution of star formation in the solar neighbourhood: do all stars form in dense clusters?, 2010, MNRAS, 409, L54

Burbidge, E. M., Burbidge, G. R., Fowler, W. A., & Hoyle, F., Synthesis of the Elements in Stars, 1957, Reviews of Modern Physics, 29, 547

Brogan, C. L., Hunter, T. R., Cyganowski, C. J., et al., First Results from a 1.3 cm Expanded Very Large Array Survey of Massive Protostellar Objects: G35.03+0.35, 2011, ApJL, 739, L16

Butler, M. J., & Tan, J. C., Mid-Infrared Extinction Mapping of Infrared Dark Clouds: Probing the Initial Conditions for Massive Stars and Star Clusters, 2009, ApJ, 696, 484

Carey, S. J., Clark, F. O., Egan, M. P., et al., The Physical Properties of the Midcourse Space Experiment Galactic Infrared-dark Clouds 1998, ApJ, 508, 721

Carey, S. J., Feldman, P. A., Redman, R. O., et al., Submillimeter Observations of Midcourse Space Experiment Galactic Infrared-Dark Clouds, 2000, ApJL, 543, L157

Carey, S. J., et al., MIPSGAL: A Survey of the Inner Galactic Plane at 24 and 70 microns, Survey Strategy and Early Results, 2005, Bulletin of the American Astronomical Society, 37, 1252

Carey, S. J., et al., MIPSGAL: A Survey of the Inner Galactic Plane at 24 and 70 μm, 2009, PASP, 121, 76

Cartwright, A., & Whitworth, A. P., The statistical analysis of star clusters, 2004, MNRAS, 348, 589

Cartwright, A., & Whitworth, A. P., The directional analysis of star clusters, 2008, MNRAS, 390, 807

Caselli, P., Benson, P. J., Myers, P. C., & Tafalla, M., Dense Cores in Dark Clouds. XIV. N_2H^+ (1-0) Maps of Dense Cloud Cores, 2002, ApJ, 572, 238

Cesaroni, R., Galli, D., Lodato, G., Walmsley, C. M., & Zhang, Q., Disks Around Young O-B (Proto)Stars: Observations and Theory, 2007, Protostars and Planets V, 197

Chambers, E. T., Jackson, J. M., Rathborne, J. M., & Simon, R., Star Formation Activity of Cores within Infrared Dark Clouds, 2009, ApJS, 181, 360

Chandrasekhar, S., & Fermi, E., Problems of Gravitational Stability in the Presence of a Magnetic Field., 1953, ApJ, 118, 116

Churchwell, E., Povich, M. S., Allen, D., et al., The Bubbling Galactic Disk, 2006, ApJ, 649, 759

Commerçon, B., Hennebelle, P., & Henning, T., Collapse of Massive Magnetized Dense Cores Using Radiation Magnetohydrodynamics: Early Fragmentation Inhibition, 2011, ApJL, 742, L9

Crapsi, A., Caselli, P., Walmsley, C. M., Myers, P. C., Tafalla, M., Lee, C. W., & Bourke, T. L., Probing the Evolutionary Status of Starless Cores through N_2H^+ and N_2D^+ Observations, 2005, ApJ, 619, 379

Crowther, P. A., Schnurr, O., Hirschi, R., et al., The R136 star cluster hosts several stars whose individual masses greatly exceed the accepted 150 $M_\odot$ stellar mass limit 2010, MNRAS, 408, 731

Crutcher, R. M., Magnetic Fields in Molecular Clouds: Observations Confront Theory, 1999, ApJ, 520, 706

Cyganowski, C. J., Whitney, B. A., Holden, E., et al., A Catalog of Extended Green Objects in the GLIMPSE Survey: A New Sample of Massive Young Stellar Object Outflow Candidates, 2008, AJ, 136, 2391

Cyganowski, C. J., Brogan, C. L., Hunter, T. R., & Churchwell, E., A Class I and Class II CH_3OH Maser Survey of EGOs from the GLIMPSE Survey, 2009, ApJ, 702, 1615

Dame, T. M., Hartmann, D., & Thaddeus, P., The Milky Way in Molecular Clouds: A New Complete CO Survey, 2001, ApJ, 547, 792

De Buizer, J. M., & Vacca, W. D., Direct Spectroscopic Identification of the Origin of "Green Fuzzy" Emission in Star-forming Regions 2010, AJ, 140, 196

de Geus, E. J., Interactions of stars and interstellar matter in Scorpio Centaurus, 1992, A&A, 262, 258

Deharveng, L., Schuller, F., Anderson, L. D., et al., A gallery of bubbles. The nature of the bubbles observed by Spitzer and what ATLASGAL tells us about the surrounding neutral material, 2010, A&A, 523, A6

de Wit, W. J., Testi, L., Palla, F., & Zinnecker, H., The origin of massive O-type field stars: II. Field O stars as runaways, 2005, A&A, 437, 247

Di Francesco, J., Johnstone, D., Kirk, H., MacKenzie, T., & Ledwosinska, E., The SCUBA Legacy Catalogues: Submillimeter-Continuum Objects Detected by SCUBA, 2008, ApJS, 175, 277

Diolaiti, E., Bendinelli, O., Bonaccini, D., Close, L., Currie, D., & Parmeggiani, G., Analysis of isoplanatic high resolution stellar fields by the StarFinder code, 2000, A&AS, 147, 335

Draine, B. T., & Li, A., Infrared Emission from Interstellar Dust. IV. The Silicate-Graphite-PAH Model in the Post-Spitzer Era, 2007, ApJ, 657, 810

Dunham, M. M., Crapsi, A., Evans, N. J., II, et al., Identifying the Low-Luminosity Population of Embedded Protostars in the c2d Observations of Clouds and Cores, 2008, ApJS, 179, 249

Dunham, M. K., Robitaille, T. P., Evans, N. J., II, et al., A Mid-infrared Census of Star Formation Activity in Bolocam Galactic Plane Survey Sources, 2011, ApJ, 731, 90

Edgar, R., & Clarke, C., The effect of radiative feedback on Bondi-Hoyle flow around a massive star, 2004, MNRAS, 349, 678

Egan, M. P., Shipman, R. F., Price, S. D., et al., A Population of Cold Cores in the Galactic Plane, 1998, ApJL, 494, L199

Eisenhauer, F., Schödel, R., Genzel, R., et al., A Geometric Determination of the Distance to the Galactic Center, 2003, ApJL, 597, L121

Elmegreen, B. G., & Lada, C. J., Sequential formation of subgroups in OB associations, 1977, ApJ, 214, 725

Engelbracht, C. W., et al., Absolute Calibration and Characterization of the Multiband Imaging Photometer for Spitzer. I. The Stellar Calibrator Sample and the $24\,\mu\mathrm{m}$ Calibration, 2007, PASP, 119, 994

Fazio, G. G., et al., The Infrared Array Camera (IRAC) for the Spitzer Space Telescope, 2004, ApJS, 154, 10

Fiege, J. D., & Pudritz, R. E., Helical fields and filamentary molecular clouds - I, 2000, MNRAS, 311, 85

Fiege, J. D., Johnstone, D., Redman, R. O., & Feldman, P. A., A Genetic Algorithm-based Exploration of Three Filament Models: A Case for the Magnetic Support of the G11.11–0.12 Infrared-dark Cloud, 2004, ApJ, 616, 925

Fontani, F., Giannetti, A., Beltrán, M. T., et al., High CO depletion in southern infrared dark clouds, 2012, MNRAS, 423, 2342

Foster, J. B., Jackson, J. M., Barnes, P. J., et al., The Millimeter Astronomy Legacy Team 90 GHz (MALT90) Pilot Survey, 2011, ApJS, 197, 25

Garay, G., Faúndez, S., Mardones, D., et al., Discovery of Four New Massive and Dense Cold Cores, 2004, ApJ, 610, 313

Garrod, R. T., & Herbst, E., Formation of methyl formate and other organic species in the warm-up phase of hot molecular cores, 2006, A&A, 457, 927

Garrod, R. T., Wakelam, V., & Herbst, E., Non-thermal desorption from interstellar dust grains via exothermic surface reactions, 2007, A&A, 467, 1103

Garrod, R. T., & Pauly, T., On the Formation of CO_2 and Other Interstellar Ices, 2011, ApJ, 735, 15

Gibson, D., Plume, R., Bergin, E., Ragan, S., & Evans, N., Molecular Line Observations of Infrared Dark Clouds. II. Physical Conditions, 2009, ApJ, 705, 123

Glover, S. C. O., & Clark, P. C., Is molecular gas necessary for star formation?, 2012, MNRAS, 421, 9

Gonzalez, R. C., & Woods, R. E. 1992, Reading, MA: Addison-Wesley, 1992, "Digital image processing"

Gordon, K. D., et al., Reduction Algorithms for the Multiband Imaging Photometer for Spitzer, 2005, PASP, 117, 503

Gordon, K. D., et al., Absolute Calibration and Characterization of the Multiband Imaging Photometer for Spitzer. II. 70 μm Imaging, 2007, PASP, 119, 1019

Gordon, K. D., Engelbracht, C. W., Rieke, G. H., et al., The Behavior of the Aromatic Features in M101 H II Regions: Evidence for Dust Processing, 2008, ApJ, 682, 336

Griffin, M. J., et al., The Herschel-SPIRE instrument and its in-flight performance, 2010, A&A, 518, L3

Gvaramadze, V. V., Weidner, C., Kroupa, P., & Pflamm-Altenburg, J. 2012, Accepted for publication in MNRAS, arXiv:1206.1596

Hartmann, L., & Burkert, A., On the Structure of the Orion A Cloud and the Formation of the Orion Nebula Cluste, 2007, ApJ, 654, 988

Hasegawa, T. I., Herbst, E., & Leung, C. M., Models of gas-grain chemistry in dense interstellar clouds with complex organic molecules, 1992, ApJS, 82, 167

Hasegawa, T. I., & Herbst, E., Three-Phase Chemical Models of Dense Interstellar Clouds - Gas Dust Particle Mantles and Dust Particle Surfaces, 1993, MNRAS, 263, 589

Helfand, D. J., Becker, R. H., White, R. L., Fallon, A., & Tuttle, S., MAGPIS: A Multi-Array Galactic Plane Imaging Survey, 2006, AJ, 131, 2525

Helmich, F. P., & van Dishoeck, E. F., Physical and chemical variations within the W3 star-forming region. II. The 345 GHz spectral line survey, 1997, A&AS, 124, 205

Hennemann, M., Multiwavelength observations of massive star-forming regions selected in the far-infrared, 2009, PhD Thesis, University of Heidelberg

Hennemann, M., Birkmann, S. M., Krause, O., & Lemke, D., An infrared-submillimeter study of starforming regions selected by the ISOSS 170 μm survey 2008, A&A, 485, 753

Hennemann, M., Birkmann, S. M., Krause, O., Lemke, D., Pavlyuchenkov, Y., More, S., & Henning, T., Star-Forming Cores Embedded in a Massive Cold Clump: Fragmentation, Collapse, and Energetic Outflows, 2009, ApJ, 693, 1379

Henning, T., Cosmic Silicates, 2010, ARAA, 48, 21

Hernandez, A. K., Tan, J. C., Caselli, P., et al. 2011, ApJ, 738, 11

Herpin, F., Chavarría, L., van der Tak, F., et al., The massive protostar W43-MM1 as seen by Herschel-HIFI water spectra: high turbulence and accretion luminosity, 2012, A&A, 542, A76

Holland, W. S., et al., SCUBA: a common-user submillimetre camera operating on the James Clerk Maxwell Telescope, 1999, MNRAS, 303, 659

Hollenbach, D. J., Werner, M. W., & Salpeter, E. E., Molecular Hydrogen in H I Regions, 1971, ApJ, 163, 165

Hollenbach, D., & McKee, C. F., Molecule formation and infrared emission in fast interstellar shocks. III - Results for J shocks in molecular clouds, 1989, ApJ, 342, 306

Hollenbach, D. J., & Tielens, A. G. G. M., Dense Photodissociation Regions (PDRs), 1997, ARAA, 35, 179

Houck, J. R., et al., The Infrared Spectrograph (IRS) on the Spitzer Space Telescope, 2004, ApJS, 154, 18

Indebetouw, R., et al., he Wavelength Dependence of Interstellar Extinction from 1.25 to 8.0 μm Using GLIMPSE Data 2005, ApJ, 619, 931

Jackson, J. M., et al., The Boston University-Five College Radio Astronomy Observatory Galactic Ring Survey, 2006, ApJS, 163, 145

Jackson, J. M., Finn, S. C., Chambers, E. T., Rathborne, J. M., & Simon, R., The "Nessie" Nebula: Cluster Formation in a Filamentary Infrared Dark Cloud, 2010, ApJL, 719, L185

Kainulainen, J., Alves, J., Beuther, H., Henning, T., & Schuller, F., Mass reservoirs surrounding massive infrared dark clouds. A view by near-infrared dust extinction, 2011, A&A, 536, A48

Kang, M., Choi, M., Bieging, J. H., et al., Submillimeter Observations of Dense Clumps in the Infrared Dark Cloud G049.40–00.01 2011, ApJ, 743, 198

Kaufman, M. J., & Neufeld, D. A., Far-Infrared Water Emission from Magnetohydrodynamic Shock Waves, 1996, ApJ, 456, 611

Kaufman, M. J., Wolfire, M. G., & Hollenbach, D. J., [Si II] , [Fe II] , [C II] , and H_2 Emission from Massive Star-forming Regions, 2006, ApJ, 644, 283

Kauffmann, J., & Pillai, T., How Many Infrared Dark Clouds Can form Massive Stars and Clusters?, 2010, ApJL, 723, L7

Kemper, F., Vriend, W. J., & Tielens, A. G. G. M., The Absence of Crystalline Silicates in the Diffuse Interstellar Medium, 2004, ApJ, 609, 826

Kocsis, E., Trus, B.L., Steer, C.J., Bisher, M.E. and Steven, A.C 1991, J. Struct. Biol. 107, 6

Krist, J. 2002, TinyTIM/SIRTF Users Guide (Pasadena: SSC)

Krause, O., Lemke, D., Tóth, L. V., et al., A very young star forming region detected by the ISOPHOT Serendipity Survey, 2003, A&A, 398, 1007

Krause, O., Vavrek, R., Birkmann, S., Klaas, U., Stickel, M., Tóth, L. V., & Lemke, D., Early Stages of Massive Star Formation Revealed by ISO, 2004, Baltic Astronomy, 13, 407

Krumholz, M. R., McKee, C. F., & Klein, R. I., How Protostellar Outflows Help Massive Stars Form, 2005, ApJL, 618, L33

Krumholz, M. R., Klein, R. I., & McKee, C. F., Radiation Pressure in Massive Star Formation, 2005, Protostars and Planets V, 8271

Krumholz, M. R., Klein, R. I., & McKee, C. F., Radiation-Hydrodynamic Simulations of Collapse and Fragmentation in Massive Protostellar Cores, 2007, ApJ, 656, 959

Krumholz, M. R., & McKee, C. F., A minimum column density of $1\,\mathrm{g\,cm^{-2}}$ for massive star formation, 2008, Nature, 451, 1082

Kuchar, T. A., & Bania, T. M., Kinematic distances of Galactic H II regions from H I absorption studies, 1994, ApJ, 436, 117

Kuiper, R., Klahr, H., Beuther, H., & Henning, T., Circumventing the Radiation Pressure Barrier in the Formation of Massive Stars via Disk Accretion, 2010, ApJ, 722, 1556

Lada, C. J., Star formation - From OB associations to protostars, 1987, Star Forming Regions, 115, 1

Ladd, N., Purcell, C., Wong, T., & Robertson, S., Beam Size, Shape and Efficiencies for the ATNF Mopra Radio Telescope at $86 - 115\,\mathrm{GHz}$, 2005, PASA, 22, 62

Lahuis, F. et al. 2006, c2d Spectroscopy Explanatory Supplement, Tech. rep., Cores to Disks, Spitzer legacy team, Pasadena: Spitzer Science Center

Lahuis, F., van Dishoeck, E. F., Jørgensen, J. K., Blake, G. A., & Evans, N. J., c2d Spitzer IRS spectra of embedded low-mass young stars: gas-phase emission lines, 2010, A&A, 519, A3

Larson, R. B., Turbulence and star formation in molecular clouds, 1981, MNRAS, 194, 809

Larson, R. B., Thermal physics, cloud geometry and the stellar initial mass function, 2005, MNRAS, 359, 211

Lemke, D., The short history of infrared space telescopes, 2009, Astronomische Nachrichten, 330, 562

Li, Y., Klessen, R. S., & Mac Low, M.-M., The Formation of Stellar Clusters in Turbulent Molecular Clouds: Effects of the Equation of State, 2003, ApJ, 592, 975

MacLaren, I., Richardson, K. M., & Wolfendale, A. W., Corrections to virial estimates of molecular cloud masses, 1988, ApJ, 333, 821

Mac Low, M.-M., & Klessen, R. S., Control of star formation by supersonic turbulence, 2004, Reviews of Modern Physics, 76, 125

Makovoz, D., & Marleau, F. R., Point-Source Extraction with MOPEX, 2005, PASP, 117, 1113

McKee, C. F., & Tan, J. C., Massive star formation in 100,000 years from turbulent and pressurized molecular clouds 2002, Nature, 416, 59

McKee, C. F., & Tan, J. C., The Formation of Massive Stars from Turbulent Cores, 2003, ApJ, 585, 850

Molinari, S., Schisano, E., Faustini, F., et al. Source extraction and photometry for the far-infrared and sub-millimeter continuum in the presence of complex backgrounds, 2011, A&A, 530, A133

Monaco, P., On the destruction of star-forming clouds, 2004, MNRAS, 354, 151

Miettinen, O., Hennemann, M., & Linz, H., Deuterium fractionation and the degree of ionisation in massive clumps within infrared dark clouds, 2011, A&A, 534, A134

Miettinen, O., A molecular line study of the filamentary infrared dark cloud G304.74+01.32, 2012, A&A, 540, A104

Motte, F., Bontemps, S., Schilke, P., Schneider, N., Menten, K. M., & Broguière, D., The earliest phases of high-mass star formation: a 3 square degree millimeter continuum mapping of Cygnus X, 2007, A&A, 476, 1243

Müller, H. S. P., Thorwirth, S., Roth, D. A., & Winnewisser, G., The Cologne Database for Molecular Spectroscopy, CDMS, 2001, A&A, 370, L49

Nagasawa, M., Gravitational Instability of the Isothermal Gas Cylinder with an Axial magnetic Field, 1987, Progress of Theoretical Physics, 77, 635

Nakano, T., Star Formation in Magnetic Clouds, 1998, ApJ, 494, 587

Ormel, C. W., Shipman, R. F., Ossenkopf, V., & Helmich, F. P., The modelling of infrared dark cloud cores, 2005, A&A, 439, 613

Osorio, M., Lizano, S., & D'Alessio, P., Hot Molecular Cores and the Formation of Massive Stars, 1999, ApJ, 525, 808

Ossenkopf, V., & Henning, T., Dust opacities for protostellar cores, 1994, A&A, 291, 943

Ossenkopf, V., Ormel, C. W., Simon, R., Sun, K., & Stutzki, J., Spectroscopic [C I] mapping of the infrared dark cloud G48.65–0.29, 2011, A&A, 525, A9

Ostriker, J., The Equilibrium of Polytropic and Isothermal Cylinders., 1964, ApJ, 140, 1056

Padoan, P., & Nordlund, Å., The Stellar Initial Mass Function from Turbulent Fragmentation, 2002, ApJ, 576, 870

Pavlyuchenkov, Y. N., Wiebe, D. S., Akimkin, V. V., Khramtsova, M. S., & Henning, T., Stochastic grain heating and mid-infrared emission in protostellar cores, 2012, MNRAS, 2407

Peeters, E., Hony, S., Van Kerckhoven, C., Tielens, A. G. G. M., Allamandola, L. J., Hudgins, D. M., & Bauschlicher, C. W., The rich 6 to 9 μm spectrum of interstellar PAHs, 2002, A&A, 390, 1089

Perault, M., Omont, A., Simon, G., et al., First ISOCAM images of the Milky Way., 1996, A&A, 315, L165

Peretto, N., & Fuller, G. A., The initial conditions of stellar protocluster formation. I. A catalogue of Spitzer dark clouds, 2009, A&A, 505, 405

Peretto, N., Fuller, G. A., Plume, R., et al., Mapping the column density and dust temperature structure of IRDCs with Herschel, 2010, A&A, 518, L98

Peretto, N., André, P., Könyves, V., et al., The Pipe Nebula as seen with Herschel: formation of filamentary structures by large-scale compression?, 2012, A&A, 541, A63

Pilbratt, G. L., Riedinger, J. R., Passvogel, T., et al., Herschel Space Observatory. An ESA facility for far-infrared and submillimetre astronomy, 2010, A&A, 518, L1

Pillai, T., Wyrowski, F., Carey, S. J., & Menten, K. M., Ammonia in infrared dark clouds, 2006, A&A, 450, 569

Poglitsch, A., Waelkens, C., Geis, N., et al., The Photodetector Array Camera and Spectrometer (PACS) on the Herschel Space Observatory, 2010, A&A, 518, L2

Prim, R. C., 1957, Bell System Technical Journal, 36, 1389

Quanz, S. P., Henning, T., Bouwman, J., van Boekel, R., Juhász, A., Linz, H., Pontoppidan, K. M., & Lahuis, F., Evolution of Dust and Ice Features around FU Orionis Objects, 2007, ApJ, 668, 359

Ragan, S. E., Bergin, E. A., Plume, R., et al., Molecular Line Observations of Infrared Dark Clouds: Seeking the Precursors to Intermediate and Massive Star Formation, 2006, ApJS, 166, 567

Ragan, S. E., Bergin, E. A., & Gutermuth, R. A., Detection of Structure in Infrared-Dark Clouds with Spitzer: Characterizing Star Formation in the Molecular Ring 2009, ApJ, 698, 324

Ragan, S. E., Bergin, E. A., & Wilner, D., Very Large Array Observations of Ammonia in Infrared-dark Clouds. I. Column Density and Temperature Structure, 2011, ApJ, 736, 163

Ragan, S., Henning, T., Krause, O., et al., The Earliest Phases of Star Formation (EPoS): A Herschel Key Program - The precursors to high-mass stars and clusters, 2012, accepted to A&A, arXiv:1207.6518

Rathborne, J. M., Jackson, J. M., Chambers, E. T., Simon, R., Shipman, R., & Frieswijk, W., Massive Protostars in the Infrared Dark Cloud MSXDC G034.43+00.24, 2005, ApJL, 630, L181

Rathborne, J. M., Jackson, J. M., & Simon, R., Infrared Dark Clouds: Precursors to Star Clusters, 2006, ApJ, 641, 389

Reach, W. T., Megeath, S. T., Cohen, M., et al., Absolute Calibration of the Infrared Array Camera on the Spitzer Space Telescope, 2005, PASP, 117, 978

Reid, M. J., Menten, K. M., Zheng, X. W., et al., Trigonometric Parallaxes of Massive Star-Forming Regions. VI. Galactic Structure, Fundamental Parameters, and Noncircular Motions, 2009, ApJ, 700, 137

Rieke, G. H., Young, E. T., Engelbracht, C. W., et al., The Multiband Imaging Photometer for Spitzer (MIPS), 2004, ApJS, 154, 25

Robitaille, T. P., Whitney, B. A., Indebetouw, R., Wood, K., & Denzmore, P., Interpreting Spectral Energy Distributions from Young Stellar Objects. I. A Grid of 200,000 YSO Model SEDs, 2006, ApJS, 167, 256

Robitaille, T. P., Whitney, B. A., Indebetouw, R., & Wood, K., Interpreting Spectral Energy Distributions from Young Stellar Objects. II. Fitting Observed SEDs Using a Large Grid of Precomputed Models 2007, ApJS, 169, 328

Rosenthal, D., Bertoldi, F., & Drapatz, S., ISO-SWS observations of OMC-1: H_2 and fine structure lines, 2000, A&A, 356, 705

Roussel, H. 2012, submitted to A&A(arXiv:1205.2576)

Russeil, D., Zavagno, A., Motte, F., et al., The earliest phases of high-mass star formation: the NGC 6334-NGC 6357 complex, 2010, A&A, 515, A55

Sakai, T., Sakai, N., Kamegai, K., et al., A Molecular Line Observation toward Massive Clumps Associated with Infrared Dark Clouds, 2008, ApJ, 678, 1049

Sakai, T., Sakai, N., Hirota, T., & Yamamoto, S., A Survey of Molecular Lines Toward Massive Clumps in Early Evolutionary Stages of High-mass Star Formation, 2010, ApJ, 714, 1658

Sakai, T., Sakai, N., Furuya, K., et al., DNC/HNC Ratio of Massive Clumps in Early Evolutionary Stages of High-mass Star Formation, 2012, ApJ, 747, 140

Sato, M., Reid, M. J., Brunthaler, A., & Menten, K. M., Trigonometric Parallax of W51 Main/South, 2010, ApJ, 720, 1055

Schmalzl, M., Kainulainen, J., Quanz, S. P., et al., Star Formation in the Taurus Filament L 1495: From Dense Cores to Stars, 2010, ApJ, 725, 1327

Schuller, F., Menten, K. M., Contreras, Y., et al., ATLASGAL - The APEX telescope large area survey of the galaxy at 870 μm, 2009, A&A, 504, 415

Schuster, K.-F., Boucher, C., Brunswig, W., et al., A 230 GHz heterodyne receiver array for the IRAM 30 m telescope, 2004, A&A, 423, 1171

Selier, R., Heydari-Malayeri, M., & Gouliermis, D. A., An interesting candidate for isolated massive-star formation in the Small Magellanic Cloud, 2011, A&A, 529, A40

Semenov, D., Hersant, F., Wakelam, V., et al., Chemistry in disks. IV. Benchmarking gas-grain chemical models with surface reactions, 2010, A&A, 522, A42

Shu, F. H., Adams, F. C., & Lizano, S., Star formation in molecular clouds - Observation and theory 1987, ARAA, 25, 23

Simon, R., Rathborne, J. M., Shah, R. Y., Jackson, J. M., & Chambers, E. T. 2006, ApJ, 653, 1325

Shipman, R. F., Frieswijk, W., & Helmich, F. P., The Characterization and Galactic Distribution of Infrared Dark Clouds, 2003, Galactic Star Formation Across the Stellar Mass Spectrum, 287, 252

Smith, H. A., Hora, J. L., Marengo, M., & Pipher, J. L., The Characterization and Galactic Distribution of Infrared Dark Clouds, 2006, ApJ, 645, 1264

Smith, J. D. T., et al., The Mid-Infrared Spectrum of Star-forming Galaxies: Global Properties of Polycyclic Aromatic Hydrocarbon Emission, 2007, ApJ, 656, 770

Sodroski, T. J., Odegard, N., Arendt, R. G., et al., A Three-dimensional Decomposition of the Infrared Emission from Dust in the Milky Way, 1997, ApJ, 480, 173

Solomon, P. M., & Rivolo, A. R., A face-on view of the first galactic quadrant in molecular clouds, 1989, ApJ, 339, 919

Sridharan, T. K., Beuther, H., Schilke, P., Menten, K. M., & Wyrowski, F., High-Mass Protostellar Candidates. I. The Sample and Initial Results, 2002, ApJ, 566, 931

Sridharan, T. K., Beuther, H., Saito, M., Wyrowski, F., & Schilke, P., High-Mass Starless Cores, 2005, ApJL, 634, L57

Stutz, A. M., Rieke, G. H., Bieging, J. H., et al., Spitzer and Heinrich Hertz Telescope Observations of Starless Cores: Masses and Environments, 2009, ApJ, 707, 137

Swain, M. R., Bouwman, J., Akeson, R. L., Lawler, S., & Beichman, C. A., The Mid-Infrared Spectrum of the Transiting Exoplanet HD 209458b, 2008, ApJ, 674, 482

Tackenberg, J., Beuther, H., Henning, T., et al., Search for starless clumps in the ATLASGAL survey, 2012, A&A, 540, A113

Takami, M., Chen, H.-H., Karr, J. L., et al., Emission Mechanism of "Green Fuzzies" in High-mass Star-forming Regions, 2012, ApJ, 748, 8

Teyssier, D., Hennebelle, P., & Pérault, M., Radio-millimetre investigation of galactic infrared dark clouds, 2002, A&A, 382, 624

Tielens, A. G. G. M., & Hagen, W., Model calculations of the molecular composition of interstellar grain mantles, 1982, A&A, 114, 245

Tielens, A. G. G. M., Interstellar Polycyclic Aromatic Hydrocarbon Molecules, 2008, ARAA, 46, 289

Urquhart, J. S., Hoare, M. G., Lumsden, S. L., Oudmaijer, R. D., & Moore, T. J. T., The RMS Survey: A Galaxy-wide Sample of Massive Young Stellar Objects, 2008, Massive Star Formation: Observations Confront Theory, 387, 381

van der Wiel, M. H. D., & Shipman, R. F., Characterizing star formation activity in infrared dark cloud MSXDC G048.65–00.29 2008, A&A, 490, 655

van Dishoeck, E. F., Wright, C. M., Cernicharo, J., Gonzalez-Alfonso, E., de Graauw, T., Helmich, F. P., & Vandenbussche, B., The ISO-SWS $2.4 - 45.2\,\mu\mathrm{m}$ Spectrum Toward Orion IR c2, 1998, ApJL, 502, L173

Van Kerckhoven, C., et al., The C-C-C bending modes of PAHs: a new emission plateau from 15 to $20\,\mu\mathrm{m}$, 2000, A&A, 357, 1013

Vasyunina, T., Linz, H., Henning, T., et al., Physical properties of Southern infrared dark clouds, 2009, A&A, 499, 149

Vasyunina, T., Linz, H., Henning, T., Zinchenko, I., Beuther, H., & Voronkov, M., Chemistry in infrared dark clouds, 2011, A&A, 527, A88

Vasyunina, T., Vasyunin, A. I., Herbst, E., & Linz, H., Chemical Modeling of Infrared Dark Clouds: The Role of Surface Chemistry, 2012, ApJ, 751, 105

Wakelam, V., Herbst, E., Loison, J.-C., et al., A KInetic Database for Astrochemistry (KIDA), 2012, ApJS, 199, 21

Wang, K., Zhang, Q., Wu, Y., & Zhang, H., Hierarchical Fragmentation and Jet-like Outflows in IRDC G28.34+0.06: A Growing Massive Protostar Cluster, 2011, ApJ, 735, 64

Weingartner, J. C., & Draine, B. T., Dust Grain-Size Distributions and Extinction in the Milky Way, Large Magellanic Cloud, and Small Magellanic Cloud, 2001, ApJ, 548, 296

Werner, M. W., et al., The Spitzer Space Telescope Mission, 2004, ApJS, 154, 1

White, R. L., Becker, R. H., & Helfand, D. J., New Catalogs of Compact Radio Sources in the Galactic Plane, 2005, AJ, 130, 586

White, D. W., Gerakines, P. A., Cook, A. M. & Whittet, D. C. B., Laboratory Spectra of the CO_2 Bending-Mode Feature in Interstellar Ice Analogues Subject to Thermal Processing, 2009, ApJS, 180, 182

Wilcock, L. A., Ward-Thompson, D., Kirk, J. M., et al., Cores in infrared dark clouds (IRDCs) seen in the Hi-GAL survey between l= 300° and 330°, 2012, MNRAS, 422, 1071

Williams, J. P., de Geus, E. J., & Blitz, L., Determining structure in molecular clouds, 1994, ApJ, 428, 693

Wilson, T. L., & Rood, R., Abundances in the Interstellar Medium, 1994, ARAA, 32, 191

Wright, C. M., van Dishoeck, E. F., Black, J. H., Feuchtgruber, H., Cernicharo, J., González-Alfonso, E., & de Graauw, T., ISO-SWS observations of pure rotational H_2O absorption lines toward Orion-IRc2, 2000, A&A, 358, 689

Yorke, H. W., & Sonnhalter, C., On the Formation of Massive Stars, 2002, ApJ, 569, 846

Zhang, S. B., Yang, J., Xu, Y., Pandian, J. D., Menten, K. M., & Henkel, C., Early Phase of Massive Star Formation: A Case Study of the Infrared Dark Cloud G084.81–01.09, 2011, ApJS, 193, 10

Zinnecker, H., & Yorke, H. W., Toward Understanding Massive Star Formation, 2007, ARAA, 45, 481

Parts of this Dissertation were published here:

Pitann, J., Hennemann, M., Birkmann, S., et al., *Infrared Spectroscopy of Intermediate-mass Young Stellar Objects*, 2011, ApJ, 743, 93

Nomenclature

ATLASGAL ..... APEX Telescope Large Area Survey of the Galaxy
BGPS ..... Bolocam Galactic Plane Survey
BN/KL ..... Becklin-Neugebauer/Kleinman-Low nebular in Orion
CDMS ..... Cologne Database for Molecular Spectroscopy
EMST ..... Euclidean minimum spanning tree
EPoS ..... Herschel Key Program: Earliest Phases Of Star-Formation
FIR ..... Far-infrared ($3 - 300\,\mu\mathrm{m}$)
FUV ..... Far ultraviolet
GLIPSE ..... Galactic Legacy Infrared Mid-Plane Survey Extraordinaire
GMA ..... Giant Molecular Association
GMC ..... Giant Molecular Cloud
GTO ..... Guaranteed Time Observations
HCH II ..... Hypercompact H II region
Hi-GAL ..... Herschel Key Program: Herschel Infrared Galactic Plane Survey
HIFI ..... Heterodyne Instrument for Far Infrared on-board Herschel
HMC ..... Hot Molecular Core
HMPO ..... High-Mass Protostellar Objects
HMSC ..... High-Mass Starless Cores
IRAC ..... Infrared Array Camera on-board the Spitzer Space Telescope
IRAF ..... The "Image Reduction and Analysis Facility" software package
IRAM ..... Institut de Radioastronomie Millimétrique
IRAS ..... Infrared Astronomical Satellite
IRDC ..... Infrared Dark Cloud
IRS ..... Infrared Spectrograph on-board the Spitzer Space Telescope
ISM ..... Interstellar Medium
ISO ..... Infrared Space Observatory
ISOSS ..... ISOPHOT Serendipity Survey
JCMT ..... James Clerk Maxwell Telescope
KIDA ..... Kinetic Database for Astrochemistry
LAMBDA ..... Leiden Atomic and Molecular Database
LMC ..... Large Magellanic Cloud
MIPS ..... Multiband Imaging Photometer for Spitzer
MIPSGAL ..... MIPS Inner Galactic Plane Survey
MIR ..... Mid-infrared ($3 - 40\,\mu\mathrm{m}$)
MST ..... Minimum spanning tree
NIR ..... Near-infrared ($0.8 - 3\,\mu\mathrm{m}$)
PACS ..... Photodetector Array Camera and Spectrometer on-board Herschel
PAH ..... Polycyclic Aromatic Hydrocarbons
PDF ..... Probability Density Function

PDR ..... Photon dissociation region
PSF ..... Point spread function
RSRF ..... Relative spectral response function
SCUBA ..... Submillimetre Common-User Bolometer Array at JCMT
SED ..... Spectral energy distribution
SHA ..... Spitzer Heritage Archive
SMC ..... Small Magellanic Cloud
SPIRE ..... Spectral and Photometric Image Receiver on-board Herschel
SSC ..... Spitzer Science Center
UCH II ..... Ultracompact H II region
YSO ..... Young stellar object

Appendix A.
PACS point source extraction: Table and Figures

In Table A.1 the results from the photometric extraction described in Chapter 3 are shown. This are the raw results without source temperature corrections applied. The given coordinates are the source positions in the blue filter band. The labeling of the source in a particular region can differ from the IDs in the EPoS overview paper (Ragan et al. 2012). The temperatures and masses are results of a modified blackbody fitted to the raw fluxes of the three PACS bands. In the last column it is indicated how many sources were not detected by the pipeline (but found by visual inspection). Moreover, the listed sources are labeled as real point source detection (✓) or artifacts (✕).

In Figure A.1 to A.15 all high-mass regions of the EPoS sample are shown. The detections by the pipeline are overplotted. True point sources are indicted by a box point; false detections are marked with a cross.

Table A.1. – Nominal extraction for the EPoS-sample

Source	RA (J2000) [hh:mm:ss]	Dec (J2000) [dd:mm:ss]	Dist [kpc]	$F_{70\mu m}$ [Jy]	$F_{100\mu m}$ [Jy]	$F_{160\mu m}$ [Jy]	T [K]	M [$M_\odot$]	Comments
IRDC004.36									2 missed
1	17:55:48	-25:13:00	3.28	0.09	0.15	0.46	21.0	0.34	✕
IRDC009.86									2 missed
1	18:07:33	-20:26:20	2.66	3.56	4.80	6.30	25.8	1.53	✓
2	18:07:38	-20:26:22	2.66	0.55	0.77	1.05	25.4	0.27	✓
3	18:07:39	-20:26:40	2.66	0.36	0.48	1.02	23.4	0.33	✓
IRDC010.70									9 missed
1	18:09:16	-19:42:27	3.46	51.42	116.55	154.17	23.0	107.19	✓
2	18:09:15	-19:42:43	3.46	7.98	12.51	18.69	24.2	9.68	✓
3	18:09:45	-19:42:08	3.46	2.59	7.14	13.25	20.8	13.65	✓
4	18:09:56	-19:48:22	3.46	2.03	3.37	2.75	27.4	1.04	✓
5	18:09:48	-19:43:44	3.46	1.82	5.60	8.73	21.0	9.04	✓
6	18:09:36	-19:43:09	3.46	1.58	2.65	3.25	24.9	1.59	✓
7	18:10:06	-19:46:39	3.46	0.94	3.13	4.88	20.7	5.46	✓
8	18:09:34	-19:43:07	3.46	0.90	2.22	4.08	21.2	3.74	✓
9	18:10:08	-19:43:31	3.46	0.46	1.18	1.79	21.8	1.52	✓
10	18:09:42	-19:47:07	3.46	0.39	0.94	1.62	21.6	1.39	✓
11	18:09:33	-19:44:04	3.46	0.39	1.30	2.43	20.1	2.99	✓
12	18:10:03	-19:43:52	3.46	0.37	1.00	3.84	18.5	5.92	✓
13	18:10:08	-19:44:55	3.46	0.15	0.45	1.50	18.5	2.36	✓
14	18:09:51	-19:45:45	3.46	0.13	0.56	1.01	19.2	1.63	✕
15	18:09:56	-19:45:41	3.46	0.11	0.49	1.71	17.4	3.88	✕
16	18:09:54	-19:44:12	3.46	0.09	0.45	1.66	16.9	4.40	✕
17	18:10:05	-19:49:11	3.46	0.08	0.67	1.89	16.4	6.90	✕
18	18:09:16	-19:45:17	3.46	1.25	1.88	1.39	28.7	0.45	✓
19	18:09:35	-19:42:54	3.46	0.82	1.14	1.95	24.2	0.97	✓
20	18:09:37	-19:41:43	3.46	0.73	1.39	3.58	21.0	3.11	✓
21	18:09:39	-19:45:14	3.46	0.58	1.52	2.99	20.7	3.04	✓

Table A.1. – Continuation of Table A.1.

Source	RA (J2000) [hh:mm:ss]	Dec (J2000) [dd:mm:ss]	Dist [kpc]	$F_{70\mu m}$ [Jy]	$F_{100\mu m}$ [Jy]	$F_{160\mu m}$ [Jy]	T [K]	M [$M_\odot$]	Comments
IRDC011.11									5 missed
1	18:10:28	-19:22:29	3.41	75.87	134.97	137.75	25.6	62.56	✓
2	18:10:07	-19:29:15	3.41	4.41	12.19	20.43	21.1	19.26	✓
3	18:10:38	-19:19:50	3.41	4.17	6.61	6.77	26.3	2.74	✓
4	18:10:05	-19:26:34	3.41	3.38	5.98	7.19	24.7	3.59	✓
5	18:10:27	-19:18:12	3.41	2.54	4.04	5.84	24.3	2.92	✓
6	18:10:09	-19:25:55	3.41	1.79	2.05	2.16	28.3	0.64	✓
7	18:10:33	-19:22:07	3.41	1.48	2.62	3.68	23.9	2.01	✓
8	18:10:34	-19:22:14	3.41	0.77	0.21	1.40	26.2	0.30	×
9	18:10:32	-19:24:50	3.41	0.57	0.93	2.08	22.2	1.37	✓
10	18:10:35	-19:16:19	3.41	0.52	1.11	1.65	22.7	1.13	✓
11	18:10:42	-19:19:57	3.41	0.44	1.02	1.50	22.4	1.10	✓
12	18:10:38	-19:19:01	3.41	0.43	0.82	0.96	24.4	0.51	✓
13	18:10:07	-19:26:00	3.41	0.40	1.04	1.60	21.7	1.34	✓
14	18:10:31	-19:22:27	3.41	0.39	0.96	-1.87	-1.87	-1.87	✓
15	18:10:34	-19:19:18	3.41	0.20	0.46	1.29	1.29	1.29	✓
16	18:10:32	-19:18:48	3.41	0.10	0.20	1.01	1.01	1.01	×
17	18:10:35	-19:15:16	3.41	0.08	0.37	0.93	0.93	0.93	×
18	18:10:19	-19:24:24	3.41	0.61	1.19	2.12	2.12	2.12	✓
IRDC013.90									0 missed
1	18:17:35	-17:06:54	2.59	5.53	8.25	12.90	24.3	3.65	✓
2	18:17:34	-17:06:38	2.59	2.77	5.66	9.58	22.4	3.89	✓
3	18:17:27	-17:05:34	2.59	1.80	4.19	5.26	23.1	2.04	✓
4	18:17:24	-17:07:04	2.59	1.32	1.67	2.75	24.9	0.68	✓
5	18:17:23	-17:06:51	2.59	1.10	1.21	2.35	24.8	0.56	✓
6	18:17:21	-17:04:25	2.59	0.50	1.11	1.64	22.6	0.67	✓
7	18:17:34	-17:07:39	2.59	0.45	0.84	1.74	21.9	0.73	×
8	18:17:27	-17:03:34	2.59	0.35	0.78	1.11	22.7	0.44	×
9	18:17:29	-17:03:44	2.59	0.28	0.85	1.34	20.9	0.79	×
10	18:17:24	-17:02:27	2.59	0.17	0.42	1.41	19.2	1.01	×
11	18:17:23	-17:02:39	2.59	0.17	0.46	1.06	20.1	0.68	×
12	18:17:32	-17:05:47	2.59	0.16	0.29	0.59	22.2	0.23	×
13	18:17:33	-17:05:01	2.59	0.16	0.33	0.82	20.9	0.41	×
14	18:17:38	-17:05:55	2.59	0.14	0.73	0.95	19.8	0.81	×
15	18:17:32	-17:04:33	2.59	0.14	0.42	0.95	19.8	0.66	×
16	18:17:39	-17:07:34	2.59	0.14	0.56	2.14	17.4	2.69	×
17	18:17:33	-17:08:00	2.59	0.14	0.49	1.29	18.7	1.19	×
18	18:17:39	-17:07:15	2.59	0.13	0.50	2.15	17.1	2.87	×
19	18:17:26	-17:02:37	2.59	0.11	0.37	0.99	19.0	0.83	×
20	18:17:23	-17:02:34	2.59	0.09	0.37	1.31	17.4	1.66	×
21	18:17:25	-17:02:10	2.59	7.26	7.73	8.91	28.2	1.49	✓
22	18:17:16	-17:11:04	2.59	1.00	1.96	2.56	23.8	0.86	✓
23	18:17:24	-17:04:01	2.59	0.62	2.59	4.40	19.5	3.64	✓
24	18:17:28	-17:07:15	2.59	0.38	0.43	1.09	23.4	0.31	×
25	18:17:37	-17:05:54	2.59	0.19	0.43	0.63	22.4	0.27	×
IRDC015.05									0 missed
1	18:17:39	-15:49:03	2.95	3.31	5.24	6.38	25.3	2.14	✓
2	18:17:35	-15:48:43	2.95	0.09	1.50	2.05	16.2	7.48	×
3	18:17:35	-15:48:32	2.95	0.08	0.33	2.20	16.1	4.89	×

Table A.1. – Continuation of Table A.1.

Source	RA (J2000) [hh:mm:ss]	Dec (J2000) [dd:mm:ss]	Dist [kpc]	$F_{70\mu m}$ [Jy]	$F_{100\mu m}$ [Jy]	$F_{160\mu m}$ [Jy]	T [K]	M [$M_\odot$]	Comments
IRDC019.30									3 missed
1	18:25:58	-12:03:58	2.36	12.61	37.46	61.21	20.9	29.24	✓
2	18:25:58	-12:04:20	2.36	2.53	3.40	3.72	26.9	0.64	✓
3	18:25:52	-12:04:50	2.36	1.09	4.51	10.77	18.5	8.88	✓
4	18:25:51	-12:07:09	2.36	0.53	1.00	2.23	21.6	0.82	✓
5	18:25:58	-12:10:00	2.36	0.24	0.90	2.32	18.6	1.81	×
6	18:26:01	-12:03:50	2.36	0.09	0.29	1.43	17.3	1.42	×
7	18:26:04	-12:05:31	2.36	0.08	0.17	0.53	20.1	0.25	×
8	18:25:52	-12:05:12	2.36	0.15	-0.02	1.87	1.87	1.87	✓
9	18:26:01	-12:02:43	2.36	0.09	0.32	0.79	0.79	0.79	×
IRDC028.34									5 missed
1	18:42:26	-04:01:28	4.52	195.78	242.98	185.33	30.0	85.59	✓
2	18:42:37	-04:02:01	4.52	145.25	171.24	150.80	29.4	72.27	✓
3	18:42:52	-03:59:54	4.52	43.05	141.39	221.73	20.7	418.84	✓
4	18:42:41	-03:57:05	4.52	11.20	17.26	17.32	26.6	11.82	✓
5	18:42:41	-04:02:17	4.52	5.44	6.49	3.97	32.3	1.53	✓
6	18:42:32	-04:01:08	4.52	5.06	9.68	15.00	23.1	16.51	✓
7	18:42:54	-04:02:32	4.52	3.13	7.22	11.28	22.2	15.01	✓
8	18:42:50	-04:03:11	4.52	1.52	5.35	13.82	18.8	37.28	✓
9	18:42:50	-04:01:58	4.52	1.40	4.09	6.37	21.2	10.62	✓
10	18:42:42	-04:01:35	4.52	1.28	3.03	6.20	21.0	9.88	✓
11	18:42:51	-03:59:24	4.52	0.68	4.56	9.09	17.7	39.25	✓
12	18:42:43	-04:05:01	4.52	0.61	1.50	4.27	19.7	8.64	✓
13	18:42:29	-04:02:33	4.52	0.46	0.83	2.39	20.8	3.54	×
14	18:42:54	-04:02:21	4.52	0.46	1.34	3.94	19.0	9.56	✓
15	18:42:49	-04:02:32	4.52	0.35	1.16	2.64	19.4	6.32	✓
16	18:42:45	-03:57:59	4.52	0.26	0.60	3.34	17.9	9.26	×
17	18:42:51	-04:03:36	4.52	0.19	0.67	0.69	22.1	1.07	×
18	18:43:00	-03:59:31	4.52	0.14	0.41	1.40	18.5	3.72	✓
19	18:42:49	-04:03:59	4.52	0.10	0.46	1.23	18.0	4.21	×
20	18:42:50	-04:04:04	4.52	0.09	0.57	1.23	17.6	5.21	×
21	18:42:34	-04:00:33	4.52	2.20	5.86	7.55	22.3	10.36	✓
22	18:42:47	-03:58:14	4.52	0.09	0.54	3.37	15.2	26.42	×
IRDC048.66									3 missed
1	19:21:50	13:49:39	2.63	4.53	7.18	10.32	24.4	3.04	✓
2	19:21:49	13:49:31	2.63	2.19	4.23	6.95	22.8	2.70	✓
3	19:21:50	13:48:18	2.63	2.12	3.79	4.57	24.6	1.37	✓
4	19:21:47	13:49:20	2.63	0.61	1.93	4.56	19.4	3.58	✓
5	19:21:40	13:51:17	2.63	0.45	0.51	0.67	26.9	0.13	✓
6	19:21:40	13:50:54	2.63	0.15	0.32	0.86	20.3	0.51	✓
7	19:21:45	13:49:20	2.63	0.37	0.87	1.32	22.2	0.59	✓
IRDC079.31									2 missed
1	20:32:29	40:16:05	1.56	65.54	88.50	126.01	25.3	11.08	✓
2	20:32:22	40:20:18	1.56	13.61	46.56	68.38	20.8	15.42	✓
3	20:32:28	40:19:43	1.56	11.54	13.77	14.50	28.0	0.94	✓
4	20:32:22	40:19:40	1.56	10.50	14.11	17.04	26.3	1.35	✓
5	20:31:58	40:18:37	1.56	6.66	10.41	16.03	24.1	1.71	✓
6	20:32:20	40:19:51	1.56	4.92	7.00	86.26	17.1	28.37	✓
7	20:32:23	40:19:24	1.56	3.00	4.12	6.77	24.5	0.66	✓
8	20:31:45	40:19:20	1.56	2.80	4.26	5.20	25.5	0.47	✓

Table A.1. – Continuation of Table A.1.

Source	RA (J2000) [hh:mm:ss]	Dec (J2000) [dd:mm:ss]	Dist [kpc]	$F_{70\mu m}$ [Jy]	$F_{100\mu m}$ [Jy]	$F_{160\mu m}$ [Jy]	T [K]	M [$M_\odot$]	Comments
9	20:32:02	40:18:40	1.56	2.30	4.13	6.61	23.2	0.83	✓
10	20:31:41	40:17:55	1.56	2.23	3.56	6.21	23.4	0.73	✓
11	20:32:14	40:19:45	1.56	1.94	4.87	8.85	21.2	1.66	×
12	20:32:21	40:16:06	1.56	1.65	2.31	1.75	29.1	0.11	✓
13	20:31:47	40:18:59	1.56	1.40	1.69	1.33	30.0	0.07	✓
14	20:31:52	40:18:33	1.56	1.23	2.91	4.50	22.1	0.73	✓
15	20:31:45	40:18:47	1.56	0.95	1.73	2.39	23.9	0.28	✓
16	20:32:01	40:15:05	1.56	0.55	1.00	1.77	22.7	0.24	×
17	20:32:06	40:15:05	1.56	0.35	0.49	0.67	25.3	0.06	×
18	20:31:47	40:19:21	1.56	0.30	0.55	1.14	22.0	0.17	✓
19	20:31:48	40:19:03	1.56	0.28	0.46	0.63	24.3	0.07	✓
20	20:31:53	40:19:07	1.56	0.28	0.47	0.82	23.1	0.10	✓
21	20:31:54	40:21:43	1.56	0.24	0.48	0.76	22.7	0.11	✓
22	20:31:55	40:17:24	1.56	0.20	0.56	1.09	20.5	0.24	✓
23	20:32:01	40:13:46	1.56	0.22	0.36	0.56	23.8	0.06	✓
IRDC18102									1 missed
1	18:13:11	-17:59:57	2.60	73.36	128.08	162.41	24.5	47.94	✓
2	18:13:12	-17:59:40	2.60	23.41	35.31	52.55	24.5	14.74	✓
3	18:13:12	-17:56:19	2.60	18.96	24.32	28.30	26.8	5.81	✓
4	18:13:13	-17:59:27	2.60	11.14	16.34	40.81	22.2	15.14	✓
5	18:13:05	-18:00:13	2.60	8.40	10.27	9.61	28.6	1.64	✓
6	18:13:00	-18:02:48	2.60	3.62	7.15	15.33	21.5	6.99	✓
7	18:13:13	-17:56:17	2.60	1.90	5.82	8.82	21.1	5.06	×
8	18:13:01	-18:02:45	2.60	1.47	4.40	14.96	18.5	13.36	✓
9	18:12:58	-18:01:02	2.60	1.33	1.92	3.23	24.1	0.93	✓
10	18:13:13	-18:02:11	2.60	1.08	2.37	4.04	22.0	1.78	✓
11	18:13:13	-17:57:20	2.60	0.23	0.73	1.59	19.7	1.17	×
12	18:13:13	-17:57:17	2.60	0.13	0.38	0.75	20.2	0.50	×
13	18:13:05	-18:01:50	2.60	0.06	0.20	0.79	17.8	0.83	×
14	18:13:11	-18:02:17	2.60	0.06	0.33	1.17	16.6	2.00	×
15	18:12:55	-18:02:29	2.60	1.49	3.66	5.36	22.2	2.41	✓
IRDC18151									0 missed
1	18:17:58	-12:07:24	2.65	465.04	585.53	484.87	29.3	82.27	✓
2	18:17:50	-12:07:53	2.65	20.00	59.51	102.27	20.8	63.51	✓
3	18:17:52	-12:06:48	2.65	18.42	21.01	34.14	25.6	7.91	✓
4	18:17:57	-12:05:44	2.65	0.78	2.50	11.10	17.6	12.79	×
5	18:17:49	-12:09:17	2.65	0.73	1.92	18.83	16.1	28.67	✓
6	18:18:06	-12:06:56	2.65	0.64	2.32	5.85	18.8	5.48	×
7	18:17:50	-12:10:47	2.65	0.64	1.42	2.58	21.7	1.23	×
8	18:17:29	-12:06:48	2.65	0.48	1.52	2.92	20.1	2.04	✓
9	18:17:58	-12:02:20	2.65	0.47	0.91	1.84	21.9	0.83	×
10	18:17:58	-12:03:49	2.65	0.40	0.51	3.06	19.5	1.72	×
11	18:17:52	-12:09:52	2.65	0.39	1.04	3.79	18.7	3.25	✓
12	18:17:59	-12:03:48	2.65	0.37	0.84	2.49	19.8	1.64	×
13	18:17:36	-12:06:39	2.65	0.33	0.64	2.10	20.0	1.25	×
14	18:18:07	-12:09:09	2.65	0.32	1.28	6.76	16.6	10.59	×
15	18:18:10	-12:08:39	2.65	0.32	2.13	2.38	19.3	2.53	×
16	18:18:00	-12:08:31	2.65	0.32	2.38	6.69	16.5	13.68	✓
17	18:17:41	-12:13:12	2.65	0.31	0.66	1.79	20.4	1.05	×
18	18:17:44	-12:03:48	2.65	0.30	0.66	1.96	20.0	1.24	×
19	18:17:53	-12:10:20	2.65	0.30	0.78	1.57	20.7	0.93	✓

Table A.1. – Continuation of Table A.1.

Source	RA (J2000) [hh:mm:ss]	Dec (J2000) [dd:mm:ss]	Dist [kpc]	$F_{70\mu m}$ [Jy]	$F_{100\mu m}$ [Jy]	$F_{160\mu m}$ [Jy]	T [K]	M [$M_\odot$]	Comments
20	18:18:07	-12:09:04	2.65	0.30	0.81	7.06	16.3	10.33	×
21	18:17:36	-12:05:19	2.65	0.23	0.76	1.74	19.3	1.45	×
22	18:18:00	-12:02:02	2.65	0.22	0.65	1.12	20.8	0.68	×
23	18:18:07	-12:11:30	2.65	0.22	0.51	1.30	20.2	0.81	✓
24	18:17:59	-12:04:41	2.65	0.19	0.48	0.72	21.9	0.36	×
25	18:17:41	-12:06:20	2.65	0.18	0.53	3.58	16.7	4.97	×
26	18:17:41	-12:06:21	2.65	0.17	0.55	2.82	17.1	3.61	×
27	18:17:35	-12:04:20	2.65	0.16	0.43	0.93	20.3	0.59	×
28	18:17:34	-12:11:20	2.65	0.16	0.35	0.51	22.6	0.22	×
29	18:18:06	-12:11:58	2.65	0.15	0.34	0.59	21.7	0.29	✓
30	18:17:49	-12:12:50	2.65	0.14	0.39	1.55	18.4	1.42	×
31	18:17:47	-12:05:34	2.65	0.14	0.72	1.58	18.1	1.94	×
32	18:17:31	-12:08:00	2.65	0.14	0.80	1.70	17.9	2.32	×
33	18:17:52	-12:05:10	2.65	0.14	0.58	1.47	18.3	1.64	×
34	18:17:30	-12:07:32	2.65	0.12	0.40	3.19	16.1	5.36	×
35	18:17:38	-12:04:34	2.65	0.08	0.39	0.97	18.1	1.16	×
36	18:17:31	-12:06:06	2.65	0.40	1.59	4.54	18.2	4.97	×
37	18:17:33	-12:09:04	2.65	0.31	0.74	1.72	20.5	1.04	×
IRDC18182									1 missed
1	18:21:09	-14:31:48	3.44	295.35	534.18	569.54	25.2	274.75	✓
2	18:21:15	-14:33:02	3.44	5.45	10.57	16.28	23.0	10.48	✓
3	18:21:30	-14:30:41	3.44	5.41	7.33	8.51	26.5	3.22	✓
4	18:21:05	-14:31:22	3.44	2.74	4.30	5.06	25.5	2.25	✓
5	18:21:23	-14:33:24	3.44	2.68	6.20	9.92	22.1	7.78	✓
6	18:21:01	-14:33:11	3.44	2.52	4.62	6.38	23.8	3.65	✓
7	18:20:58	-14:31:02	3.44	1.93	2.67	3.40	25.8	1.39	✓
8	18:20:59	-14:33:38	3.44	1.74	2.48	2.31	27.5	0.81	✓
9	18:21:00	-14:33:48	3.44	1.38	2.23	2.72	25.2	1.26	✓
10	18:21:15	-14:28:39	3.44	0.69	1.40	1.93	23.4	1.21	✓
11	18:21:10	-14:29:39	3.44	0.58	1.40	2.43	21.5	2.10	✓
12	18:21:00	-14:33:15	3.44	0.48	1.04	2.01	21.6	1.64	✓
13	18:21:15	-14:28:54	3.44	0.42	0.81	0.70	26.1	0.32	✓
14	18:21:18	-14:31:32	3.44	0.25	0.51	1.07	21.5	0.87	✓
15	18:21:24	-14:27:10	3.44	0.25	0.56	1.01	21.7	0.83	✓
16	18:21:15	-14:32:36	3.44	0.24	1.23	3.98	17.1	10.22	✓
17	18:21:18	-14:31:26	3.44	0.21	0.29	0.88	21.6	0.62	✓
18	18:20:50	-14:32:25	3.44	0.14	0.39	1.20	19.0	1.65	✓
19	18:21:17	-14:34:31	3.44	0.13	0.47	1.27	18.6	2.08	✓
20	18:20:49	-14:32:57	3.44	0.12	0.38	1.18	18.6	1.82	✓
21	18:20:56	-14:30:59	3.44	0.11	0.47	2.65	16.2	7.91	✓
22	18:20:57	-14:33:27	3.44	0.10	0.46	1.79	16.8	4.82	✓
23	18:21:22	-14:33:02	3.44	0.09	0.50	7.95	13.8	55.53	×
24	18:21:15	-14:34:19	3.44	0.07	0.37	1.09	17.3	2.66	×
25	18:21:12	-14:35:25	3.44	0.07	0.40	1.21	16.9	3.52	×
26	18:21:25	-14:32:23	3.44	0.21	0.68	2.16	18.5	3.51	✓
IRDC18223									1 missed
1	18:25:10	-12:42:23	3.50	78.05	159.94	219.54	23.3	144.39	✓
2	18:25:09	-12:44:06	3.50	10.29	15.47	20.14	25.2	9.42	✓
3	18:25:08	-12:45:22	3.50	7.85	24.36	42.05	20.6	47.55	✓
4	18:25:09	-12:43:14	3.50	7.32	10.87	12.57	26.0	5.40	✓
5	18:25:11	-12:41:49	3.50	3.11	6.22	29.45	18.8	39.01	✓

Table A.1. – Continuation of Table A.1.

Source	RA (J2000) [hh:mm:ss]	Dec (J2000) [dd:mm:ss]	Dist [kpc]	$F_{70\mu m}$ [Jy]	$F_{100\mu m}$ [Jy]	$F_{160\mu m}$ [Jy]	T [K]	M [$M_\odot$]	Comments
6	18:25:12	-12:41:47	3.50	2.63	4.85	20.38	19.4	23.30	✓
7	18:25:07	-12:47:51	3.50	1.33	3.86	6.68	20.8	7.10	✓
8	18:25:17	-12:48:26	3.50	0.86	2.12	4.82	20.5	5.09	✓
9	18:25:20	-12:51:21	3.50	0.76	2.27	3.86	20.8	4.18	✓
10	18:25:22	-12:52:33	3.50	0.68	0.87	0.97	27.1	0.35	✓
11	18:25:13	-12:44:29	3.50	0.66	1.55	2.79	21.5	2.46	✓
12	18:25:19	-12:52:10	3.50	0.54	1.26	2.19	21.7	1.88	✓
13	18:25:20	-12:45:41	3.50	0.47	0.88	1.48	22.8	1.01	✓
14	18:25:08	-12:50:11	3.50	0.27	0.65	1.66	20.2	1.82	×
15	18:25:24	-12:52:31	3.50	0.19	0.27	0.64	22.6	0.40	×
16	18:25:21	-12:54:19	3.50	0.15	0.48	0.73	21.0	0.77	×
17	18:25:21	-12:52:22	3.50	0.09	0.25	0.87	18.5	1.40	×
18	18:25:18	-12:52:14	3.50	0.07	0.31	1.18	17.2	2.86	×
19	18:25:06	-12:45:57	3.50	2.77	5.70	9.87	22.2	7.46	✓
20	18:25:19	-12:45:49	3.50	0.04	0.20	0.77	16.6	2.36	×
IRDC18306									0 missed
1	18:33:23	-08:33:33	3.64	69.09	174.72	282.15	21.6	271.92	✓
2	18:33:17	-08:33:22	3.64	38.25	56.91	60.97	26.4	27.12	✓
3	18:33:27	-08:34:42	3.64	1.18	0.57	2.02	26.4	0.59	×
4	18:33:29	-08:27:27	3.64	0.41	0.88	2.00	21.0	2.01	✓
5	18:33:30	-08:28:44	3.64	0.13	0.40	5.90	14.9	25.31	×
6	18:33:34	-08:31:50	3.64	0.09	0.42	1.02	18.1	2.31	×
7	18:33:37	-08:31:10	3.64	0.07	0.24	0.99	17.7	2.11	×
8	18:33:17	-08:31:42	3.64	0.07	0.32	0.89	17.7	2.21	×
9	18:33:16	-08:34:24	3.64	0.60	1.38	3.37	20.5	3.74	✓
10	18:33:31	-08:28:41	3.64	0.12	0.47	1.71	17.5	4.10	×
11	18:33:20	-08:31:09	3.64	0.09	0.32	0.75	19.2	1.21	×
IRDC18308									0 missed
1	18:33:32	-08:39:16	4.43	56.48	100.47	157.31	23.4	155.71	✓
2	18:33:29	-08:38:35	4.43	18.92	24.25	26.82	27.2	15.48	✓
3	18:33:34	-08:38:40	4.43	3.41	6.50	8.99	23.6	8.86	✓
4	18:33:30	-08:41:53	4.43	0.48	1.26	2.00	21.5	2.94	✓
5	18:33:30	-08:36:24	4.43	0.18	0.58	2.38	17.8	7.42	×
6	18:33:31	-08:37:16	4.43	0.09	0.27	0.57	19.9	1.16	×
7	18:33:27	-08:38:50	4.43	-0.02	0.87	3.42	3.42	3.42	✓
IRDC18310									0 missed
1	18:33:47	-08:23:33	4.91	65.05	89.82	131.76	25.0	119.61	✓
2	18:33:43	-08:21:21	4.91	47.62	133.95	214.77	21.2	416.65	✓
3	18:33:47	-08:23:46	4.91	20.28	30.32	400.71	16.8	1427.36	✓
4	18:33:43	-08:25:19	4.91	10.53	21.85	28.60	23.5	36.45	✓
5	18:33:44	-08:24:03	4.91	4.33	6.73	7.78	25.7	6.90	✓
6	18:33:46	-08:24:44	4.91	3.54	4.85	5.81	26.2	4.63	✓
7	18:33:41	-08:25:15	4.91	1.35	2.52	3.56	23.6	4.27	✓
8	18:33:39	-08:21:56	4.91	0.60	1.21	2.04	22.5	2.92	✓
9	18:33:37	-08:20:44	4.91	0.10	0.61	1.32	17.6	6.75	×
10	18:33:49	-08:19:06	4.91	0.06	2.49	1.36	16.0	20.23	×
11	18:33:37	-08:21:49	4.91	0.12	0.50	1.33	18.1	5.22	×
IRDC18337									4 missed
1	18:36:27	-07:40:33	3.66	39.72	48.05	43.07	29.0	14.05	✓
2	18:36:18	-07:40:56	3.66	4.32	12.80	20.45	21.0	23.15	✓

Table A.1. – Continuation of Table A.1.

Source	RA (J2000) [hh:mm:ss]	Dec (J2000) [dd:mm:ss]	Dist [kpc]	$F_{70\mu m}$ [Jy]	$F_{100\mu m}$ [Jy]	$F_{160\mu m}$ [Jy]	T [K]	M [$M_\odot$]	Comments
3	18:36:12	-07:41:39	3.66	3.72	8.86	15.19	21.6	14.47	✓
4	18:36:10	-07:44:06	3.66	2.37	6.25	15.88	19.8	20.93	✓
5	18:36:08	-07:43:18	3.66	0.44	2.34	4.72	18.3	10.86	×
6	18:36:19	-07:41:39	3.66	0.35	0.71	2.32	19.9	2.78	✓
7	18:36:16	-07:45:14	3.66	0.33	1.45	3.03	18.7	5.92	×
8	18:36:19	-07:41:26	3.66	0.17	0.25	1.45	19.2	1.72	×
9	18:36:27	-07:42:37	3.66	0.13	0.69	2.04	17.3	5.68	×
10	18:36:18	-07:43:54	3.66	0.11	0.78	1.44	17.8	4.00	×
11	18:36:19	-07:41:09	3.66	0.57	0.77	1.31	24.4	0.71	✓
IRDC18385									2 missed
1	18:41:13	-05:09:00	3.13	498.98	665.02	520.32	29.3	126.08	✓
2	18:41:25	-05:10:04	3.13	19.52	22.60	20.61	29.2	4.75	✓
3	18:41:20	-05:07:57	3.13	6.09	9.23	10.96	25.7	3.91	✓
4	18:41:17	-05:09:55	3.13	0.51	1.20	3.35	19.9	3.06	✓
5	18:41:23	-05:10:17	3.13	0.23	0.61	1.26	20.5	1.08	✓
6	18:41:19	-05:11:09	3.13	0.09	0.33	0.91	18.6	1.23	×
7	18:41:23	-05:07:11	3.13	0.31	0.72	1.96	20.0	1.77	✓
IRDC18437									0 missed
1	18:46:25	-02:19:13	5.40	84.76	131.61	150.98	25.7	160.87	✓
2	18:46:25	-02:17:40	5.40	27.48	54.79	66.24	24.0	93.61	✓
3	18:46:24	-02:15:20	5.40	16.89	30.58	34.66	24.9	42.79	×
4	18:46:22	-02:14:23	5.40	8.01	13.32	20.03	23.9	26.89	✓
5	18:46:16	-02:15:36	5.40	3.99	9.57	15.83	21.8	32.32	✓
6	18:46:21	-02:12:22	5.40	2.94	4.76	8.98	23.0	13.43	✓
7	18:46:24	-02:19:49	5.40	0.45	1.12	3.93	19.0	12.82	✓
8	18:46:20	-02:16:07	5.40	0.25	0.87	2.61	18.4	10.94	×
9	18:46:20	-02:11:15	5.40	0.24	0.45	0.81	22.4	1.39	✓
10	18:46:12	-02:16:47	5.40	0.17	0.40	0.78	21.3	1.68	×
11	18:46:13	-02:15:10	5.40	0.14	0.62	0.97	19.7	3.45	×
12	18:46:17	-02:13:32	5.40	0.13	0.54	1.89	17.5	10.25	×
13	18:46:14	-02:12:09	5.40	0.08	0.55	2.02	16.2	17.23	×
14	18:46:23	-02:11:36	5.40	0.06	0.21	0.60	18.7	2.29	×
15	18:46:24	-02:15:21	5.40	10.96	30.07	34.35	22.7	64.43	×
16	18:46:06	-02:16:44	5.40	0.35	0.83	1.88	20.6	4.56	×
17	18:46:14	-02:15:45	5.40	0.32	0.89	2.88	18.9	10.07	✓
18	18:46:14	-02:16:39	5.40	0.14	0.87	1.60	18.2	8.49	×
IRDC18454									1 missed
1	18:47:38	-01:57:43	5.35	285.07	505.47	590.03	24.9	712.79	✓
2	18:47:39	-01:57:23	5.35	214.20	260.20	274.60	27.8	212.66	✓
3	18:47:47	-01:54:26	5.35	117.84	481.70	949.82	19.2	3556.29	✓
4	18:47:38	-01:56:44	5.35	78.89	136.70	330.82	21.6	601.71	✓
5	18:47:35	-01:56:33	5.35	38.48	95.76	176.87	21.2	392.49	✓
6	18:47:39	-01:56:10	5.35	36.55	51.31	58.19	26.4	54.58	×
7	18:47:39	-01:56:51	5.35	35.14	107.73	328.65	18.8	1196.97	×
8	18:48:08	-01:56:50	5.35	10.78	19.70	36.51	22.5	59.82	✓
9	18:47:51	-01:49:21	5.35	10.55	15.76	23.70	24.5	28.03	✓
10	18:48:02	-01:55:40	5.35	10.06	49.14	58.64	20.2	194.98	✓
11	18:47:57	-01:54:55	5.35	3.62	4.70	14.76	21.8	23.50	×
12	18:47:39	-01:53:54	5.35	3.60	23.51	131.96	15.3	1419.75	×
13	18:48:21	-01:56:20	5.35	3.45	3.03	2.79	31.5	1.42	×

Table A.1. – Continuation of Table A.1.

Source	RA (J2000) [hh:mm:ss]	Dec (J2000) [dd:mm:ss]	Dist [kpc]	$F_{70\mu m}$ [Jy]	$F_{100\mu m}$ [Jy]	$F_{160\mu m}$ [Jy]	T [K]	M [$M_\odot$]	Comments
14	18:47:51	-01:58:03	5.35	3.39	6.38	12.01	22.3	20.42	✓
15	18:47:59	-01:57:08	5.35	2.99	5.03	5.29	25.7	5.70	×
16	18:48:00	-01:57:22	5.35	2.85	4.22	6.68	24.3	8.07	×
17	18:48:05	-01:53:25	5.35	2.53	7.24	10.36	21.6	22.69	✓
18	18:48:09	-01:56:49	5.35	1.58	4.23	36.57	16.4	213.01	×
19	18:48:02	-01:56:41	5.35	1.50	1.96	4.58	23.0	6.17	×
20	18:48:11	-01:55:00	5.35	1.49	2.80	3.87	23.7	5.49	✓
21	18:48:05	-01:47:41	5.35	1.28	2.88	3.92	22.9	6.57	×
22	18:47:55	-01:53:23	5.35	0.73	3.30	18.49	16.1	139.26	✓
23	18:48:20	-01:54:12	5.35	0.66	2.14	3.22	20.9	8.28	✓
24	18:48:01	-01:51:16	5.35	0.53	1.07	3.14	20.3	7.48	×
25	18:48:04	-01:55:08	5.35	0.49	2.03	6.27	17.8	30.57	×
26	18:47:57	-01:55:01	5.35	2.98	5.05	12.11	21.8	21.41	×
27	18:48:11	-01:58:05	5.35	2.88	6.99	11.72	21.7	23.96	✓
28	18:48:12	-01:58:19	5.35	2.62	3.83	4.05	26.6	3.80	✓
29	18:47:50	-01:49:49	5.35	1.27	3.32	3.43	23.4	5.67	×
30	18:48:04	-01:50:28	5.35	1.04	1.00	3.05	23.3	3.57	×
31	18:47:49	-02:01:12	5.35	0.79	2.73	8.84	18.2	37.50	×
32	18:48:06	-01:49:36	5.35	0.31	0.95	2.84	18.8	10.31	×
33	18:48:02	-01:49:43	5.35	0.27	0.61	2.78	18.5	9.58	×
34	18:47:51	-01:58:20	5.35	0.02	6.01	25.88	10.5	8181.22	×
IRDC18530									0 missed
1	18:55:33	02:19:09	4.60	187.31	254.09	380.44	25.0	301.34	✓
2	18:55:21	02:17:04	4.60	0.74	2.35	3.85	20.7	7.47	✓
3	18:55:25	02:17:43	4.60	0.06	0.20	0.50	18.9	1.38	×
4	18:55:43	02:18:08	4.60	0.05	0.38	0.90	17.1	4.64	×
IRDC19175									0 missed
1	19:19:48	14:02:47	0.78	21.45	46.36	68.89	22.7	2.49	✓
2	19:19:55	14:04:59	0.78	21.39	22.23	16.16	32.0	0.18	✓
3	19:19:41	14:01:19	0.78	15.10	17.95	21.74	27.1	0.38	✓
4	19:19:48	14:02:25	0.78	11.13	16.27	20.37	25.6	0.45	✓
5	19:19:37	14:01:17	0.78	7.41	10.52	11.26	26.7	0.22	✓
6	19:19:43	14:01:21	0.78	5.13	5.52	5.09	29.7	0.07	✓
7	19:19:40	14:02:14	0.78	3.45	3.61	3.37	29.9	0.04	✓
8	19:19:42	14:01:48	0.78	1.22	2.69	4.83	21.8	0.20	×
9	19:19:55	14:03:49	0.78	1.17	1.74	4.05	22.4	0.13	✓
10	19:19:55	14:03:51	0.78	1.14	3.11	8.93	19.3	0.60	✓
11	19:19:56	14:03:35	0.78	1.03	2.79	3.34	22.6	0.13	✓
12	19:19:53	14:03:44	0.78	1.00	2.88	8.04	19.2	0.56	✓
13	19:19:57	14:01:21	0.78	0.64	1.43	3.56	20.5	0.18	×
14	19:19:52	14:03:48	0.78	0.56	1.60	8.16	17.5	0.79	×
15	19:19:52	14:00:52	0.78	0.52	1.00	1.89	22.2	0.07	×
16	19:19:48	14:01:17	0.78	0.47	0.82	1.70	22.2	0.06	✓
17	19:19:40	14:01:47	0.78	0.44	1.36	3.32	19.4	0.23	×
18	19:19:50	14:01:49	0.78	0.33	0.87	2.07	20.0	0.12	×
19	19:19:39	14:00:02	0.78	0.16	0.52	1.12	19.6	0.08	×
20	19:19:42	14:00:06	0.78	0.16	0.49	1.28	19.2	0.09	×
21	19:19:42	14:03:07	0.78	0.09	0.35	0.73	19.3	0.05	×
22	19:19:35	14:00:54	0.78	0.57	1.63	2.53	21.3	0.12	×
23	19:19:41	13:59:54	0.78	0.16	0.46	1.22	19.4	0.08	×

Table A.1. – Continuation of Table A.1.

Source	RA (J2000) [hh:mm:ss]	Dec (J2000) [dd:mm:ss]	Dist [kpc]	$F_{70\mu m}$ [Jy]	$F_{100\mu m}$ [Jy]	$F_{160\mu m}$ [Jy]	T [K]	M [$M_\odot$]	Comments
IRDC20081									0 missed
1	20:10:18	27:27:19	1.07	1.33	2.71	4.48	22.5	0.31	✓
IRDC310.39									0 missed
1	13:56:00	-62:13:59	5.02	6.37	8.00	13.13	25.0	12.12	✓
2	13:56:01	-62:14:18	5.02	4.50	20.56	52.60	18.0	225.15	✓
IRDC316.72									0 missed
1	14:44:55	-59:47:59	2.76	145.02	221.47	235.51	26.3	61.53	✓
2	14:44:30	-59:49:01	2.76	19.07	23.30	40.49	24.8	11.36	✓
3	14:44:20	-59:46:30	2.76	2.37	4.03	5.37	24.4	1.79	✓
4	14:44:52	-59:46:43	2.76	1.96	4.83	13.68	19.7	10.28	✓
5	14:44:20	-59:44:50	2.76	1.69	3.28	8.15	21.1	4.47	✓
6	14:45:08	-59:45:00	2.76	0.97	2.34	3.39	22.3	1.67	✓
7	14:44:23	-59:45:04	2.76	0.79	2.24	6.72	19.1	5.95	✓
8	14:44:37	-59:48:14	2.76	0.74	2.36	7.24	18.6	7.28	×
9	14:44:22	-59:49:08	2.76	0.72	1.31	2.72	22.1	1.25	✓
10	14:44:35	-59:48:17	2.76	0.44	1.58	6.62	17.4	8.95	×
11	14:44:16	-59:43:45	2.76	0.41	1.11	5.92	17.6	6.96	✓
12	14:44:32	-59:50:05	2.76	0.41	0.50	2.74	20.0	1.51	✓
13	14:44:22	-59:47:24	2.76	0.36	0.61	2.04	20.4	1.18	✓
14	14:44:33	-59:46:08	2.76	0.28	0.57	1.37	20.9	0.78	✓
15	14:44:54	-59:46:56	2.76	0.26	1.48	5.61	16.5	11.13	✓
16	14:44:21	-59:48:55	2.76	0.24	0.59	2.77	18.2	2.76	✓
17	14:44:39	-59:46:32	2.76	0.23	1.00	3.43	17.4	5.03	✓
18	14:44:48	-59:45:22	2.76	0.21	1.22	4.26	16.6	8.46	✓
19	14:45:04	-59:45:14	2.76	0.09	0.48	0.93	18.4	1.17	✓
20	14:45:08	-59:45:12	2.76	0.75	1.73	3.30	21.4	1.84	×
21	14:44:15	-59:44:57	2.76	0.55	1.85	4.95	18.8	4.89	✓
IRDC320.27									0 missed
1	15:07:25	-57:53:20	2.25	0.92	0.44	0.95	29.9	0.08	×
2	15:07:57	-57:54:16	2.25	0.56	2.11	5.38	18.6	3.82	✓
3	15:07:49	-57:55:10	2.25	0.07	0.10	0.41	20.2	0.16	✓
4	15:07:40	-57:54:31	2.25	0.05	0.18	0.36	19.4	0.22	×
5	15:07:26	-57:52:01	2.25	0.05	0.25	1.57	15.6	2.59	×
IRDC321.73									0 missed
1	15:17:58	-57:28:01	2.32	19.05	33.94	51.69	23.5	13.83	✓
2	15:18:01	-57:22:05	2.32	2.91	5.33	9.02	22.9	2.64	✓
3	15:18:26	-57:21:57	2.32	2.49	10.50	23.78	18.6	18.67	✓
4	15:18:05	-57:24:31	2.32	1.68	3.19	4.02	24.1	1.03	✓
5	15:18:00	-57:21:11	2.32	0.68	1.39	2.51	22.1	0.85	✓
6	15:18:28	-57:21:53	2.32	0.49	1.80	4.33	18.9	3.09	✓
7	15:18:39	-57:21:52	2.32	0.29	0.87	1.56	20.6	0.76	✓
8	15:18:31	-57:21:53	2.32	0.25	0.82	1.55	20.0	0.88	✓
9	15:18:20	-57:20:39	2.32	0.21	0.21	0.70	22.7	0.17	✓
10	15:18:01	-57:24:50	2.32	0.15	0.45	1.33	19.0	0.86	✓
11	15:18:49	-57:21:28	2.32	0.10	0.30	-0.01	-0.01	-0.01	✓
12	15:17:53	-57:26:57	2.32	0.08	0.15	0.36	21.2	0.14	✓
13	15:17:42	-57:18:17	2.32	0.07	0.19	0.59	19.2	0.35	✓
14	15:18:05	-57:24:19	2.32	0.07	0.18	0.58	19.0	0.36	✓
15	15:18:02	-57:24:25	2.32	0.05	0.12	0.23	21.4	0.09	✓
16	15:17:51	-57:26:42	2.32	0.05	0.11	0.53	18.5	0.33	✓

Table A.1. – Continuation of Table A.1.

Source	RA (J2000) [hh:mm:ss]	Dec (J2000) [dd:mm:ss]	Dist [kpc]	$F_{70\mu m}$ [Jy]	$F_{100\mu m}$ [Jy]	$F_{160\mu m}$ [Jy]	T [K]	M [$M_\odot$]	Comments
ISOSSJ04225									3 missed
1	04:22:32	51:50:29	4.24	20.46	29.38	34.51	26.1	21.26	✓
2	04:22:30	51:50:36	4.24	5.88	9.78	11.82	25.0	8.58	✓
3	04:22:26	51:50:44	4.24	2.74	6.25	13.85	20.9	19.62	✓
ISOSSJ06114									0 missed
1	06:11:23	17:26:27	5.91	37.63	45.09	43.32	28.6	38.08	✓
2	06:11:32	17:26:05	5.91	0.30	0.65	0.99	22.6	2.09	✓
3	06:11:29	17:27:37	5.91	0.19	0.79	0.99	20.6	3.56	✓
4	06:11:29	17:27:07	5.91	0.14	0.18	0.92	19.9	2.42	✓
5	06:11:03	17:27:14	5.91	0.10	0.25	0.47	21.0	1.31	✓
6	06:11:26	17:29:38	5.91	0.08	0.18	0.61	19.4	2.16	×
7	06:11:26	17:28:34	5.91	0.05	0.15	0.36	19.6	1.34	×
8	06:11:28	17:27:42	5.91	0.19	0.75	0.62	22.6	1.61	×
ISOSSJ06527									0 missed
1	06:52:45	01:40:21	4.80	49.67	88.25	105.32	24.7	103.99	✓
2	06:52:46	01:40:17	4.80	9.69	18.04	30.64	22.8	39.08	✓
ISOSSJ18364									0 missed
1	18:36:36	-02:21:49	2.35	18.31	33.01	36.82	25.0	8.46	✓
2	18:36:29	-02:21:58	2.35	3.33	4.82	5.99	25.7	1.18	✓
ISOSSJ19357									2 missed
1	19:35:44	19:50:35	4.75	0.43	0.75	1.15	23.5	1.28	✓
2	19:35:44	19:50:48	4.75	0.25	0.60	1.31	20.7	2.41	✓
ISOSSJ19486									0 missed
1	19:48:35	25:56:45	2.75	6.28	11.11	12.79	24.9	4.04	✓
2	19:48:37	25:57:15	2.75	1.77	3.69	7.20	21.7	3.66	✓
3	19:48:39	25:57:09	2.75	0.42	0.96	6.90	17.2	8.23	✓
ISOSSJ19557									1 missed
1	19:55:47	28:25:39	3.52	3.21	5.61	13.52	21.6	10.69	✓
2	19:55:45	28:25:39	3.52	0.40	0.87	1.63	21.7	1.39	✓
3	19:55:50	28:24:32	3.52	0.38	0.74	1.05	23.4	0.67	✓
ISOSSJ20093									1 missed
1	20:09:19	27:29:37	1.15	3.23	4.51	8.07	24.0	0.46	✓
2	20:09:23	27:29:48	1.15	2.39	2.99	3.69	26.6	0.15	✓
3	20:09:16	27:29:06	1.15	1.15	1.53	2.01	25.9	0.09	✓
ISOSSJ20153									0 missed
1	20:15:21	34:53:45	1.23	25.49	44.49	50.49	25.1	3.12	✓
ISOSSJ20298									0 missed
1	20:29:48	35:59:28	0.95	6.76	6.45	8.37	28.2	0.18	✓
2	20:29:45	35:58:48	0.95	0.83	1.85	3.05	22.1	0.18	✓
3	20:29:36	35:58:18	0.95	0.71	1.04	1.71	24.1	0.07	✓
4	20:29:47	35:58:48	0.95	0.42	0.62	1.15	23.5	0.05	✓
5	20:29:49	35:59:15	0.95	0.26	0.93	3.07	18.0	0.43	✓
6	20:29:42	35:58:33	0.95	0.10	0.19	0.68	19.6	0.06	✓
ISOSSJ21311									0 missed
1	21:31:12	51:27:35	5.85	5.69	5.14	11.36	25.2	12.21	✓
2	21:31:11	51:27:48	5.85	3.80	6.38	11.97	22.8	21.72	✓

Table A.1. – Continuation of Table A.1.

Source	RA (J2000) [hh:mm:ss]	Dec (J2000) [dd:mm:ss]	Dist [kpc]	$F_{70\mu m}$ [Jy]	$F_{100\mu m}$ [Jy]	$F_{160\mu m}$ [Jy]	T [K]	M [$M_\odot$]	Comments
ISOSSJ22164									0 missed
1	22:16:32	60:04:40	5.29	5.95	8.73	11.35	25.4	11.82	✓
2	22:16:19	60:03:08	5.29	3.74	4.71	4.89	27.7	3.81	✓
3	22:16:29	60:03:29	5.29	3.62	5.39	8.44	24.3	9.98	✓
4	22:16:21	60:03:48	5.29	0.13	0.53	1.72	17.7	8.41	×
5	22:16:20	60:03:36	5.29	0.19	0.53	1.76	18.8	5.96	×
ISOSSJ22478									2 missed
1	22:47:53	63:55:57	3.23	0.62	1.01	1.10	25.7	0.43	✓
2	22:47:48	63:56:44	3.23	0.38	0.79	1.39	22.1	0.91	✓
3	22:47:46	63:56:32	3.23	0.35	0.46	1.21	22.4	0.65	✓
4	22:47:50	63:56:57	3.23	0.33	0.58	1.14	22.4	0.68	✓
5	22:47:50	63:56:45	3.23	0.27	0.38	1.47	20.7	1.04	✓
6	22:47:56	63:57:34	3.23	0.20	0.34	0.61	23.0	0.33	×
7	22:47:46	63:56:49	3.23	0.21	0.54	1.99	18.7	2.54	✓
ISOSSJ23053									0 missed
1	23:05:23	59:53:53	4.31	22.23	45.72	64.54	23.1	65.69	✓
2	23:05:21	59:53:42	4.31	9.34	23.31	34.61	22.0	43.97	✓
3	23:05:14	59:54:05	4.31	0.09	0.15	0.26	23.2	0.25	✓
4	23:05:15	59:53:15	4.31	0.09	0.00	0.20	25.9	0.03	✓
ISOSSJ23129									1 missed
1	23:12:56	59:43:41	3.05	0.14	0.15	0.74	20.8	0.41	×
ISOSSJ23287									0 missed
1	23:28:46	60:39:25	2.80	5.20	5.32	8.04	26.7	1.78	✓
HMSC07029									0 missed
1	07:05:10	-12:18:57	0.63	11.55	32.14	50.54	21.4	1.58	✓
2	07:05:00	-12:16:41	0.63	0.51	0.98	1.61	22.8	0.04	✓
3	07:05:05	-12:16:48	0.63	0.47	0.56	0.90	25.5	0.01	✓
4	07:05:10	-12:21:33	0.63	0.35	0.81	1.19	22.5	0.03	✓
5	07:05:03	-12:16:30	0.63	0.34	1.33	3.16	18.7	0.18	✓
6	07:04:58	-12:16:47	0.63	0.17	0.21	0.79	21.2	0.02	✓
7	07:05:27	-12:18:45	0.63	0.07	0.22	0.38	20.8	0.01	×
8	07:05:22	-12:20:12	0.63	1.68	3.14	6.81	21.7	0.17	×
9	07:04:57	-12:16:53	0.63	0.58	0.89	1.81	22.9	0.04	✓

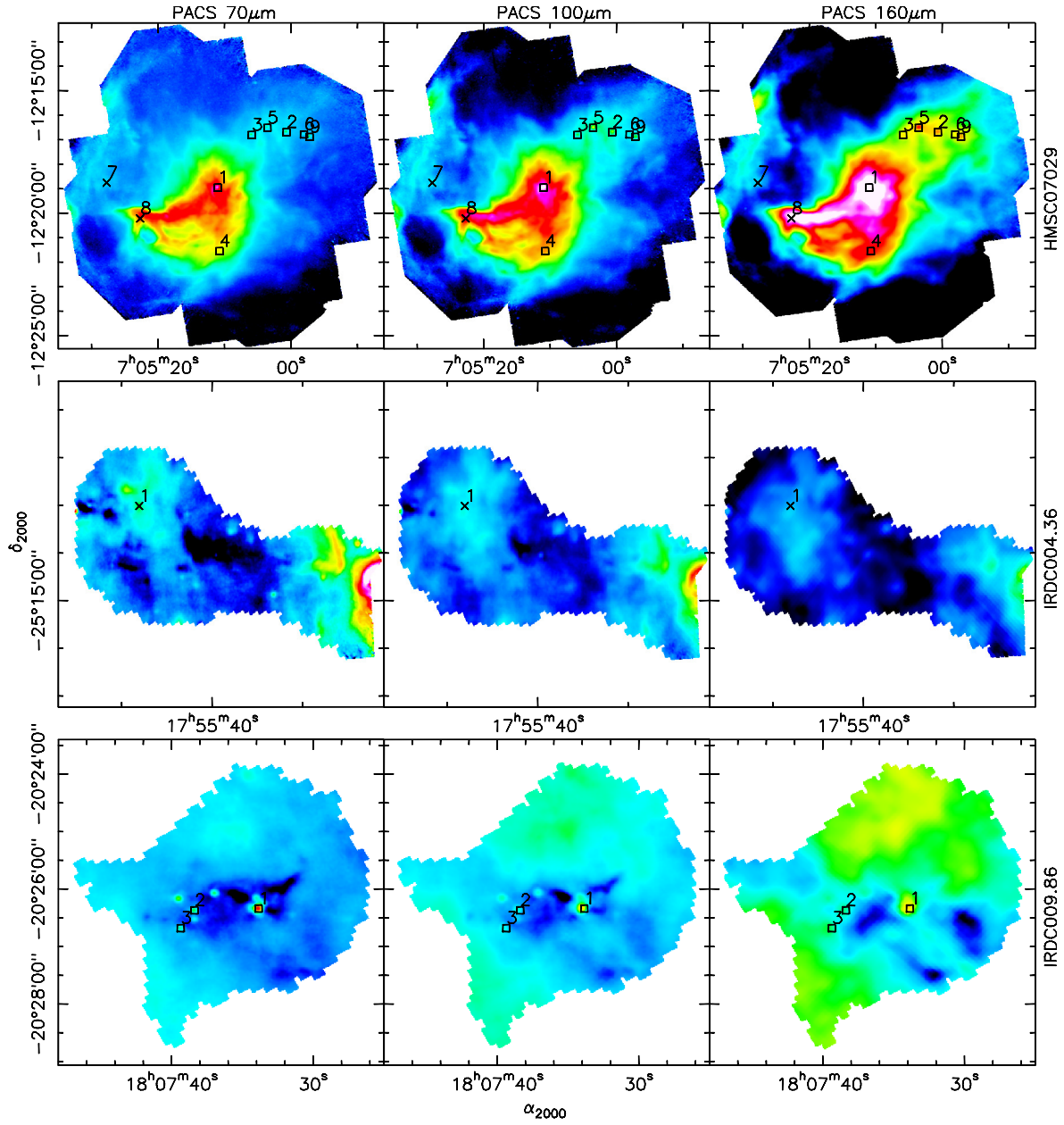

Figure A.1. – The shown PACS maps for 70 μm, 100 μm, and 160 μm are masked already with the ATLAS or SCUABA masks, if available. The results from the nominal extraction are overplotted. Real point sources are marked by □ and false detections by ×.

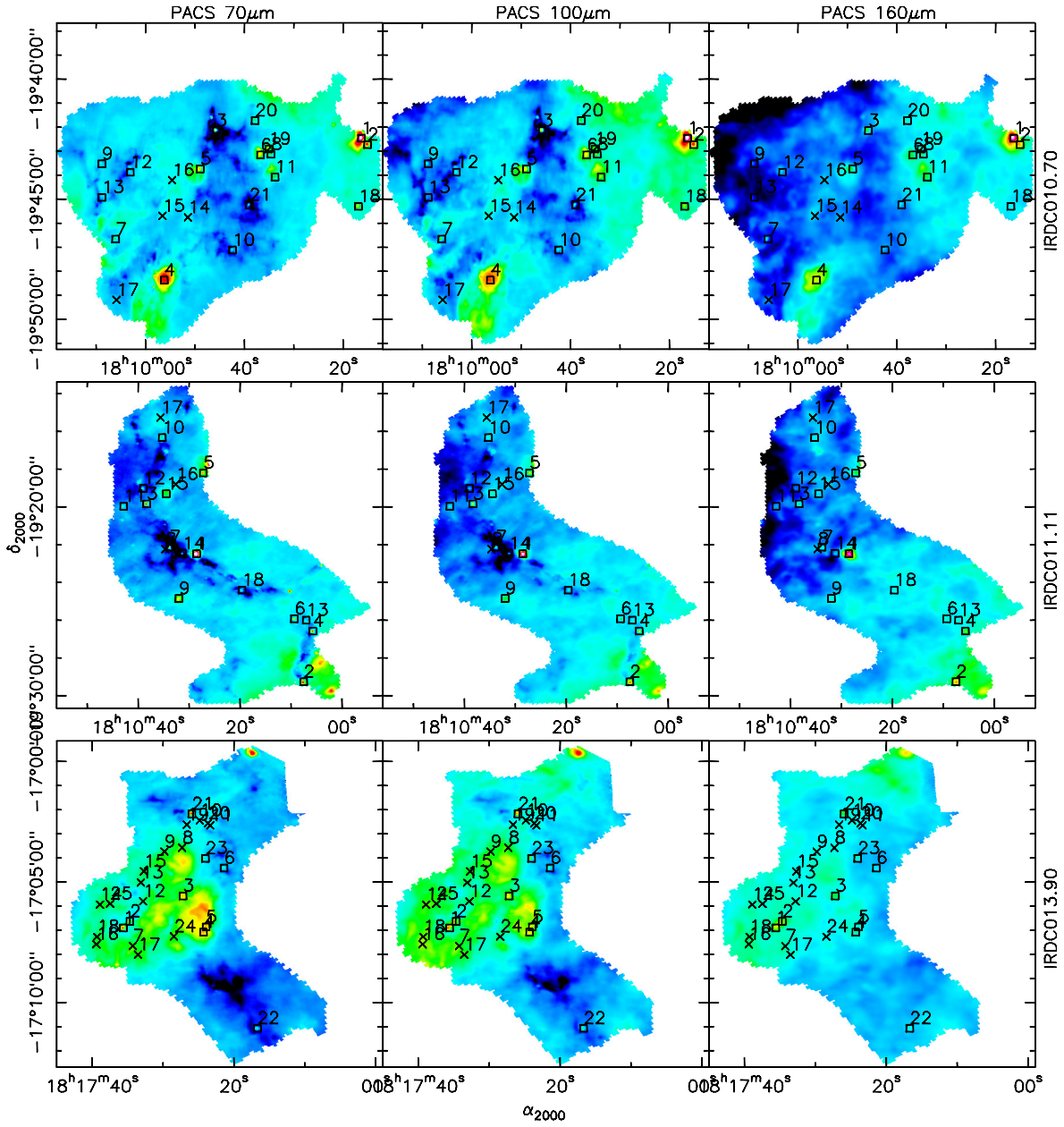

Figure A.2. – Plotted as in Figure A.1.

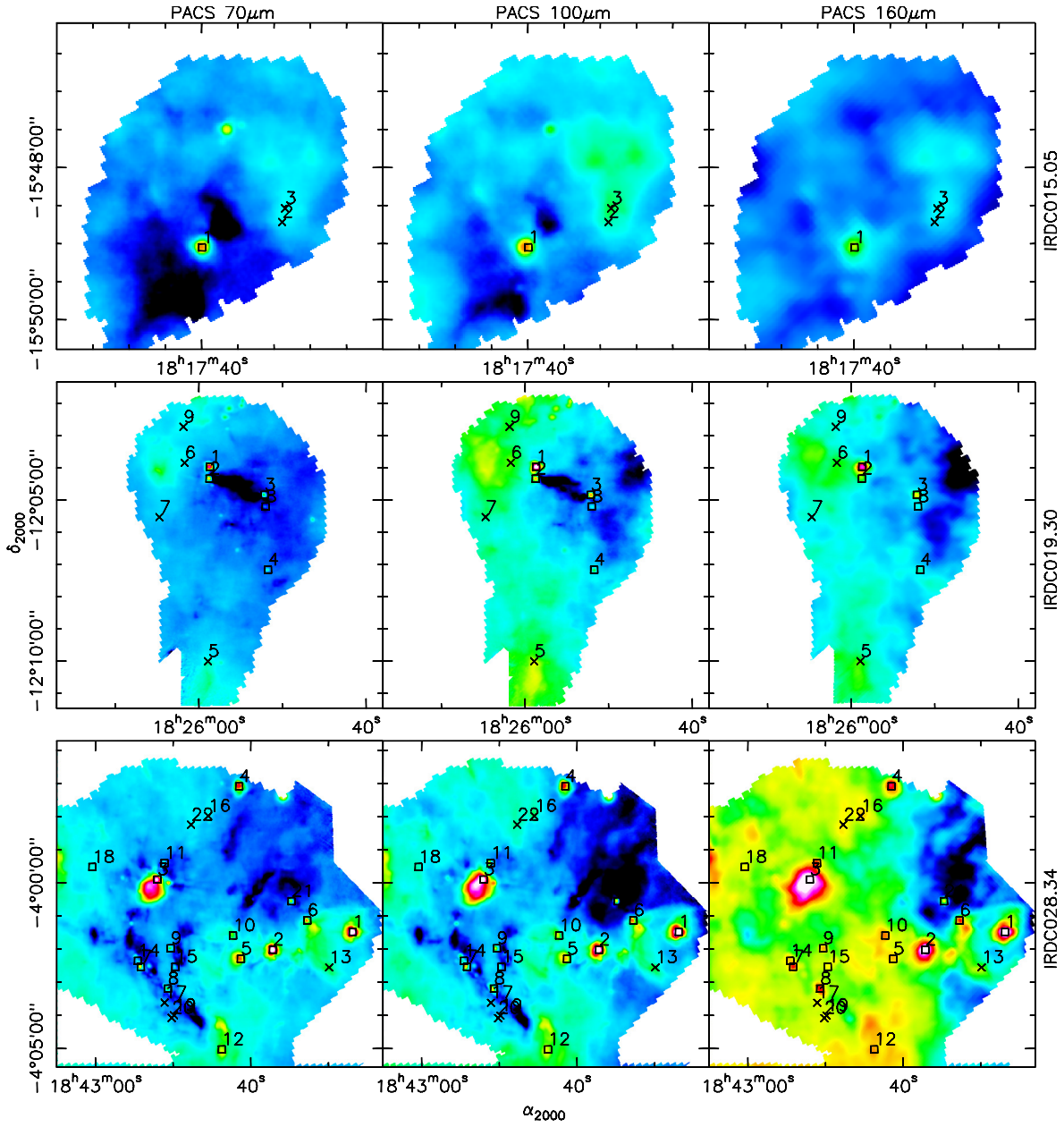

Figure A.3. – Plotted as in Figure A.1.

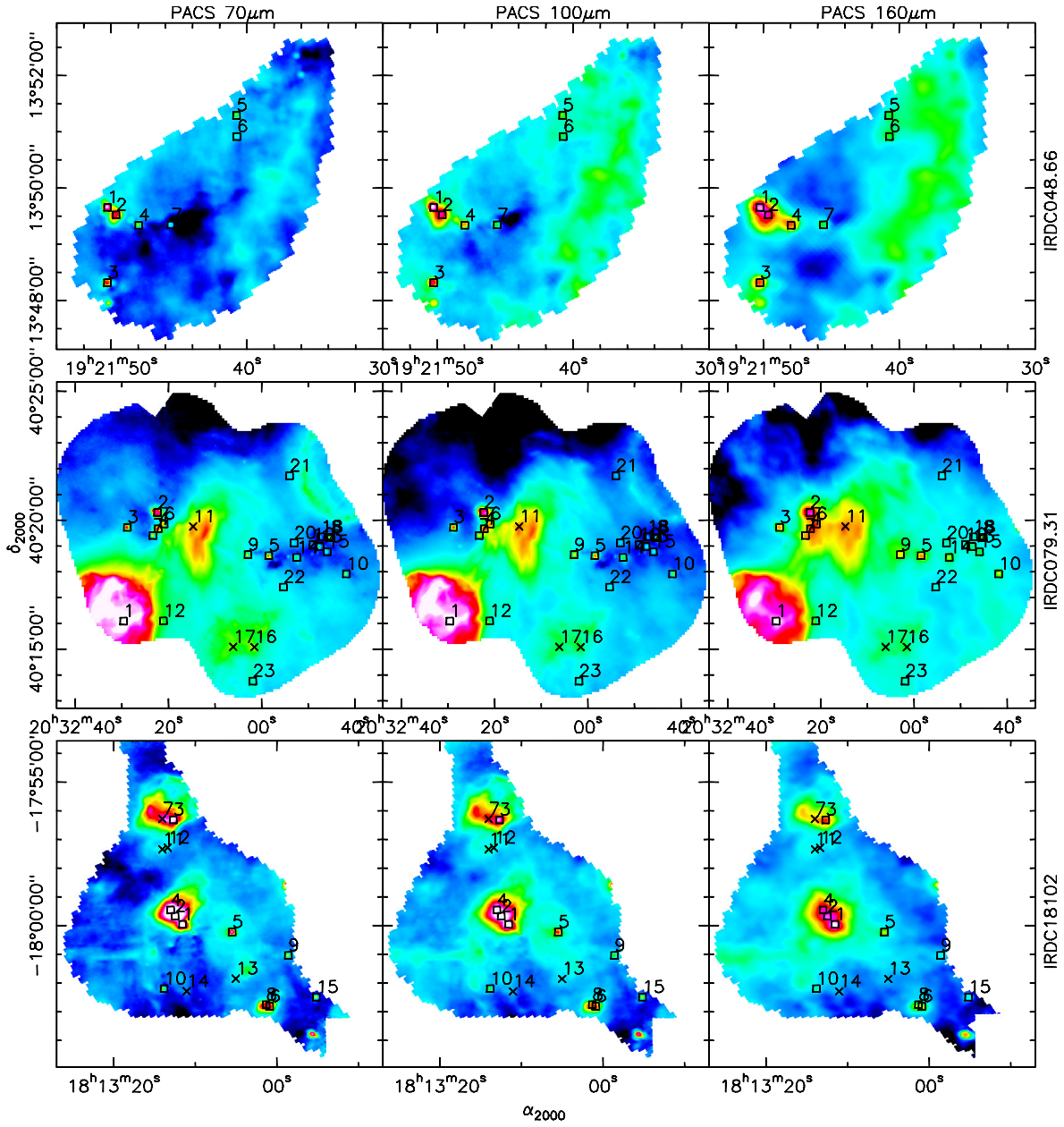

Figure A.4. – Plotted as in Figure A.1.

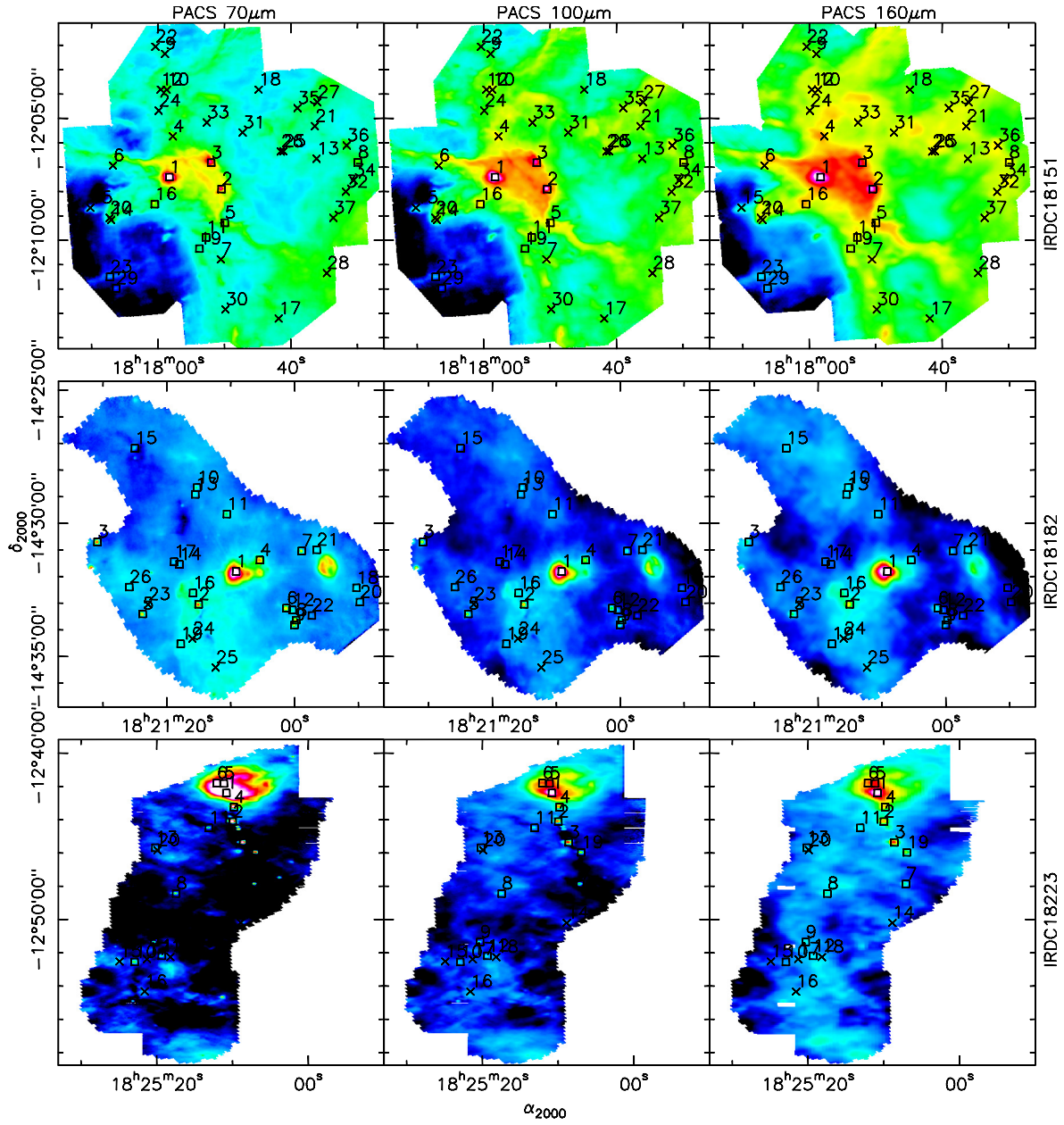

Figure A.5. – Plotted as in Figure A.1.

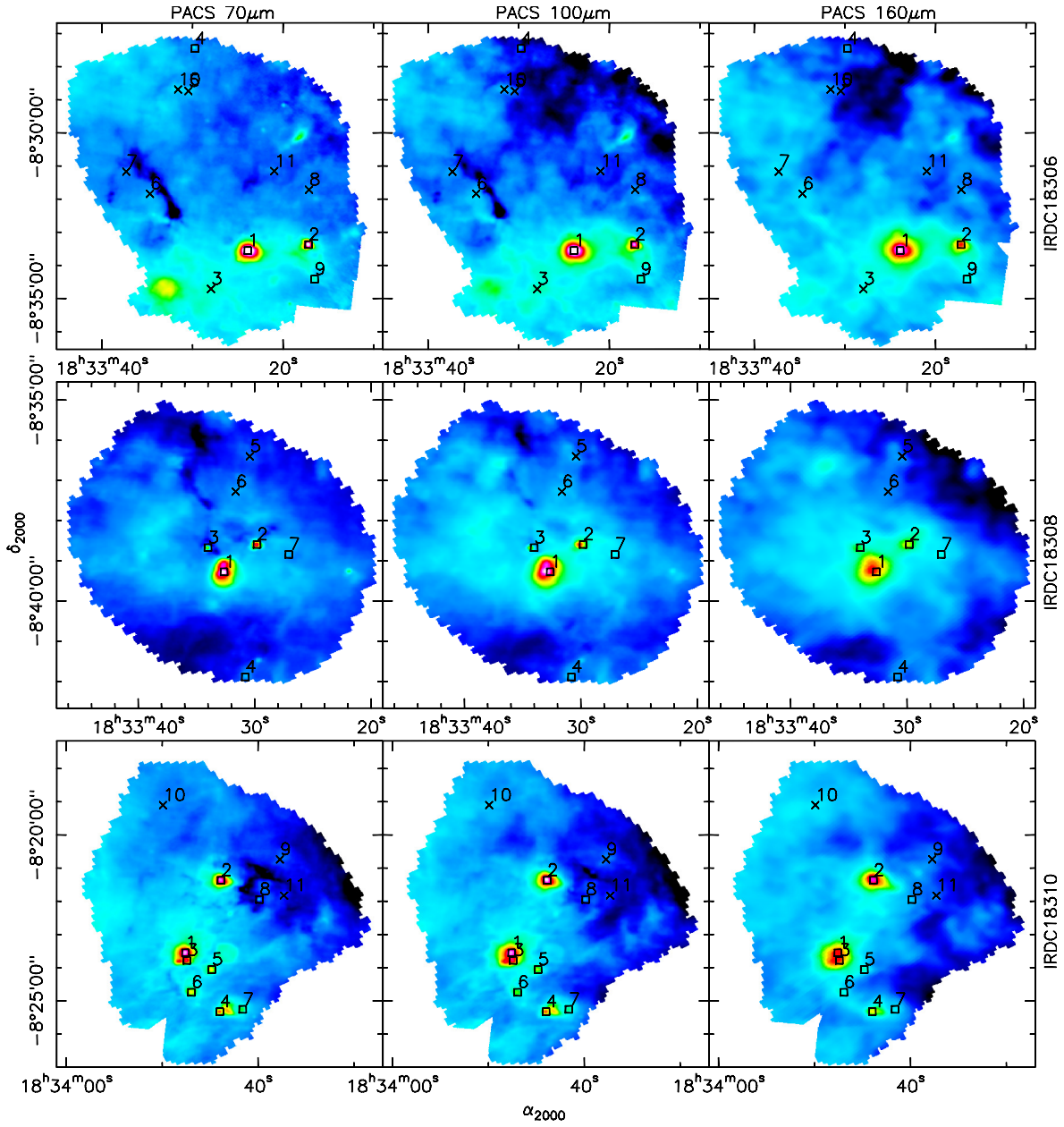

Figure A.6. – Plotted as in Figure A.1.

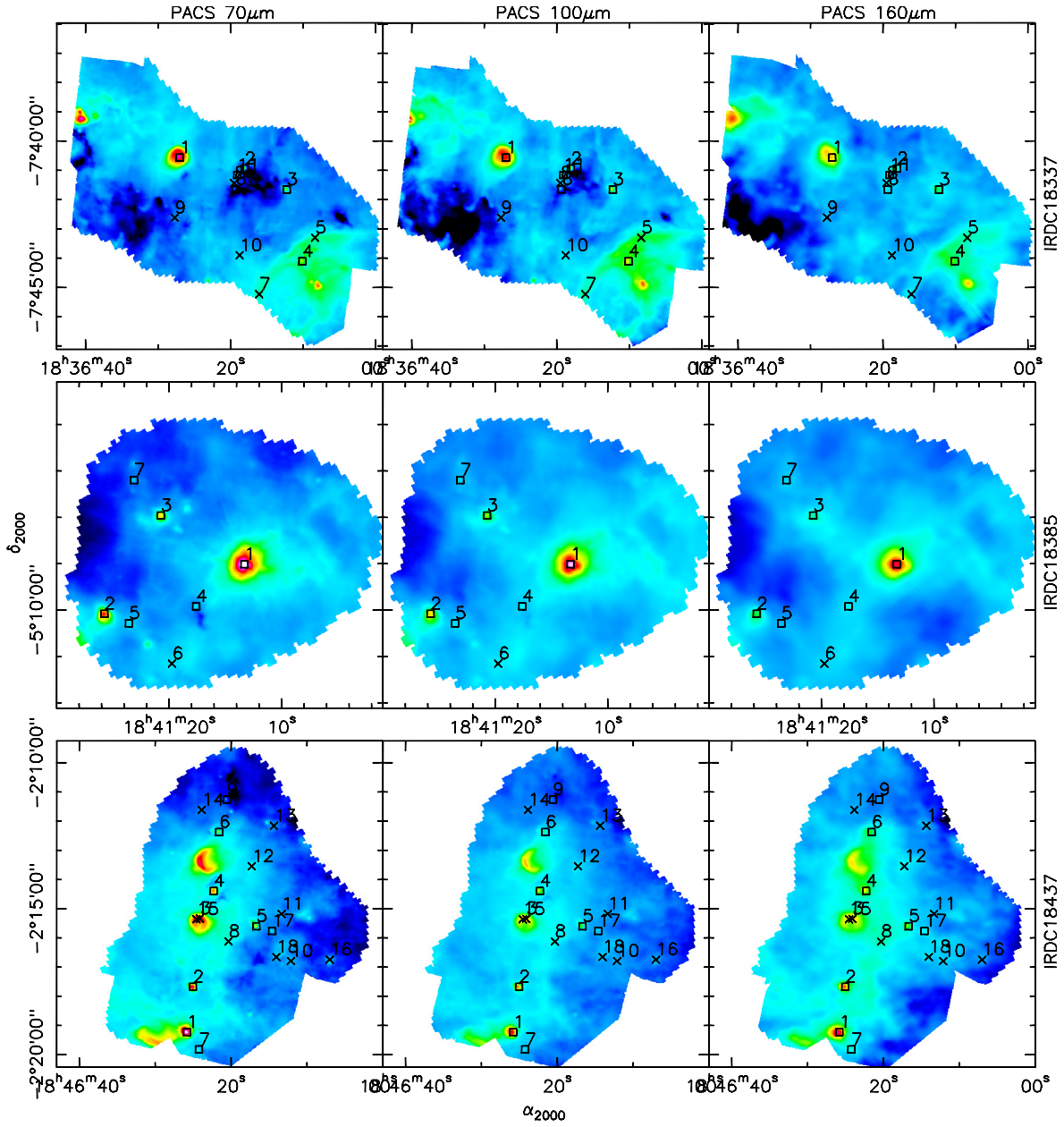

Figure A.7. – Plotted as in Figure A.1.

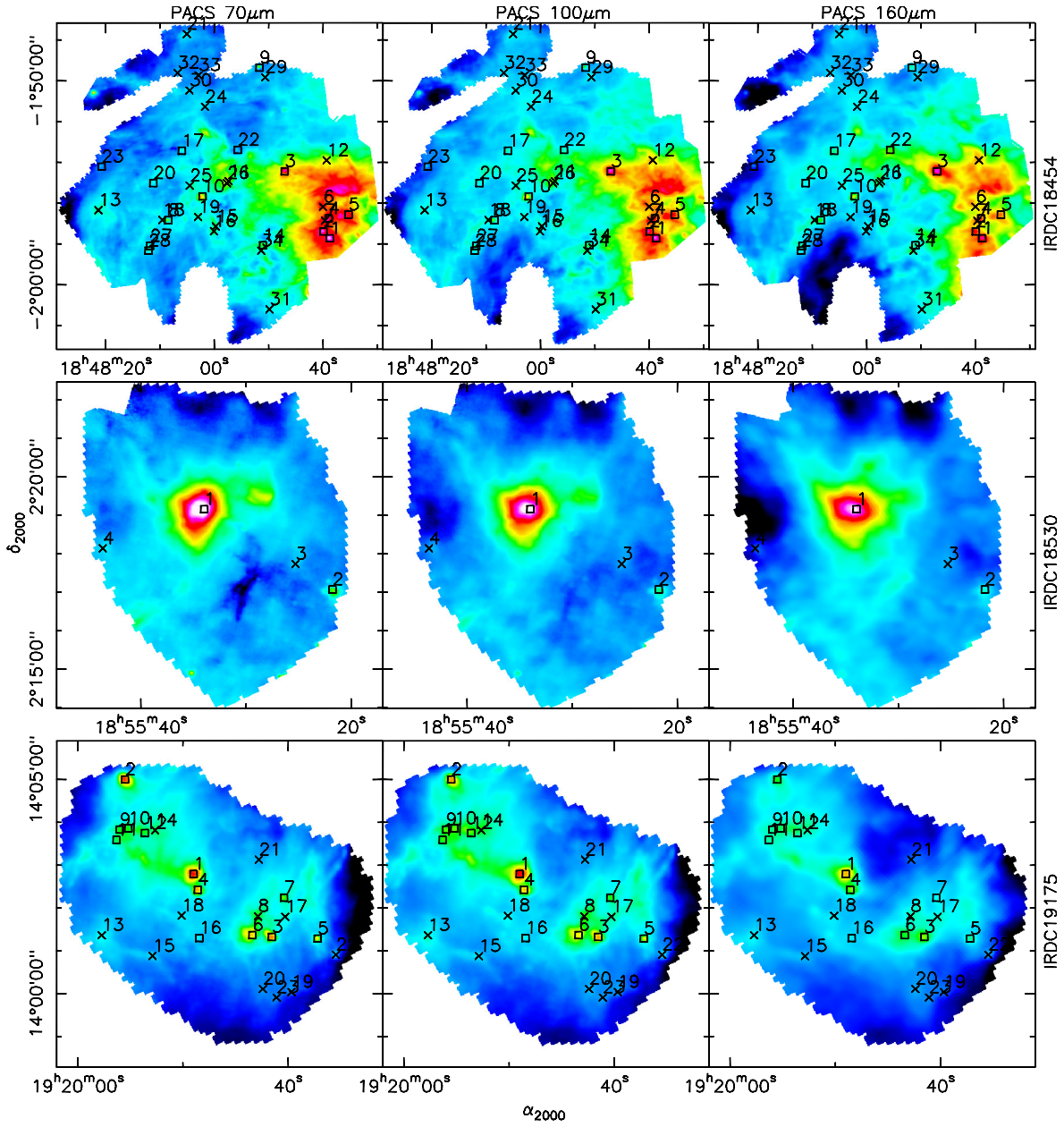

Figure A.8. – Plotted as in Figure A.1.

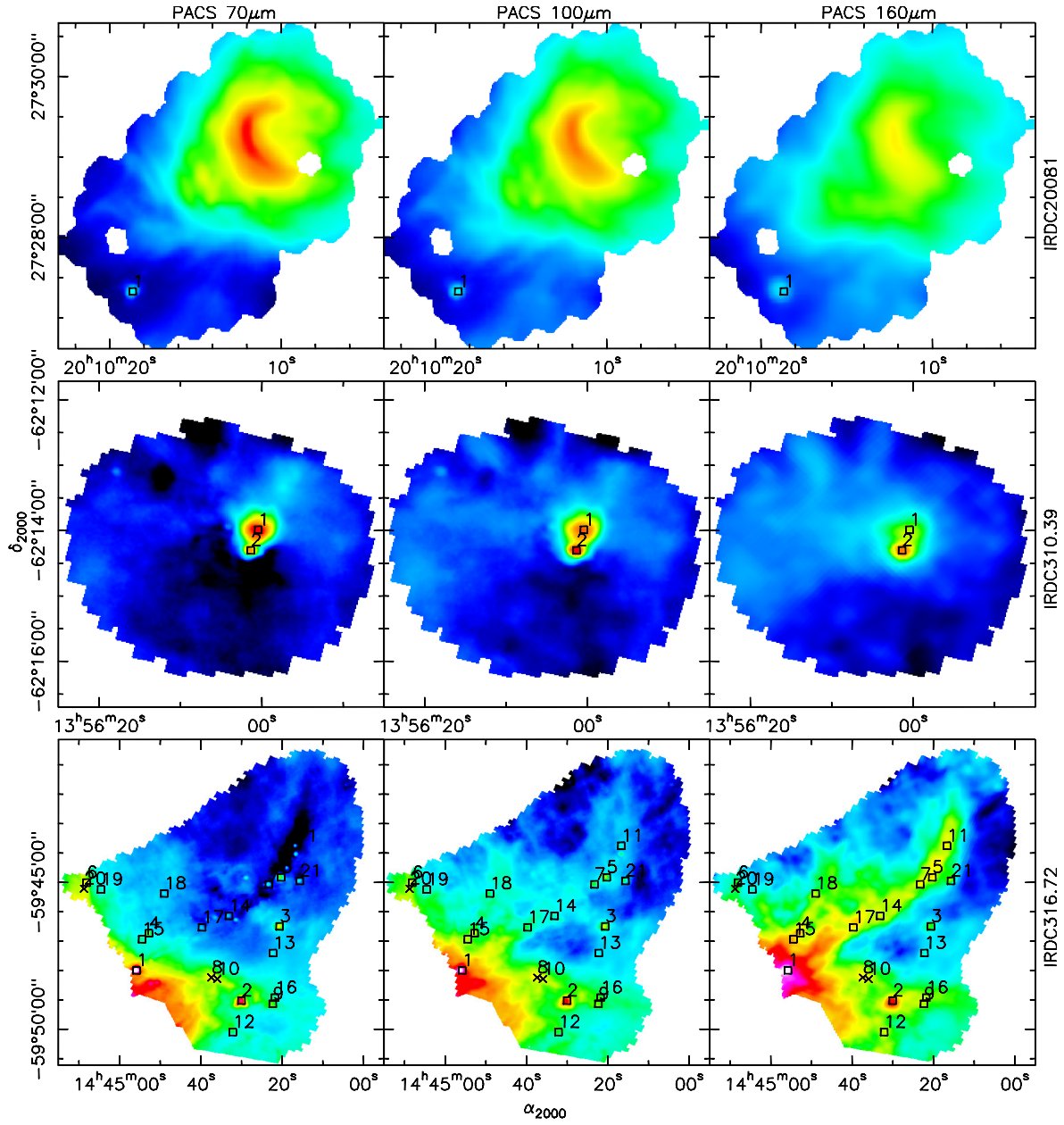

Figure A.9. – Plotted as in Figure A.1.

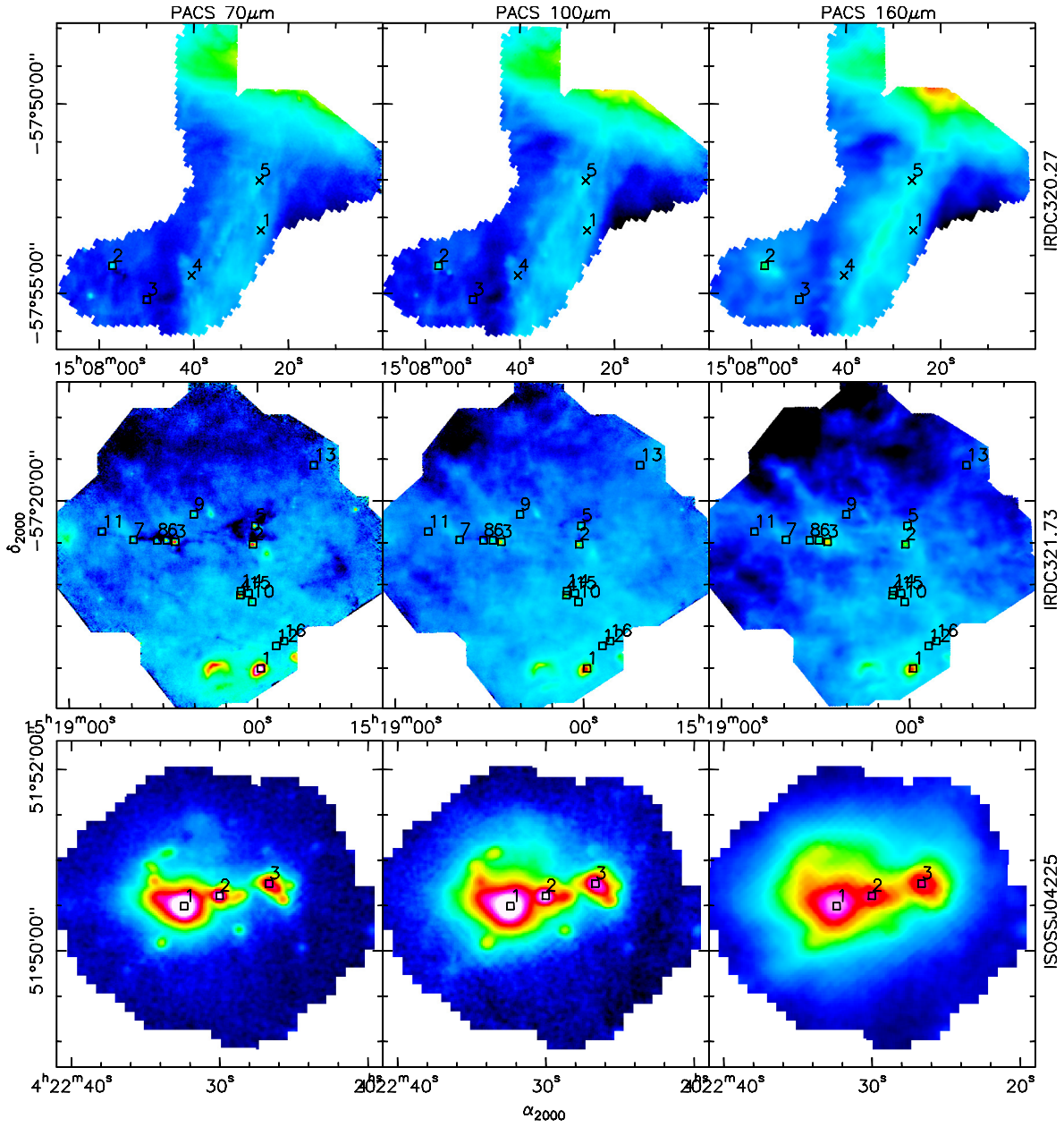

Figure A.10. – Plotted as in Figure A.1.

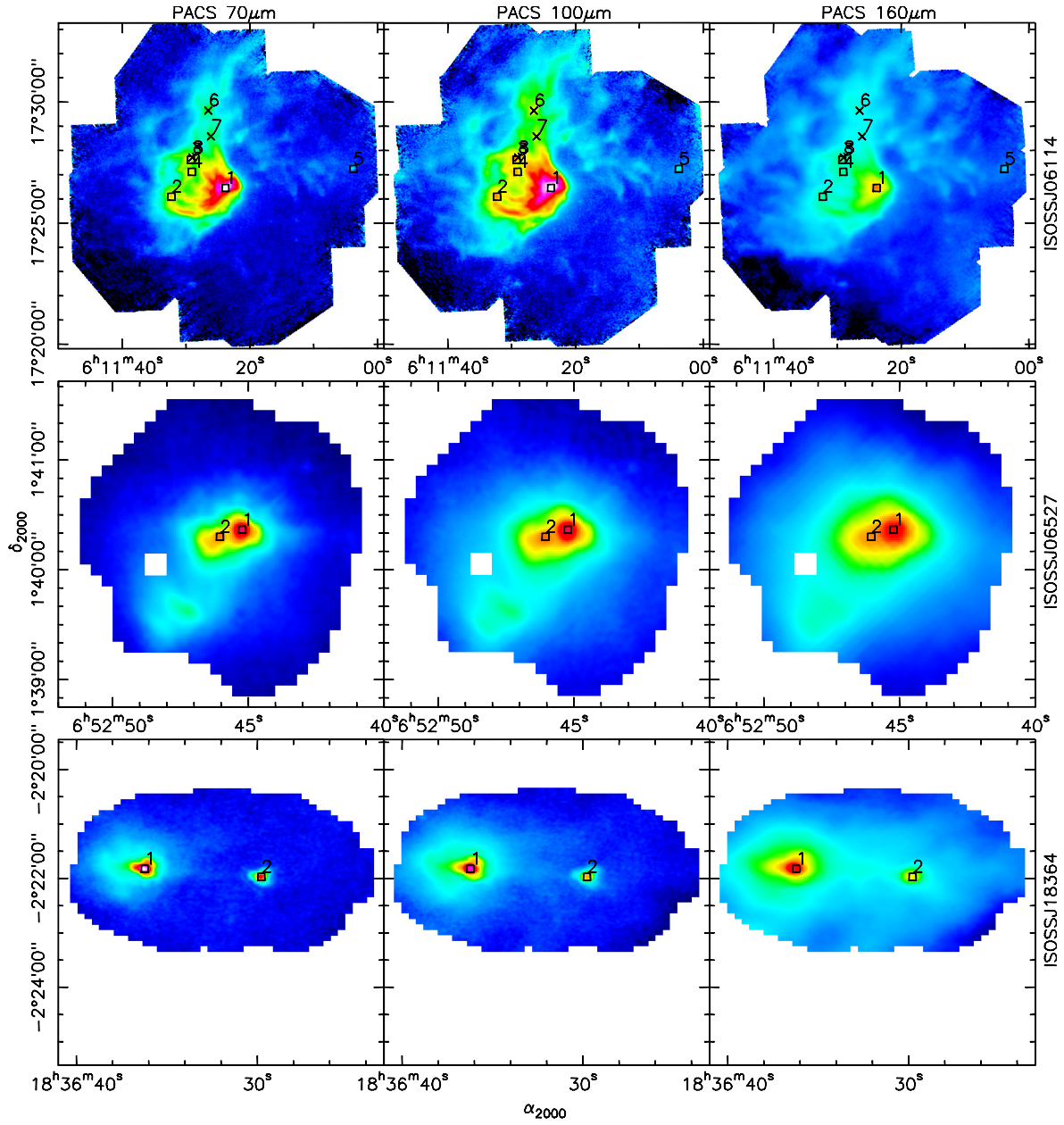

Figure A.11. – Plotted as in Figure A.1.

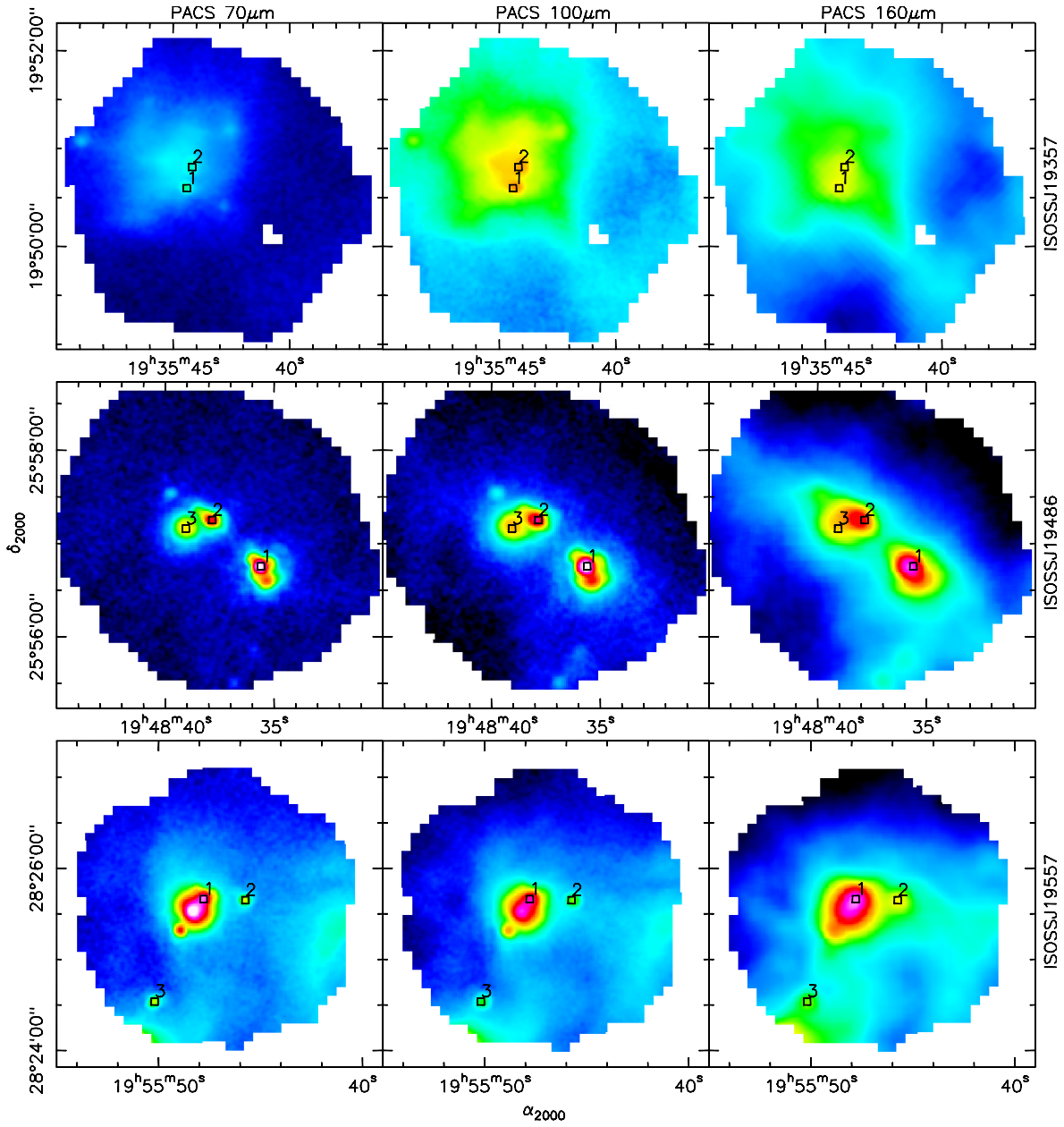

Figure A.12. – Plotted as in Figure A.1.

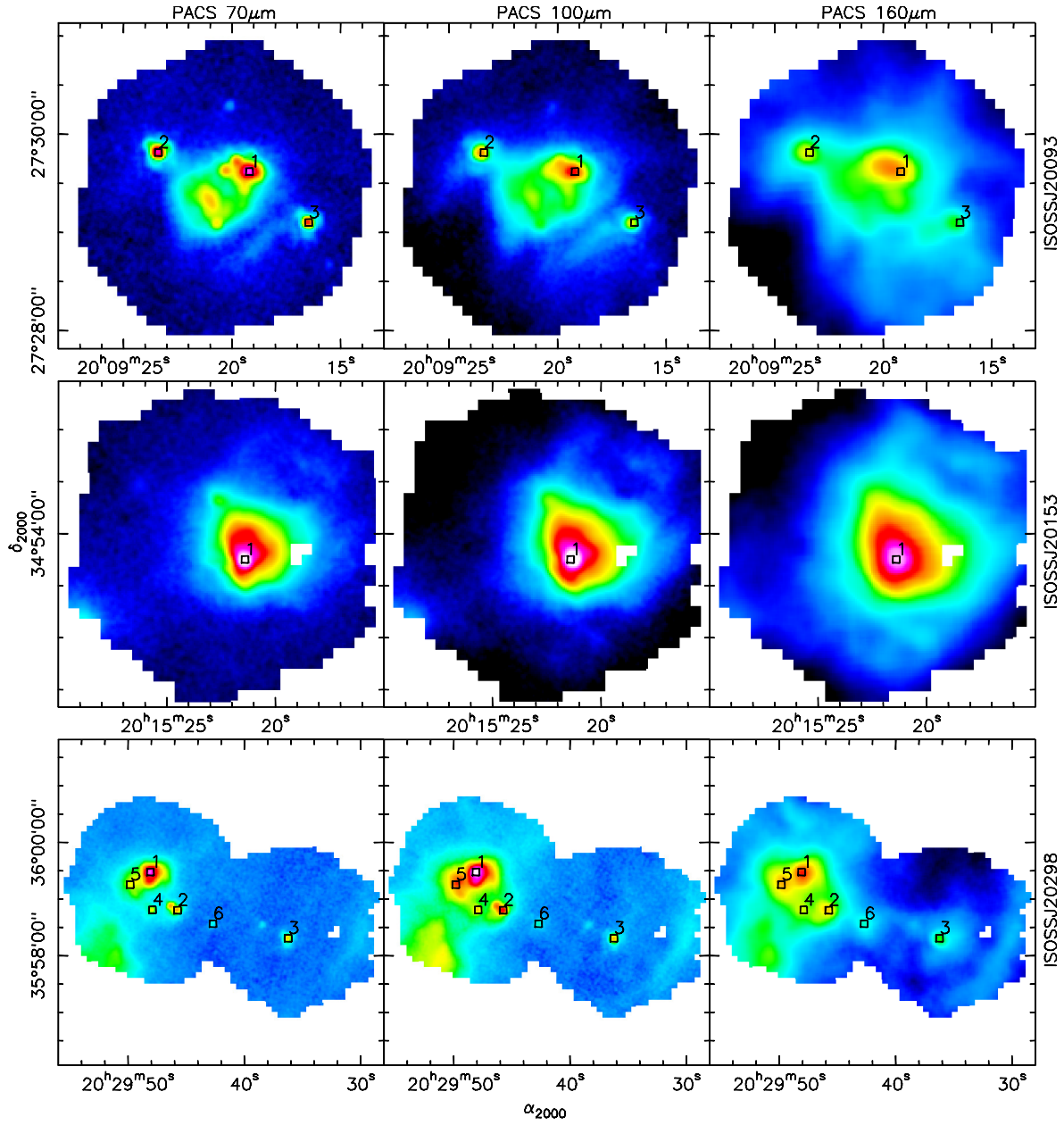

Figure A.13. – Plotted as in Figure A.1.

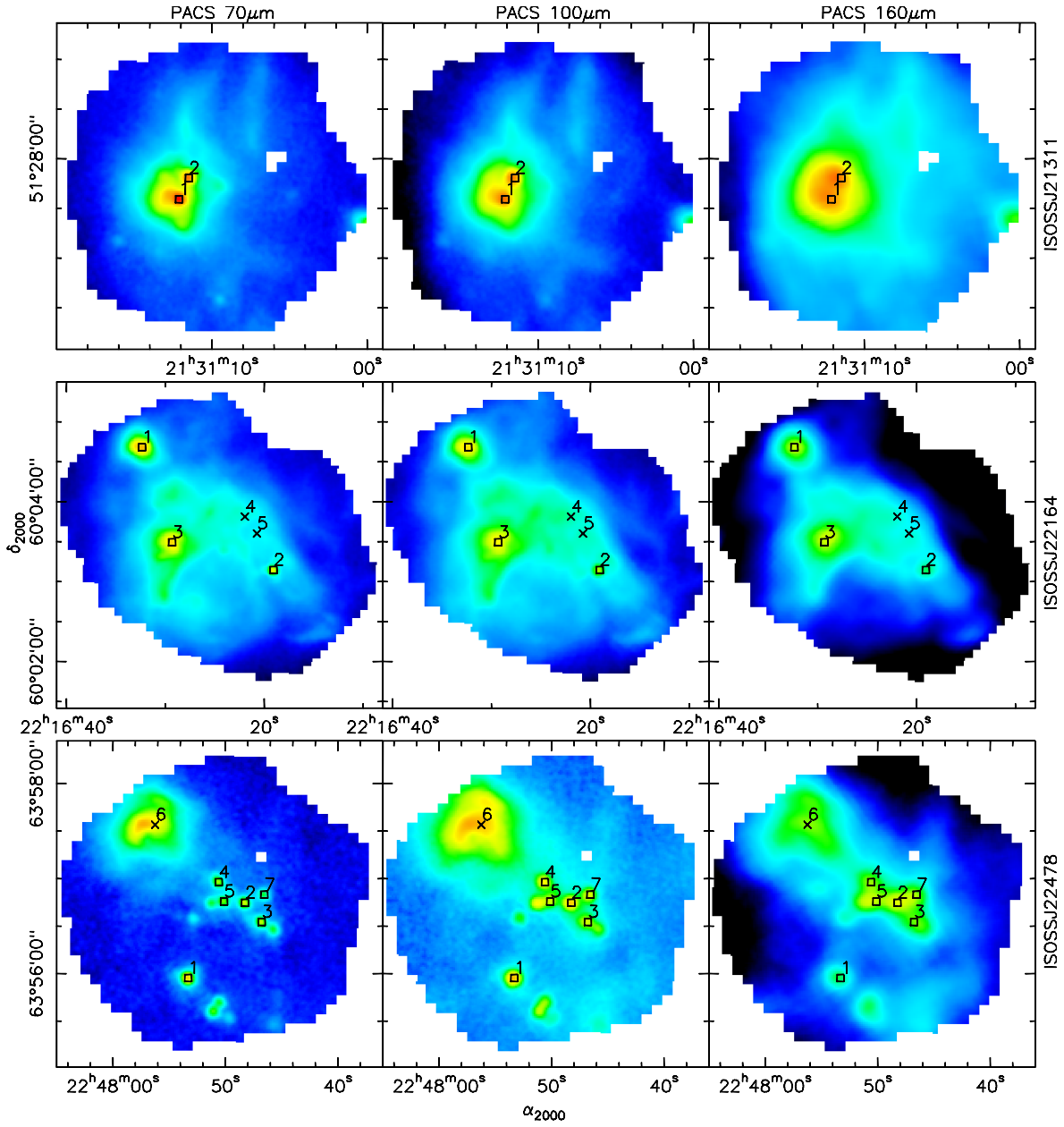

Figure A.14. – Plotted as in Figure A.1.

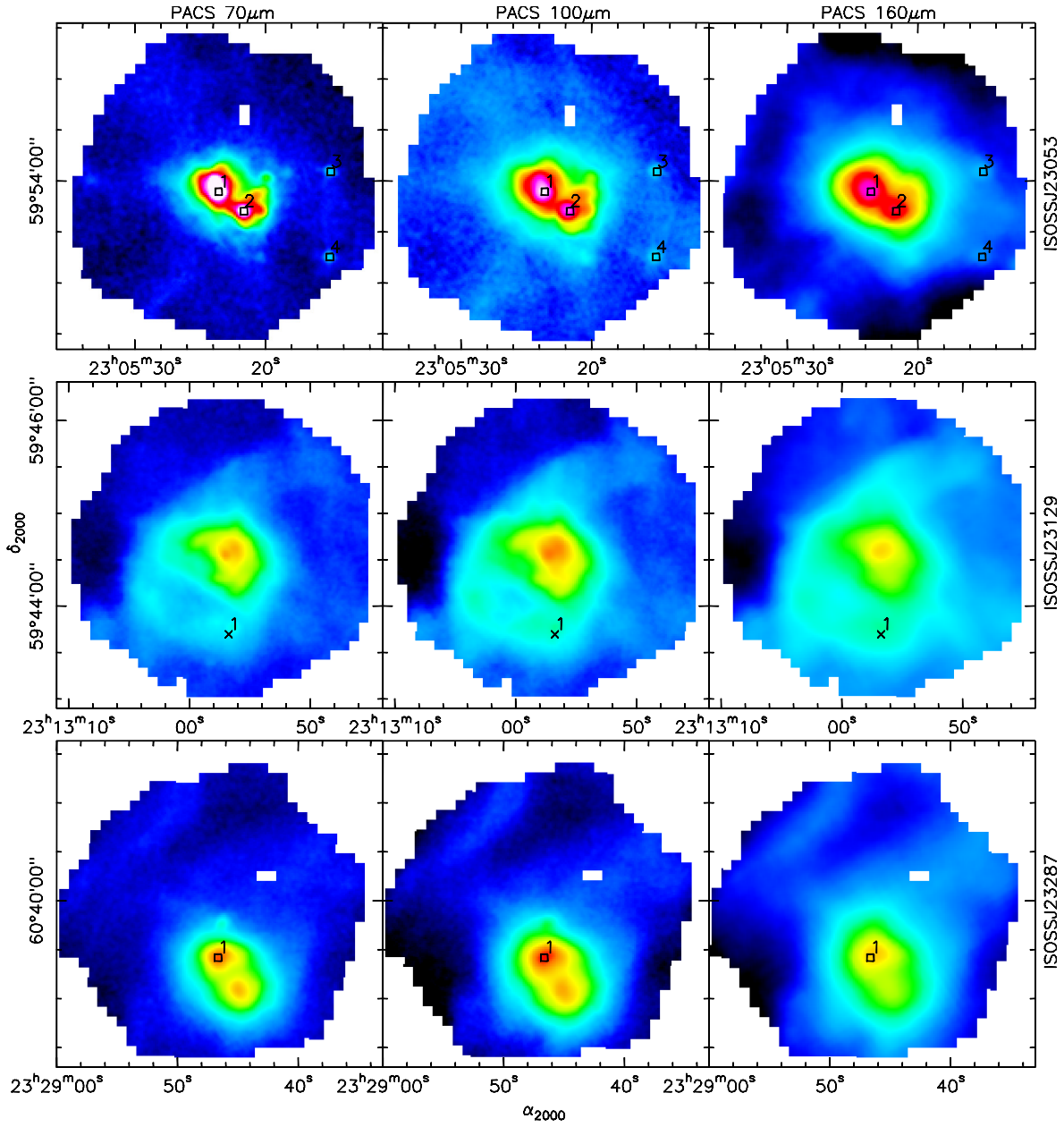

Figure A.15. – Plotted as in Figure A.1.

Danksagung

Ich danke allen die zum Gelingen dieser Arbeit beigetragen haben.
Insbesondere danke ich Prof. Dr. Thomas Henning, der mir bereits mit der Diplomarbeit die Mitarbeit am Max-Planck-Institut für Astronomie ermöglichte und mir mit seinen scharfsinnigen Kommentaren stets neue Ideen und Perspektiven für meine Dissertation und die entstandenen Publikationen gab. Ihm und Prof. Dr. Reinhard Mundt möchte ich zudem danken, dass sie die Begutachtung meiner Dissertation übernommen haben. Meinem Betreuer Dr. Oliver Krause danke ich dafür, dass er mir das Wirken an dieser Doktorarbeit ermöglichte.
Mein besonderer Dank gilt Dr. Amelia Stutz, Dr. Hendrik Linz, Dr. Sarah Ragan, PD Dr. Henrik Beuther, Dr. Dmitry Semenov, Dr. Tatiana Vasyunina und Dr. Jeroen Bouwman für das Korrekturlesen von Teilen meiner Arbeit und die zahlreichen sehr fruchtbaren Diskussionen die letztendlich entscheidend zum Gelingen dieser Arbeit beigetragen haben.
Mein ganz besonderer Dank gilt Dr. Martin Hennemann, der mich in die Thematik der massereichen Sternentstehung eingeführt hat und mir während des ersten Drittels der Doktorarbeit Hilfestellungen gab.
Ohne die Spektroskopie-Software, welche von Dr. Jeroen Bouwman zur Verfügung gestellt wurde, und einiger Routinen zum Fitten des Hintergrunds von Bernhard Sturm, wäre die Qualität der gewonnenen Spektren in Kapitel 2 nicht sicher zu stellen gewesen. Jochen Tackenberg danke ich für seine Einführung in die Radio- und Sub-Millimeter-Beobachtungen. Dr. Ralf Launhardt sei für die Hilfe beim Erstellen der Temperatur-Karte in Kapitel 4 und seine Einführung in das SED-Fitten gedankt.
Darüber hinaus gilt mein Dank all meinen Freunden, insbesondere Paul Boley und Wolfgang Gässler, die mich unterstützt und stets in meiner Arbeit bestärkt haben. Und nicht zuletzt gilt mein Dank meiner lieben Freundin Manuela für Ihre Geduld, Ihren Zuspruch und Ihre Unterstützung, gerade in den letzten anstrengenden Monaten. Natürlich soll auch der Rückhalt durch meine Familie nicht unerwähnt bleiben. Insbesondere die profunden Englischkenntnisse meiner Mutter haben mir geholfen so manche sprachliche Klippe zu umschiffen.